Hierarchically Porous Titania Nanostructures with High Crystallinity: Synthesis and Photocatalytic Application

Lu Cao

Submitted in total fulfillment of the requirements of the degree of Doctor of Philosophy

September 2017

School of Chemistry

The University of Melbourne

Abstract

Water pollution is one of the most pressing issues affecting society, consequently using titanium dioxide (TiO_2) as a photocatalyst for the treatment of polluted water has attracted immense attention over past decades. However, low photocatalytic performance as a result of the fast recombination of photogenerated electron-hole pairs, few active sites and poor light utilization has restrained its real application. This thesis reports the synthesis of various novel TiO_2 photocatalysts with high crystallinity and tailored nanostructures obtained by sol-gel chemistry, templating, self-assembly, solvothermal treatment and calcination.

Mixed-phased hierarchically porous TiO_2 networks (PTN) were prepared through sol-gel chemistry and a templating technique, followed by calcination. The PTN materials possessed reduced contact areas between TiO_2 nanocrystals, significantly retarding the anatase to rutile transformation and rutile crystal growth. Compared to control samples prepared without the template, hierarchical PTN materials showed enhanced photocatalytic activity towards the degradation of methylene blue (MB) under UV light illumination. The material calcined at 600 °C for 6 h contained 15.4 % rutile and had a specific surface area of 32.2 $m^2\ g^{-1}$, giving the highest photocatalytic activity. This enhancement was attributed to optimal rutile content and increased active sites resulting from the high surface area.

Micrometer-size, monodisperse amorphous TiO_2 spheres with controllable sizes were fabricated through a sol-gel process. The monodispersity, spherical shape and size were tuned by varying experimental parameters including the amount of structure-directing hexadecylamine, salt species and concentration, water amount and reaction temperature. The diameter of the spheres was determined by a competitive process between the solubility of Ti oligomers and the hydrolysis rate of titanium isopropoxide, the TiO_2 precursor. Spheres with diameters up to 5.39 ± 0.68 μm were achieved.

The amorphous TiO_2 spheres were readily converted by a solvothermal treatment and calcination process to anatase TiO_2 spheres with three fascinating morphologies: ‘fluffy’ core/shell, yolk/shell and hollow nanostructures. Direct evidence was found that a surface seeding and subsequent inwards hollowing through an Ostwald ripening

process lead to the formation of diverse nanostructures. The hollow microsphere calcined at 650 °C displayed a higher degradation MB rate than the benchmark, commercial Degussa (Evonik) P25. The superior photocatalytic activity of the anatase hollow structures resulted from the unique hollow structure, hierarchically porous shell and high crystallinity.

The amorphous TiO_2 spheres were also readily converted by a solvothermal process to pure anatase TiO_2 with high thermal stability. The resultant microspheres were composed of well-crystallized anatase nanocrystals with a uniform size of 24 nm and a 77 nm pore after calcination at 900 °C. The superior thermal stability was primarily attributed to increased Ti-O-Ti bond strength and narrow crystal size distribution. Microspheres calcined at 800 or 900 °C displayed higher photocatalytic performance than P25 treated at the same temperatures. The excellent performance of the microspheres was attributed to the retention of anatase phase, presence of large pores, high crystallinity and high surface area.

Overall, TiO_2 photocatalyst nanostructures were fabricated by sol-gel chemistry, templating, self-assembly, solvothermal and calcination processes, and exhibited UV light photocatalytic activity that surpassed P25.

Declaration

This is to certify that:

(i) The thesis comprises only my original work towards the PhD except where indicated in the Preface,

(ii) Due acknowledgement has been made in the text to all other material used,

(iii) The thesis is fewer than 100 000 words in length, exclusive of tables, maps, bibliographies and appendices.

Lu Cao

Preface

The work presented in this PhD thesis was discussed and/or carried out after consultation with my principal supervisor, Associate Professor & Reader Rachel A. Caruso (School of Chemistry, University of Melbourne).

The following contributions were also made to this work:

Chapter 3: This chapter contains the following multi-author paper: Cao, L.; Chen, D. H.; Li, W.; Caruso, R. A. Hierarchically Porous Titania Networks with Tunable Anatase:Rutile Ratios and Their Enhanced Photocatalytic Activities. *ACS Applied Materials & Interfaces* 2014, 6, 13129-13137. The thesis author was the primary author, who performed all of the synthesis and writing (with contributions from co-authors), and the majority of data collection and analysis. Dr. Dehong Chen (School of Chemistry) acquired the transmission electron microscopy (TEM) images, contributed important suggestions and comments, and revised the manuscript. Dr. Wei Li (CSIRO Clayton) contributed suggestions and comments, and revised the manuscript. Except for the publication as specified, and notwithstanding discussions held with co-authors, the thesis author asserts that all other work in this chapter is original.

Chapter 4: The thesis author was the primary author, who performed all of the synthesis and writing and the majority of data collection and analysis. Dr. Dehong Chen acquired TEM images and some of the scanning electron microscopy images, contributed important suggestions and comments, and helped to revise the manuscript. Notwithstanding discussions held with colleagues, the thesis author asserts that all other work in this chapter is original.

Chapter 5: This chapter contains the following multi-author paper: Cao, L.; Chen, D. H.; Caruso, R. A. Surface-Metastable Phase-Initiated Seeding and Ostwald Ripening: A Facile Fluorine-Free Process towards Spherical Fluffy Core/Shell, Yolk/Shell, and Hollow Anatase Nanostructures. *Angewandte Chemie International Edition* 2013, 52, 10986-10991. The thesis author was the primary author, who performed all of the synthesis and writing (with contributions from co-authors), and the majority of data collection and analysis. Dr. Dehong Chen acquired TEM images, contributed important suggestions and comments, and revised the manuscript. Dr. Simon

Crawford (Melbourne Advanced Microscopy Facility) ultramicrotomed samples in preparation for TEM characterization. Dr. Xiaofei Duan and Dr. David Parris (both School of Chemistry) acquired X-ray photoelectron spectroscopy (XPS) and X-ray diffraction (XRD) results, respectively. Except for the publication as specified, and notwithstanding discussions held with co-authors, the thesis author asserts that all other work in this chapter is original.

Chapter 6: This chapter contains the following multi-author paper: Cao, L.; Chen, D. H.; Wu, W. Q.; Caruso, R. A. Monodisperse Anatase Titania Microspheres with High-thermal Stability and Large Pore Size (~80 nm) as Efficient Photocatalysts. *J .Mater. Chem. A* 2017, 5, 3645-3654. The thesis author was the primary author, who performed all of the synthesis and writing (with contributions from co-authors), and the majority of data collection and analysis. Dr Dehong Chen acquired TEM images, contributed important suggestions and comments, and helped to revise the manuscript. Mr Wuqiang Wu (School of Chemistry) contributed suggestions and comments, and helped to revise the manuscript. Ms Jennie Ziang Yie Tan (CSIRO, Clayton) collected Raman data, contributed suggestions and comments, and helped to revise the manuscript. Dr. Simon Crawford ultramicrotomed samples in preparation for TEM characterization. Dr. Xiaofei Duan and Dr. David Parris acquired XPS and XRD results, respectively. Except for the publication as specified, and notwithstanding discussions held with co-authors, the thesis author asserts that all other work in this chapter is original.

List of Publications and Activities during PhD

Publications:

1. **Cao, L.**, Chen, D. H., Wu, W. Q., Tan J. Z. Y., Caruso, R. A.,
Monodisperse Anatase Titania Microspheres with High-thermal Stability and Large Pore Size (~80 nm) as Efficient Photocatalysts
J .Mater. Chem. A, *5*, 3645-3654, **2017**.

2 Rodriguez, E. F., Chen, D. H., Hollenkamp A. F., **Cao, L.**, Caruso, R. A.,
Monodisperse mesoporous anatase beads as high performance and safer anodes for lithium ion batteries
Nanoscale, *7*, 17947-17956, **2015**.

3. **Cao, L.**, Chen, D. H., Li, W., Caruso, R. A.,
Hierarchically Porous Titania Networks with Tunable Anatase:Rutile Ratios and Their Enhanced Photocatalytic Activities
ACS Appl. Mater. Interfaces, *6*, 13129-13137, **2014**.

4. Huang, F. Z., Chen, Y., Xiang, W. C., Chen, D. H., **Cao, L.**, Spiccia, L., Caruso, R. A., Cheng, Y. B.
Effect of TiO_2 Microbead Pore Size on the Performance of DSSCs with Cobalt-based Electrolyte
Nanoscale, *6*, 13787-13794, **2014**.

5. **Cao, L.**, Chen, D. H., Caruso, R. A.,
Surface-Metastable Phase Initiated Seeding and Ostwald Ripening: A Facile Fluorine-Free Process towards Spherical Fluffy Core/Shell, Yolk/Shell, and Hollow Anatase Nanostructures
Angew. Chem. Int. Ed., *52*, 10986-10991, **2013**. (Frontispiece paper & highlighted in 'Chemistry in Australia' magazine)

6. Wang, X. D., **Cao, L.**, Chen, D. H., Caruso, R. A.,
Engineering of Monodisperse Mesoporous Titania Beads for Photocatalytic Applications
ACS Appl. Mater. Interfaces, *5*, 9421-9428, **2013**.

7. Wang, X. J., Chen, D. H., **Cao, L.**, Li, Y., Boyd B. J., Caruso, R. A.,
Mesoporous Titanium Zirconium Oxide Nanospheres with Potential for Drug Delivery Applications
ACS Appl. Mater. Interfaces, *5*, 10926-10932, **2013**.

8. Chen, D. H., Huang, F. Z., **Cao, L.**, Cheng, Y. B., Caruso, R. A.,
Spiky Mesoporous Anatase Titania Beads: a Metastable Ammonium Titanate-Mediated Synthesis
Chem. Eur. J., *18*, 13762-13769, **2012**.

9. Chen, D. H., **Cao, L.**, Hanley T. L., Caruso, R. A.,
Facile Synthesis of Monodisperse Mesoporous Zirconium Titanium Oxide

Microspheres with Varying Compositions and High Surface Areas for Heavy Metal Ion Sequestration
Adv. Funct. Mater., *22*, 1966-1971, **2012**.

10. Huang, F. Z., Chen, D. H., **Cao, L.**, Caruso, R. A., Cheng, Y. B.,
Flexible Dye-sensitized Solar Cells Containing Multiple Dyes in Discrete Layers
Energy Environ. Sci., *4*, 2803-2806, **2011**.

11. Chen, Y., Huang, F. Z., Chen, D. H., **Cao, L.**, Zhang, X. L., Caruso, R. A., Cheng, Y. B.,
Effect of Mesoporous TiO_2 Bead Diameter in Working Electrodes on Dye-sensitized Solar Cell Efficiency
ChemSusChem, *4*, 1498-1503, **2011**.

Conference and workshop presentation:

1. **Cao, L.**, Chen, D. H., Li, W., Caruso, R. A.,
Hierarchically Porous Titania Networks with Tunable Anatase:Rutile Ratios and Their Enhanced Photocatalytic Activities
3rd biennial conference of the Combined Australian Materials Societies (CAMS2014), Charles Perkins Center, The University of Sydney, Sydney, Australia, 26-28 November, **2014**. (Oral)

2. **Cao, L.**, Chen, D. H., Caruso, R. A.,
Fluffy Core/Shell, Yolk/Shell and Hollow Anatase Nanostructures for High Efficiency Photocatalysis Application
8th Pacific Rim International Conference on Advanced Materials and Processing (PRICM-8), Hillton Waikoloa Village, Waikoloa, Hawaii, USA, 4-9 August., **2013**. (Poster**)**

3. **Cao, L.**, Chen, D. H., Caruso, R. A.,
Self-templating Synthesis of TiO_2 Hollow Particles and their Excellent Photocatalytic Activities
7th International Conference on Materials for Advanced Technologies (ICMAT-2013), Suntec Convention Centre, Singapore, 30 June-5 July, **2013.** (Oral)

4. **Cao, L.**, Chen, D. H., Caruso, R. A.,
Monodisperse Mesoporous Titania Microspheres with Tunable Diameter and Pore Size, and Pd Loading Capacities for Effective Reduction Catalysis
7th International Conference on Materials for Advanced Technologies (ICMAT-2013), Suntec Convention Centre, Singapore, 30 June-5 July, **2013.** (Oral)

5 **Cao, L.**, Chen, D. H., Caruso, R. A.,
Porous Titania Networks with Controllable Rutile Ratios and their Enhanced

Photocatalytic Activities
The 16th International Sol-Gel Conference, Hangzhou, China, 28 August-2 September, **2011**. (Oral)

6. **Cao, L.**, Chen, D. H., Caruso, R. A.,
Porous Titania Heterostructures with High Surface Areas and their Enhanced Photocatalytic Activities
The 9th International Meeting of Pacific Rim Ceramic Societies (PacRim 9), Cairns Convention Centre, Cairns, Queensland, Australia, 10-14 July, **2011**. (Oral)

7. **Cao, L.**, Chen, D. H., Caruso, R. A.,
Porous Titania Networks with Controllable Rutile Ratios and Enhanced Photocatalytic Activities
5th Victorian Chinese PhD Students and Young Scholars Research Workshop, The University of Melbourne, Melbourne, Australia, 12 November, **2011**. (Oral)

8. **Cao, L.**, Chen, D. H., Caruso, R. A.,
Spherical Anatase Titania with Integrated Features and their Photovoltaic Application
5th Victorian Chinese PhD Student and Young Scholars Research Workshop, The University of Melbourne, Melbourne, Australia, 12 November, **2011**. (Best poster award)

Awards:

1. Chinese Government Award for Outstanding Self-financed Students Abroad, **2014.**
2. Australian Postgraduate Award, The University of Melbourne, **2011-2014**.
3. MMI-CSIRO Materials Science PhD Top-up Scholarship, Melbourne Materials Institute, The University of Melbourne, **2011-2014**.
4. Australian Ceramic Society bursary to attend CAMS2014 conference at The University of Sydney, **2014**.
5. T. W. Healy Travel Award, The University of Melbourne, **2013**.
6. Travel Award, Particulate Fluids Processing Centre, The University of Melbourne, **2011**.
7. Best poster award, 5th Victorian Chinese PhD Student and Young Scholars Research Workshop, **2011**.

Acknowledgments

There are many people who I would like to thank when looking back over my years at the University of Melbourne.

First and foremost, I am deeply indebted to my supervisor Associate Professor & Reader Rachel A. Caruso. Rachel's continuous support of my research all these years, as well as her patience, motivation, enthusiasm and immense knowledge, was essential for the completion of this work. I really appreciated the flexible work time I have had, and the understanding from her that allowed me to have my son and daughter and take good care of them during my PhD study – it has meant a lot to me. In addition, I was generally afforded several opportunities by her to attend national and international conferences – it has been really much appreciated.

It is also a great pleasure for me to thank the rest of my thesis committee, Professor Frances Separovic and Professor Muthupandian Ashokkumar for their encouragement, guidance and insightful suggestions throughout my PhD study.

I would like to thank and acknowledge Professor Yi-Bing Cheng of Monash University for his guidance in the early stages of my PhD study.

I am grateful for the financial support for my PhD study. I acknowledge receipt of an Australia Postgraduate Award and a MMI-CSIRO PhD Materials Science Top-up. I also acknowledge the receipt of a Particulate Fluids Processing Centre (PFPC) travel award. This award enabled me to travel to Hangzhou, China to attend the 16th International Sol-Gel Conference. I thank the School of Chemistry for a T. W. Healy Award for supporting me to travel to Singapore to attend the 7th International Conference on Materials for Advanced Technologies (ICMAT-2013). It was a great opportunity to meet and learn from devoted experts in the field. I acknowledge the receipt of a bursary from the Australian Ceramic Society to allow me to attend the 3rd Biennial Conference of the Combined Australian Materials Societies (CAMS2014) at the University of Sydney. I also thank the Chinese Association of Professionals and Scholars for organizing research workshops every year and presenting me the best poster award in the 5th Victorian Chinese PhD Student and Young Scholars Research Workshop.

I would like to acknowledge the School of Chemistry, Particulate Fluids Processing Center (PFPC), Surface and Chemical Analysis Network (SCAN) and Materials Characterisation and Fabrication Platform all at the University of Melbourne for access to facilities and infrastructure, as well as the Melbourne Advanced Microscopy Facility, Bio21 Institute, where the electron microscopy studies were conducted.

I wish to express my appreciation to the wonderful people that I have been fortunate to come across. To my fellow group members (University and CSIRO, past and present), the Sonochemistry group and my friends: Thank you for sharing your knowledge and passion for science, and for the encouragement and great times together! Here, I would like to especially mention some people. A big thank to Dr. William McMaster for his invaluable advice and kind help in many aspects including TGA training. I wish him all the best for the future! I thank Dr. David Parris for conducting XRD characterization, teaching me some laboratory methods and showing me how to use the UV-vis instruments. I really appreciate Dr. Ida E. Widnersson for showing me how to measure particle size and other laboratory methods. I also thank Mr. Hao Wei for running XRD samples.

There are staff at the University of Melbourne who should be recognized for their help over the years: Dr. Simon Crawford, Mr. Bryan McGown, Mrs. Sioe See Volaric, Mr. Ross Lineham, Mr. Brendan Mangan, Mr. Les Gamel, Mr. Roger Curtain, Dr. Sergey Rubanov and Dr. Xiaofei Duan. Specifically, Simon from Botany is thanked for ultramicrotoming samples in preparation for TEM characterization; Sioe See is thanked for providing assistance with the ATR-IR measurements; Ross from the Chemistry Store is appreciated for supplying chemicals and laboratory accessories promptly; Roger at the Melbourne Advanced Microscopy Facility (Bio21) is thanked for helping me with SEM, and; Xiaofei from SCAN is appreciated for acquiring XPS results and helpful discussions.

I consider myself immensely fortunate to have Xiaolan Zhu, Lianying Hao and Jinghua Fang as my best friends. I thank you all for being beside me in such critical phases of my personal life.

Last, but not least, I would like to thank my amazing family for the priceless love, constant support and encouragement I have received over the years. In particularly, I

would like to thank my parents-in-law from the bottom of my heart for taking care of my children with natural love and treating me as their daughter. I undoubtedly could not have completed my thesis without their unselfish dedication. I also would like to thank my husband for being with me at every step of the journey. In addition, I am very grateful to have two healthy and lovely children during my PhD study, Ethan and Kailin, who bring numerous times of happiness and pleasant surprises for me every day and motivate me to work hard to provide a better future for them.

Table of contents

List of Figures

List of Tables

List of Schemes

List of Abbreviations

AOT	Advanced Oxidation Technology
APS	Amorphous Precursor Spheres
BET	Brunauer-Emmett-Teller
BJH	Barrett-Joyner-Halenda
CB	Conduction Band
DRS	Diffuse Reflectance Spectroscopy
DTA	Differential Thermal Analysis
e^-	Electron
E_{gb}	Bandgap Energy
h^+	Hole
IPCE	Incident Photon-to-current Conversion Efficiency
OH	Hydroxyl
MB	Methylene Blue
MATSs	Monodisperse Amorphous Titania Spheres
MMTSs	Micrometer-sized Monodisperse Mesoporous Titania Spheres
MTS	Monodisperse Titania Spheres (MTS)
PTN	Porous Titania Networks
SAED	Selected Area Electron Diffraction
SEM	Scanning Electron Microscopy
TEM	Transmission Electron Microscopy
TGA	Thermogravimetric Analysis
TiO_2	Titanium Dioxide
TIP	Titanium(IV) Isopropoxide
UV	Ultraviolet
VB	Valence Band
Vis	Visible
XRD	X-ray Diffraction
XPS	X-ray Photoelectron Spectrometer

Chapter 1. Introduction

1.1 The Global Water Issue

With increasing global population growth and urbanization, environmental pollution, such as contaminated water, has emerged as one of the most pressing issues affecting the sustainable development of society. Water becomes polluted from toxic substances that are discharged from household sewage, livestock waste, agricultural pesticides and fertilizers and industrial waste. Every day, two million tons of sewage from human activities are released into the world's water.[1] These pollutants come in the forms of organic, inorganic, and sometimes even radioactive waste. Clean freshwater is an essential element for a healthy human life, but it is limited on Earth. Up to 1.1 billion people cannot access sufficient water. In addition, 2.5 billion have no adequate sanitation and 70% of these people live in Asia.[2] People who drinking polluted water are subject to waterborne diseases and a myriad of health concerns. Waterborne disease is the world leading killer of children under 5 years old. More people die from contaminated and polluted water annually than from all forms of violence including war.[3] Each year there are approximately 4 billion cases of diarrhoea caused by unsafe water around the world, resulting in 2.2 million deaths. A large number of people with health problems caused by polluted water are from developing countries, such as Bangladesh, China, India and Vietnam. In India alone, half a million children die each year from diarrhoea caused by polluted water.[4] Nearly 70 million people living in Bangladesh are either directly or indirectly exposed to groundwater contaminated with arsenic beyond the recommended limits (10 μg/L) of the World Health Organization (WHO).[5] In China, more than 26 million people suffer from dental fluorosis as a result of elevated fluoride in their daily drinking water.

1.2 Water Treatment Techniques

To ensure that water quality is suitable for its end use, treatments are applied to polluted water to either remove the majority of contaminants or reduce them to safe levels. Different water treatment processes are employed for a range of purposes, such as human consumption, agriculture, industry and recreation. In general, the technologies conventionally used include physical processes such as heat treatment, sedimentation or distillation; chemical processes such as chlorination or coagulation, and; biological processes including aerated lagoons or activated sludge.[6] In real

applications worldwide, combinations of approaches are employed for water treatment.

However, conventional wastewater treatment technologies cannot meet the demand for the purification of polluted water due to both the increasing levels and complexity of pollutant effluents.[7] Recently, a range of advanced chemical processes termed advanced oxidation technology (AOT) have been developed to treat polluted water through degrading a variety of biological contaminants and organic pollutants. Although different processes utilize various reaction mechanisms, all are characterized by the production of highly oxidative hydroxyl (•OH) radicals. •OH radicals are known as extraordinarily reactive species, usually attacking most organic molecules with high rate constants of 10^6-10^9 $M^{-1}s^{-1}$.[8] In addition, chain reactions can be triggered by the produced radicals under suitable conditions. Therefore, a non-selective high reaction rate and potential chain reaction of •OH radicals give AOT processes a much more powerful oxidation capacity than conventional chemical oxidation methods.

There are a number of different AOT reactant possibilities, such as H_2O_2/Fe^{2+} (Fetton), H_2O_2/Fe^{3+} (Fetton-like), $H_2O_2/Fe^{2+}(Fe^{3+})$/UV (photo-assisted Fetton), $TiO_2/h\nu/O_2$ (photocatalysis) and ozone chemistry. Amongst them, semiconductor TiO_2 photocatalysis has received increasing attention,[9-12] because it is a promising environmentally friendly technology to reduce or eliminate hazardous substances. TiO_2 photocatalysts have been widely studied with the aim to clean up pollution since the 1970s.[13] However, practical technology was not developed until the late 1990s. For example, as shown in Figure 1, a pilot plant was installed in a factory in Wolfsburg, Germany during the summer of 1998 for the solar photocatalytic treatment of biologically pre-treated industrial wastewater.[14] In addition, Japanese scientists have constructed practical systems using TiO_2 photocatalysts for the purification of wastewater from agriculture and soils polluted by volatile organic compounds.[13] One technology was developed to purify wastewater obtained from rice hull disinfection, which contains highly concentrated agricultural chemicals. The approach was straightforward with the wastewater being poured onto glass wool mats containing the photocatalyst, which were widely spread on the ground in open areas. After a few days of exposure to solar light, the chemicals in the wastewater were

completely decomposed. Another example is a water recycling system using a TiO_2 photocatalyst constructed in a hydroponic tomato culturing system. Organic contaminations in the wastewater caused by nutrient compounds were easily decomposed under solar light in a shallow container with an area of 4 m^2 and a depth of 10 cm.

Figure 1.1. A pilot plant for the solar photocatalytic treatment of a biologically pre-treated wastewater. Reproduced with permission.[14] Copyright 2014, Elsevier.

The past few decades have seen many advances in the fabrication of diverse nanomaterials and exploration of novel applications. New physical and chemical properties of TiO_2 emerge when particle size, crystal phase, crystallinity, composition, specific surface area, porosity and morphology are varied, giving rise to considerable improvements in the performance of the resultant TiO_2 materials.

1.3 Objectives and Thesis Outline

TiO_2 nanomaterials with complex morphologies exhibit unique properties that have led to their improved effectiveness in diverse applications. This thesis aims to prepare TiO_2 materials with tailored nanostructures to enhance their performance in (photo-) catalysis. To meet this aim, three objectives were set for this thesis:

1) To use a highly porous template to control the crystal phase composition (anatase/rutile) of a porous TiO_2 network by sol-gel chemistry and templating.

2) To increase the size of amorphous TiO_2 spheres, which are the precursor material to mesoporous TiO_2 spheres, by changing the synthesis parameters (amount of surfactant, salt species and concentration, water amount and reaction temperature).

3) To vary solvothermal conditions (solvent composition, solvothermal treatment time and reaction temperature) to control the morphology of the mesoporous TiO_2 spheres including the pore diameter, surface area, crystallinity and structure evolution.

A review of relevant literature in Chapter 2 gives the background for the research in this thesis. The significance of TiO_2 research and TiO_2 as a photocatalyst is highlighted. Then the structural properties of TiO_2 nanomaterials, along with the thermodynamic stability of different crystal phases and the kinetics of the phase transformation are discussed. Research on the fabrication of porous TiO_2 spheres, hollow TiO_2 spheres and hierarchically porous TiO_2 networks is summarised. Lastly, the application of highly crystalline porous TiO_2 nanostructures in photocatalysis is described.

Chapter 3 presents the synthesis and characterisation of mixed-phase hierarchically porous TiO_2 networks with three-dimensional interconnected porous frameworks and tunable rutile content. These networks are applied as photocatalysts for the degradation of methylene blue (MB). This chapter appears as a publication by the thesis author and is presented in the published format.[15]

In Chapter 4 the synthesis of micrometer-size, monodisperse precursor TiO_2 spheres with controlled size is detailed. Crystallized mesoporous TiO_2 spheres with varying pore sizes are obtained when the precursor spheres are solvothermally treated. The mesoporous TiO_2 spheres are then loaded with Pd nanoparticles and their catalytic performance tested by monitoring the reaction of 4-nitrophenol in the presence of sodium borohydride.

Surface seeding and subsequent inwards hollowing of TiO_2 spheres through an Ostwald ripening process is demonstrated in Chapter 5 for the formation of diverse TiO_2 nanostructures (spherical ‘fluffy’ core/shell, yolk/shell and hollow). The photocatalytic activity of these materials is tested, and the correlation between material properties and photocatalytic activity is discussed. This chapter appears as a publication by the thesis author and is presented in the published format.[16]

The fabrication of monodisperse dopant-free anatase TiO_2 microspheres with high-thermal stability and large pore size (approximately 80 nm) is described in Chapter 6. Possible reasons for the superior thermal stability of these microspheres are investigated and discussed. The photocatalytic activity of the TiO_2 microspheres is evaluated by degradation of MB under UV illumination.

Chapter 7 summarizes the key research findings and closes with an outlook for further research based on the findings from this thesis.

1.4 References

1. UN WWAP. 2003. United Nations World Water Assessment Programme. The World Water Development Report 1: Water for People, Water for Life. UNESCO: Paris, France.
2. UNICEF WHO 2008. UNICEF and World Health Organization Joint Monitoring Programme for Water Supply and Sanitation. Progress on Drinking Water and Sanitation: Special Focus on Sanitation. UNICEF, New York and WHO, Geneva, 2008.
3. World Health Organization (WHO). (2002). World Health Report: Reducing Risks, Promoting Healthy Life. France. Retrieved 14 July 2009, from http://www.who.int/whr/2002/en/whr02_en.pdf.
4. World Health Organization and United Nations Children's Fund. (WHO and UNICEF). (2000). Global Water Supply and Sanitation Assessment 2000 Report. WHO and UNICEF Joint Monitoring Programme for Water Supply and Sanitation.
5. UN WWAP. 2009. United Nations World Water Assessment Programme. The World Water Development Report 3: Water in a Changing World. UNESCO: Paris, France.
6. Cheremisinoff, N. P., *Handbook of Water and Wastewater Treatment Technologies, Butterworth-Heinemann*. 2002.
7. Abdel-Raouf, N.; Al-Homaidan, A. A.; Ibraheem, I. B. M., *Saudi J. Biological Sci.* **2012**, *19*, 257-275.
8. Andreozzi, R.; Caprio, V.; Insola, A.; Marotta, R., *Catal. Today* **1999**, *53*, 51-59.
9. Chen, X.; Mao, S. S., *Chem. Rev.* **2007**, *107*, 2891-2959.

10. Hoffmann, M. R.; Martin, S. T.; Choi, W. Y.; Bahnemann, D. W., *Chem. Rev.* **1995**, *95*, 69-96.
11. Linsebigler, A. L.; Lu, G. Q.; Yates, J. T., *Chem. Rev.* **1995**, *95*, 735-758.
12. Schattka, J. H.; Shchukin, D. G.; Jia, J. G.; Antonietti, M.; Caruso, R. A., *Chem. Mater.* **2002**, *14*, 5103-5108.
13. Hashimoto, K.; Irie, H.; Fujishima, A., *Japanese J. Appl. Phys.* **2005**, *44*, 8269-8285.
14. Alfano, O. M.; Bahnemann, D.; Cassano, A. E.; Dillert, R.; Goslich, R., *Catal. Today* **2000**, *58*, 199-230.
15. Cao, L.; Chen, D. H.; Li, W.; Caruso, R. A., *ACS Appl. Mater. Interfaces* **2014**, *6*, 13129-13137.
16. Cao, L.; Chen, D.; Caruso, R. A., *Angew. Chem. Int. Ed.* **2013**, *52*, 10986-10991.

Chapter 2. Highly Crystalline Porous TiO_2 Nanostructures: Synthesis and Photocatalytic Applications

2.1 Introduction

In 1972, Japanese chemists Fujishima Akira and Kenichi Honda reported the possibility of photocatalytically splitting H_2O into H_2 and O_2 on a TiO_2 electrode irradiated with ultraviolet (UV) light and reported this breakthrough in Nature.[1] Since then, a tremendous research effort has been devoted to the study of TiO_2 materials, particularly since the beginning of this century (Figure 2.1). This makes sense when one considers the distinguishing properties of TiO_2 including its nontoxicity, excellent photo- and chemical stability, superior photocatalytic activity, as well as being abundant and low cost. Hence it has a myriad of applications from pigment, cosmetic, toothpaste, and paint to promising functional areas, such as photocatalysis, photovoltaics, lithium ion batteries and catalysis. These emerging functional applications of TiO_2 mainly fall within the scope of energy and environment, two important and challenging themes facing humanity that need to be addressed urgently.

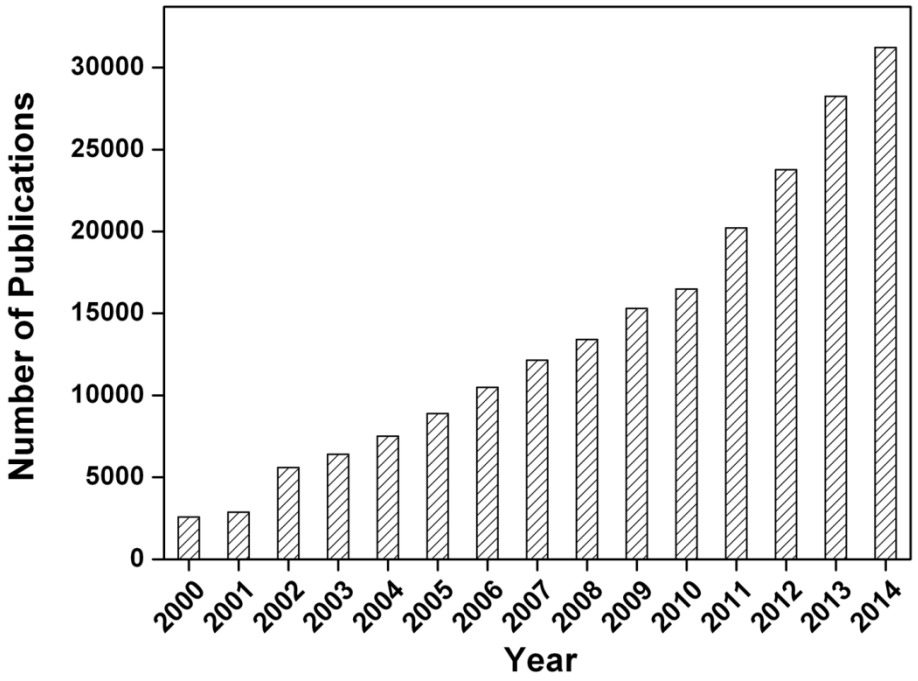

Figure 2.1. The annual number of publications on TiO_2 from 2000 to 2014. The data was collected based on the Web of Science database when a retrieval search for the topic "TiO_2 or titanium dioxide or titania" was performed on 8 August 2015.

2.1.1 TiO_2 Materials as Photocatalysts

Although a broad spectrum of semiconductors have been extensively investigated as photocatalysts, including traditional materials such as TiO_2,[1] WO_3,[2, 3] CdS,[4] and $SrTiO_3$[5] and recently reported novel materials like CoO,[6] Ag_3PO_4,[7] C_3N_4,[8] and metal–organic framework based materials,[9, 10] TiO_2 remains to date the most popular material due to its aforementioned unique properties and is widely considered as a benchmark in the domain of photocatalysis. The areas for application of TiO_2 as a photocatalyst involve: 1) sterilization, e.g., anti-bacterial, anti-viral and fungicide, 2) self-cleaning surfaces, 3) deodorizing and air purification systems, 4) water treatment (organic decomposition), 5) anti-fogging highly hydrophilic materials, and 6) hydrogen generation. This thesis will mainly focus on the photocatalytic decomposition of organics for the remediation of polluted water. Degradation of organic dyes in aqueous solutions, such as methylene blue,[11-13] rhodamine B,[14-17] methyl orange,[18, 19] and sulforhodamine B,[20] have been widely applied to assess liquid phase photocatalytic performance.

The principle of the TiO_2 semiconductor photocatalytic reaction is straightforward, and the photocatalytic progress can be represented by the following reactions:

Excitation $TiO_2+h\nu \rightarrow h^+ + e^-$ (1)

Hole charge transfer $h^+ + H_2O \rightarrow \bullet OH + H^+$ (2)

Electron charge transfer $e^- + O_2 \rightarrow \bullet O_2^- + H_2O \rightarrow \bullet OH$ (3)

Oxidation $\bullet OH + O_2 + C_xO_yH_{(2x-2y+2)} \rightarrow xCO_2 + (x-y+1)H_2O$ (4)

Recombination $TiO_2^- + \bullet OH + H^+ \rightarrow TiO_2 + H_2O$ (5)

In the photocatalytic reaction, organic waste is broken down into harmless substances in the presence of the TiO_2 photocatalysts, an energetic light source (e. g., UV or visible light), and an oxidizing agent (e.g., oxygen or air).[21] The photocatalyst itself remains unconsumed during the process. The first step in the heterogeneous photocatalysis of organic chemicals is the interaction of the semiconductor with light, which results in the creation of electron–hole pairs in the semiconductor particles. When a photon with an energy, *hv*, equal to or exceeding the band gap energy, ΔE_{bg}, of TiO_2 is adsorbed, an electron (e^-) is excited and transfers from the valence band (VB) to the conduction band (CB), while a positive hole (h^+) is left in the VB, thus creating active electron–hole (e^-–h^+) pairs (equation 1). The photogenerated positive holes migrate to the TiO_2 surface and typically interact with adsorbed water molecules,

producing hydroxyl radicals (•OH) (equation 2). Meanwhile, excited electrons in the CB migrate to the surface and react with molecular oxygen to generate superoxide radical anions (O_2^-), which oxidize water and form •OH (equation 3). Ultimately, the very oxidative •OH are generated in both reactions, giving rise to the decomposition of the organic pollutants adsorbed on the TiO_2 surface (equation 4). However, another type of de-excitation process, in which the electron-hole pair undergoes recombination on the surface or inside the bulk of TiO_2 competes with photocatalysis (equation 5) and can significantly decrease the overall efficiency of the photoinduced catalytic process.

The photocatalytic activity of a semiconductor catalyst is principally dominated by the following three aspects: 1) the light absorption performance, 2) reduction and oxidation rates, and 3) the electron-hole recombination rate.[22] Many factors can affect the photocatalytic activity of a catalyst, such as its crystallinity, surface area and crystal phase. As photocatalytic reactions take place on the surfaces of photocatalysts, a high surface area is favourable for photocatalytic reactions as it usually provides more reaction sites. However, high surface area materials usually also contain high quantities of crystal defects, which enhance the recombination of electrons and holes and render poor photoactivity. High crystallinity benefits the photocatalytic performance because it could decrease the recombination rate of the photogenerated charge carriers and increase the electron diffusion lengths and lifetimes. Improved crystallinity and fewer defects can be achieved by some heat treatment approaches (e.g., calcination or solvothermal treatment). However, in most cases, heat treatment results in decreased surface area. The relationship between physical properties and the photocatalytic performance of a material is very complicated, therefore, a balance in the material properties must be sought in order to optimise photocatalytic efficiency.

Nanostructured TiO_2 materials have been widely used in photocatalysis. Recently, the construction of TiO_2 nanostructures with fascinating morphologies and unique properties has attracted attention. Consequently, versatile TiO_2 nanostructures, such as nanorods, fibers (wires), tubes, sheets, spheres and interconnected architectures have been prepared. The structure of TiO_2 materials can significantly affect properties and capabilities, including specific surface area, pore size, porosity, crystallinity, light

adsorption, reflectance and scattering, dispersion, adhesion, and charge carrier transportation properties, and most importantly photocatalytic performance.

The aim of this literature review is to establish the background for the thesis research presented in Chapter 3 to 6. Research on the synthesis of TiO_2 nanostructures and their application in photocatalysis is very broad. This chapter presents a brief introduction to the fabrication of porous TiO_2 spheres, hollow TiO_2 spheres and hierarchically porous TiO_2 networks, and then the photocatalytic application of highly crystalline porous TiO_2 nanostructures. Finally, a summary of the reviewed research along with a brief future perspective is provided.

2.2 Properties of TiO_2 Nanomaterials

2.2.1 Structural Properties of TiO_2 Nanomaterials

There are at least eleven crystalline phases for TiO_2 including anatase, rutile, brookite, TiO_2(B), the hollandite-like phase TiO_2(H), the ramsdellite (MnO_2 or VO_2)-like phase TiO_2(R), the columbite (α-PbO_2)-like phase TiO_2(II), the baddeleyite (ZrO_2)-like phase, the fluorite (CaF_2)-like cubic phase, TiO_2-OI and the cotunnite ($PbCl_2$)-like phase TiO_2-OII.[23] The stability of these phases has been investigated in previous work and summarized by Zhang *et al.*[23] The first six phases are stable at ambient or low-pressure while the latter five are high pressure phases. Their densities range from approximately 3.5 g cm^{-3} for TiO_2(H) to 5.8 g cm^{-3} for cubic phase TiO_2. Of all the TiO_2 crystal phases, anatase and rutile have been the most studied.

Figure 2.2 shows ball-and-stick and polyhedron models of anatase and rutile TiO_2.[23] These two structures are depicted in terms of chains of TiO_6 octahedron fundamental building blocks, where each Ti^{4+} ion is encircled by six O^{2-} ions in the form of an octahedron. The differences between these two crystal structures are the distortion of each octahedron and the assembly pattern of the octahedron chains. The octahedron in rutile is not that regular, demonstrating a slight orthorhombic distortion. However, the symmetry of anatase is lower than orthorhombic because the octahedron in anatase is significantly distorted. The Ti-Ti distances in rutile are 3.57 and 2.96 Å, while distances in anatase are larger at 3.79 and 3.04 Å. Conversely, the Ti-O distances in anatase at 1.934 and 1.980 Å are shorter than rutile, 1.949 and 1.980 Å. In the anatase structure, each octahedron is in contact with eight neighbours, four share edge oxygen pairs and four share corner oxygen atoms. While in the rutile structure, two share an

edge and eight share a corner, that is each octahedron is in contact with ten neighbour octahedrons. These differences in lattice structures lead to different mass densities (3.8-3.9 and 4.2-4.3 g cm^{-3} for anatase and rutile, respectively) and electron band structures for the two main TiO_2 phases.[23, 24]

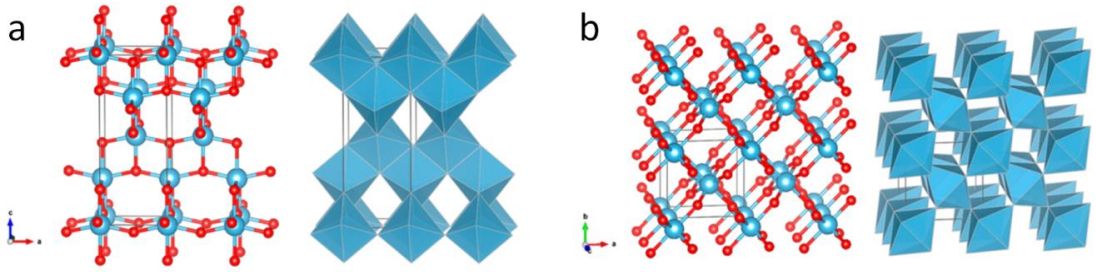

Figure 2.2. Ball-and-stick and polyhedron models of (a) anatase and (b) rutile TiO_2. The red balls and blue balls represent O atoms and Ti atoms, respectively. Unit cells are outlined using thin lines. Reproduced with permission.[23] Copyright 2014, American Chemical Society.

2.2.2 Thermodynamic and Kinetic Properties of TiO_2 Nanomaterials

Thermodynamically, rutile is generally considered the most stable phase, while anatase is metastable and can be easily transformed into rutile at elevated temperature. Anatase phased nanomaterials can be found in natural or synthesised systems. High temperature annealing (500-700 °C) usually gives rise to rutile TiO_2 and this phase transformation process is irreversible. Control of the experimental conditions to manipulate the anatase to rutile phase transformation is critical and meaningful, particularly for high-temperature applications. For example, in the case of gas sensors and porous membranes for gas separation or catalysis, the anatase to rutile phase transformation may occur, thereby affecting or even altering the performance of these devices.[25] For the use of TiO_2 in self-sterilizing photocatalytic coatings, the coatings applied on ceramic substrates need to be processed at high temperature (≥800 °C).[26] Therefore, employing a high performance anatase photocatalyst that can withstand the sintering temperature of the ceramic substrates is required. Thus, understanding the kinetics of their phase transformation and factors affecting the kinetics is essential to obtain desirable TiO_2 composites (single phase or mixed phase) and therefore material properties.

The phase transformation process from anatase to rutile is reconstructive, which involves the breaking and reforming of 7 of 24 Ti-O bonds per unit cell[27] and sufficient thermal energy is required to facilitate the rearrangement of Ti and O atoms. The required activation energy is diverse, ranging from 150 to 850 kJ mol^{-1}.[27] A contraction of the c-axis occurs for the reconstructive anatase to rutile transformation and the overall volume contraction is about 8%. A phase diagram of titania as a function of both temperature and pressure is shown in Figure 2.3 as below.

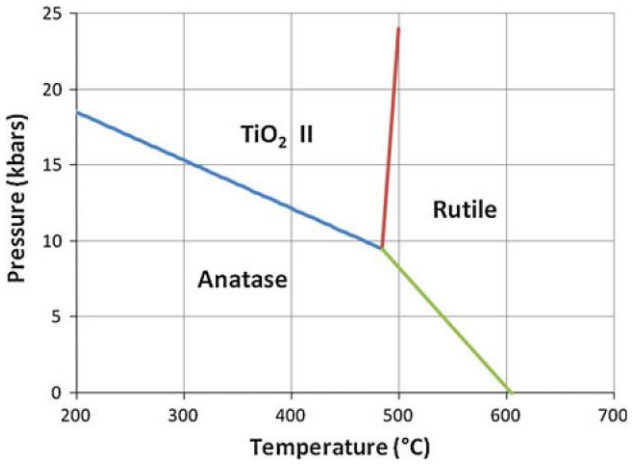

Figure 2.3. Phase diagram of titania. The reaction boundaries of phase transitions are shown as different colour lines. TiO_2 II is a high-pressure phase of titania with a lead oxide structure.[25] Copyright 2011, Springer publisher.

2.2.2.1 Factors Affecting the Anatase to Rutile Phase Transformation

The kinetics of the anatase to rutile phase transformation depend on the material properties including impurities/dopants, initial anatase crystal size and packing characteristics.

1) Impurities/dopants

The presence of intentional dopants or unintentional impurities in the samples shows an obvious effect on the kinetics of the anatase to rutile transformation. The dopants can be cations or anions. Variable results have been reported that impurities/dopants may either inhibit or promote the transformation to rutile. Yang *et al*. demonstrated that Zr ions doping can significantly inhibit the TiO_2 phase transformation.[28] As indicated by differential thermal analysis (DTA) curves, the transformation temperature is around 800 °C for pure TiO_2 powder, while for a sample with molar ratio Zr/Ti=0.1, the temperature increases to about 1100 °C. Francisco *et al*. reported

that the anatase-rutile phase transformations of TiO_2 and TiO_2-CuO samples were retarded by the addition of CeO_2.[29] The inhibition observed for the phase transformation not only prevented substantial surface loss but also pore growth associated with this process. In the report by Yu *et al*., F^- doping was investigated.[30] Fluoride ions not only enhanced the crystallinity of anatase but also prevented phase transformation of anatase to rutile. A recent study reported by Luo *et al*. demonstrated that vanadium doping promoted the anatase−rutile transformation. The transformation temperature was decreased from 1000 to 600 °C with 10 % vanadium doping while mesopore structure in the mixed-phase TiO_2 was preserved.[11]

Impurities/dopants can also be produced by heating samples in different atmospheres. In 1964, Shannon found that the rate of anatase to rutile phase transformation was accelerated in hydrogen gas atmospheres but retarded in vacuum.[31] Gamboa *et al*. reported that an Ar-Cl_2 atmosphere favoured the TiO_2 phase transformation and was approximately 300 times faster than in air at 950°C.[32]

As discussed above, doping of TiO_2 provides an effective approach to alter the kinetics of the anatase to rutile transformation. The promotion of the phase transformation is attributed to an increase of oxygen vacancies through an increase in lattice relaxation (i.e. lessening of structural rigidity) while transformation inhibition is mainly ascribed to the formation of Ti^{3+} interstitials through an increase in lattice constraint.[25, 33]

2) Crystal size

The effect of crystal size on the anatase to rutile transformation has been extensively investigated and the transformation is very strongly size dependent.[34-37] It is worth noting that contrary results have been reported due to differences in sample preparation methods. Zhang and Banfield reported that prepared TiO_2 nanoparticles with anatase structures transformed to rutile when they reached a critical particle size, and that once rutile was formed, it developed much faster than anatase. Anatase is more stable than rutile if the particle size is below ~14 nm.[34] In a later study, they found that the thermodynamic phase stability and transformation sequence highly depended on the initial particle size of anatase. A conclusion was drawn that for nanoparticles with equal size, anatase was thermodynamically stable for sizes less than 11 nm, and rutile was stable for sizes larger than 35 nm.[35] Li *et al*. found that

with a decrease of initial anatase particle size the onset phase transition temperature was decreased.[36] The calculated activation energies for phase transformation were 299, 236 and 180 kJ mol^{-1} for TiO_2 nanoparticles with a crystal size of 23, 17 and 12 nm, respectively. The decreased thermal stability in the finer nanoparticles was primarily ascribed to the reduced activation energy owing to the increase of the size-related surface enthalpy and stress energy. Similarly, Zhang *et al*. also found that the initial particle size of TiO_2 is the critical parameter determining the onset transition temperature and nucleation behavior.[37] In this study, the effect of particle size on outer and inner particle phase transformation was investigated by preparing ultrafine TiO_2 particles with a narrow size distribution. The phase transformation took place at lower temperatures for small particles (<10 nm). The transformation temperature increased with the increase of initial particle size, as shown in Figure 2.4. Rutile nucleates at the interfaces of contacting anatase particles that are smaller than 60 nm) while for particle size greater than 60 nm, three rutile nucleation modes, interface-, free surface- and bulk-nucleation are all likely to exist.

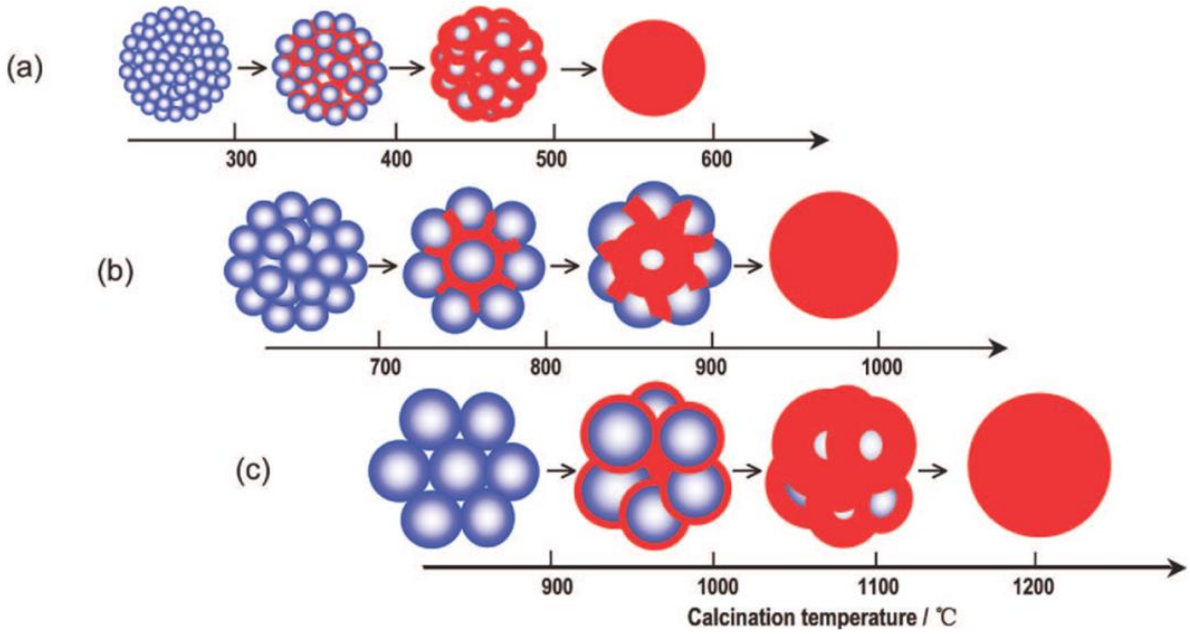

Figure 2.4. A proposed scheme for the anatase to rutile phase transformation of TiO_2 with diverse particle size: (a) less than 10 nm, (b) 10-60 nm, and (c) greater than 60 nm (blue, anatase; red, rutile). Adapted with permission.[37] Copyright 2009, American Chemical Society.

3) Packing characteristics

Packing characteristics have a significant effect on the anatase to rutile transformation. Solid-state phase transformation is a process of nucleation and growth, and three nucleation modes, interface-, free surface- and bulk-nucleation have been used to explain the anatase to rutile phase transformation.[12, 25, 27, 35, 38-43] At relatively low annealing temperatures (below 620 °C), interface-nucleation usually triggers and dominates the phase transformation. The anatase twin boundaries built from two slabs of octahedral zigzag chains show structural elements common to those of the rutile phase.[27] Such twin interfaces can serve as nuclei for the rutile phase. Such twin interfaces can serve as nuclei for the rutile phase, by initializing the phase transformation due to the relatively low activation barrier for nucleation. This nucleation is different from the surface or bulk nucleation which is a high energy-favoured process. As reported by Banfield *et al*. (Figure 2.5),[40] rutile primarily nucleates at interfaces between contacting anatase particles in TiO_2 samples with denser particle packing and inclusion of alumina particles can effectively decrease the probability of anatase interface nucleation.

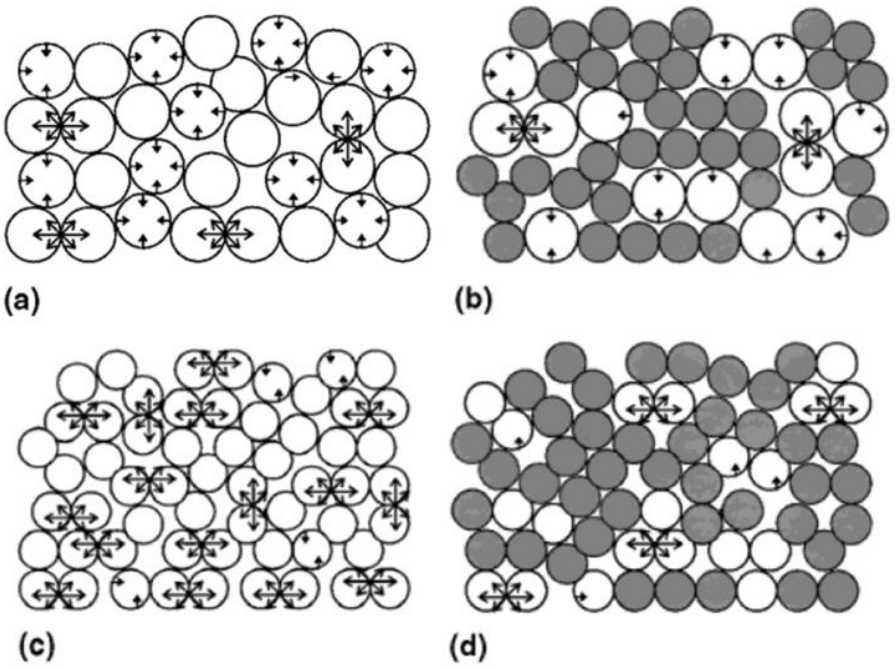

Figure 2.5. Diagram illustrating the relationship between anatase particle packing and possible nucleation mode: (a) 8 nm anatase sample with less dense particle packing, (b) 8 nm anatase sample mixed with 6 nm γ-Al_2O_3, (c) 6 nm anatase sample with compact packing, and (d) 6 nm anatase sample mixed with 6 nm γ-Al_2O_3. The white

circle represents anatase, grey circle represents γ-Al_2O_3, anchor arrow represents interface nucleation and the single arrow represents surface nucleation. Adapted with permission.[40] Copyright 2000, Materials Research Society.

2.2.2.2 Band Alignment of Anatase and Rutile

It is generally regarded that anatase TiO_2 shows higher photocatalytic performance than rutile TiO_2. In order to achieve highly active TiO_2 photocatalysts, most research has focused on synthesizing phase-pure anatase TiO_2. However, the commercially available photocatalyst, Evonik (Degussa) P25 TiO_2, is a mixed-phase TiO_2 with about 80% anatase and 20% rutile.[44] The mixed-phase P25 is more active than the individual anatase or rutile phase.[45] Therefore, extensive investigations of mixed-phase TiO_2 composites have been carried out in recent years that have exhibited enhanced photocatalytic activities. Although the explanation for the enhanced performance is unanimously regarded as the spatial separation of photogenerated electrons and holes induced by the synergistic effect between anatase and rutile, there is one long-standing dispute on the energetic alignment of the band edges of the anatase and rutile TiO_2.[46, 47] Kavan *et al*. determined by electrochemical impedance analysis that the flat band potential of anatase was approximately 0.2 eV more negative than rutile (Figure 2.6a), indicating that the CB of anatase was 0.2 eV above that of rutile.[48] This result suggested that this band alignment favoured the photogenerated electron transfer from anatase to rutile, whereas holes migrated from rutile to anatase. Contrastingly, a later study by Xiong *et al*. reported that the anatase CB was 0.2 eV lower than rutile (Figure 2.6b) on the basis of photoemission measurements.[49] Research by Scanlon *et al*. using combined periodic hybrid density functional theory calculations and X-ray photoelectron spectroscopy experimental measurements supported the latter theory.[47] They found that the CB and VB of rutile were 0.22 and 0.44 eV higher than those of anatase, demonstrating that this band alignment favoured photogenerated electron flow from rutile to anatase. This finding was consistent with previous results conducted by electron paramagnetic resonance (EPR) spectroscopy, in which electrons migrate from rutile into anatase, while holes transfer in the opposite direction.[50, 51]

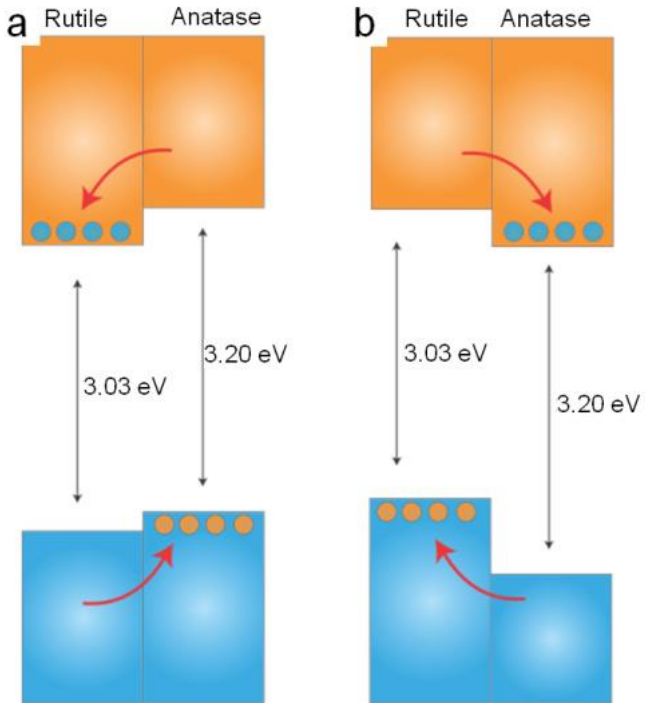

Figure 2.6. A proposed scheme for VB (blue) and CB (orange) alignment mechanisms for the anatase and rutile interface: (a) type-II (rutile); (b) type-II (anatase). Blue and orange dots indicate electrons and holes, respectively, and red arrows represent their respective flow in the CB and VB Reproduced with permission.[47] Copyright 2013, Nature Publishing Group.

2.2.2.3 Strategies for Synthesizing Anatase and Rutile Mixed Phase

The band alignment mechanism discussed above makes explicit that charge transport processes critically depend on the interface between anatase and rutile TiO_2. Therefore, although the simplest way to fabricate mixed-phase TiO_2 is to directly mix variable ratios of anatase and rutile nanoparticles together, the interface contact between anatase and rutile is not ideal by just mechanical mixing. In order to obtain mixed-phase TiO_2 with a better interface contact, the following two main strategies can be employed.

1) Converting anatase or amorphous TiO_2 into mixed-phase TiO_2.[11, 12, 37, 52, 53] This process can be realized by annealing as-prepared anatase or amorphous TiO_2 at an elevated temperature. The anatase/rutile ratio can be simply tuned by annealing duration or temperature.

2) Direct preparation of mixed-phase TiO_2. The materials can be obtained by hydrothermal treatment, flame spray pyrolysis or reactive DC magnetron sputtering.[54-57]

2.3 Porous TiO_2 Spheres

Spherical TiO_2 nanostructures are an important class of materials that have been widely investigated and have found extensive applications for energy-storage and conversion, chromatography, light-induced chemistry, electro-rheology and catalysis.[58] Numerous synthesis strategies have been applied to obtain porous TiO_2 spheres. The research in this thesis will employ a sol-gel technique along with a hydrothermal/solvothermal procedure for the development of porous TiO_2 spheres. Therefore, the following section provides an overview of these two techniques that enable preparation of diverse spherical TiO_2 morphologies.

2.3.1 Sol-Gel Templating Technique

The sol-gel method has been applied to prepare various oxide ceramic materials for a long time. The term sol-gel refers to a process in which the inorganic polymerization of molecular precursors dispersed in a liquid (referred to as sol) aggregate to form a solid, continuous three-dimensional (3D)-network extending throughout the liquid (referred to as gel).[59] Hence, sol-gel is a process through which a liquid sol transitions into a solid gel. The most common precursors used in sol-gel syntheses are metal alkoxides. The whole sol-gel process includes two parts: hydrolysis and condensation reactions of the alkoxide precursors:

Hydrolysis:

$$M(OR)_4+H_2O\rightarrow HO\text{-}M(OR)_3+ROH \quad (6)$$

M represents the inorganic element, such as Ti or Zr, and the OR stands for an alkoxy group and ROH is an alcohol. Depending on the amount of added water and catalyst, hydrolysis may go to completion.

$$M(OR)_4+4H_2O\rightarrow M(OH)_4+4ROH \quad (7)$$

Condensation:

$$(RO)_3M\text{-}OH+HO\text{-}M(OR)_3\rightarrow(OR)_3M\text{-}O\text{-}M(OR)_3+H_2O \quad (8)$$

$$(RO)_3M\text{-}OR+HO\text{-}M(OR)_3\rightarrow(OR)_3M\text{-}O\text{-}M(OR)_3+ROH \quad (9)$$

Template growth is a very flexible and diverse synthesis method that forms nanostructures with a morphology following a porous template. Templates are used in

conjunction with sol-gel chemistry to direct the assembly of the TiO_2 network formed during the sol-gel process. Porous TiO_2 spheres can be fabricated through a hard templating method via nanocasting of various porous spherical materials, such as carbon, silica or polymers.[60-64] In this process, the TiO_2 precursor is impregnated in dispersed template beads and undergoes hydrolysis and condensation within the template pore structures, resulting in a template/TiO_2 hybrid, where the TiO_2 is generally amorphous. A following heating process is usually applied to obtain crystalline TiO_2 remove the template; chemical etching is employed to remove the template in the case of silica. The size of the TiO_2 spheres can be controlled by using different size templates, which can range in size from several hundred nanometres to several millimetres.

Dong *et al*. demonstrated a two-step nanocasting route to fabricate monodisperse mesoporous TiO_2 spheres.[62] In this process, monodisperse mesoporous silica beads were first prepared and then the silica beads acted as a template to produce mesoporous carbon spheres by nanocasting. The pores of the carbon template were then infiltrated with a titanium (IV) isopropoxide precursor followed by exposure to moisture in air to hydrolyse the Ti precursor. The carbon template was removed by annealing the composite in an air atmosphere. The size of the resulting anatase TiO_2 spheres was 500-600 nm and the surface area was around 150 $m^2\ g^{-1}$.

Kimling *et al*. synthesized hierarchically porous millimetre-sized TiO_2 beads using sol-gel chemistry within preformed alginate beads.[64] The alginate beads were first synthesized via an extrusion external gelation method. This involved the dripping of a sodium alginate solution into a calcium gelation bath using a peristaltic pump. The alginate beads served as sacrificial templates, successfully providing the spherical shape and controlling the structural properties of the TiO_2 matrix. The properties of TiO_2 were tuned by adjusting the alginate bead synthesis conditions and the annealing temperature. The specific surface area of these anatase TiO_2 beads was as high as 170 $m^2\ g^{-1}$ when the hybrid beads were calcined at 450 °C. These large size, porous inorganic beads show potential in applications such as adsorption-separation and catalysis.

2.3.2 One-Pot Hydrothermal/Solvothermal Method

Hydrothermal synthesis was first performed in 1839 by Robert Bunsen to synthesise crystals of barium carbonate and strontium carbonate at temperatures above 200 °C and pressures more than 100 bar. Typically, hydrothermal synthesis is a process that utilises single or heterogeneous phase reactions in aqueous media at elevated temperature and pressure to crystallise ceramic material. The reaction is normally carried out in steel pressure vessels called autoclaves with or without Teflon liners (Figure 2.7). The internal pressure of the autoclave depends upon the reaction temperature and volume of solution added. The solvothermal method is almost identical to the hydrothermal method, except that the solvent used is primarily non-aqueous.

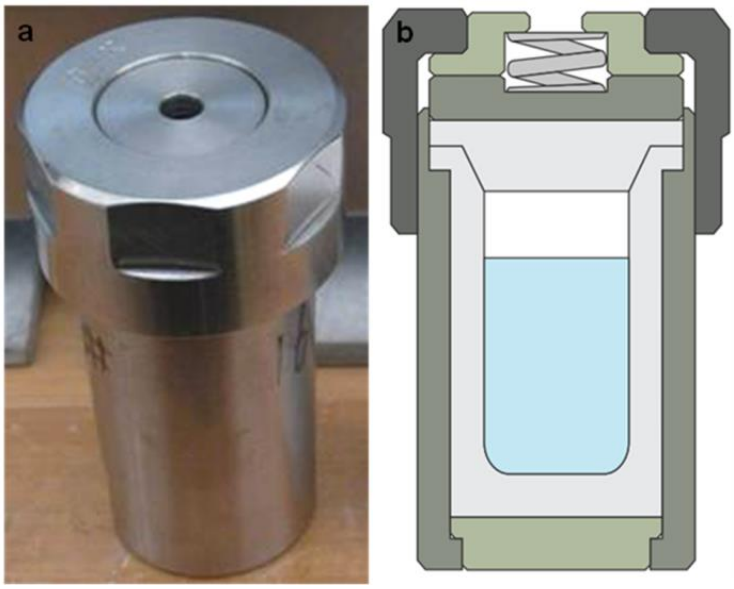

Figure 2.7. Steel autoclaves with Teflon liner as used in this thesis: (a) Photograph and (b) cross-sectional schematic showing the Teflon liner part filled.

Porous spherical TiO_2 nanostructures with well-defined morphologies can be prepared by the hydrothermal or solvothermal method via different formation mechanisms, including reaction-limited oriented growth of nanocrystals, controlled agglomeration of *in situ* formed particles, dissolution-recrystallization and topotactic transformation. In contrast to the sol-gel process (templating and autogenesis), hydrothermal and solvothermal processes usually directly gives rise to crystalline porous TiO_2 nanostructures, making subsequent crystallization heating unnecessary. The TiO_2 nanoparticles are subject to reaction parameters including the type of precursor, solvent, pH, temperature, time as well as any additives in the fluid.

Sun *et al*. prepared novel 3D dendritic TiO_2 nanostructures consisting of rutile nanorod, nanoribbon or nanowire subunits via a simple one-pot hydrothermal synthesis in the presence of cetyltrimethyl ammonium bromide (CTAB) and hydrochloric acid (HCl).[65] The morphology of the constituent nano-units and the size of the 3D TiO_2 dendrites was readily controlled by adjusting the surfactant aggregation structure and the precursor hydrolysis rate. The size and specific surface areas of the TiO_2 nanostructures varied from 1.3 to 10 μm and 25 to 97 m^2 g^{-1}, respectively, by adjusting experimental parameters including concentrations of titanium (IV) isopropoxide, CTAB, ethylene glycol and urea. The addition of ethylene glycol and urea in the reaction system can slow down the hydrolysis rate of titanium (IV) isopropoxide and accordingly influence the morphological development of the constituent units from nanorods to nanoribbons and nanowires. Additionally, all TiO_2 nanostructures were well-crystallized rutile phase as revealed by X-ray diffraction (XRD) and Raman spectroscopy.

Alternatively, the fabrication of porous TiO_2 spheres can be realized through fluoride-assisted hydrothermal and solvothermal reactions.[66, 67] The presence of fluoride in the synthesis can effectively promote the crystallization of anatase crystals, therefore resulting in well-crystallized porous TiO_2 spheres. Moreover, fluoride can also stabilize the highly reactive (001) facets, giving rise to an increased percentage of those facets in the generated spheres. Fang *et al*. prepared spherical TiO_2 nanostructures that consisted of single-crystal anatase nanosheets dominated by well-faceted (001) planes through solvothermal treatment in a mixture of titanium (IV) butoxide, isobutanol and hydrogen fluoride (HF) at 180-200 °C.[67] The as-prepared spheres with a size of approximately 2.0 μm were assembled from two-dimensional anatase nanosheets, which had a thickness of 10-20 nm and a length of around 1.2 μm and served as the basic building units. Similar TiO_2 nanostructures were also synthesized by in a diethylene glycol solvothermal reaction, in which TiF_4 was used as a Ti precursor.[66] The uniform spheres with a diameter of 250 nm were prepared at a TiF_4 concentration of 10 mM. The diameter of the spheres decreased to 200 nm when the TiF_4 concentration increased to 30 mM, and featured two mesopore sizes centred at 2.5 and 17.9 nm.

The presence of hydrogen peroxide in hydrothermal/solvothermal reactions also facilitates the formation of porous TiO_2 spheres. In a synthesis developed by Wu *et al.*, hierarchical TiO_2 spheres assembled from nanospindles were fabricated via a two-step solvothermal and hydrothermal method.[68] First, the yellowish peroxotitanium complex $[Ti(H_2O_2)\cdot(OH)_{4-n}]^{n+}(OH)n$ was formed via dissolution of P25 powder in a mixture of 30 wt% hydrogen peroxide and 26-28 wt% ammonia.[69] The peroxotitanium precursor was then solvothermally treated at 160 °C for 6 h in a water-ethanol solution, producing nanospindle-embedded TiO_2 precursor spheres, followed by hydrothermal treatment at 180 °C. The as-prepared spheres composed of anatase nanospindles had a size of 450 nm and a surface area of 88 $m^2\ g^{-1}$.

2.3.3 Combined Sol-Gel Autogenesis and Hydrothermal/Solvothermal Process

Besides the intuitive templating method, where the size and monodispersity of TiO_2 spheres are controlled by the templates employed, micrometre- or submicrometre-sized TiO_2 spheres can also be obtained by an autogenesis sol-gel process. In this process, it is necessary to slow down the alkoxide hydrolysis because of the high reactivity of titanium alkoxides. The synthesis of TiO_2 spheres can be conducted in a solvent (typically alcohol) containing either a small amount of water or in the presence of diverse chelating agents (e.g., acetylacetone or ethylene glycol). These methods allow for more control of the material properties. However, the resulting TiO_2 spheres are usually amorphous, which generally requires a further heat treatment process, like hydrothermal/solvothermal treatment, to obtain porous crystalline TiO_2 spheres. By combining sol-gel autogenesis and the hydrothermal/solvothermal process, TiO_2 spheres with a number of desirable properties including well-defined spherical morphology, monodisperse particle size, high specific surface area, variable pore size and high crystallinity can be achieved.

The autogenesis sol-gel process was first reported by Stöber *et al*. for the preparation of monodisperse SiO_2 spheres in the late 1960s.[70] The synthesis involves the hydrolysis and condensation of tetraethyl orthosilicate in alcohol solvents in the presence of water and a catalyst (e.g., ammonia) at ambient temperature. Particle sizes ranged from 50 nm to 2 μm, and were obtained by careful adjustment of the concentration of the reactants, which controlled the nucleation and growth rates of the nuclei. Since then, tremendous efforts have been made to similarly prepare alternative

metal oxides, e.g. TiO_2, which is of high importance for both fundamental research and potential applications in environmental remediation, clean energy generation and storage. For example, Eidan-Assmann *et al.* investigated the use of salts and polymers as stabilizing agents to prevent the aggregation of the TiO_2 spheres, thereby enabling discrete monodisperse TiO_2 spheres and control over the morphological features of the spheres.[71] In another process demonstrated by Jiang *et al.*, monodisperse spherical titanium glycolate colloids were fabricated by using a less reactive titanium precursor that was obtained by mixing highly reactive titanium(IV) butoxide with ethylene glycol.[72]

Recently, Caruso and co-workers successfully combined sol-gel autogenesis and a hydrothermal/solvothermal process to produce porous TiO_2 with controllable features.[73, 74] The formation process is illustrated in Figure 2.8.

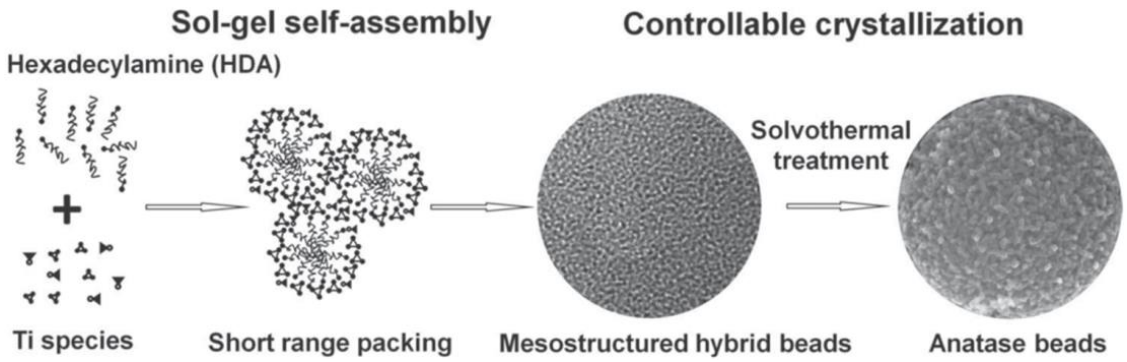

Figure 2.8. A scheme illustrating the synthesis of monodisperse mesoporous TiO_2 spheres by combining sol-gel self-assembly and a solvothermal process. Adapted with permission.[73] Copyright 2010, American Chemical Society.

Amorphous spherical TiO_2 agglomerates were first produced by a sol-gel cooperative self-assembly process. The reaction takes place in ethanol in the presence of a structure-directing agent, hexadecylamine. During this process, the morphology, monodispersity in size and the diameter of the mesostructured hybrid spheres were controlled. For example, the diameters of the precursor spheres were adjusted from 300 to 1150 nm by tuning the H_2O:Ti mole ratio from 10:1 to 3:1. The precursor spheres are nonporous structures as revealed by N_2 sorption.[73] If a direct calcination treatment is applied, the amorphous precursor beads crystallize into anatase TiO_2

materials with a very low specific surface area (approximately 3 m^2 g^{-1}) and pore volume (approximately 0.01 cm^3 g^{-1}). To prepare mesoporous TiO_2 spheres with a highly crystalline framework and controllable mesoporosity, solvothermal treatment was carried out in an ethanol-water mixture in the presence of different amounts of ammonia.[73-75] In this process, the specific surface area, crystallite size, pore size distribution and surface roughness of the TiO_2 spheres was controlled by the ammonia concentration or the solvothermal crystallization and calcination temperature. For example, the specific surface area of the mesoporous TiO_2 spheres can be as high as 108 m^2 g^{-1} with a pore size of around 14 nm in the absence of ammonia. The pore size was enlarged from 14 to 18 and then 23 nm when 0.5 and 1.0 mL 25 % ammonia solution was added to the solvothermal fluid. Additionally, the size of the anatase nanocrystallite constructing TiO_2 spheres was tuned from approximately 55×100 nm to 160×410 nm by increasing the ammonia concentration employed in the solvothermal treatment step from 2.2 to 17.4 wt.%. The transformation of amorphous TiO_2 into crystalline TiO_2 involved dissolution, anatase nucleation and crystal growth mechanism.[76] Hence, crystalline porous spheres can be prepared by transforming nonporous amorphous spheres just as well as porous amorphous spheres.[71]

In 2012, Hong *et al.* prepared monodisperse mesoporous TiO_2 spheres 0.6-3.1 μm in diameter by adopting a similar strategy.[77] They investigated the effects of reaction temperature (-41 to 23 °C), Ti source purity and carbon chain length of *n*-alkylamines (C_8-C_{16}) on the monodispersity and particle size of amorphous precursor spheres. In this work, titanium (IV) isopropoxide was purified by vacuum-distillation in order to remove any pre-existing nuclei. The nuclei were formed by inadvertently introducing moisture during the handling and storage of titanium(IV) isopropoxide (TIP). In addition, to precisely control the hydrolysis of TIP during the sol-gel synthesis of the precursor spheres, ethanol was dried by distillation from an activated molecular sieve and the synthesis was also conducted in a glove box charged with dry Ar. The monodispersity of the resulting amorphous precursor spheres was enhanced by removing the pre-existing nuclei in the as-received TIP and using *n*-alkylamine surfactants containing 10-14 carbon atoms in the alkyl chain. In this research, *n*-dodecylamine (DDA, C_{12}) gave the highest monodispersity. After solvothermal treatment and calcination, the amorphous TiO_2 spheres readily transformed into mesoporous anatase TiO_2 spheres with a specific surface area up to 152.8 m^2 g^{-1}. By

increasing the carbon chain length of the *n*-alkylamine from 8 to 16, the pore diameters increased from 5.1 to 12.6 nm and the corresponding pore volumes increased from 0.12 to 0.41 $cm^3 g^{-1}$.

Another procedure for the synthesis of highly crystalline TiO_2 spheres was developed by Pan *et* al. via a fluoride-assisted solvothermal process.[78] The synthesis of nonporous TiO_2 precursor spheres with a diameter of about 270 nm was achieved from the direct precipitation of titanium (IV) alkoxides in an ethanol-acetonitrile mixed solution that also contained water.[79] This reaction occurred in the presence of the structure directing agent of (DDA) at room temperature. TiO_2 spheres consisting of well-packed uniform nanocrystals were generated by a subsequent solvothermal reaction at 180 °C in the presence of NH_4F and then post-calcination at 450 °C. Some shrinkage was observed due to the removal of the DDA surfactant and crystallization of TiO_2 after thermal treatment. The TiO_2 spheres exhibited mesoporosity with an average pore size of 9.2 nm and a Brunauer-Emmett-Teller (BET) surface area of 132 $m^2 g^{-1}$. For comparison, the amorphous precursor beads were directly calcined at 450 °C without solvothermal treatment, giving rise to TiO_2 spheres with a very low specific surface area of 16.3 $m^2 g^{-1}$.

2.4 Hollow TiO_2 Spheres

As an important family of functional materials, hollow structures featuring low density, high specific surface area, large void space and high loading capacity have attracted considerable attention in various areas including adsorption and storage, catalysis, drug delivery and photocatalysis. Following the 1998 publication of Caruso *et al.*,[80] various synthesis strategies have been developed to generate inorganic hollow spheres. The templating approach, hydrothermal/solvothermal procedure and combined method are covered in this chapter.

2.4.1 Templating Method

The template-assisted approach undoubtedly provides a convenient, flexible and versatile procedure for the fabrication of hollow nanostructures. In this thesis, this approach can be broadly divided into two categories: conventional hard templating and soft templating.

2.4.1.1 Conventional Hard Templating

Fabrication of hollow TiO_2 spheres by templating rigid particles is effective and conceptually straightforward. In this method, solid particles (*e.g.*, polystyrene (PS), carbon or silica spheres) are employed as the core template, which can be subsequently removed through thermal treatment (calcination) or selective solvent etching (dissolution) after the formation of the inorganic shells around the template cores. This process mainly involves four steps as illustrated in Figure 2.9: (1) preparing the original hard template, (2) functionalizing/modifying the template surface to achieve any required surface properties, (3) coating a TiO_2 precursor onto the surface of the template by the sol-gel process, and (4) selectively removing the original template and controlling crystallinity as well as crystal phase of the hollow TiO_2 nanostructures. The properties of the resultant hollow spheres, such as the inner and outer diameter of the sphere, and the size distribution (monodispersity), are usually controlled based on the employed hard template and the coating process. In this thesis, the focus is the sol-gel coating process in which TiO_2 sols were formed by hydrolysis. Consequently, the use of performed TiO_2 particles coated on the surface of hard templates (*e.g.*, a using the layer-by-layer assembly technique[80-82]) is not included.

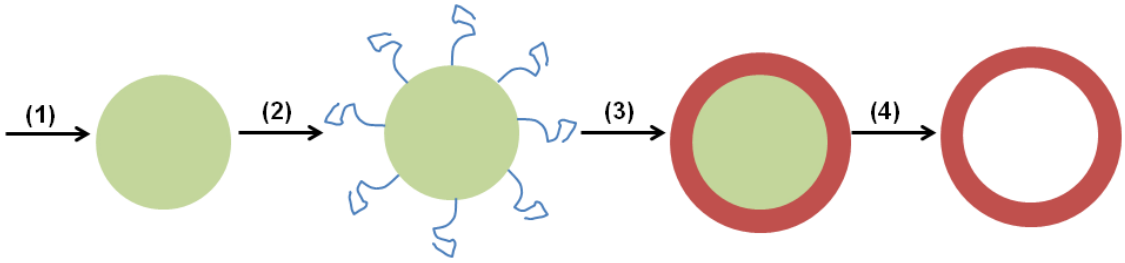

Figure 2.9. A schematic illustration of the procedure to prepare a hollow sphere using a sacrificial hard template. (1) preparation of the hard template, (2) functionalization of the template surface, (3) coating the template with TiO_2 and (4) removal of the template.

Chemical deposition is a shell-forming strategy commonly employed in the synthesis of hollow structures. It is crucial to control the hydrolysis rate and heterocoagulation for the success of the process. Yin *et al*. developed a procedure for the preparation of hollow TiO_2 microspheres with tunable shell thickness by the hydrolysis of titanium (IV) butoxide in an ethanol solution containing polystyrene microspheres at 105 °C.[83] Polyvinylpyrrolidone (PVP) was used to stabilize the cationic PS sphere in the solution. Although the hydrolysis rate of titanium alkoxide is usually very fast, the

slight negative charge on the hydrolyzed TiO_2 species promoted rapid deposition on the positively charged PS spheres. The thickness of the coated layers was controlled by the concentrations of titanium (IV) butoxide and PS. Anatase TiO_2 shells were obtained by calcining the PS/TiO_2 composites at 600 °C. During this step PS templates were removed. Kim *et al.* later prepared hollow TiO_2 microspheres using surface-modified PS spheres as templates (Figure 2.10).[84] The template was first treated by plasma to introduce hydroxyl groups on the surface and then dispersed in a mixture containing ammonia, ethanol and titanium (IV) isopropoxide, finally giving rise to a PS/TiO_2 core/shell hybrid structure via a sol-gel process. The template core was selectively removed with tetrahydrofuran (THF). These hollow TiO_2 spheres obtained by this procedure had a mesoporous shell of around 25 nm in thickness, were highly porous with a BET surface area of 67.8 m^2 g^{-1} and have an average pore size of 3.7 nm. It is worth noting that the as-prepared hollow TiO_2 spheres were composed of amorphous nanoparticles. Further thermal treatment was required to transform the amorphous TiO_2 spheres into crystalline hollow TiO_2 spheres.

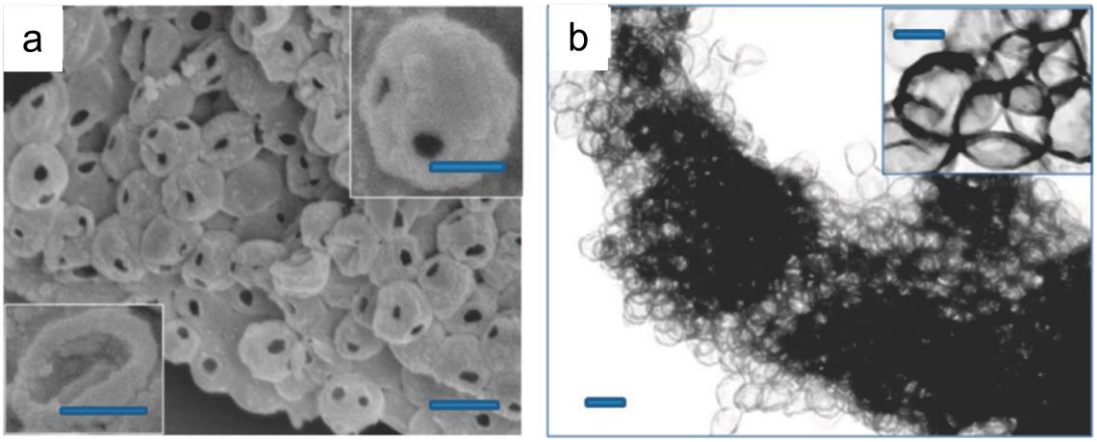

Figure 2.10. (a) SEM and (b) TEM images of hollow TiO_2 spheres. The scale bars are 400 nm in the main images and 200 nm the insets. Reproduced with permission.[84] Copyright 2008, American Chemical Society.

Alternatively, TiO_2 shells can be prepared using pre-synthesized TiO_2 sols. In a procedure developed by Guo *et al.*, hollow TiO_2 spheres with thick mesoporous walls were prepared by coating polymethyl methacrylate (PMMA) beads with a TiO_2 sol containing *n*-hexadecyltrimethylammonium bromide surfactant micelles.[85] Prior to coating with the TiO_2 sol, the surface of the PMMA polymer spheres was modified by ionic liquids. This modification was made to control the interfacial properties for

enhancing the deposition of TiO_2 sols. The sols on the surface of PMMA were then solidified by the addition of ammonia solution to form a mesoporous gel. Finally, the polymer core was removed by calcination in air at 650 °C for 4 h. This coating procedure produced hollow TiO_2 spheres with a disordered mesoporous shell, which exhibited a very high BET surface area of up to 256 $m^2 g^{-1}$. In addition, the size of the cavity in the hollow spheres was tuned by choosing different size PMMA templates (2-60 μm).

The use of mesoporous carbon hollow spheres as a template to prepare crystalline TiO_2 hollow spheres was demonstrated by Xia *et al*. The carbon template was first produced using mesoporous silica SBA-15 as a sacrificial template via chemical vapour deposition.[86, 87] The pores of the carbon template were then infiltrated with the titanium alkoxide precursor at room temperature, followed by exposure to air to hydrolyse the precursor. The carbon template was subsequently removed by annealing the composite in air at 550 °C for 8 h. The hollow sphere morphology of the mesoporous carbon template was successfully replicated in the crystalline TiO_2. The resulting porous TiO_2 hollow spheres obtained by nanocasting had a high surface area of 100 $m^2 g^{-1}$, pore size of about 6.0 nm and pore volume of 0.16 $cm^3 g^{-1}$.[87]

Besides polymer and carbon beads, silica beads are also commonly used as hard templates to prepare hollow spheres due to their low cost, easy coating process and size controllability.[17, 88] The procedure generally involves coating of the silica beads by the surface precipitation of TiO_2 sols containing surfactants for porosity control, and then the removal of the silica templates by etching using HF or an alkaline solution. In addition, the thickness of the TiO_2 shell can be easily increased by repeating the coating process. The TiO_2 samples obtained by the typical sol-gel process are amorphous and therefore require further thermal treatment to produce crystalline counterparts. Calcination at elevated temperatures is usually considered to be a simple and effective approach to induce crystallization of amorphous TiO_2. However, direct calcination of SiO_2@TiO_2 core-shell followed by selective etching of the SiO_2 core cannot maintain the porosity and hollow morphology due to the extensive crystallization and grain growth of the TiO_2. To overcome this issue, Yin and co-workers group developed a process involving the sol-gel deposition of a thin layer of protective silica. The protective silica coating as well as the silica template

core can be removed during the final etching with alkali bases.[17, 88] The as-prepared hollow TiO_2 spheres with mesoporous shell had a very high BET surface area of 311 $m^2 g^{-1}$.[17]

2.4.1.2 Soft Templating

Unlike hard templating, soft templating is very attractive for producing hollow nanostructures because the templates can be easily removed by gentle evaporation or dissolution in solvents. Soft templates are typically formed by long-chain polymers, surfactants, or viruses, which are usually amphiphilic compounds with hydrophilic and hydrophobic groups. By carefully adjusting experimental parameters, these materials can self-assemble into well-defined aggregates such as micelles or reverse micelles, vesicles, emulsions or liquid crystal phases. The assemblies act as templates directing the growth of guest structures, finally producing hollow structures. In a synthesis developed by Nakashima et al., TiO_2 hollow spheres were prepared using toluene microdroplets as templates, which were formed in an ionic liquid, 1-butyl-3-methylimidazolium hexaflurophosphate ($[C_4mim]PF_6$).[89] In this process, the Ti precursor, $Ti(OBu)_4$,was first dissolved in anhydrous toluene and then underwent emulsification with $[C_4mim]PF_6$ by intensive stirring, forming microsized droplets. $Ti(OBu)_4$ molecules in the droplets hydrolyzed selectively at the interface with a small amount of water in the ionic liquid phase. The as-prepared TiO_2 hollow spheres with a diameter of 3-20 μm were amorphous. Calcination at 500 °C facilitated the phase conversion to anatase.

Gas bubbles are another promising soft template for the synthesis of hollow nanostructures. In this approach, as-prepared fine nanoparticles aggregate around the bubbles to form a compact wall. It has been reported that gas bubbles can be produced by blowing gas into a solution, sonochemical methods or chemical reaction.[90] Li et al. designed a bubble-template approach to fabricate well-crystallized rutile-phase TiO_2 hollow spheres.[91] In this synthesis, a dark-red solution containing potassium titanium oxalate, H_2O, H_2O_2 and HCl was heated at 150 °C for 8 h, producing TiO_2 hollow spheres with a diameter if around 1 μm. The bubble template, O_2, was generated from the decomposition of H_2O_2. The spheres had pores with diameters of approximately 50 nm and a BET surface area of 130.2 $m^2 g^{-1}$.

2.4.2 One-Pot Hydrothermal/Solvothermal Technique

Analogous to the porous TiO_2 spheres demonstrated in the previous section, porous hollow TiO_2 spheres can be easily prepared by fluoride-assisted hydrothermal/solvothermal approaches.[14, 92-97] The growth of homogeneous TiO_2 shells is generally very difficult due to the high chemical reactivity of most titanium precursors, such as titanium alkoxides and chlorides. Therefore, the hydrolysis and condensation of titanium species are usually controlled by either the strict synthesis conditions or the addition of polyelectrolytes. The Ti-F bond in TiF_4 is relatively stable, so rapid hydrolysis and condensation of the titanium precursor can be dramatically retarded in the absence of stabilizing agents. In the hydrothermal/solvothermal process, the presence of fluoride not only induces the hollowing process of TiO_2 spheres, but also enhances the crystallization of TiO_2 materials, giving rise to well-crystallized porous TiO_2 hollow spheres in a one pot reaction. For example, in a procedure developed by Yang *et al*., hollow anatase spheres were obtained by a fluoride-assisted hydrothermal reaction.[92] In this synthesis, TiF_4 solution was heated in an autoclave at 180 °C. Solid TiO_2 spheres composed of anatase nanocrystals formed at the beginning of the reaction, while a hollowing effect was observed after longer reaction time. The core portion of the spheres gradually dissolved and re-deposited on the shell; the cavity of the spheres increased with the increase in hydrothermal time. Moreover, a higher concentration of TiF_4 in the reaction gave a thicker shell due to a higher growth rate. XRD confirmed that the crystallinity of the materials also increased with increasing reaction time. Although solid TiO_2 spheres can be formed at much lower temperatures, it is worth noting that the hollowing process does not commence at reaction temperatures below 160 °C. Pan *et al*. later found that the addition of H_2SO_4 in the hydrothermal reaction solution could greatly promote HF etching.[93]

Besides using expensive TiF_4 as the TiO_2 precursor, hollow TiO_2 spheres can be obtained in hydrothermal/solvothermal reactions using low cost inorganic fluorides, such as NH_4F and NaF. In a synthesis demonstrated by Liu *et al*., porous TiO_2 hollow spheres were prepared in a hydrothermal reaction containing $Ti(SO_4)_2$ and NH_4F.[14] The reaction in Teflon-lined autoclaves at 160 °C for 6 h produced TiO_2 hollow spheres with diameters of 500-800 nm, and mesoporous walls formed out of 13 nm anatase nanocrystals. The spheres had a BET surface area of 168 m^2 g^{-1} and a pore size of 12 nm.

The hydrogen peroxide-assisted hydrothermal/solvothermal methods described in section 2.3.2 can also prepare hollow TiO_2 spheres by simply varying experimental conditions. Wu et al. prepared monodisperse TiO_2 hollow spheres via a facile solvothermal reaction at 160 °C of peroxotitanium complex precursors, as shown in Figure 2.11.[69] The morphology and crystal evolution occurred in a one-step chemical conversion from amorphous Ti complex microspheres to anatase TiO_2 hierarchical hollow spheres. The process was revealed by a series of time dependent experiments. The unique nanostructure was assembled from well-crystallized nanospindles with lengths ranging from 10 to 200 nm. By simply adjusting the ammonia dosage in the precursor solution, the diameter of the hollow spheres could be adjusted from 400 to 1000 nm. Moreover, the as-prepared TiO_2 hollow spheres were highly porous. As an example, hollow spheres with a diameter of 750 nm featured mesoporosity with a pore size of about 20 nm and a BET surface area of 84.9 $m^2 g^{-1}$.

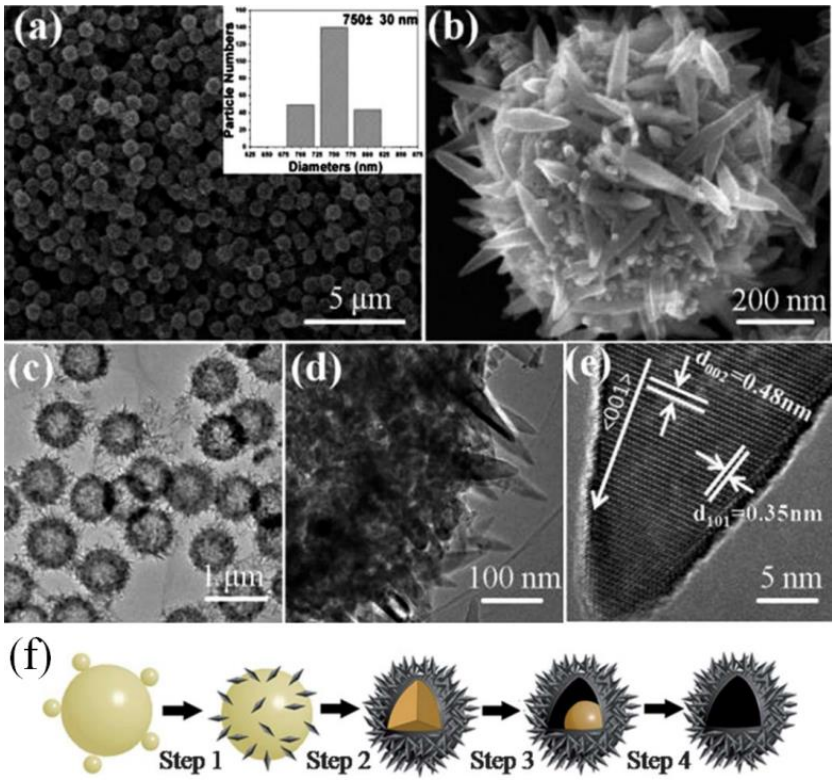

Figure 2.11. (a, b) SEM and(c-e) TEM images of hierarchical TiO_2 hollow spheres fabricated via a hydrothermal reaction of peroxotitanium complex precursors at 160 °C for 24 h. The inset in (a) shows the histogram of the diameter distribution of the TiO_2 hollow spheres. The scheme in (f) illustrates the development of the

morphology from a solid amorphous sphere to a hierarchical hollow sphere. Reproduced with permission.[69] Copyright 2012, Royal Society of Chemistry.

Considering the highly corrosive nature of fluoride and hydrogen peroxide in the material preparation, some groups have developed methods for the fabrication of hollow TiO_2 spheres in one-pot hydrothermal/solvothermal reactions without fluoride and hydrogen peroxide. For example, Li *et al*., prepared hollow TiO_2 spheres in an autoclave containing a mixture of $TiOSO_4$, alcohol (methanol, ethanol or propanol), glycerol and ethyl ether in a molar ratio of 1:40:16:11.[98] The solvothermal treatment was conducted at the relatively low temperature of 110 °C, producing amorphous TiO_2 spheres with diameters ranging from 1.6 to 5.2 μm, followed by calcination at 550 °C to obtain the crystallized hollow TiO_2 spheres. In this synthesis, variable morphologies from solid, core-shell, sphere-in-sphere to hollow spheres can be obtained by varying reaction times and alcohol. In a synthesis developed by Shang *et al*., hollow TiO_2 spheres were fabricated via solvothermal treatment in a reaction solution containing titanium (IV) chloride, ethanol and acetone.[99] The reaction at 220 °C for 12 h led to the formation of well-crystallized anatase hollow TiO_2 spheres with a shell thickness of 40-60 nm and a size of 0.8-1.0 μm. The water required for the Ostwald ripening process was absent from the reaction mixture, instead being generated via an etherification reaction during solvothermal treatment. The size of the hollow spheres was adjusted by varying the ratio of alcohol to acetone. After calcining the solvothermally-treated samples at 600 °C, the resulting hollow TiO_2 spheres were mesoporous with a pore size of 7.0 nm and a BET surface area of 58 $m^2 g^{-1}$.

2.4.3 Combined Templating Technique and Hydrothermal/Solvothermal Process

Considering the complexity of the synthetic procedures and the high chemical reactivity of the TiO_2 precursors, it is very challenging to prepare hollow TiO_2 spheres that simultaneously possess well-defined spherical morphology, good monodispersity, tunable particle size, adjustable shell thickness, high specific surface area, tunable pore size, high porosity, high crystallinity and controllable architecture. However, this can be realized by combining templating techniques with hydrothermal/solvothermal processes. The spherical morphology, monodispersity and size of the nanostructures are determined by the template, whereas shell thickness, surface area, pore size, and

crystallinity and internal morphology can be controlled by the conditions of the hydrothermal/solvothermal treatment such as solvent, pH, reaction temperature and time.

Ding et al. obtained uniform hollow TiO_2 spheres from a solvothermal reaction using sulfonated PS hollow spheres as templates.[100] The hollow TiO_2 spheres were constructed of highly crystalline anatase nanosheets containing large numbers of exposed (001) facets. In the process, the templates were first dispersed in isopropyl alcohol by ultrasonication. After mixing with diethylenetriamine and titanium (IV) isopropoxide, the suspension was sealed in an autoclave and solvothermally treated at 200 °C for 24 h. The presence of hydrophilic functional groups in the polymeric gel shell led to the growth of the TiO_2 nanosheets within the polymer gel matrix, giving rise to a hierarchical structure. After being calcined in air at 400 °C, the PS/TiO_2 composite was readily converted into hollow TiO_2 spheres. The resulting hollow spheres possessed a mesoporous shell with a high specific surface area of 134.9 $m^2 g^{-1}$ and a relatively narrow pore size distribution (5-7 nm).

Besides polymer spheres, carbon spheres are popular templates for the preparation of porous TiO_2 hollow spheres.[16, 18] The preparation of the carbon template is very easy by simple thermal decomposition of glucose in an autoclave. The resulting carbon sphere surface is hydrophilic and rich with functional groups (e.g. -OH and -C=O), so further surface modification is unnecessary for TiO_2 precursor coating.[101] Moreover, the size of the carbon sphere can be easily controlled. Zhang et al. developed a facile procedure to fabricate hollow TiO_2 spheres through a solvothermal process using $TiOSO_4$ as the titanium source and carbon spheres as the template.[18] During solvothermal processing, a slow hydrolysis of $TiOSO_4$ on the carbon surface produced C-TiO_2 core-shell structures. Calcination of the composite at 450 °C in air led to the formation of crystalline porous TiO_2 hollow spheres with a high BET surface area of 106 $m^2 g^{-1}$ and mesoporous walls with a pore size centred at 5.5 nm. The spheres retained the hollow structure even when calcined at 600 °C, indicating very good thermal stability of the materials.

Compared to polymer or carbon templates that can be easily burned out during thermal treatment or dissolved in certain organic solvents, silica is both more robust and stable. In some reports the silica template was etched by highly corrosive alkaline

solution or HF during the synthesis of hollow TiO_2 spheres,[102, 103] with the formation of crystalline TiO_2 materials being accompanied by silica etching. In a procedure by Leshuk *et al.*, silica bead templates were first coated by a layer of amorphous TiO_2 sols in a sol-gel process before the formed silica/TiO_2 composite was dispersed in water with a PH of 12.[102] Subsequent hydrothermal treatment at 140 °C enabled the amorphous TiO_2 to convert into anatase crystalline TiO_2 via a dissolution-precipitation mechanism while the silica core gradually dissolved from the outer surface inward. The prepared crystalline TiO_2 hollow spheres possessed a highly porous shell and a large BET surface area of around 300 $m^2 g^{-1}$.

In another synthesis, the template was itself involved as a reactant in the shell material synthesis process during hydrothermal/solvothermal treatment. Analogous to conventional hard templates, this type of template directly determines the shape of the resultant hollow structures. The hollowing process has been widely explained by the Ostwald ripening mechanism. This self-templating strategy is very attractive as it provides a facile route for the fabrication of porous hollow TiO_2 spheres. Several examples are given below.

Fluoride-mediated hydrothermal/solvothermal reactions using a self-templating technique have been employed to prepare porous hollow TiO_2 spheres.[104-106] For example, Yu *et al.* used the fluoride-assisted crystallization of amorphous TiO_2 solid spheres in hydrothermal reactions (as shown in Figure 2.12).[105] In this synthesis, amorphous porous TiO_2 spheres with a surface area of 103.1 $m^2 g^{-1}$ were first formed in a sol-gel process from titanium (IV) butoxide in ethanol with the addition of KCl.[71] The as-prepared amorphous spheres were then autoclaved at 180 °C for 12 h in an aqueous solution of NH_4F. An outward diffusion initiated from the spherical interiors, creating a hollow structure. This fluoride-assisted hydrothermal treatment not only induced the transformation of the amorphous solid TiO_2 spheres to hollow TiO_2 spheres but also promoted the crystallization of anatase nanocrystals. The nanocrystals increased in size from 6.6 to 13.3 to 18.8 nm when the hydrothermal treatment time was prolonged from 0.5 to 1 to 12 h, along with an increased diameter of the hollow interior. The hollow TiO_2 spheres were mesoporous with an average pore size of 11.2 nm and a BET surface area of 62.9 $m^2 g^{-1}$. Moreover, the molar ratio of NH_4F to TiO_2 significantly influenced the morphology of the TiO_2 materials. The

crystallite size increased while the surface area decreased with an increase in the F/Ti molar ratio.

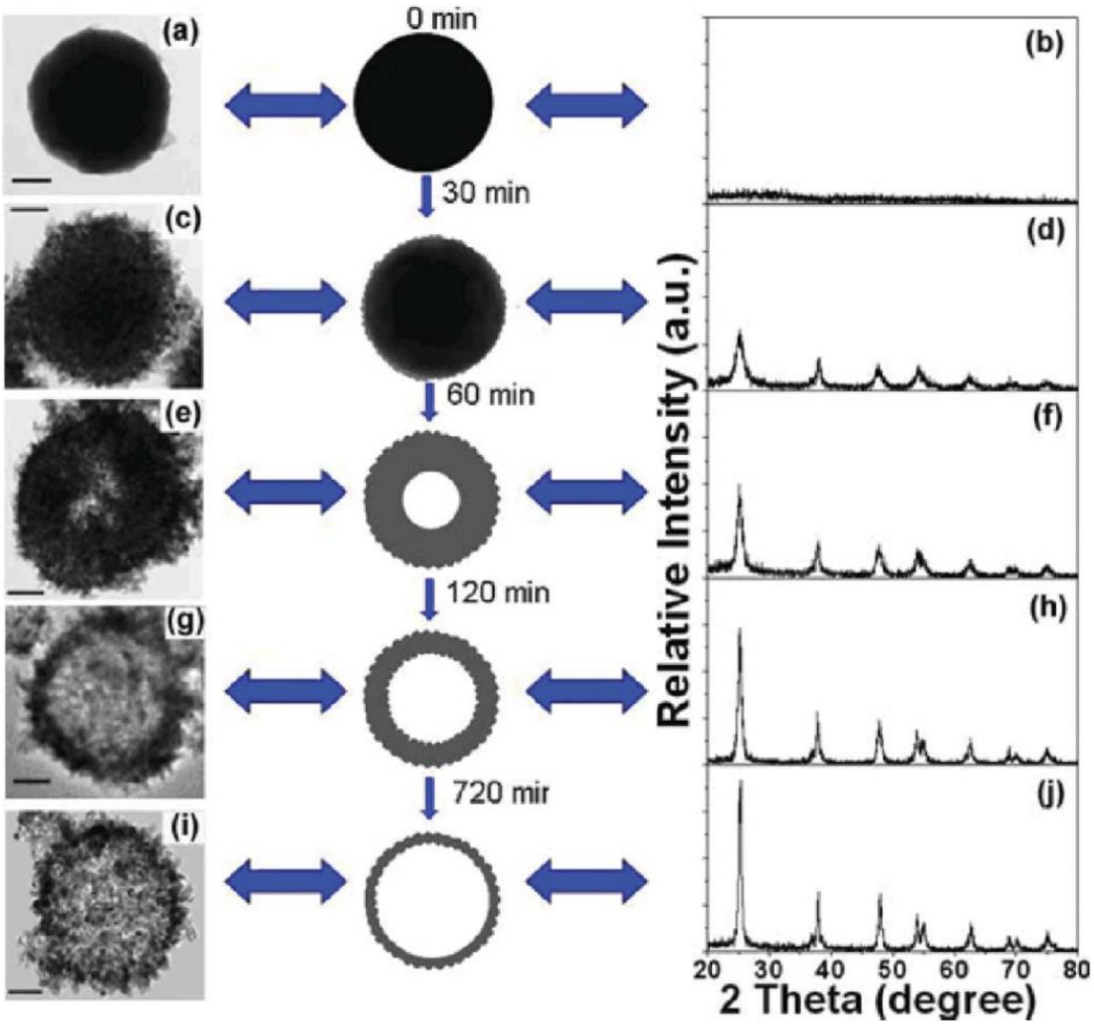

Figure 2.12. A schematic representation (centre) of the synthesis of hollow TiO_2 spheres by transforming amorphous TiO_2 solid spheres via hydrothermal treatment in the presence of NH_4F. The molar ratio of F/Ti=1. TEM images (left) and corresponding XRD patterns (right) of the intermediate products obtained at 180 °C for different time periods. The scale bar in the TEM images is 100 nm. Adapted with permission.[105] Copyright 2010, Royal Society of Chemistry.

Pan *et al.* developed another approach where uniform urchin-like mesoporous TiO_2 hollow spheres were achieved via a fluoride-assisted, low-temperature (110 °C) hydrothermal method in the presence of a surface coating of PVP.[106] The spheres consisted of 1D single crystal anatase (101) facet nanothorns. The synthesis started

with the fabrication of amorphous porous TiO_2 solid spheres. The spheres were prepared by direct precipitation of titanium (IV) isopropoxide in a mixed ethanol-acetonitrile solution with small amounts of H_2O and ammonia. The precursor spheres showed a highly porous structure with a high surface area of 328.6 m^2 g^{-1} and an average pore size of 3.4 nm. The porous structure facilitated the uniform adsorption of F^- throughout the spheres. The inner cores of the amorphous spheres were selectively etched and hollowed by the adsorbed F^-. The PVP coating played a crucial role in the formation of the TiO_2 hollow spheres, by not only protecting the hollow structure from damage, but also helped to incubate the crystallization in the mother sphere during the hollowing process. Upon calcination at 350 °C, the synthesized TiO_2 hollow spheres showed a large surface area of up to 128.6 m^2 g^{-1} and a pore size of 12.5 nm. By applying this combined method, gram quantities of TiO_2 hollow spheres can be readily synthesized.

2.5 Hierarchically Porous TiO_2 Networks

In the late 20th century, both Stucky's and Stein's groups reported the preparation of hierarchically porous materials with well-organized multi-size pores, which opened a new era in the field of porous materials.[107, 108] Hierarchically porous networks refer to materials that possess a porous structure comprising of interconnected pores on multiple length scales from micro- (< 2 nm) to meso- (2-50 nm) and macropores (> 50 nm). Materials with hierarchical porosity simultaneously combine the merits of the different pore size regimes. The presence of micro- and mesopores provides shape and size selectivity for guest species, such as organic pollutants, enhancing the host-guest interactions, whereas macropores can significantly facilitate the diffusion to, and accessibility of, active sites by guest species. Since 1998,, hierarchically porous TiO_2 materials have attracted the interest of researchers from various areas because of their applicability in the context of heavy metal-ion adsorption,[64, 109] photocatalysis,[12, 110, 111] catalysis,[112] separation,[113, 114] energy conversion and storage,[115, 116] and biochemistry.[117] Significant efforts have been devoted to the fabrication of these kinds of materials. In this thesis, template-directed approaches and template-free methods will be covered.

2.5.1 Template-Directed Method

Templating is one of the most popularly employed methods for the preparation of hierarchically porous materials. TiO_2 materials with a range of porous structures can be produced from natural templates such as starch, plant leaves, butterfly wing, wood and eggshell membrane. The advantages of a wide range of sources, low cost and environmental friendliness of natural templates make this strategy applicable to industrial production.

Iwasaki et al. reported a strategy in which starch gels were used to hierarchical meso-/ macroporous TiO_2 monoliths in combination with preformed TiO_2 nanoparticles.[118] In the synthesis, starch gel sponges consisting of intact 3D bicontinuous macroporous networks were obtained by freezing and thawing potato starch gels. The prepared sponges were then infiltrated with colloidal suspensions of TiO_2 nanoparticles that were deposited as coherent layers on the thin walls of the starch framework. The last step was to remove the starch templates by calcination. No significant disruption for the TiO_2 framework occurred. Although there was some local collapse and disorganization, the calcined TiO_2 monolith still featured continuous macropores. Depending on the TiO_2 loading and starch concentration, the macropores were up to 200 in size. The monolith composed of loosely packed aggregates of TiO_2 nanoparticles with of about 10 nm, and had wormhole-like mesoporosity and a BET surface area of 65 $m^2 g^{-1}$.

Another natural template eggshell membrane, can be employed as a removable template for the synthesis of porous materials with mesopores and macropores. Eggshell membrane shows good stability in aqueous and alcoholic media. Yang *et al.* used eggshell membrane as a template to prepare hierarchically ordered macroporous networks comprised of anatase nanocrystals (Figure 2.13).[119] The membrane, which consisted of interwoven and coalescing fibers ranging from 0.5 to 1.5 μm, was obtained by rinsing the eggshell with diluted HCl to dissolve the $CaCO_3$ shell. A sol-gel coating procedure was performed by the hydrolysis of titanium (IV) butoxide under neutral or acidic conditions in the presence of acetyl acetone. Upon heating the eggshell membrane template underwent pyrolysis and was finally removed by calcination at 500 °C. The TiO_2 networks possessed a macroscopic thin film morphology of around 25 μm thick. The film was a macroporous network consisting of interwoven TiO_2 tubes. The diameter of the tubes was less than 1.4 μm and the tube

walls were comprised of anatase nanocrystals with a diameter of around 10 nm. Gas sorption characterization indicated mesoporosity with a BET surface area of 62 m^2 g^{-1} and an average pore size of 8.2 nm.

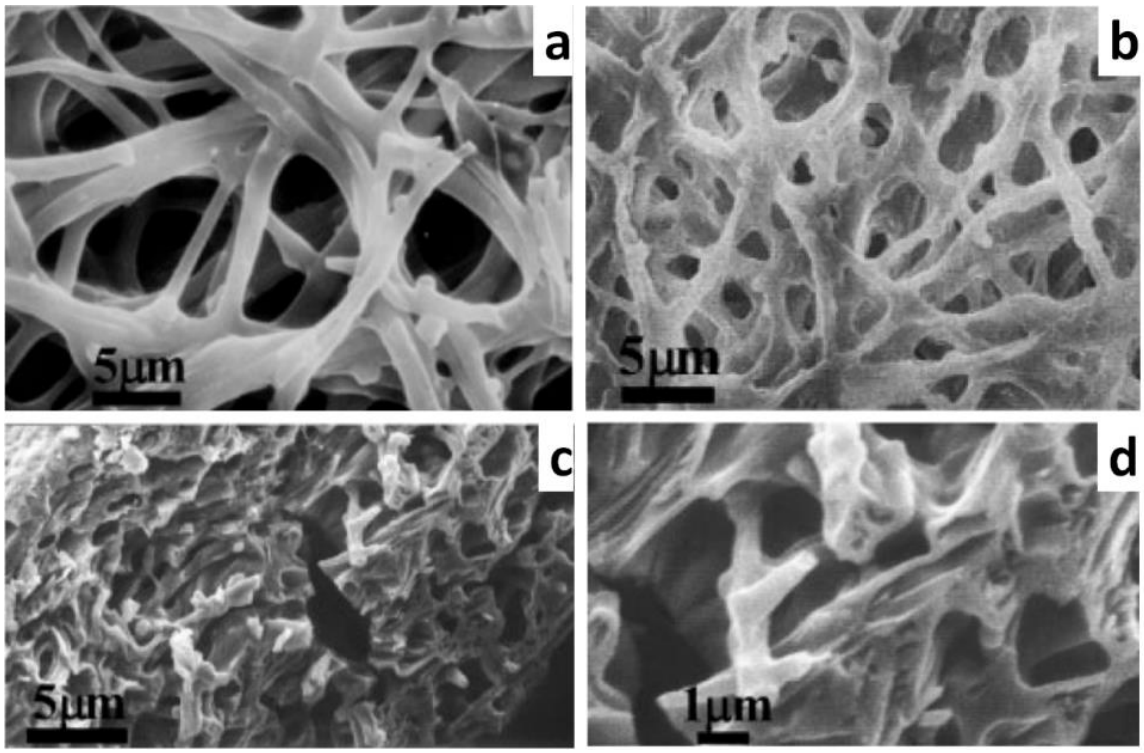

Figure 2.13. SEM images of (a) eggshell membrane, and the TiO_2 network obtained by templating the eggshell membrane using a neutral hydrolysis method in (b) overview of the surface, (c) cross section and (d) high magnification of the cross section displaying broken hollow tubes. Reproduced with permission.[119] Copyright 2002, Wiley.

Agarose, a polysaccharide generally extracted from seaweed, can form a porous gel by heating agarose powder in water and cooling at room temperature. The gel can serve as a template for the preparation of porous TiO_2 nanostructures.[120] In a synthesis reported by Cao *et al.*, hierarchically porous TiO_2 networks with 3D interconnected porous frameworks were prepared using agarose gel as template; the gel was obtained by heating agarose powder in water (1 wt.%) under stirring, then placing it into a glass mould and aging at room temperature. Before serving as the template, the water in the agarose gel was removed by solvent exchange. TiO_2 was coated on the agarose structure by a sol-gel process. The hybrids were calcined at 500 °C producing anatase TiO_2 networks. The networks contained interconnected macropores which ranged

from 80 to 200 nm in diameter. The specific surface area was 71.0 m^2 g^{-1}. After calcination at 600 °C, the macroporous structure was retained while slightly enlarged titania crystals were observed, giving a decreased surface area of 36.6 m^2 g^{-1} and 11.7 % rutile phase.

Besides natural templates, hierarchically porous TiO_2 can also be produced by synthetic templates. A macroporous synthetic polymer is an excellent template candidate for a template due to its good stability, easy removability and structural variability. The chemical and mechanical stabilities of the polymer in the templating process are critical to maintaining structural integrity, while the removal of the polymer is relatively easy, which can be realized by either pyrolysis or solvation. Polymers are available in a wide variety of sizes, shapes and porous structures, giving final materials with versatile morphological characteristics. For instance, Caruso *et al*. demonstrated a polymer gel templating procedure to fabricate hierarchically porous TiO_2.[121] The homogeneous and porous polymer gel was prepared by heating a mixture of Brij 58 (surfactant), acrylamide and glycidyl methacrylates (monomers) and ethylene glycol (cross-linker). To remove the added surfactant, the polymer was cleaned by Soxhlet extraction in ethanol and agitation in water. Next, a solvent exchange process was applied to replace water by 2-propanol. The solvent exchanged polymer gel pellets were soaked in titanium (IV) isopropoxide for 6 h under stirring and then transferred into a mixed solution of 2-propanol and water (50:50 by volume) to induce hydrolysis. To pyrolyze the organic component, the dried hybrids were calcined at 450 °C. TiO_2 was also crystallized during the calcination process. The resulting TiO_2 showed a coral-like structure with a wall of about 100-150 nm in thickness and macropores ranging from 100 nm to micrometers in diameter. Following this work, various other polymer gels with different chemical and physical properties were employed to produce TiO_2 and the effect of template properties on the structure of the final network was studied.[122] Variations in pore morphology and size depended on the template, pore diameters ranged from 3 nm to 3 μm.

Colloidal crystals are another commonly employed synthetic template to produce macroporous (>50 nm) or large mesoporous (>10 nm) structures. Both inorganic (e.g., colloidal silica particles) and organic materials (e.g., polymer spheres) can be employed as colloidal crystal templates. Colloidal crystals are an ideal template for

producing well-ordered, periodic pore structures. To produce a hierarchically porous structure, this approach can be combined with either hard or soft templating approaches. For example, Du *et al.* prepared hierarchically ordered macro-mesoporous TiO_2 films through a confinement self-assembly method within the regular voids of a 3D periodic colloidal crystal.[123] Copolymer surfactant Pluronic P123 and PS spheres served as the mesostructured template and macrostructured scaffold, respectively. PS opal templates with a size of 300 nm, synthesized by a surfactant-free emulsion polymerization reaction, were settled on a glass substrate by the vertical deposition method.[124] The glass substrate covered with the PS film was then immersed vertically into a sol suspension containing Pluronic P123, ethanol (or THF), titanium (IV) chloride and titanium (IV) isopropoxide. During the immersion process, the sol slowly penetrated the voids in the template due to the action of capillary forces. Complete hydrolysis and condensation of the TiO_2 precursor only happened after withdrawing the template out of the solution. Following rinsing with water and drying in vacuum, the resulting film was calcined to produce macro-mesoporous anatase TiO_2 networks. The macropores with a size of approximately 200 nm were directly derived from the colloidal crystal template.

However, this was smaller than the original colloid (300 nm) due to pyrolysis of the template and subsequent shrinkage of the framework during calcination. The macropores were well-interconnected, while the macropore wall contained mesopores of around 3 nm.

2.5.2 Self-Assembly Method

The synthesis and removal of templates is not only labor intensive but also environmentally unfriendly due to the use of chemical solvents or high temperatures, therefore rendering scaling-up a great challenge. In recent years, the self-assembly method has become a facile and versatile bottom-up approach to prepare hierarchically porous materials with well-defined morphologies.

In 2004, Collins *et al*. described a facile procedure to produce hierarchical porous TiO_2, in which ordered macroporous TiO_2 was spontaneously formed by simply dropping titanium alkoxides (e.g. ethoxide, propoxide, isopropoxide or butoxide) into an aqueous? ammonia solution (5 wt%) without agitation and in the absence of surfactants.[125] SEM revealed that the fragments of titanium (IV) *n*-propoxide-derived

TiO_2 materials consisted of a pseudo-hexagonally ordered porous interior of co-aligned channels. The channels radiated inwards from a smooth and curved particle surface and were typically up to 100 μm in length and 1 to 10 μm across. Channel ordering levels and diameters highly depended on the hydrolysis rates of the titanium alkoxide precursors. The total BET surface area of the as-synthesized TiO_2 sample derived from titanium (IV) isopropoxide was 368 m^2 g^{-1} and the micropore area was up to 270 m^2 g^{-1}. Accordingly, the pore size distribution was centred at about 1.5 nm, which was determined by the Barrett-Joyner-Halenda method. After calcination at 800 °C, the amorphous TiO_2 wall structures were converted into a mixture of crystalline anatase and rutile, resulting in a decreased total surface area of 92 m^2 g^{-1}. The decrease in surface area was attributed to an increase of crystal size in the channel walls during sintering, along with an increase in pore size to 3.5 nm.

Extending the work by Collins *et al.*, Yu *et al.* fabricated hierarchical macro-/mesoporous TiO_2 materials by simple dropwise addition of titanium (IV) butoxide to water in the absence of templates or additives at ambient temperature.[111] The TiO_2 materials were amorphous, exhibiting relatively homogeneous and long-range periodical pores. The pores were 2–4 μm in diameter and the walls of the pores were 1–2 μm in thickness. The specific surface area was as high as 328 m^2 g^{-1} with a high pore volume of 0.21 cm^3 g^{-1}. Upon calcination at 300 °C, macropore structure was well preserved and the materials were converted into anatase TiO_2 with a crystal size of 5.9 nm, specific surface area of 206 m^2 g^{-1} and pore volume 0.19 cm^3 g^{-1}. The same group reported the preparation of sponge-like macro-/mesoporous TiO_2 by a hydrothermal treatment of the precipitates of titanium (IV) butoxide in water in the absence of any templates or additives.[110] In this study the as-prepared materials exhibited an increase in crystallinity, average anatase crystallite size, pore size and pore volume for increasing hydrothermal time, while specific surface area decreased. All TiO_2 samples hydrothermally treated at 180 °C displayed trimodal pore-size distributions in the macro-/mesopore range: fine intraparticle mesopores (peak pore diameters of 3.7–6.9 nm), larger interparticle mesopores (peak pore diameters of 23–39 nm), and macropores (pore diameters of 0.5–3.0 μm).

Alternatively, combining sol-gel chemistry and phase separation is another promising technique for fabricating hierarchical porous materials, which has attracted great

interest in recent years. In 1999, Nakanishi *et al*. first demonstrated that the structure of macroporous silica can be controlled through a sol-gel process accompanied by phase separation.[126] The fabrication of a silica gel with well-defined, interconnected macropore was realized by incorporating a water-soluble polymer into an alkoxysilane-based sol-gel process. Later, this method was extended to the synthesis of macroporous TiO_2 materials using the high reactivity of the titanium alkoxide precursors. For example, Konishi *et al*. prepared TiO_2 monoliths with well-defined macro- and mesopores by combining the sol-gel process and phase separation.[127] In this synthesis, monolithic TiO_2 gels were generated from the starting solution containing titanium (IV) isopropoxide, HCl, formamide and H_2O. The desired pore structure was achieved by carefully controlling the hydrolysis and condensation reactions of the titanium alkoxide. Large size anatase TiO_2 monoliths were obtained by increasing the solution pH. The well-defined interconnected macropores in the TiO_2 monoliths were produced by concurrent phase separation and sol-gel transition induced by the polymerization reaction; the size and porosity of the macropores were controlled by using different starting compositions. By heating the sample to 300 °C, TiO_2 monoliths composed of anatase particles of 5.0 nm were formed. The calcined materials had BET surface areas of 150 m^2 g^{-1} and mesopores centred at 5 nm. Additionally, Hasegawa *et al*. recently developed a facile method for the fabrication of hierarchical porous TiO_2 monoliths via the sol-gel route in combination with phase separation in the presence of chelating agent and mineral salts.[114, 128, 129] In a typical synthesis of hierarchically TiO_2 monoliths,[114] polyethylene oxide was added to a homogeneous yellow solution of titanium (IV) *n*-propoxide, 1-propanol and the chelating agent ethyl acetoacetate. Then, ammonium nitrate was added at 40 °C and the solution was kept at this temperature for 24 h. To obtain crack-free monoliths, the gels underwent a stepwise solvent exchange process from ethanol to water. After drying of the wet gels, the resulting gels were calcined to obtain TiO_2 monoliths with high crystallinity. The monolithic TiO_2 constructed from anatase crystallites had a specific surface area higher than 200 m^2 g^{-1}.

2.6 Applications of Highly Crystalline Porous TiO_2 Nanostructures in Photocatalysis

As mentioned in the introduction (section 2.1), TiO_2 materials have been widely investigated and show high promise in a range of applications. The following sections present photocatalysis applications that relate to this thesis.

2.6.1 Pure TiO_2 Photocatalysts

TiO_2 nanoparticles are promising candidates for photocatalysis. It has been demonstrated that the crystal size has a significant effect on the photocatalysis performance.[130-132] Chae *et al*. reported the preparation of TiO_2 nanoparticles by the hydrothermal reaction of titanium isopropoxide stabilized in acidic ethanol/water solution at 240 °C.[132] The size of the TiO_2 nanoparticles was controlled from 7 to 25 nm by simply tailoring the composition of the solvent system along with the concentration of the Ti precursor. The photocatalytic activity of the TiO_2 nanoparticles for the decomposition of 2-propanol was also studied: 7- nm-sized particles demonstrated a 1.6 times better photocatalytic performance 1.6 times better than that of commercial Degussa P25, whereas 15- and 30 -nm-sized particles displayed lower photocatalytic efficiencies.

One-dimensional (1D) TiO_2 nanostructures, such as nanowires (nanofibers), nanobelts, nanorods and nanotubes, are often regarded as highly efficient photocatalysts due to their fast charge transport and the reduced recombination rate of hole–electron pairs.[133, 134] By a simple hydrothermal post-treatment of titanate nanotubes, Yu *et al*. prepared mesoporous anatase TiO_2 nanofibers before examining their potential for the photocatalytic oxidation of acetone. The effects of hydrothermal post-treatment time on the material properties, such as phase structure, crystallinity, crystal size, morphology, specific surface area and pore structure were investigated, and the relationship between these properties and the photocatalytic activity of the mesoporous TiO_2 nanofibers was discussed. TiO_2 nanofibers treated at 200 °C for between 3 and 24 h showed better photocatalytic activity than P25. The enhanced photocatalytic performance was attributed to the smaller crystal size, larger specific surface area and higher pore volume of the TiO_2 nanofibers. Wu *et al*. designed single-crystalline anatase TiO_2 nanobelts with two dominant surfaces of the (101) facet and assessed the photocatalytic activity by measuring the degradation of methyl orange under UV-A light radiation.[135] The nanobelt structure exhibited enhanced photocatalytic activity over nanoparticle counterparts with an identical crystal phase,

similar specific surface area and similar photo adsorption efficiency. The promoted performance was attributed to exposed (101) facets of the nanobelts producing an enhanced reactivity with O_2 molecules, which facilitated the generation of O_2^-, and the lower electron-hole recombination rate of the nanobelts compared to the nanospheres. The results indicated that the photocatalytic activity of nanocrystals is remarkably affected by tailoring the shape and the surface crystal structure of photocatalysts.

Progress in the synthesis of sub-micrometer mesoporous TiO_2 beads promises well for their widespread use in photocatalysis. Compared to nanoparticulate photocatalysts, sub-micrometer beads could improve the recyclability of the catalytic materials at the finish of the photocatalytic reaction because they can be relatively easily removed either by traditional sedimentation methods or by combining with membrane filtration technology. Wang *et al.* recently prepared monodisperse mesoporous TiO_2 beads by calcining hybrid TiO_2 beads at temperatures from 500 to 800 °C for 2 to 24 h and then studied their photocatalytic activities by the photodegradation of methylene blue under UV light radiation.[136] They successfully established a correlation between calcination conditions, materials properties (i.e. crystal phase, crystallinity, crystallite size, surface area, porosity, pore size and diameter, and surface hydroxyl groups) and photocatalytic activities. For example, with increasing calcination temperature and time, the crystal size increased and the crystallinity of the anatase TiO_2 materials was enhanced. The high crystallinity of the anatase phase effectively decreased the recombination of photogenerated electrons and holes due to less surface defects being present. However, the surface area decreased with prolonged calcination temperature and time which limited the diffusion of organic species and accessibility to the active sites on the TiO_2 surface. Ultimately, maximum activity was achieved when the hybrid beads were calcined at 650 °C for 2−8 h, with the resultant anatase bead having a diameter of approximately 700 nm.

Hollow structured TiO_2 spheres have been widely investigated for photocatalytic decomposition of organic pollutants.[97, 98, 103, 105, 111, 137] One of the early works carried out by Li *et al*. utilized hollow TiO_2 spheres with tunable interior structures as heterogeneous catalysts for the photodegradation of phenol.[98] The resulting TiO_2 hollow spheres possessed a relatively large specific surface area and the possibility for

multiple reflections of UV light, endowing the spheres with properties that greatly favoured photocatalytic reaction

Anatase TiO_2 nanocrystals with exposed high-energy, highly reactive (001) facets show a high photocatalytic performance. On the basis of theoretical predictions, Yang *et al*. first succeeded in synthesizing anatase TiO_2 single crystals with large amounts of (001) facets (47 %) via a hydrothermal treatment method utilizing HF as a capping agent.[138] Later, employing a water/2-propanol solvothermal synthetic route, the same group prepared anatase TiO_2 single-crystal nanosheets possessing 64% (001) facets.[139] In this synthesis, 2-propanol served as a synergistic capping agent as well as a reaction medium together with HF. By evaluating the active hydroxyl radicals species with a terephthalic acid scavenger, anatase TiO_2 single crystals with high percentages of reactive facets exhibited superior photoreactivity (more than 5 times) over the benchmarking material, P25. Following these pioneering studies by Yang and co-workers, various anatase TiO_2 crystals with exposed (001) facets have been prepared.[15, 100, 140-148] Recently, TiO_2 spheres containing (001) facets were demonstrated to have greatly enhanced photocatalytic activity. For example, Zhao *et al*. synthesized mesoporous anatase TiO_2 spheres with a high surface area and exposed (001) facets using a fluorine-free hydrothermal method,[15] conducting the hydrolysis and condensation of titanium (IV) butoxide in a dilute H_2SO_4 solution during hydrothermal processing. H_2SO_4 solution during the hydrothermal process. H_2SO_4 played a dual role acting as a phase inducer for anatase and as a capping agent to stabilize the (001) facet. The capping agent was removed by water. The resulting TiO_2 spheres were comprised of pearl-like, long 1D nanorod crystals with an average diameter of approximately 3.60 μm. The nanorods were about ~20 nm wide and 0.5–1.5 μm long. To investigate the photocatalytic performance, rhodamine B was employed as a probe molecule. The nanostructured TiO_2 spheres displayed enhanced photocatalytic degradation in comparison to P25.

Hierarchically porous TiO_2 networks are frequently used as photocatalysts. For example, Li *et al*. prepared porous TiO_2 material with an aligned channel structure via a dual surfactant template, and evaluated photocatalytic activity through the degradation of rhodamine B.[149] The materials possessed a unique structure with 10-20 nm pores at the surface and 100-200 nm channels in the interior, showing good

activity for rhodamine B degradation. In addition, the photocatalytic activity of the material was higher than that of a randomly orientated macroporous system. The improvement in the photocatalytic activity was ascribed to increased photon scattering and absorption efficiency, while the well-patterned channels effectively assisted the diffusion and transport of reactants within the TiO_2 frameworks. Caruso *et al*. obtained highly porous TiO_2 networks by templating polymer gels and tested the photocatalytic activity of these structures by decomposing salicylic acid in an aqueous solution under air.[122] The porosities of the resulting networks were as high as 99 % and surface areas were in the range of 5-100 $m^2 g^{-1}$. The TiO_2 materials displayed 75 % of the photocatalytic activity of P25.

Mixed-phase TiO_2 structures, such as anatase-rutile and anatase-TiO_2(B) show great potential in photocatalysis applications. Yang *et al*. synthesized mixed-phase nanofibers with an anatase shell and TiO_2(B) single crystal core.[20] The materials were prepared from $H_2Ti_3O_7$ nanofibers by two consecutive partial phase transition processes, in which the hydrothermal treatment was combined with heating processes. The mixed-phase nanofibers with well-matched anatase and TiO_2(B) phase interfaces exhibited excellent photocatalytic activity for the degradation of the organic dye sulforhodamine B under UV light. The performance of the materials was superior to the benchmark photocatalyst P25.

2.6.2 Modifications of TiO_2 Photocatalysts

As mentioned previously, the light absorption ability and the rate of electron-hole recombination are crucial factors influencing TiO_2 photocatalytic activity. Hence, considerable research has been devoted to these areas. Currently, two main routes are adopted to enhance the light absorption of TiO_2. The first method is to tailor TiO_2 nanostructures to prolong the effective path length of incident light by applying physical concepts (e.g., multiple reflections in hollow TiO_2 spheres,[98, 137] or Mie scattering by TiO_2 spheres of size comparable to the incident wavelength[150, 151]) or spatial structuring (e.g., the slow-light effect in periodic TiO_2 photonic crystals[152]). The second method to enhance light absorption by TiO_2 is to change the band gap; the highly efficient use of light in TiO_2 materials is significantly prevented by the wide band gap. Anatase TiO_2 has a band gap of 3.2 eV, meaning it can only absorb UV light with wavelengths less than 387 nm, which is only 5 % of the solar spectrum.[153]

Therefore, shifting the onset of the optical response from the UV to the visible or near infrared region is an effective and feasible approach to improve light absorption. Ways to achieve this goal include chemical doping with metal or non-metal elements and sensitizing TiO_2 with inorganic or organic compounds. In addition, the photocatalytic performance of TiO_2 can be promoted by suppressing electron-hole recombination, which can be realized by introducing foreign elements, sensitizing or forming semiconductor hetero-structures. The following three sections give a brief introduction to the fabrication of modified TiO_2 materials and their applications in photocatalysis.

2.6.2.1. Metal Modified TiO_2

Metal ion doping is beneficial for the formation of new energy levels, enhancing visible light absorption or altering the lifetime of charge carriers.[154] Various metal ions, such as Fe^{3+},[155-158] V^{4+},[159] Sn^{2+},[160] and Sn^{4+},[161] have been successfully doped into TiO_2 nanomaterials and enhanced photocatalytic activities for the degradation of organic pollutants were achieved. For example, Wu *et al*. reported that vanadium doping showed great potential to improve the photocatalytic activity of TiO_2 under visible light irradiation.[159] The V-doped TiO_2 was prepared using modified sol–gel methods. UV-visible (UV-Vis) absorption spectra demonstrated that the absorption of light shifted towards the visible region with increasing vanadium doping. According to X-ray absorption spectroscopy, V^{4+} was regarded as having either substituted for Ti^{4+} or been embedded in the vacancy of the TiO_2 structure. The photocatalytic activity of the V-doped TiO_2 photocatalyst was evaluated by the degradation of crystal violet and methylene blue and an enhanced photocatalytic performance was observed compared to pure TiO_2. Recently, efforts have been made to dope TiO_2 with Fe^{3+}ions.[155-158] The ions are easily incorporated into the crystal lattice of TiO_2 as the radius of Fe^{3+} (0.79 Å) is similar to that of Ti^{4+} (0.75 Å). Ambrus *et al*. prepared Fe(III)-doped TiO_2 photocatalysts by a co-precipitation approach using acidic solutions of $TiCl_3$ and $FeCl_3$. Photocatalytic activity was assessed by the degradation of phenol under UV-vis irradiation and visible light irradiation. Diffuse reflectance spectroscopy indicated that the light absorption of the Fe-doped samples was red shifted compared to the pure sample. The best photocatalytic performances were 3.0 at.% for UV-vis irradiation and 1.2 at.% for visible irradiation. However, the role of metal ions in TiO_2 is controversial, because they can also serve as electron-hole

recombination centres, resulting in a reduction of the photocatalytic activity. Martin *et al*. reported V-doped TiO_2 nanoparticles showed inferior photocatalytic activity on the photooxidation of 4-chlorophenol compared to pure TiO_2 nanoparticles.[162]

Loading noble metal nanoparticles of Ag, Au, Os, Pd, Pt, Ru, or Rh onto the TiO_2 surface can greatly enhance photocatalytic activity.[154, 163] The mechanisms for enhanced photocatalytic activity under UV and visible light are different. For photocatalysis under UV light, the noble metal serves as an electron sink,[164] while under visible light the metal acts as a sensitizer to enhance the absorption over a broad UV/Vis/NIR spectroscopic range due to its strong localized surface plasmon resonance.[165]

2.6.2.2 Non-metal Modified TiO_2

There are three main mechanisms to explain the effect of non-metal doping on the photocatalytic activities of TiO_2 catalysts: 1) band gap narrowing;[13] 2) creation of oxygen vacancies,[166]; and 3) formation of intra-band gap surface states.[167] In some cases, combinations of these mechanisms are required.[168] A schematic diagram in Figure 2.14 illustrates the possible changes of band gap structure of anatase TiO_2 on doping with versatile non-metals.[169]

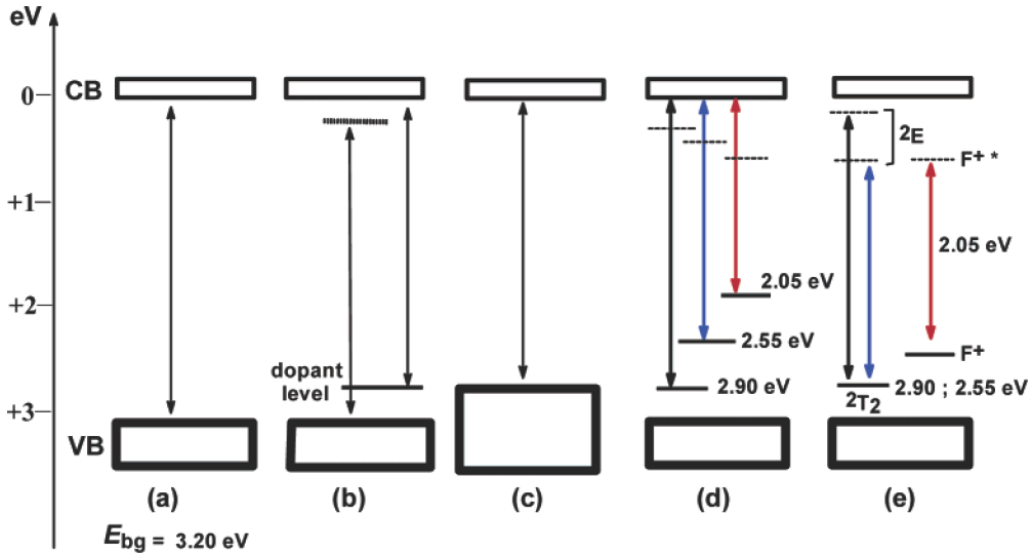

Figure 2.14. Scheme displaying the possible changes of the band gap structure of TiO_2 on doping with various non-metals: (a) pure anatase TiO_2; (b) doped TiO_2 with localized dopant levels near CB and VB; (c) band gap narrowing from VB broadening;

(d) localized dopant levels and electronic transitions to the CB, and; (e) electronic transitions of dopant levels near the VB to corresponding excited states for Ti^{3+} and F^{+} centres. Adapted with permission.[169] Copyright 2006, American Chemical Society.

Doping TiO_2 with non-metal elements, such as C,[170] N[13] and S[171] can readily induce band gap narrowing and extend the photocatalytic response to the visible light range, leading to improved photocatalytic activity under visible light. N doping has been the most studied. In 2001, Asahi *et al*. prepared N-doped crystalline TiO_2 by sputtering a TiO_2 target in a N_2(40%)/Ar gas before annealing at 550 °C in N_2 gas for 4 h. As determined by XRD, the resultant material was a mixture of the anatase and rutile phases. Compared to undoped TiO_2 material, the N-doped TiO_2 showed noticeable absorption of light over 400 nm. The photocatalytic activity was evaluated by measuring the degradation of methylene blue. N-doped TiO_2 showed much higher photocatalytic performance than pure TiO_2 in the visible light region.[13]

Although N-doped TiO_2 shows great optical response to solar radiation, its absorption in the visible and infrared region is not sufficient and can be further improved. Recently, Chen et al. reported that optical absorption in the visible light and near-infrared regions was significantly enhanced and photocatalytic activity was greatly improved through a hydrogenation process.[172] By treating highly crystalline TiO_2 nanocrystals in a 20.0 bar H_2 atmosphere at 200 °C for 5 days, TiO_2 with a crystalline core and a highly disordered surface layer (approximately 1 nm) was prepared (as shown in Figure 2.15). The VB position was shifted up by 2.18 eV, resulting in the energy gap between the VB and CB being dramatically narrowed. Diffusive reflectance and absorbance spectroscopy revealed that the onset of optical absorption was drastically shifted from the UV region to the near-infrared (approximately 1200 nm). The enhancement in the light absorption of hydrogenated TiO_2 was attributed to surface disorder and the formation of oxygen vacancies. Furthermore, hydrogenated TiO_2 exhibited greatly improved photocatalytic performance in the decomposition of methylene blue and phenol under solar light. Although absorption was improved in the visible light region, the enhanced photocatalytic activity was mainly ascribed to the inhibited recombination of photogenerated charge carriers in the midgap state in the UV region according to incident photon-to-current efficiency measurements.[172-174]

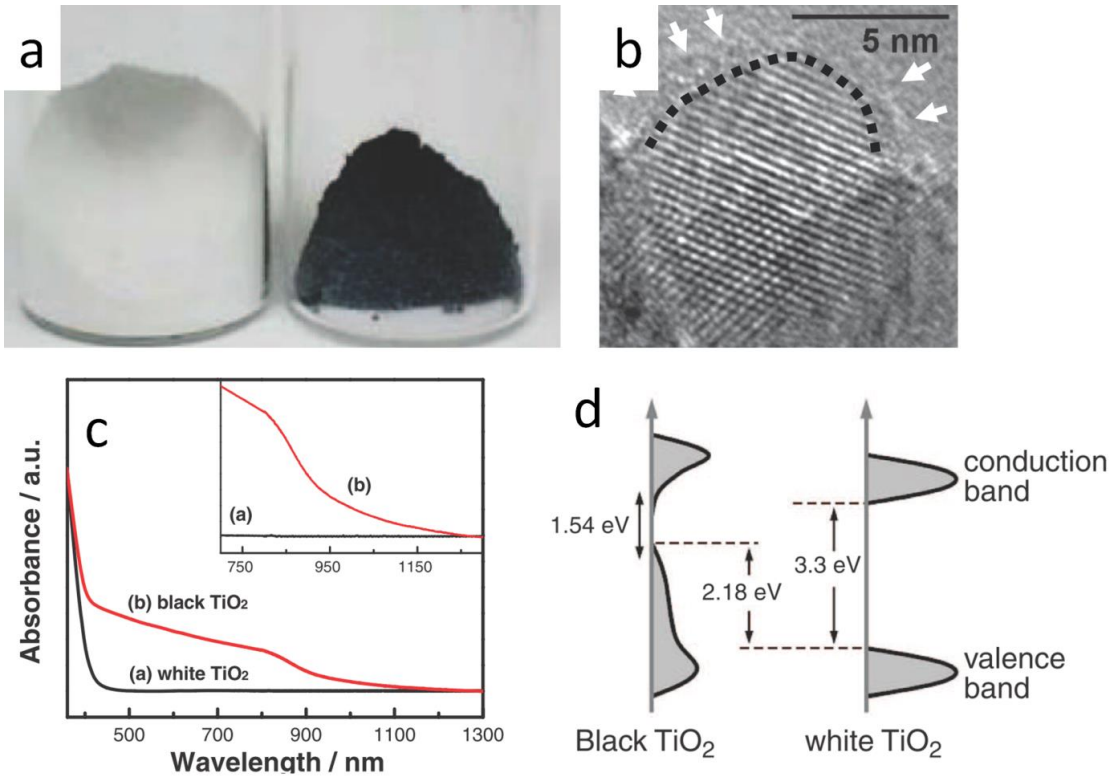

Figure 2.15. (a) Photograph of pure (white, left) and hydrogenated TiO_2 (black, right). (b) High resolution TEM images of hydrogenated TiO_2; (c) UV-vis spectra of pure and hydrogenated TiO_2. (d) A schematic illustrating the density of states of pure and hydrogenated TiO_2. Reproduced with permission.[172] Copyright 2011, Science.

2.6.2.3 Coupled Semiconductor Photocatalysts

Recently, much effort has been dedicated to the preparation of coupled semiconductors. Compared to a single-phase photocatalyst, a UV-excited wide band gap semiconductor (e.g., TiO_2) coupled with a visible light-excited narrow band gap semiconductor (e.g., CdS or Fe_2O_3 as shown in Figure 2.16) can greatly enhance charge separation, as CB electrons can be easily injected from the narrow band gap semiconductor to the wide band gap semiconductor, as well as effectively improve solar energy utilization efficiency since the synergistic absorption of the two semiconductors extends the light response range.

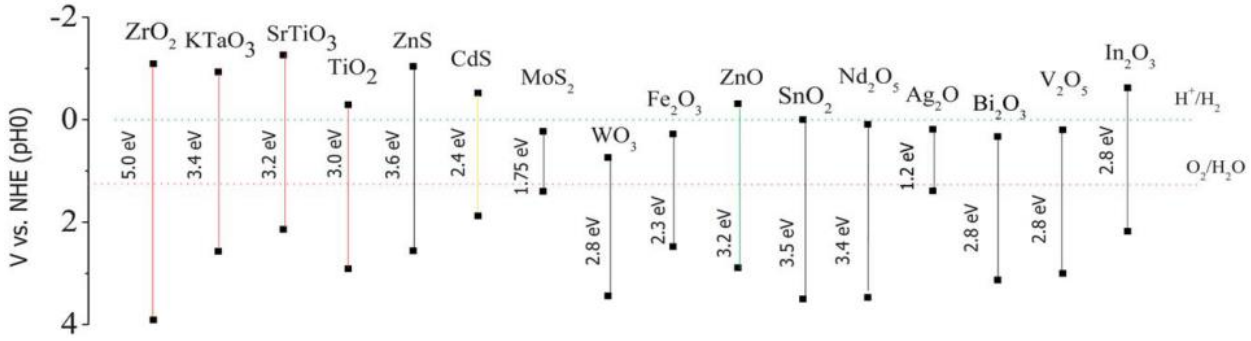

Figure 2.16. The band edge position of several widely studied semiconductors using the normal hydrogen electrode as a reference. Adapted with permission.[175] Copyright 2013, Royal Society of Chemistry.

Since early 1980s, the coupling effect between TiO_2 and CdS has been studied, usually with CdS as the primary component in the CdS/TiO_2 couple.[154] Recent research has reversed this trend by using only a small amount of CdS. In this case, CdS absorbs visible light and serves as a sensitizer. As shown in Figure 2.16 the position of both the CB and VB in CdS is higher than that in TiO_2. The smaller band gap of CdS (approximately 2.4 eV) makes it possible to absorb visible light to induce the generation of electrons and holes. Excited electrons can be subsequently injected from the CB of CdS to the CB of the TiO_2. Owing to this charge separation under visible light illumination, coupled TiO_2/CdS has been widely employed to enhance photocatalytic performance. For example, Yu *et al*. reported that utilization of nanosized CdS to couple with nanocrystalline TiO_2 improved photocatalytic activity under visible light irradiation.[176] The CdS/TiO_2 composite was prepared by a microemulsion-mediated solvothermal method. In the synthesis, titanium isopropoxide was first added to water under stirring, then $Cd(NO_3)_2$ and $(NH_4)_2S$ were successively added under vigorous stirring. After co-precipitation of $Cd(NO_3)_2$ and$(NH_4)_2S$ in water droplets, microemulsion colloids containing CdS and TiO_2 were generated. Finally, to obtain nanosized CdS-sensitized TiO_2 nanocrystals, the colloids were transferred to a Teflon-lined stainless steel autoclave and solvothermally treated at 200 °C for 12 h. The photocatalytic activity of the CdS/TiO_2 photocatalyst was evaluated by the degradation rate of methylene blue in an aqueous solution under visible light irradiation (λ > 400 nm). Compared with pure TiO_2, CdS/TiO_2 nanocrystals exhibited greatly enhanced performance due to effective separation of photogenerated carriers through the interaction of CdS and TiO_2. This efficient

separation results in the formation of Ti^{3+} which was observed using EPR spectroscopy.

In another type of coupled semiconductor system, the position of the CB and VB of TiO_2 is higher than the semiconducting counterpart, e.g. WO_3/TiO_2 and SnO_2/TiO_2. Such coupled semiconductors show greatly enhanced photocatalytic activity towards organic pollutant degradation, which is mainly attributed to improved spatial separation between the electrons and holes in the photocatalysts, along with increased surface acidity.[154, 163] For example, Leghari *et al*. prepared WO_3/TiO_2 composites by a template-free synthesis approach in a hydrothermal reaction.[19] Compared to pure TiO_2, P25 and pure WO_3, a 5.0% WO_3 composite exhibited the highest photocatalytic activity for degradation of methyl orange and 2,4-dichlorophenol under both UV and visible light illumination. The enhanced performance was ascribed to the inhibition of electron-hole recombination due to WO_3 incorporation as shown in this equation:

$$W^{6+} + e^- \rightarrow W^{5+} \qquad (10)$$

Recently, the use of conventional photocatalysts like TiO_2 and ZnO hybridized with a p-conjugated material (e.g. graphene or C_3N_4,) has been considered to be an effective strategy for promoting visible light-responsive photocatalytic performance.[177] The enhanced photocatalytic activity of the p-conjugated materials is mainly ascribed to the presence of their p-conjugated electron systems, high mobility charge carriers and high absorption coefficients in the visible light part of the spectrum.[177] Zhang *et al*. prepared a P25-graphene composite using a facile one-step hydrothermal method.[178] The P25-graphene photocatalyst demonstrated a significant enhancement over bare P25 and P25-carbon nanotubes in the photodegration of methylene blue under both UV and visible light irradiation. The enhanced photocatalytic activity was attributed to not only the greater adsorptivity of the dye and the extended light absorption range, but also to the enhanced charge separation and transportation.

2.7 Conclusions

To date, TiO_2-based photocatalysis has been universally considered as one of the most promising strategies for treating wastewater due to its unique features including high physical and chemical stability, low cost, low toxicity, easy availability and excellent photoactivity. Among TiO_2 crystal phases, anatase and rutile are the most studied for photocatalysis, where rutile represents the thermodynamically stable form while

anatase shows higher photocatalytic performance than rutile. However, enhanced photocatalytic activities were often observed for anatase-rutile mixed phase TiO_2 (e.g. commercial P25). The improved performance is explained by the spatial separation of photogenerated electrons and holes induced by the synergistic effect between anatase and rutile. The reaction conditions such as impurities/dopants and anatase crystal size, as well as packing characteristics can affect the kinetics of the anatase-to-rutile phase transformation.

Besides the phase composition, morphology, crystal size, surface properties, surface area, porosity and crystallinity all have a great effect on photocatalytic efficiency. Over the past decade, substantial progress has been made in the synthesis of a variety of TiO_2 nanostructures. Porous TiO_2 spheres can be prepared in several ways, including sol-gel templating techniques, direct hydrothermal/solvothermal methods or by combining sol-gel chemistry and hydrothermal/solvothermal processes. Extending the area of TiO_2 spheres further, in the preparation of hollow TiO_2 spheres similar techniques can be employed (e.g. hard and soft templating, one-pot hydrothermal/solvothermal technique and the combined processes of templating technique and hydrothermal/solvothermal treatments). Hierarchically porous TiO_2 networks can also be fabricated by similar means. The materials were prepared by template-directed methods or self-assembly approaches.

Among the wide spectrum of metal oxide semiconductors, TiO_2 has attracted attention owing to its recognized excellent performance as a photocatalyst under UV light irradiation. The main drawbacks of TiO_2-based photocatalysts arise from the wide band gap (3.2 eV for anatase and 3.0 eV for rutile), which restricts light absorption to the UV-light region, and the rapid recombination of photogenerated charge carriers, which suppress the quantum efficiency. Together these limit the industrial applications of TiO_2-based photocatalysts. To promote TiO_2 photocatalytic performance a number of strategies have been adopted, such as introducing foreign elements (metal/non-metal), sensitizing and forming heterostructures between two semiconductors with different energy band gaps.

TiO_2 photocatalysts have been widely investigated for the decomposition of organic pollutants, with the results holding great promise for the further development of sustainable environmental remediation technologies based on photocatalytic reactions.

Although great progress in the heterogeneous photocatalytic treatment of organic species in aqueous media using TiO_2 photocatalysts has been achieved, the limited photocatalytic performance as a result of the fast recombination between photogenerated electrons and holes, few and inaccessible active sites and low light utilization efficiency has restrained its practical application.

Based on above literature review, it is clear that the most relevant features affecting the photocatalytic activity of titania materials include 1) crystallinity, this feature controls the defects within the titania matrix and therefore affects the recombination between photogenerated electrons and holes; 2) specific surface area and porosity: high surface area and porosity can ensure the presence of abundant and accessible active catalytic sites for reaction; 3) crystal phase and the anatase to rutile phase ratios of the materials that affect the formation of junctions between anatase and rutile phases and therefore enhance the lifetimes of the photogenerated electrons and holes. To achieve high performance titania photocatalysts, simultaneously optimising the above features of the titania materials would lead to highly efficient materials suitable for photocatalysis application.

2.8 References

1. Fujishima, A.; Honda, K., *Nature* **1972**, *238*, 37-38.
2. Chen, D.; Ye, J., *Adv. Funct. Mater.* **2008**, *18*, 1922-1928.
3. Zheng, H.; Ou, J. Z.; Strano, M. S.; Kaner, R. B.; Mitchell, A.; Kalantar-zadeh, K., *Adv. Funct. Mater.* **2011**, *21*, 2175-2196.
4. Zhai, T.; Fang, X.; Li, L.; Bando, Y.; Golberg, D., *Nanoscale* **2010**, *2*, 168-187.
5. Kanhere, P.; Chen, Z., *Molecules* **2014**, *19*, 19995-20022.
6. Liao, L.; Zhang, Q.; Su, Z.; Zhao, Z.; Wang, Y.; Li, Y.; Lu, X.; Wei, D.; Feng, G.; Yu, Q.; Cai, X.; Zhao, J.; Ren, Z.; Fang, H.; Robles-Hernandez, F.; Baldelli, S.; Bao, J., *Nat. Nanotechnol.* **2014**, *9*, 69-73.
7. Yi, Z. G.; Ye, J. H.; Kikugawa, N.; Kako, T.; Ouyang, S. X.; Stuart-Williams, H.; Yang, H.; Cao, J. Y.; Luo, W. J.; Li, Z. S.; Liu, Y.; Withers, R. L., *Nat. Mater.* **2010**, *9*, 559-564.

8. Wang, X. C.; Maeda, K.; Thomas, A.; Takanabe, K.; Xin, G.; Carlsson, J. M.; Domen, K.; Antonietti, M., *Nat. Mater.* **2009**, *8*, 76-80.
9. Hu, X. L.; Sun, C. Y.; Qin, C.; Wang, X. L.; Wang, H. N.; Zhou, E. L.; Li, W. E.; Su, Z. M., *Chem. Commun.* **2013**, *49*, 3564-3566.
10. Laurier, K. G. M.; Vermoortele, F.; Ameloot, R.; De Vos, D. E.; Hofkens, J.; Roeffaers, M. B. J., *J. Am. Chem. Soc.* **2013**, *135*, 14488-14491.
11. Luo, Z.; Poyraz, A. S.; Kuo, C. H.; Miao, R.; Meng, Y. T.; Chen, S. Y.; Jiang, T.; Wenos, C.; Suib, S. L., *Chem. Mater.* **2015**, *27*, 6-17.
12. Cao, L.; Chen, D. H.; Li, W.; Caruso, R. A., *ACS Appl. Mater. Interfaces* **2014**, *6*, 13129-13137.
13. Asahi, R.; Morikawa, T.; Ohwaki, T.; Aoki, K.; Taga, Y., *Science* **2001**, *293*, 269-271.
14. Liu, Z. Y.; Sun, D. D.; Guo, P.; Leckie, J. O., *Chem. Eur. J.* **2007**, *13*, 1851-1855.
15. Zhao, Z.; Sun, Z.; Zhao, H.; Zheng, M.; Du, P.; Zhao, J.; Fan, H., *J. Mater. Chem.* **2012**, *22*, 21965-21971.
16. Ming, J.; Wu, Y. Q.; Nagarajan, S.; Lee, D. J.; Sun, Y. K.; Zhao, F. Y., *J. Mater. Chem.* **2012**, *22*, 22135-22141.
17. Joo, J. B.; Zhang, Q.; Lee, I.; Dahl, M.; Zaera, F.; Yin, Y. D., *Adv. Funct. Mater.* **2012**, *22*, 166-174.
18. Zhang, H. J.; Du, G. D.; Lu, W. Q.; Cheng, L. L.; Zhu, X. F.; Jiao, Z., *CrystEngComm* **2012**, *14*, 3793-3801.
19. Leghari, S. A. K.; Sajjad, S.; Chen, F.; Zhang, J., *Chem. Eng. J.* **2011**, *166*, 906-915.
20. Yang, D. J.; Liu, H. W.; Zheng, Z. F.; Yuan, Y.; Zhao, J. C.; Waclawik, E. R.; Ke, X. B.; Zhu, H. Y., *J. Am. Chem. Soc.* **2009**, *131*, 17885-17893.
21. Linsebigler, A. L.; Lu, G. Q.; Yates, J. T., *Chem. Rev.* **1995**, *95*, 735-758.
22. Chen, X.; Mao, S. S., *Chem. Rev.* **2007**, *107*, 2891-2959.
23. Zhang, H.; Banfield, J. F., *Chem. Rev.* **2014**, *114*, 9613-9644.
24. Zhang, R.; Elzatahry, A. A.; Al-Deyab, S. S.; Zhao, D., *Nano Today* **2012**, *7*, 344-366.
25. Hanaor, D. A. H.; Sorrell, C. C., *J. Mater. Sci.* **2011**, *46*, 855-874.
26. Machida, M.; Norimoto, K.; Kimura, T., *J. Am. Ceram. Soc.* **2005**, *88*, 95-100.
27. Penn, R. L.; Banfield, J. F., *Am. Mineral.* **1999**, *84*, 871-876.

28. Yang, J.; Ferreira, J. M. F., *Mater. Res. Bull.* **1998**, *33*, 389-394.
29. Francisco, M. S. P.; Mastelaro, V. R., *Chem. Mater.* **2002**, *14*, 2514-2518.
30. Yu, J. C.; Yu, J. G.; Ho, W. K.; Jiang, Z. T.; Zhang, L. Z., *Chem. Mater.* **2002**, *14*, 3808-3816.
31. Shannon, R. D., *J. Appl. Phys.* **1964**, *35*, 3414-3416.
32. Gamboa, J. A.; Pasquevich, D. M., *J. Am. Ceram. Soc.* **1992**, *75*, 2934-2938.
33. Shannon, R. D.; Pask, J. A., *J. Am. Ceram. Soc.* **1965**, *48*, 391-&.
34. Zhang, H. Z.; Banfield, J. F., *J. Mater. Chem.* **1998**, *8*, 2073-2076.
35. Zhang, H. Z.; Banfield, J. F., *J. Phys. Chem. B* **2000**, *104*, 3481-3487.
36. Li, W.; Ni, C.; Lin, H.; Huang, C. P.; Shah, S. I., *J. Appl. Phys.* **2004**, *96*, 6663-6668.
37. Zhang, J.; Xu, Q.; Li, M. J.; Feng, Z. C.; Li, C., *J. Phys. Chem. C* **2009**, *113*, 1698-1704.
38. Shannon, R. D.; Pask, J. A., *Am. Mineral.* **1964**, *49*, 1707-&.
39. Zhang, H. Z.; Banfield, J. F., *Am. Mineral.* **1999**, *84*, 528-535.
40. Zhang, H. Z.; Banfield, J. F., *J. Mater. Res.* **2000**, *15*, 437-448.
41. Zhang, H. Z.; Banfield, J. F., *Chem. Mater.* **2005**, *17*, 3421-3425.
42. Gribb, A. A.; Banfield, J. F., *Am. Mineral.* **1997**, *82*, 717-728.
43. Lee, G. H.; Zuo, H. M., *J. Am. Ceram. Soc.* **2004**, *87*, 473-479.
44. Hurum, D. C.; Gray, K. A.; Rajh, T.; Thurnauer, M. C., *J. Phys. Chem. B* **2005**, *109*, 977-980.
45. Liu, Z.; Zhang, X.; Nishimoto, S.; Jin, M.; Tryk, D. A.; Murakami, T.; Fujishima, A., *Langmuir* **2007**, *23*, 10916-10919.
46. Deak, P.; Aradi, B.; Frauenheim, T., *J. Phys. Chem. C* **2011**, *115*, 3443-3446.
47. Scanlon, D. O.; Dunnill, C. W.; Buckeridge, J.; Shevlin, S. A.; Logsdail, A. J.; Woodley, S. M.; Catlow, C. R. A.; Powell, M. J.; Palgrave, R. G.; Parkin, I. P.; Watson, G. W.; Keal, T. W.; Sherwood, P.; Walsh, A.; Sokol, A. A., *Nat. Mater.* **2013**, *12*, 798-801.
48. Kavan, L.; Gratzel, M.; Gilbert, S. E.; Klemenz, C.; Scheel, H. J., *J. Am. Chem. Soc.* **1996**, *118*, 6716-6723.
49. Xiong, G.; Shao, R.; Droubay, T. C.; Joly, A. G.; Beck, K. M.; Chambers, S. A.; Hess, W. P., *Adv. Funct. Mater.* **2007**, *17*, 2133-2138.
50. Hurum, D. C.; Agrios, A. G.; Gray, K. A.; Rajh, T.; Thurnauer, M. C., *J. Phys. Chem. B* **2003**, *107*, 4545-4549.

51. Hurum, D. C.; Agrios, A. G.; Crist, S. E.; Gray, K. A.; Rajh, T.; Thurnauer, M. C., *J. Electron Spectrosc. Relat. Phenom.* **2006**, *150*, 155-163.
52. Zhang, J.; Xu, Q.; Feng, Z.; Li, M.; Li, C., *Angew. Chem. Int. Ed.* **2008**, *47*, 1766-1769.
53. Jiang, D.; Zhang, S.; Zhao, H., *Environ. Sci. Technol.* **2007**, *41*, 303-308.
54. Kho, Y. K.; Iwase, A.; Teoh, W. Y.; Madler, L.; Kudo, A.; Amal, R., *J. Phys. Chem. C* **2010**, *114*, 2821-2829.
55. van der Meulen, T.; Mattson, A.; Oesterlund, L., *J. Catal.* **2007**, *251*, 131-144.
56. Hsu, Y. C.; Lin, H. C.; Chen, C. H.; Liao, Y. T.; Yang, C. M., *J. Solid State Chem.* **2010**, *183*, 1917-1924.
57. Chen, L.; Graham, M. E.; Li, G.; Gray, K. A., *Thin Solid Films* **2006**, *515*, 1176-1181.
58. Chen, D.; Caruso, R. A., *Adv. Funct. Mater.* **2013**, *23*, 1356-1374.
59. Brinker, C. J.; Scherer, G. W., *Sol-gel science: the physics and chemistry of sol-gel processing*. Academic Press, INC.: 1990.
60. Deshpande, A. S.; Shchukin, D. G.; Ustinovich, E.; Antonietti, M.; Caruso, R. A., *Adv. Funct. Mater.* **2005**, *15*, 239-245.
61. Zhang, H.; Hardy, G. C.; Khimyak, Y. Z.; Rosseinsky, M. J.; Cooper, A. I., *Chem. Mater.* **2004**, *16*, 4245-4256.
62. Dong, A. G.; Ren, N.; Tang, Y.; Wang, Y. J.; Zhang, Y. H.; Hua, W. M.; Gao, Z., *J. Am. Chem. Soc.* **2003**, *125*, 4976-4977.
63. Du, K.-F.; Yang, D.; Sun, Y., *Ind. Eng. Chem. Res.* **2009**, *48*, 755-762.
64. Kimling, M. C.; Caruso, R. A., *J. Mater. Chem.* **2012**, *22*, 4073-4082.
65. Sun, Z.; Kim, J. H.; Zhao, Y.; Bijarbooneh, F.; Malgras, V.; Lee, Y.; Kang, Y.-M.; Dou, S. X., *J. Am. Chem. Soc.* **2011**, *133*, 19314-19317.
66. Yang, W.; Li, J.; Wang, Y.; Zhu, F.; Shi, W.; Wan, F.; Xu, D., *Chem. Commun.* **2011**, *47*, 1809-1811.
67. Fang, W. Q.; Zhou, J. Z.; Liu, J.; Chen, Z. G.; Yang, C.; Sun, C. H.; Qian, G. R.; Zou, J.; Qiao, S. Z.; Yang, H. G., *Chem. Eur. J.* **2011**, *17*, 1423-1427.
68. Wang, B.; Wu, H. B.; Zhang, L.; Lou, X. W., *Angew. Chem. Int. Ed.* **2013**, *52*, 4165-4168.
69. Wu, D.; Zhu, F.; Li, J.; Dong, H.; Li, Q.; Jiang, K.; Xu, D., *J. Mater. Chem.* **2012**, *22*, 11665-11671.
70. Stober, W.; Fink, A.; Bohn, E., *J. Colloid Interface Sci.* **1968**, *26*, 62-69.

71. Eiden-Assmann, S.; Widoniak, J.; Maret, G., *Chem. Mater.* **2004**, *16*, 6-11.
72. Jiang, X. C.; Herricks, T.; Xia, Y. N., *Adv. Mater.* **2003**, *15*, 1205-1209.
73. Chen, D.; Cao, L.; Huang, F.; Imperia, P.; Cheng, Y.-B.; Caruso, R. A., *J. Am. Chem. Soc.* **2010**, *132*, 4438-4444.
74. Chen, D. H.; Huang, F. Z.; Cheng, Y. B.; Caruso, R. A., *Adv. Mater.* **2009**, *21*, 2206-2210.
75. Chen, D.; Huang, F.; Cao, L.; Cheng, Y.-B.; Caruso, R. A., *Chem. Eur. J.* **2012**, *18*, 13762-13769.
76. Xia, F.; Chen, D.; Scarlett, N. V. Y.; Madsen, I. C.; Lau, D.; Leoni, M.; Ilavsky, J.; Brand, H. E. A.; Caruso, R. A., *Chem. Mater.* **2014**, *26*, 4563-4571.
77. Hong, M. P.; Kim, J. Y.; Vemula, K.; Kim, H. S.; Yoon, K. B., *Chem. Commun.* **2012**, *48*, 4250-4252.
78. Pan, J. H.; Cai, Z. Y.; Yu, Y.; Zhao, X. S., *J. Mater. Chem.* **2011**, *21*, 11430-11438.
79. Tanaka, S.; Nogami, D.; Tsuda, N.; Miyake, Y., *J. Colloid Interface Sci.* **2009**, *334*, 188-194.
80. Caruso, F.; Caruso, R. A.; Mohwald, H., *Science* **1998**, *282*, 1111-1114.
81. Caruso, F.; Shi, X. Y.; Caruso, R. A.; Susha, A., *Adv. Mater.* **2001**, *13*, 740-744.
82. Chen, G. C.; Kuo, C. Y.; Lu, S. Y., *J. Am. Ceram. Soc.* **2005**, *88*, 277-283.
83. Yin, J. L.; Chen, H. J.; Li, Z. K.; Qian, X.; Yin, J.; Shi, M. W.; Zhou, G. T., *J. Mater. Sci.* **2003**, *38*, 4911-4916.
84. Li, H.; Ha, C.-S.; Kim, I., *Langmuir* **2008**, *24*, 10552-10556.
85. Guo, X.-F.; Kim, Y.-S.; Kim, G.-J., *J. Phys. Chem. C* **2009**, *113*, 8313-8319.
86. Xia, Y. D.; Mokaya, R., *Adv. Mater.* **2004**, *16*, 886-891.
87. Xia, Y. D.; Mokaya, R., *J. Mater. Chem.* **2005**, *15*, 3126-3131.
88. Joo, J. B.; Zhang, Q.; Dahl, M.; Lee, I.; Goebl, J.; Zaera, F.; Yin, Y. D., *Energy Environ. Sci.* **2012**, *5*, 6321-6327.
89. Nakashima, T.; Kimizuka, N., *J. Am. Chem. Soc.* **2003**, *125*, 6386-6387.
90. Lou, X. W.; Archer, L. A.; Yang, Z., *Adv. Mater.* **2008**, *20*, 3987-4019.
91. Li, X. X.; Xiong, Y. J.; Li, Z. Q.; Xie, Y., *Inorg. Chem.* **2006**, *45*, 3493-3495.
92. Yang, H. G.; Zeng, H. C., *J. Phys. Chem. B* **2004**, *108*, 3492-3495.
93. Pan, J. H.; Zhang, X.; Du, A. J.; Sun, D. D.; Leckie, J. O., *J. Am. Chem. Soc.* **2008**, *130*, 11256-11257.

94. Li, J.; Zeng, H. C., *J. Am. Chem. Soc.* **2007**, *129*, 15839-15847.
95. Yu, J.; Guo, H.; Davis, S. A.; Mann, S., *Adv. Funct. Mater.* **2006**, *16*, 2035-2041.
96. Zhou, J. K.; Lv, L.; Yu, J.; Li, H. L.; Guo, P.-Z.; Sun, H.; Zhao, X. S., *J. Phys. Chem. C* **2008**, *112*, 5316-5321.
97. Yu, J.; Liu, S.; Yu, H., *J. Catal.* **2007**, *249*, 59-66.
98. Li, H.; Bian, Z.; Zhu, J.; Zhang, D.; Li, G.; Huo, Y.; Li, H.; Lu, Y., *J. Am. Chem. Soc.* **2007**, *129*, 8406-8407.
99. Shang, S. Q.; Jiao, X. L.; Chen, D. R., *ACS Appl. Mater. Interfaces* **2012**, *4*, 860-865.
100. Ding, S.; Chen, J. S.; Wang, Z.; Cheah, Y. L.; Madhavi, S.; Hu, X.; Lou, X. W., *J. Mater. Chem.* **2011**, *21*, 1677-1680.
101. Sun, X. M.; Li, Y. D., *Angew. Chem. Int. Ed.* **2004**, *43*, 597-601.
102. Leshuk, T.; Linley, S.; Baxter, G.; Gu, F., *ACS Appl. Mater. Interfaces* **2012**, *4*, 6062-6070.
103. Yu, J.; Liu, W.; Yu, H., *Cryst. Growth Des.* **2008**, *8*, 930-934.
104. Li, J.; Wang, D.; He, Z.; Zhu, Z., *J. Am. Ceram. Soc.* **2011**, *94*, 1639-1642.
105. Yu, J.; Zhang, J., *Dalton Trans.* **2010**, *39*, 5860-5867.
106. Pan, J. H.; Wang, X. Z.; Huang, Q. Z.; Shen, C.; Koh, Z. Y.; Wang, Q.; Engel, A.; Bahnemann, D. W., *Adv. Funct. Mater.* **2014**, *24*, 95-104.
107. Yang, P. D.; Zhao, D. Y.; Margolese, D. I.; Chmelka, B. F.; Stucky, G. D., *Nature* **1998**, *396*, 152-155.
108. Holland, B. T.; Blanford, C. F.; Stein, A., *Science* **1998**, *281*, 538-540.
109. Sun, W.; Chen, M.; Zhou, S.; Wu, L., *J. Mater. Chem. A* **2014**, *2*, 14004-14013.
110. Yu, J.; Zhang, L.; Cheng, B.; Su, Y., *J. Phys. Chem. C* **2007**, *111*, 10582-10589.
111. Yu, J.; Su, Y.; Cheng, B., *Adv. Funct. Mater.* **2007**, *17*, 1984-1990.
112. Tidahy, H. L.; Siffert, S.; Lamonier, J. F.; Zhilinskaya, E. A.; Aboukais, A.; Yuan, Z. Y.; Vantomme, A.; Su, B. L.; Canet, X.; De Weireld, G.; Frere, M.; N'Guyen, T. B.; Giraudon, J. M.; Leclercq, G., *Appl. Catal. A-Gen.* **2006**, *310*, 61-69.
113. Konishi, J.; Fujita, K.; Nakanishi, K.; Hirao, K.; Morisato, K.; Miyazaki, S.; Ohira, M., *J. Chromatogr. A* **2009**, *1216*, 7375-7383.

114. Hasegawa, G.; Morisato, K.; Kanamori, K.; Nakanishi, K., *J. Sep. Sci.* **2011**, *34*, 3004-3010.
115. Tetreault, N.; Graetzel, M., *Energy Environ. Sci.* **2012**, *5*, 8506-8516.
116. Li, Y.; Fu, Z.-Y.; Su, B.-L., *Adv. Funct. Mater.* **2012**, *22*, 4634-4667.
117. McMaster, W. A.; Wang, X.; Caruso, R. A., *ACS Appl. Mater. Interfaces* **2012**, *4*, 4717-4725.
118. Iwasaki, M.; Davis, S. A.; Mann, S., *J. Sol-Gel Sci. Technol.* **2004**, *32*, 99-105.
119. Yang, D.; Qi, L. M.; Ma, J. M., *Adv. Mater.* **2002**, *14*, 1543-1546.
120. Zhou, J. F.; Zhou, M. F.; Caruso, R. A., *Langmuir* **2006**, *22*, 3332-3336.
121. Caruso, R. A.; Giersig, M.; Willig, F.; Antonietti, M., *Langmuir* **1998**, *14*, 6333-6336.
122. Caruso, R. A.; Antonietti, M.; Giersig, M.; Hentze, H. P.; Jia, J. G., *Chem. Mater.* **2001**, *13*, 1114-1123.
123. Du, J.; Lai, X.; Yang, N.; Zhai, J.; Kisailus, D.; Su, F.; Wang, D.; Jiang, L., *ACS Nano* **2011**, *5*, 590-596.
124. Nishimura, S.; Abrams, N.; Lewis, B. A.; Halaoui, L. I.; Mallouk, T. E.; Benkstein, K. D.; van de Lagemaat, J.; Frank, A. J., *J. Am. Chem. Soc.* **2003**, *125*, 6306-6310.
125. Collins, A.; Carriazo, D.; Davis, S. A.; Mann, S., *Chem. Commun.* **2004**, 568-569.
126. Nakanishi, K.; Soga, N., *J. Am. Ceram. Soc.* **1991**, *74*, 2518-2530.
127. Konishi, J.; Fujita, K.; Nakanishi, K.; Hirao, K., *Chem. Mater.* **2006**, *18*, 6069-6074.
128. Hasegawa, G.; Kanamori, K.; Nakanishi, K.; Hanada, T., *J. Am. Ceram. Soc.* **2010**, *93*, 3110-3115.
129. Hasegawa, G.; Kanamori, K.; Nakanishi, K.; Hanada, T., *J. Sol-Gel Sci. Technol.* **2010**, *53*, 59-66.
130. Anpo, M.; Shima, T.; Kodama, S.; Kubokawa, Y., *J. Phys. Chem.* **1987**, *91*, 4305-4310.
131. Wang, C. C.; Zhang, Z. B.; Ying, J. Y., *Nanostructured Materials* **1997**, *9*, 583-586.
132. Chae, S. Y.; Park, M. K.; Lee, S. K.; Kim, T. Y.; Kim, S. K.; Lee, W. I., *Chem. Mater.* **2003**, *15*, 3326-3331.
133. Almquist, C. B.; Biswas, P., *J. Catal.* **2002**, *212*, 145-156.

134. Wang, X. D.; Li, Z. D.; Shi, J.; Yu, Y. H., *Chem. Rev.* **2014**, *114*, 9346-9384.
135. Wu, N. Q.; Wang, J.; Tafen, D.; Wang, H.; Zheng, J. G.; Lewis, J. P.; Liu, X. G.; Leonard, S. S.; Manivannan, A., *J. Am. Chem. Soc.* **2010**, *132*, 6679-6685.
136. Wang, X.; Cao, L.; Chen, D.; Caruso, R. A., *ACS Appl. Mater. Interfaces* **2013**, *5*, 9421-9428.
137. Cao, L.; Chen, D.; Caruso, R. A., *Angew. Chem. Int. Ed.* **2013**, *52*, 10986-10991.
138. Yang, H. G.; Sun, C. H.; Qiao, S. Z.; Zou, J.; Liu, G.; Smith, S. C.; Cheng, H. M.; Lu, G. Q., *Nature* **2008**, *453*, 638-642.
139. Yang, H. G.; Liu, G.; Qiao, S. Z.; Sun, C. H.; Jin, Y. G.; Smith, S. C.; Zou, J.; Cheng, H. M.; Lu, G. Q., *J. Am. Chem. Soc.* **2009**, *131*, 4078-4083.
140. Han, X.; Kuang, Q.; Jin, M.; Xie, Z.; Zheng, L., *J. Am. Chem. Soc.* **2009**, *131*, 3152-3153.
141. Liu, G.; Yang, H. G.; Wang, X.; Cheng, L.; Pan, J.; Lu, G. Q.; Cheng, H.-M., *J. Am. Chem. Soc.* **2009**, *131*, 12868-12869.
142. Wang, B.; Lu, X. Y.; Yu, L. K.; Xuan, J.; Leung, M. K. H.; Guo, H. F., *CrystEngComm* **2014**, *16*, 10046-10055.
143. Wang, X.; He, H.; Chen, Y.; Zhao, J.; Zhang, X., *Appl. Surf. Sci.* **2012**, *258*, 5863-5868.
144. Cao, F.-L.; Wang, J.-G.; Lv, F.-J.; Zhang, D.-Q.; Huo, Y.-N.; Li, G.-S.; Li, H.-X.; Zhu, J., *Catal. Commun.* **2011**, *12*, 946-950.
145. Liu, M.; Piao, L.; Lu, W.; Ju, S.; Zhao, L.; Zhou, C.; Li, H.; Wang, W., *Nanoscale* **2010**, *2*, 1115-1117.
146. Liu, M.; Piao, L.; Zhao, L.; Ju, S.; Yan, Z.; He, T.; Zhou, C.; Wang, W., *Chem. Commun.* **2010**, *46*, 1664-1666.
147. Sun, W. W.; Sun, K.; Peng, T.; You, S. J.; Liu, H. M.; Liang, L. L.; Guo, S. S.; Zhao, X. Z., *J. Power Sources* **2014**, *262*, 86-92.
148. Li, H.; Zeng, Y.; Huang, T.; Piao, L.; Yan, Z.; Liu, M., *Chem. Eur. J.* **2012**, *18*, 7525-7532.
149. Li, X.; John, V. T.; He, G.; Zhan, J.; Tan, G.; McPherson, G.; Bose, A.; Sarkar, J., *Langmuir* **2009**, *25*, 7586-7593.
150. Xu, H.; Chen, X.; Ouyang, S.; Kako, T.; Ye, J., *J. Phys. Chem. C* **2012**, *116*, 3833-3839.

151. Tsai, M.-C.; Lee, J.-Y.; Chen, P.-C.; Chang, Y.-W.; Chang, Y.-C.; Yang, M.-H.; Chiu, H.-T.; Lin, I. N.; Lee, R.-K.; Lee, C.-Y., *Appl. Catal., B* **2014**, *147*, 499-507.
152. Chen, J. I. L.; von Freymann, G.; Choi, S. Y.; Kitaev, V.; Ozin, G. A., *Adv. Mater.* **2006**, *18*, 1915-1919.
153. Xu, H.; Ouyang, S.; Liu, L.; Reunchan, P.; Umezawa, N.; Ye, J., *J. Mater. Chem. A* **2014**, *2*, 12642-12661.
154. Zhang, H.; Chen, G.; Bahnemann, D. W., *J. Mater. Chem.* **2009**, *19*, 5089-5121.
155. Ambrus, Z.; Balazs, N.; Alapi, T.; Wittmann, G.; Sipos, P.; Dombi, A.; Mogyorosi, K., *Appl. Catal., B* **2008**, *81*, 27-37.
156. Sun, L.; Li, J.; Wang, C. L.; Li, S. F.; Chen, H. B.; Lin, C. J., *Sol. Energy Mater. Sol. Cells* **2009**, *93*, 1875-1880.
157. Su, R.; Bechstein, R.; Kibsgaard, J.; Vang, R. T.; Besenbacher, F., *J. Mater. Chem.* **2012**, *22*, 23755-23758.
158. Asilturk, M.; Sayilkan, F.; Arpac, E., *J. Photochem. Photobiol. A: Chem* **2009**, *203*, 64-71.
159. Wu, J. C. S.; Chen, C. H., *J. Photochem. Photobiol. A: Chem* **2004**, *163*, 509-515.
160. Boppana, V. B. R.; Lobo, R. F., *J. Catal.* **2011**, *281*, 156-168.
161. Arpac, E.; Sayilkan, F.; Asilturk, M.; Tatar, P.; Kiraz, N.; Sayilkan, H., *J. Hazard. Mater.* **2007**, *140*, 69-74.
162. Martin, S. T.; Morrison, C. L.; Hoffmann, M. R., *J. Phys. Chem.* **1994**, *98*, 13695-13704.
163. Daghrir, R.; Drogui, P.; Robert, D., *Ind. Eng. Chem. Res.* **2013**, *52*, 3581-3599.
164. Subramanian, V.; Wolf, E. E.; Kamat, P. V., *J. Am. Chem. Soc.* **2004**, *126*, 4943-4950.
165. Kowalska, E.; Mahaney, O. O. P.; Abe, R.; Ohtani, B., *Phys. Chem. Chem. Phys.* **2010**, *12*, 2344-2355.
166. Ihara, T.; Miyoshi, M.; Iriyama, Y.; Matsumoto, O.; Sugihara, S., *Appl. Catal., B* **2003**, *42*, 403-409.
167. Irie, H.; Watanabe, Y.; Hashimoto, K., *J. Phys. Chem. B* **2003**, *107*, 5483-5486.
168. Sakthivel, S.; Kisch, H., *ChemPhysChem* **2003**, *4*, 487-490.

169. Serpone, N., *J. Phys. Chem. B* **2006**, *110*, 24287-24293.
170. Choi, Y.; Umebayashi, T.; Yoshikawa, M., *J. Mater. Sci.* **2004**, *39*, 1837-1839.
171. Yamamoto, T.; Yamashita, F.; Tanaka, I.; Matsubara, E.; Muramatsu, A., *Mater. Trans.* **2004**, *45*, 1987-1990.
172. Chen, X. B.; Liu, L.; Yu, P. Y.; Mao, S. S., *Science* **2011**, *331*, 746-750.
173. Liu, L.; Chen, X., *Chem. Rev.* **2014**, *114*, 9890-9918.
174. Hu, Y. H., *Angew. Chem. Int. Ed.* **2012**, *51*, 12410-12412.
175. Wang, Y. J.; Wang, Q. S.; Zhan, X. Y.; Wang, F. M.; Safdar, M.; He, J., *Nanoscale* **2013**, *5*, 8326-8339.
176. Yu, J. C.; Wu, L.; Lin, J.; Li, P. S.; Li, Q., *Chem. Commun.* **2003**, 1552-1553.
177. Dong, S.; Feng, J.; Fan, M.; Pi, Y.; Hu, L.; Han, X.; Liu, M.; Sun, J.; Sun, J., *RSC Adv.* **2015**, *5*, 14610-14630.
178. Zhang, H.; Lv, X. J.; Li, Y. M.; Wang, Y.; Li, J. H., *ACS Nano* **2010**, *4*, 380-386.

Chapter 3. Hierarchically Porous Titania Networks with Tunable Anatase : Rutile Ratios and Their Enhanced Photocatalytic Activities

3.1 Introduction

Titania has been widely studied for photocatalytic application in recent years due to its superior photocatalytic activity, excellent photo- and chemical stability, nontoxicity and relatively low cost.[1-7] To enhance the photocatalytic activity for practical application, numerous strategies have been applied to improve the effectiveness of this photocatalyst.[8-21] Among these methods, forming anatase-rutile mixed phase photocatalysts is generally viewed as an effective and low-cost method because this can be realized through a facile and industry favored solid state phase transformation process.[21-27] However, exaggerated grain growth of rutile crystals usually occurs along with the formation of unavoidable mixed-phase titania agglomerates when the precursors are sintered at an elevated temperature. This gives rise to photocatalysts with significantly reduced specific surface area and porosity, and therefore limits their effectiveness in practical applications.

In this chapter, a simple and feasible method to fabricate mixed phase porous titania networks (PTNs) with tunable anatase : rutile ratios and high specific surface areas is demonstrated. Such mixed phase PTNs can be prepared by calcining hierarchically porous titania materials derived from a facile sol-gel templating process. The hierarchically porous titania possesses a substantially reduced contact area between particles, and hence between nanocrystals during calcination. This significantly decreases the probability of interface nucleation of the rutile crystal phase thereby retarding the phase transformation while being heated at a relatively low temperature (600 °C). The photocatalytic activities of these PTN materials with different rutile contents and specific surface areas were examined by monitoring the photodegradation of methylene blue. The results were compared to the photocatalytic activities of control samples prepared in the absence of templates showing a significant enhancement when the morphology and phase was controlled.

This study provides a feasible method for fabricating hierarchically porous titania networks by adjusting the phase transformation kinetics of the solid-state reaction, and

allows rational design of advanced photocatalysts with optimized composition and physical properties (e.g. high specific surface area and controllable porosity). This study focuses on controlling the properties of the titania photocatalysts that have potential application in water purification and environmental remediation and has been published in *ACS Applied Materials & Interfaces*. The published manuscript and the supporting information are presented in section 3.2. Reprinted from "Hierarchically Porous Titania Networks with Tunable Anatase : Rutile Ratios and Their Enhanced Photocatalytic Activities. *ACS Appl. Mater. Interfaces*, **2014**, *6*, 13129-13137", copyright (2014), with permission from the American Chemical Society.

3.2 Manuscript (attached as below)

ACS APPLIED MATERIALS & INTERFACES

Research Article

www.acsami.org

Hierarchically Porous Titania Networks with Tunable Anatase:Rutile Ratios and Their Enhanced Photocatalytic Activities

Lu Cao,[†] Dehong Chen,*[,†] Wei Li,[‡] and Rachel A. Caruso*[,†,‡]

[†]Particulate Fluids Processing Centre, School of Chemistry, The University of Melbourne, Melbourne, Victoria 3010, Australia

[‡]CSIRO Manufacturing Flagship, Private Bag 10, Clayton, Victoria 3168, Australia

Supporting Information

ABSTRACT: Mixed-phase hierarchically porous titania networks (PTNs) with 3D interconnected porous frameworks and tunable rutile contents have been synthesized via a facile sol–gel templating and calcination process. The products were characterized using scanning electron microscopy, powder X-ray diffraction, and nitrogen gas sorption analysis, and their photocatalytic activities were evaluated by measuring the photocatalytic degradation of methylene blue, a typical effluent from the textile industry, under UV light illumination. The hierarchically macro-/mesoporous titania structure formed after templating followed by calcination in air. The reduced interfaces between titania nanocrystals in these PTN materials can significantly decrease interface nucleation of the rutile phase and effectively retard the anatase to rutile phase transformation, therefore giving rise to porous titania photocatalysts featuring tunable rutile ratios (from 0 to 100 wt %), reduced crystal sizes, hierarchically porous structure, and relatively high specific surface areas (up to 71.0 m^2 g^{-1}). The photocatalytic performance of the materials was correlated to the anatase:rutile ratio and specific surface area of the materials, with the mixed-phase (rutile content of 15.4%) nanocrystalline titania calcined at 600 °C for 6 h showing the highest photocatalytic activity. This study demonstrates that a substantial improvement in photocatalytic activity of the titania can be achieved by controlling morphology and carefully tuning phase composition via a feasible solid-state phase transformation at a relatively low temperature (600 °C). This concept for the rational design and development of high-performance photocatalysts using an industrially simple process would be capable of mass production.

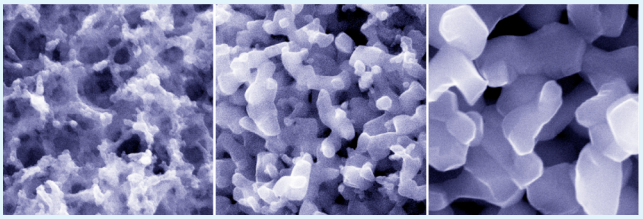

KEYWORDS: *titanium dioxide, nanostructure, porous material, phase transformation, photocatalysts, interfaces, solid-state reaction, phase junction*

INTRODUCTION

As an important industrial product, titania (TiO_2) has been widely used as an inorganic pigment, a photocatalyst, in sunscreen, sensors, energy storage and conversion devices, and electrochromics.[1−19] Because of its unique properties including superior photocatalytic activity, excellent photo- and chemical stability, nontoxicity, and relatively low cost for production, titania has been extensively studied for diverse photocatalytic applications ranging from water splitting to environmental remediation in the past several decades.[2−4,15−17,20−29] To enhance photocatalytic efficiency for practical applications, various innovative strategies, such as doping titania with diverse metal/nonmetal elements,[2,21,22,30] forming anatase–rutile mixed-phase composites,[24,31−40] creating noble metal–titania heterojunctions or coupling with narrow-band semiconductor nanoparticles (e.g., CdS/TiO_2),[41−46] and attaching titania nanocrystals to graphene nanosheets,[47−49] have been applied to optimize the performance of this photocatalyst. These modifications could effectively broaden the light absorbance of the photocatalysts,[21,22,30,47,49] promote spatial separation of photogenerated electrons and holes and therefore prevent their recombination,[35−42,44,46] facilitate electron conduction within the photocatalyst,[47,49] and thus enhance the performance of the titania photocatalyst. Among diverse strategies, forming anatase–rutile mixed-phase composites is an easy, low-cost, and scalable process, and is generally recognized as a highly practical approach for fabricating efficient titania photocatalysts for environmental remediation applications. For example, the commercially available benchmark photocatalyst, Evonik (Degussa) P25 nanoparticles,[50−53] is a mixed-phase titania with a typical anatase:rutile ratio of 80:20. Ample evidence has clearly revealed that such mixed-phase photocatalysts can significantly promote spatial separation of photogenerated electrons and holes, therefore enhancing the photocatalytic performance.[33,35−39,42,54]

Thermodynamically, rutile is the most stable phase among diverse polymorphs of titania, and anatase can be readily transformed into rutile via a solid-state phase transformation (usually by calcination at above 550 °C in air).[1,16,52] From the viewpoint of large-scale industrial production of mixed-phase titania photocatalysts, solid-state phase transformation is generally viewed as a promising process.[1,16,52] However, some

Received: May 14, 2014
Accepted: July 23, 2014
Published: August 4, 2014

obstacles still remain: (1) exaggerated grain growth of rutile crystals usually occurs with the anatase to rutile phase transformation due to the increased mobility of atoms and the heat released during the phase transformation;[52,55,56] and (2) unavoidable titania agglomerations form when sintered at elevated temperature,[52,53] and this gives rise to photocatalysts with significantly reduced specific surface area and porosity, therefore resulting in limited effectiveness in practical applications.

The phase transformation process from anatase to rutile has been extensively studied for both scientific and technological interest because crystal phase is an important factor in determining properties of titania. In general, this solid-state phase transformation proceeds via a nucleation and growth process, and three nucleation modes, interface-, surface-, and bulk-nucleation,[52,57−63] have been proposed to illustrate the anatase to rutile phase transformation. The predominant nucleation mode in a typical solid-state reaction highly depends on the calcination temperature, packing characteristic, and other physical properties of the precursors.[32,58,59,61,64] Interface-nucleation usually triggers and governs the phase transformation at a relatively low temperature (e.g., <620 °C); in contrast, a very high calcination temperature (e.g., >1000 °C) would induce the bulk-nucleation process by initializing a strong thermal fluctuation of the Ti and O atoms in anatase, and the phase transformation is usually accomplished in a short period (several minutes). For the phase transformation conducted at an intermediate temperature, it usually proceeds predominantly via a surface-nucleation process. Of these three nucleation modes, the interface-nucleation process can occur and proceed at a relatively low calcination temperature,[61] which could help to inhibit a fast growth of rutile nanocrystals. As a result, a relatively high specific surface area can be retained in the final products, which would generally enhance the effectiveness of the photocatalyst by increasing active sites available for reaction.

Besides calcination temperature, the interfaces between titania nanocrystals have been demonstrated to be another important factor in affecting the kinetics of the anatase to rutile phase transformation.[58,59,64,65] As reported by Banfield et al. and other researchers,[58,59,63,66] the anatase twin boundaries constructed from two slabs of octahedral zigzag chains have structural similarity to those of the rutile phase.[59,66] Such anatase twin interfaces can act as nuclei for the rutile phase, thus initializing the phase transformation due to their relatively low activation barriers for nucleation, in comparison to either surface- or bulk-nucleation involving an energy-intensive high temperature process.[54,59] Therefore, a reduction in anatase−anatase interface can slow the phase transformation, especially when this transformation is governed by the interface nucleation mode, which can proceed at a relatively low calcination temperature. This gives another variable to control the kinetics of phase transformation and to tailor the properties of the products.

Herein, a hierarchically porous titania network (PTN) composed of nanoparticles was prepared via a facile sol−gel templating process and employed as the precursor for fabricating mixed-phase titania photocatalysts featuring hierarchically porous structure, tunable rutile ratio, and relatively high specific surface area. As compared to conventional titania aggregates (illustrated in Scheme 1a), such PTN materials possess substantially reduced nanocrystal interfaces (Scheme 1b). This can significantly decrease interface nucleation of the rutile phase and effectively retard the phase transformation at a relatively low temperature (600 °C), therefore giving rise to porous titania photocatalysts with optimized rutile ratios and relatively high specific surface areas simply by varying calcination duration. Photocatalytic activities of the PTN with different percentages of rutile phase and specific surface areas were tested by monitoring the photodegradation of methylene blue under UV light illumination. A comparative study of photocatalytic activities of the control samples prepared in the absence of templates (macropores) was also conducted to clarify the underlying mechanism of the enhanced photocatalytic performance of the PTN materials.

Scheme 1. An Illustration of the Anatase to Rutile Phase Transformation in (a) Titania Aggregates with Abundant Interfaces (Highlighted as Red Lines) between Nanocrystals, and in (b) Porous Titania Networks with Much Reduced Interfaces[a]

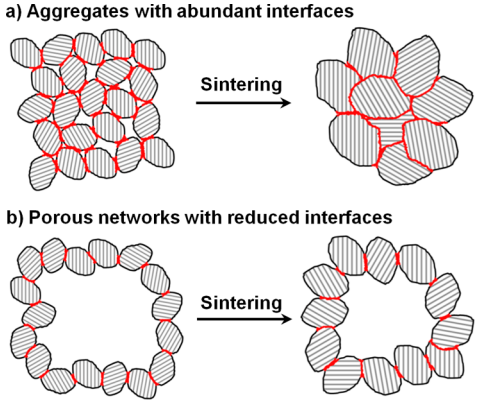

[a]A reduction in interface between nanocrystals can significantly decrease interface nucleation of the rutile phase and effectively retard the phase transformation at a relatively low temperature (e.g., 600 °C), therefore giving rise to porous titania networks featuring tunable rutile content, reduced crystal sizes, hierarchically porous structure, and relatively high specific surface areas.

EXPERIMENTAL SECTION

Chemicals. All chemical reagents were commercial products and were used without further purification. The porous agarose gel template was prepared using an agarose powder (molecular biology grade) from Scientifix. The metal alkoxide precursor, titanium(IV) isopropoxide (TIP; 97%), was purchased from Sigma-Aldrich. The isopropanol (99.5%) and ethanol (99.5%) solvents were purchased from Chem-Supply. The methylene blue (MB) used to illustrate photodegradation performance was from BDH Chemical Ltd. The Milli-Q water used in the experiment was collected on a Millipore Academic A10 purification system and had a resistivity no less than 18.2 MΩ cm.

Preparation of Agarose Gel Template. A procedure as previously detailed was employed for the preparation of a porous 1 wt % agarose gel template.[67] In brief, agarose powder (2 g) was added slowly to 198 mL of water within a beaker under stirring at room temperature. The resulting suspension was heated until a clear solution was obtained. This clear solution was then immediately poured into Pyrex test tubes and sealed with Parafilm. The test tubes were left at room temperature overnight to allow for complete gelation.

Preparation of Hierarchically Porous Titania Networks. The agarose gels were cut into small pieces (~3 × 5 × 5 mm^3) and underwent a solvent exchange from water to ethanol in three steps (water-to-ethanol volume ratio of 2:1, 1:2, then 0:1, soaking for 6 h in each solution), and similarly from ethanol to isopropanol. Subsequently, the gel pieces were soaked in 70 wt % TIP in isopropanol

solution for 18 h, before being transferred into water/isopropanol (1:1 v/v) mixed solvent for hydrolysis and condensation reactions. After 18 h, the samples were removed from solution and dried at room temperature in the fume hood for 3 days. These air-dried samples were calcined at various temperatures (500, 550, 600, 650, 700, 800, or 900 °C) for 2 h under flowing air with a ramp rate of 1.6 °C min^{-1}. To investigate the effect of prolonged calcination time, the samples were calcined at 600 °C for different durations (2, 6, 10, or 24 h). The resulting hierarchically PTN samples were labeled as PTN-*x*C-yh, where *x* indicates calcination temperature (°C) and *y* is the duration (h). For instance, PTN-600C-2h refers to the resultant porous titania calcined at 600 °C for 2 h in air. The same sol–gel synthesis (18.1 mL of 70 wt % TIP added to a mixture of 125 mL of water and 125 mL of isopropanol) and calcination procedure was employed to prepare the control samples in the absence of agarose gel templates. In this case, the control samples were denoted as Control-*x*C-*y*h.

Characterization. The morphology and average grain size of the samples were observed using a field emission environmental scanning electron microscope (FEI Quanta 200F). The samples were observed without metal sputter coating. Powder X-ray diffraction (XRD, Philips PW1800 diffractometer with Cu Kα radiation) was used to determine the crystalline phase and to estimate the rutile phase content and crystal size of the resulting titania materials. The diffractometer was set at 40 kV accelerating voltage and 20 mA applied current, and the samples were scanned from 10° to 80° at a rate of 0.02° s^{-1}. The obtained patterns were then utilized to determine weight percentage of the rutile phase titania, using the following equation:[62]

$$W_R\,(\%) = 100A_R/(0.886A_A + A_R + 2.721A_B)$$

where A_A, A_R, and A_B represent the integrated intensities of the anatase (101), rutile (110), and brookite (121) peaks, respectively. Nitrogen gas sorption isotherms were measured at −196 °C by the volumetric method on a Micromeritics Tristar 3000 surface area and porosity analyzer. Prior to the measurement, samples were evacuated at 150 °C for 18 h on a vacuum line (less than 30 mTorr). The standard multipoint Brunauer–Emmett–Teller (BET) method was utilized to calculate the specific surface area using the adsorption data in the P/P_0 range from 0.05 to 0.20. The pore size distributions of the materials were derived from the adsorption branches of the isotherms on the basis of the Barett–Joyner–Halenda (BJH) model.

Photocatalytic Activity. Photocatalytic activities of the PTN (40 mg) and the control samples (40 mg) were studied by monitoring the degradation of MB (80 mL, 55.5 mg L^{-1}) in an aqueous solution under UV irradiation with continuous magnetic stirring. Before irradiation, the suspension was equilibrated in a jacketed beaker by stirring in the dark for 1 h to equilibrate the adsorption of MB dye onto the surface of titania. The jacketed beaker was kept at 20 ± 0.5 °C with chilled water running through a thermostatic circulated bath. The MB solution was continuously bubbled with air (industrial grade, BOC) during stabilization and degradation. A 500 W Hg (Xe) globe (Oriel) with a dichroic mirror (66226, Oriel, 280 < λ < 400 nm) was used to deliver light vertically through a quartz reactor lid. Following UV-radiation exposure, the degradation of the MB dye was monitored by taking 1.5 mL aliquots at regular irradiation intervals (0, 15, 30, 45, and 60 min). These aliquots were centrifuged at 15 000 rpm for 10 min to separate the catalyst from the mixture. The supernatants were collected and analyzed by recording the characteristic absorption peak of MB (664 nm) using a UV–vis spectrophotometer (Varian Cary 50 Bio).

RESULTS AND DISCUSSION

Morphological Evolution of the PTN and Control Samples. Both the temperature during calcination treatment and the nanoparticle packing characteristics in the precursor materials play crucial roles in influencing the morphologies of the final titania materials. Figure 1 shows SEM images of both PTN and control samples obtained by calcining the titania/agarose composite and titania at temperatures ranging from 500 to 800 °C. PTN materials calcined at 500 °C (Figure 1a,b and Figure S1a in the Supporting Information) consist of titania nanocrystals <10 nm in diameter and show a hierarchically porous framework containing interconnected macropores ranging from 80 to 200 nm in diameter. After calcination at 600 °C (Figure 1c and Supporting Information Figure S1b), the macroporous structure was retained in the PTN material, and slightly enlarged titania crystals were observed. In contrast, the control sample (Figure 1d) fabricated in the absence of agarose gel templates formed a compact aggregate consisting of ~35 nm titania nanocrystals. Increasing the calcination temperature to 700 °C (Figure 1e and Supporting Information Figure S1c) or 800 °C (Figure 1g and Supporting Information Figure S1d) resulted in the PTN material becoming more "compact", mainly due to shrinkage of the inorganic framework along with the coarsening of the titania crystals (diameters up to 170 nm after being heated at 800 °C). As clearly illustrated in Figure 1f and h, at such high temperatures (>700 °C) the control samples show densely sintered and relatively large titania crystals (~170 nm at 700 °C and ~260 nm at 800 °C). The crystal size of the control samples is much larger than that in the PTN materials synthesized in the presence of agarose gel templates when calcined at 700 °C or above. Increasing the calcination temperature to 900 °C gave uniform PTN materials (Supporting Information Figure S2a,b) featuring 3D interconnected frameworks and faceted rutile crystals (Supporting Information Figure S3) ranging from 120 to 450 nm in size (Supporting Information Figure S2c,d), showing a significant growth in crystal size.

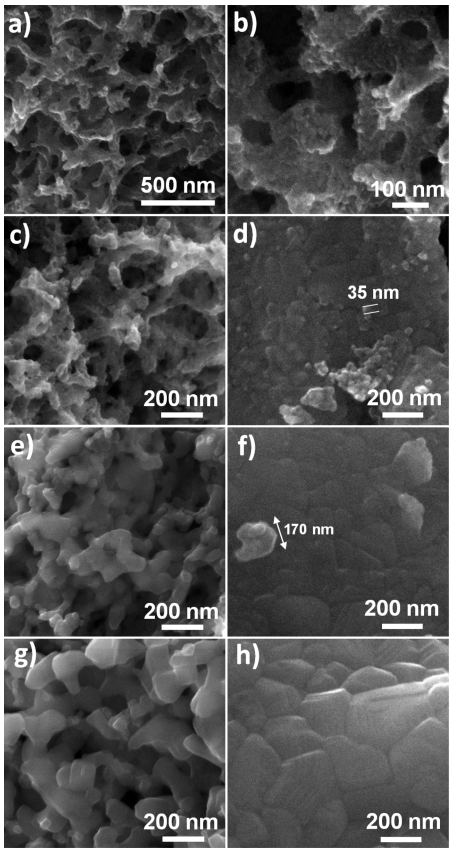

Figure 1. SEM images of the porous titania networks (a, b, c, e, and g) and control samples (d, f, and h) sintered at (a, b) 500 °C, (c, d) 600 °C, (e, f) 700 °C, and (g, h) 800 °C for 2 h in air. Note: All of these images were obtained without metal sputter coating of the samples.

As both the PTN and the control samples were prepared via an identical sol–gel reaction and calcination process, the above results clearly reveal that the reduced interfaces between titania nanocrystals can effectively retard crystal growth in the PTN materials.

The effect of the calcination time on the evolution of such PTN nanostructures was also investigated. Figure 2 shows SEM images of the PTN samples sintered at 600 °C for 2–24 h in air, and no obvious differences in the inorganic frameworks were observed for these PTN samples.

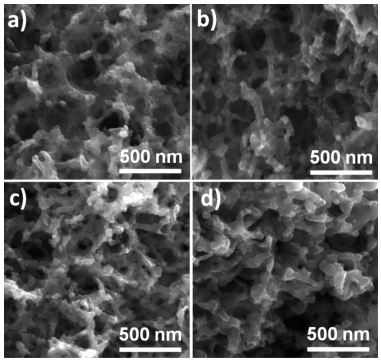

Figure 2. SEM images of the porous titania networks sintered at 600 °C for (a) 2 h, (b) 6 h, (c) 10 h, and (d) 24 h in air. Note: All of these images were obtained without metal sputter coating of the samples.

Crystal Phase Transformation and Rutile Content. The changes in crystal phase and crystallite size within the PTN and control samples were studied by powder X-ray diffraction (XRD), and the corresponding patterns of the samples calcined at different temperatures are presented in Figure 3. Rutile contents (weight percentages) in each sample were calculated according to a previously reported method,[62] and the corresponding results are listed in Table 1. There was no rutile diffraction peak observed in either the PTN sample or the control sample calcined at 500 °C (Figure 3a,b). After calcination at 550 °C for 2 h, a small peak at 2θ = 27.4° (Supporting Information Figure S5), corresponding to the (110) plane of the rutile phase titania, appeared in both the PTN and the control samples, indicating the occurrence of phase transformation from anatase to rutile at this temperature. This result is in good agreement with those reported previously.[52,55] After calcination at 550 °C for 2 h, the rutile content of the PTN-550C-2h and Control-550C-2h sample was 5.8% and 9.3%, respectively. When the calcination temperature increased to 600 °C, the amount of rutile increased slightly to 11.7%; see the PTN-600C-2h sample. This is substantially different to the Control-600C-2h sample, where the intensity of the anatase diffraction peaks decreased significantly and the intensity of the rutile diffraction peaks increased sharply (as compared to the Control-550C-2h) and that was 80.0% rutile phase. Additionally, the crystallite size of the anatase in this control sample increased drastically to 35 nm because the heat of phase transformation from anatase to rutile accelerated grain growth.[55,56] In comparison with this control sample, only a slight increase in crystallite size was observed when calcining the PTN at 600 °C (Figure 1c and Supporting Information Figure S1b, PTN-600C-2h). With a further increase in the calcination temperature, the control sample was fully converted to the rutile phase at 800 °C, while the PTN material retained 12.6% anatase at 800 °C. As summarized in Figure 4, the anatase-to-rutile phase transformation was significantly retarded in the PTN materials, especially when the calcination temperature is below 650 °C, at which an interface nucleation mechanism dominates the anatase to rutile phase transformation.[61]

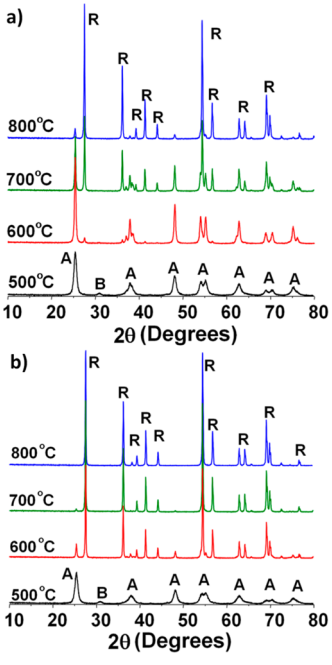

Figure 3. XRD patterns of (a) the porous titania networks and (b) control samples sintered at diverse temperatures (as noted on the individual patterns) for 2 h in air. A = anatase, B = brookite, and R = rutile titania.

Rutile contents in the PTN materials were tunable by changing calcination time as well. The PTN materials calcined at 600 °C for 2, 6, 10, and 24 h were investigated and characterized using XRD. The corresponding XRD patterns are shown as Supporting Information Figure S6, and physical properties are given in Table 1. The rutile percentage increased from 11.7 to 28.4 wt % when the calcination time was prolonged from 2 to 24 h (Table 1). Even with this prolonged calcination of 24 h, the rutile content was significantly less (28.4% for PTN-600C-24h) than that of the Control-600C-2h (80.0%) sample calcined for 2 h at the same temperature. On the basis of the above results, it is clear that the presence of the agarose gel template during sol–gel synthesis gave rise to a hierarchically porous structure that effectively reduces the interfaces between titania nanocrystals, and therefore prevented phase transformation by inhibiting nucleation of the rutile phase. Thus, controlling calcination temperature or duration at a relatively low temperature (e.g., 600 °C) renders a facile and feasible method to tune anatase to rutile ratios and adjust titania crystal sizes in the PTN materials.

Specific Surface Area and Porosity of the PTN and Control Samples. To explore the correlation between porous structure and phase transformation, and the effects of pores on photocatalytic performance, specific surface areas and pore size distributions of the PTN and control samples calcined at varying temperatures and times were characterized using nitrogen gas sorption. Specific surface areas of the PTN and control samples as a function of calcination temperature from 500 to 900 °C are given in Figure 5. For the control sample

Table 1. Physical Properties of the Porous Titania Networks (PTN) and Control Samples

sample	crystal phase[a]	W_R (wt %)[b]	surface area (m^2 g^{-1})[c]	relative surface area (%)[d]	pore diameter (nm)[e]	pore volume (cm^3 g^{-1})[f]
PTN-500C-2h	A + B	0.0	71.0 ± 1.0	100	14.9, 90	0.248
PTN-550C-2h	A + B + R	5.8	52.2 ± 0.5	73.5	14.7, 98	0.211
PTN-600C-2h	A + R	11.7	36.6 ± 0.4	51.5	16.0, 92	0.125
PTN-650C-2h	A + R	24.0	24.4 ± 0.3	34.4	16.0, 96	0.115
PTN-700C-2h	A + R	54.5	17.0 ± 0.3	23.9	102	0.112
PTN-800C-2h	A + R	87.4	10.7 ± 0.2	15.1	105	0.042
PTN-900C-2h	R	100	5.0 ± 0.2	7.0	158	0.034
PTN-600C-2h	A + R	11.7	36.6 ± 0.4	51.5	16.0, 92	0.125
PTN-600C-6h	A + R	15.4	32.2 ± 0.4	45.4	16.8, 80	0.122
PTN-600C-10h	A + R	17.3	28.2 ± 0.3	39.7	17.0, 78	0.117
PTN-600C-24h	A + R	28.4	21.9 ± 0.3	30.8	75	0.090
Control-500C-2h	A + B	0.0	92.5 ± 0.9	100	6.0	0.237
Control-550C-2h	A + B + R	9.3	34.3 ± 0.4	37.1	8.5	0.133
Control-600C-2h	A + R	80.0	4.9 ± 0.2	0.05		0.069
Control-700C-2h	A + R	91.8	3.2 ± 0.1	0.03		0.064
Control-800C-2h	R	100	2.4 ± 0.1	0.03		0.044

[a]Crystal phase of the samples determined using XRD technique, A = anatase, R = rutile, and B = brookite titania. [b]Weight percentage of the rutile titania calculated using the integrated intensities of anatase (101), rutile (110), and brookite (121) peaks according to a previously reported method.[62] [c]Specific surface area calculated from nitrogen gas adsorption data in the P/P_0 range from 0.05 to 0.20. [d]Relative specific surface area, normalized to PTN-500C-2h for PTN samples and to Control-500C-2h for control samples, respectively. [e]Pore diameter determined by the BJH model using the nitrogen adsorption branch data. [f]Cumulative volume of pores between 1.70 and 300 nm calculated from the nitrogen adsorption data.

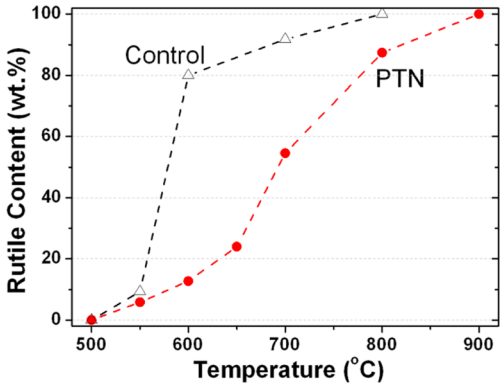

Figure 4. Rutile content of the porous titania networks (PTN) and control samples (Control) calculated from the corresponding XRD patterns. The dashed lines were added to guide the eye.

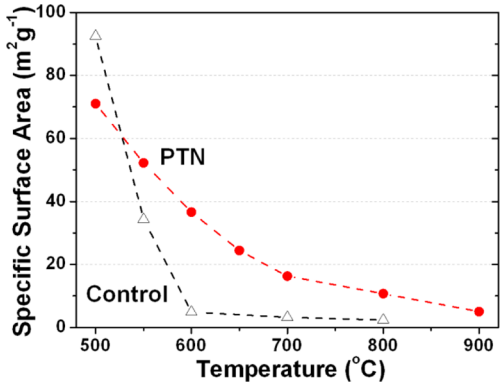

Figure 5. Specific surface areas of the porous titania networks (PTN) and control samples (Control) as a function of the calcination temperature from 500 to 900 °C. The dashed lines were added to guide the eye.

calcined at 500 °C for 2 h, the specific surface area (92.5 m^2 g^{-1}) was higher than that of the PTN material prepared under the same calcination condition, PTN-500C-2h (71.0 m^2 g^{-1}). However, the specific surface area of the control samples dropped dramatically to 4.9 m^2 g^{-1} (Table 1) by increasing the calcination temperature to 600 °C. In contrast, the specific surface area of the PTN samples decreased gradually to 36.6 m^2g^{-1} at 600 °C, and then to 10.7 m^2 g^{-1} after calcination at 800 °C for 2 h, indicating the higher thermal stability of the PTN materials. The specific surface areas of the PTN materials calcined at 600 °C for various times were also investigated and dropped gradually from 36.6 to 21.9 m^2 g^{-1} with a calcination time from 2 to 24 h (Supporting Information Figure S7). As demonstrated in the SEM images (Figures 1 and 2) and XRD patterns (Figure 3), hierarchically porous frameworks and relatively small crystal sizes can be effectively retained in the PTN materials while increasing calcination temperature and duration; thus a relatively high specific surface area can be obtained in the PTN materials (Table 1).

Nitrogen gas sorption isotherms of the PTN materials calcined at various temperatures are shown in Figure 6a. Except for the PTN-800C-2h sample, all of the isotherms showed two hysteresis loops at relative pressures (P/P_0) ranging from 0.65 to 0.96, indicating a bimodal pore size distribution (presence of both mesopores and macropores).[68] The macropores were a result of the templating process, where the coated agarose fibers, separated by hundreds of nanometers, left large voids in the final structure. These macropores in the PTN materials were preserved even when the calcination temperature was as high as 900 °C (Supporting Information Figure S2). The mesopores in the PTN materials stem from both the removal of the agarose fibrils and the interparticle voids between the titania nanocrystals. For the PTN material calcined at 500 °C for 2 h, as shown in the inset, two distinct pore size distributions centered around 14.9 and 90 nm were obtained. The abundance of mesopores decreases as the calcination temperature increases to 650 °C, while the macropore profile changes slightly from 600 to 650 °C. After calcination at 800 °C, the mesopores of the PTN material disappeared, indicating a

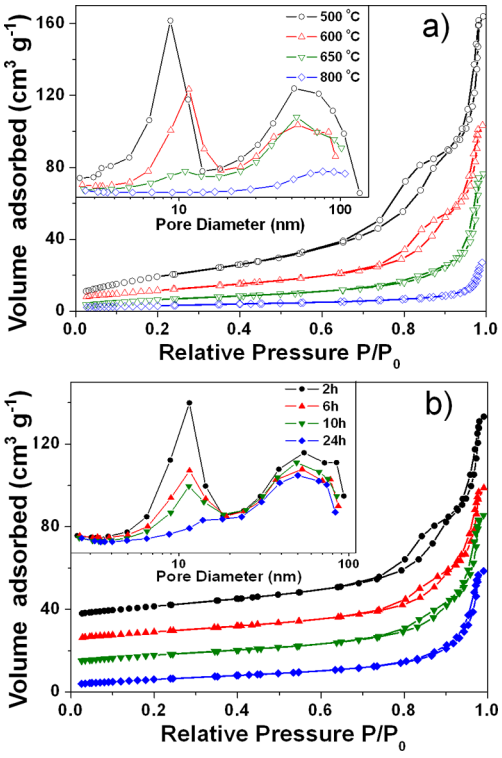

Figure 6. Nitrogen sorption isotherms and corresponding pore size distributions (insets) of the porous titania networks sintered (a) at diverse temperatures and (b) at 600 °C for varied times (from 2 to 24 h) in air.

significant crystal growth and densification of the inorganic frameworks. This can be clearly observed in the corresponding SEM images (Figure 1g and Supporting Information Figure S1d). It is worth noting that even after calcination at 900 °C, as clearly demonstrated in Supporting Information Figure S2, three-dimensional interconnected macropores remain in this PTN material, demonstrating an excellent thermal stability.

Besides the calcination temperature, the calcination duration also affects the porosity of the resulting materials. For PTN samples calcined at 600 °C for different lengths of time, as shown in Figure 6b, the mesopores gradually decreased when heated from 2 to 24 h, while only a slight decrease in the corresponding macropore profiles was observed. This varying trend in meso- and macropore profiles suggests that a gradual densification occurred mostly at the interfaces between titania nanocrystals, and this interfacial densification might proceed via the nucleation of the rutile phase located at the anatase–anatase interfaces.

Before presenting the photocatalytic results, it is instructive to discuss the relationship between porous structure and anatase-to-rutile phase transformation. According to the previous reports,[58,59,64] the packing characteristic of the titania nanocrystals has a significant effect on the crystal phase transformation. From the SEM images shown in Figure 1b, the hierarchically porous framework of the PTN samples is composed of titania nanoparticles less than 10 nm in diameter. Large porosity in such a porous structure means a decreased number of neighboring particles as compared to a dense structure (as illustrated by the control samples) and, hence, would result in a decrease in interface nucleation of the rutile phase. XRD results show that such hierarchically porous structures can effectively retard the anatase to rutile phase transformation at elevated temperatures. Employing such PTNs as parent materials, finely controllable phase transformation can be realized using a facile and feasible calcination process at an elevated temperature (e.g., 600 °C), and gives rise to PTN samples with tunable crystal phases, enhanced crystallinity, 3D interconnected porous frameworks, and relatively high specific surface areas.

Photocatalytic Performance. Photocatalytic activities of the resulting PTN materials were evaluated by the degradation of methylene blue (MB), a probe molecule, under UV light irradiation. For comparison, photocatalytic activities of the control samples (without macropores) calcined at the same temperatures were also measured under the same conditions. To compare the reaction kinetics of the MB degradation, a pseudo-first-order reaction equation, $\ln(C/C_0) = -kt$, where C_0 and C are the initial concentration and the reaction concentration of MB at an irradiation time t, respectively, and k is the apparent reaction rate constant,[28,29] was applied to the time profile of the MB absorption spectra (Figure S8 in the Supporting Information).

The calcination temperature has a great effect on the photocatalytic activities of titania materials (Figure 7a). At 500

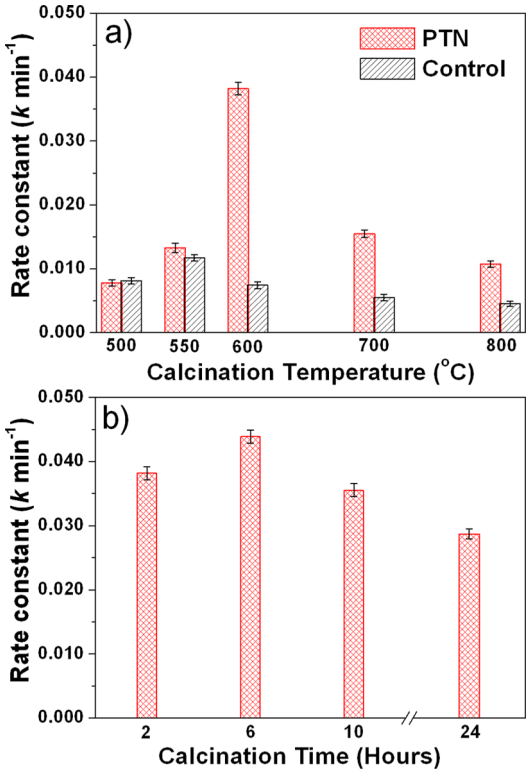

Figure 7. Comparison of the apparent rate constants in photocatalytic reactions employing (a) porous titania networks (PTN) and control samples (Control) calcined at varying temperatures for 2 h, and (b) PTN samples calcined at 600 °C for 2–24 h.

°C, the apparent reaction rate constant, k, of the PTN material is equivalent (within error) to that of the control sample. With an increase in calcination temperature to 550 °C, the degradation rate of MB increased for both the PTN and the control samples. A small amount of rutile appeared in both samples (Table 1) and is presumably the main reason for the improved photocatalytic performance. The coexistence of anatase and rutile phases can effectively inhibit the recombi-

nation of photocarriers by promoting the spatial charge separation and, therefore, enhances the efficiency of photodegradation.[8−13] Comparing the performance of these two samples, we believe that the higher surface area of the PTN-550C-2h (52.2 m^2 g^{-1}) has enhanced the photocatalytic activity. Although the specific surface area decreased with increasing calcination temperature, a sharp increase in photocatalytic activity in PTN-600C-2h (k = 0.0382 min^{-1}) was observed when the calcination temperature reached 600 °C. In contrast, a decrease in photocatalytic activity was observed for the Control-600C-2h sample, probably due to its very low specific surface area (4.9 m^2 g^{-1}) and substantial quantities of rutile (80.0 wt %) after calcination at this temperature. Increasing the temperature to 700 and 800 °C decreased the photocatalytic activities of both the PTN and the control samples as a result of the ongoing phase transformation and crystal growth, which leads to a remarkable reduction in the specific surface area (Table 1).

The effect of calcination time on photocatalytic performance of the PTN materials was also investigated, and the results are shown in Figure 7b. Although the specific surface area of the PTN materials decreased from 36.6 to 32.2 m^2 g^{-1} when increasing the calcination time from 2 to 6 h, this did not result in a decrease in the photocatalytic activity. The PTN-600C-6h sample gave the highest photocatalytic activity with an apparent reaction rate constant of 0.0439 min^{-1}. This increase in the photocatalytic activity could be attributed to the formation of more anatase/rutile phase junctions (Figure 8) and the improved crystallinity of the PTN materials.[24,28,29,36,37,39,42,53] A decrease in the photocatalytic activity was observed for calcination times of 10 h or longer when heated at 600 °C, mainly due to the decrease in reactive sites in the PTN materials as a result of the reduction in specific surface area (Table 1). On the basis of the above results, it is clear that both calcination temperature and the presence of macro-/mesopores in the parent materials play very important roles in determining the properties of the PTN materials. PTN materials with optimized rutile content (~15.4 wt %) can be obtained by annealing at a relatively low temperature (600 °C), giving enhanced photocatalytic activity due to the finely controllable anatase-to-rutile phase transformation kinetics governed by the interface nucleation process.

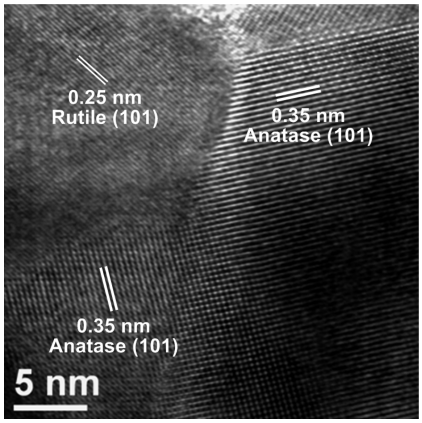

Figure 8. High-resolution TEM image of the porous titania network clearly showing the phase junctions between rutile and anatase nanocrystals.

CONCLUSIONS

Hierarchically porous titania networks with controllable rutile content and relatively high specific surface area were prepared via a facile templating and solid-state phase transformation process dominated by the interface nucleation process at a relatively low temperature (600 °C). The PTN (templated by the agarose gel) possessed reduced contact areas between titania nanocrystals and effectively suppressed the anatase to rutile phase transformation and the rutile crystal growth, thus giving rise to hierarchically porous titania photocatalysts that could be optimized for rutile content and maintain relatively high specific surface areas. Such agarose-templated PTN showed excellent thermal stability and structural homogeneity, even after being transformed into the rutile phase at 900 °C in air. The hierarchically PTN materials showed enhanced photocatalytic activity toward the degradation of methylene blue under UV light irradiation, due to optimized crystal phase composition and increased number of reactive sites (due to higher surface area), when compared to the control samples prepared in the absence of template under otherwise identical conditions. The coexistence of the anatase and rutile phases is beneficial for photocatalytic performance, relative to either individual component. This work demonstrates a facile synthesis method for fabricating tunable mixed-phase titania materials with improved photocatalytic activity. Given their hierarchically porous structures, robust inorganic frameworks, tunable anatase:rutile ratios, and relatively high specific surface areas, the resultant PTN materials are expected to find potential applications in the area of industrial oxidation catalysis.

ASSOCIATED CONTENT

Supporting Information

SEM images, XRD patterns, and rutile content of the PTN materials fabricated at varying calcination temperatures (from 500 to 900 °C) and durations (from 2 to 24 h) and photocatalytic degradation performance of both the PTN and the control samples. This material is available free of charge via the Internet at http://pubs.acs.org.

AUTHOR INFORMATION

Corresponding Authors

*Tel.: 61 3 8344 7146. Fax: 61 3 9347 5180. E-mail: rcaruso@unimelb.edu.au.

*E-mail: dehongc@unimelb.edu.au.

Notes

The authors declare no competing financial interest.

ACKNOWLEDGMENTS

This research was financially supported by an Australian Research Council Discovery Project (DP110101346). L.C. acknowledges the support of an Australian Postgraduate Award and MMI-CSIRO Ph.D. Materials Science Top-up. R.A.C. is a recipient of an Australian Research Council Future Fellowship (FT0990583). The Melbourne Advanced Microscopy Facility of The University of Melbourne is acknowledged for electron microscopy access.

REFERENCES

(1) Winkler, J. *Titanium Dioxide: Production, Properties and Effective Usage*; Vincentz Network: Hanover, Germany, 2013.

(2) Chen, X.; Mao, S. S. Titanium Dioxide Nanomaterials: Synthesis, Properties, Modifications, and Applications. *Chem. Rev.* **2007**, *107*, 2891−2959.
(3) Fujishima, A.; Zhang, X. T.; Tryk, D. A. TiO_2 Photocatalysis and Related Surface Phenomena. *Surf. Sci. Rep.* **2008**, *63*, 515−582.
(4) Fujishima, A.; Hashimoto, K.; Watanabe, T. *TiO_2 Photocatalysis: Fundamentals and Applications*; BKC, Inc.: Tokyo, Japan, 1999.
(5) Fujishima, A.; Honda, K. Electrochemical Photolysis of Water at a Semiconductor Electrode. *Nature* **1972**, *238*, 37−38.
(6) Grtäzel, M. Photoelectrochemical Cells. *Nature* **2001**, *414*, 338−344.
(7) Sauvage, F.; Chen, D. H.; Comte, P.; Huang, F. Z.; Heiniger, L. P.; Cheng, Y. B.; Caruso, R. A.; Graetzel, M. Dye-Sensitized Solar Cells Employing a Single Film of Mesoporous TiO_2 Beads Achieve Power Conversion Efficiencies over 10%. *ACS Nano* **2010**, *4*, 4420−4425.
(8) Chen, Z.; Belharouak, I.; Sun, Y. K.; Amine, K. Titanium-Based Anode Materials for Safe Lithium-Ion Batteries. *Adv. Funct. Mater.* **2013**, *23*, 959−969.
(9) Chen, D. H.; Huang, F. Z.; Cao, L.; Cheng, Y. B.; Caruso, R. A. Spiky Mesoporous Anatase Titania Beads: A Metastable Ammonium Titanate Mediated Synthesis. *Chem.—Eur. J.* **2012**, *18*, 13762−13769.
(10) Zhu, G. N.; Wang, Y. G.; Xia, Y. Y. Ti-Based Compounds as Anode Materials for Li-Ion Batteries. *Energy Environ. Sci.* **2012**, *5*, 6652−6667.
(11) Wagemaker, M.; Kentgens, A. P. M.; Mulder, F. M. Equilibrium Lithium Transport between Nanocrystalline Phases in Intercalated TiO_2 Anatase. *Nature* **2002**, *418*, 397−399.
(12) Chen, D. H.; Caruso, R. A. Recent Progress in the Synthesis of Spherical Titania Nanostructures and Their Applications. *Adv. Funct. Mater.* **2013**, *23*, 1356−1374.
(13) Enache, D. I.; Edwards, J. K.; Landon, P.; Solsona-Espriu, B.; Carley, A. F.; Herzing, A. A.; Watanabe, M.; Kiely, C. J.; Knight, D. W.; Hutchings, G. J. Solvent-Free Oxidation of Primary Alcohols to Aldehydes Using Au-Pd/TiO_2 Catalysts. *Science* **2006**, *311*, 362−365.
(14) Chen, D. H.; Huang, F. Z.; Cheng, Y. B.; Caruso, R. A. Mesoporous Anatase TiO_2 Beads with High Surface Areas and Controllable Pore Sizes: A Superior Candidate for High-Performance Dye-Sensitized Solar Cells. *Adv. Mater.* **2009**, *21*, 2206−2210.
(15) Linsebigler, A. L.; Lu, G. Q.; Yates, J. T. Photocatalysis on TiO_2 Surfaces - Principles, Mechanisms, and Selected Results. *Chem. Rev.* **1995**, *95*, 735−758.
(16) Carp, O.; Huisman, C. L.; Reller, A. Photoinduced Reactivity of Titanium Dioxide. *Prog. Solid State Chem.* **2004**, *32*, 33−177.
(17) Anpo, M.; Kamat, P. V. *Environmentally Benign Photocatalysts: Applications of Titanium Oxide-Based Materials*; Springer: New York, 2010.
(18) Huang, F. Z.; Chen, D. H.; Li, Q.; Caruso, R. A.; Cheng, Y. B. Construction of Nanostructured Electrodes on Flexible Substrates Using Pre-Treated Building Blocks. *Appl. Phys. Lett.* **2012**, *100*, 123102.
(19) Chen, Y.; Huang, F. Z.; Chen, D. H.; Cao, L.; Zhang, X. L.; Caruso, R. A.; Cheng, Y. B. Effect of Mesoporous TiO_2 Bead Diameter in Working Electrodes on the Efficiency of Dye-Sensitized Solar Cells. *ChemSusChem* **2011**, *4*, 1498−1503.
(20) Hashimoto, K.; Irie, H.; Fujishima, A. TiO_2 Photocatalysis: A Historical Overview and Future Prospects. *Jpn. J. Appl. Phys.* **2005**, *44*, 8269−8285.
(21) Asahi, R.; Morikawa, T.; Ohwaki, T.; Aoki, K.; Taga, Y. Visible-Light Photocatalysis in Nitrogen-Doped Titanium Oxides. *Science* **2001**, *293*, 269−271.
(22) Chen, X. B.; Liu, L.; Yu, P. Y.; Mao, S. S. Increasing Solar Absorption for Photocatalysis with Black Hydrogenated Titanium Dioxide Nanocrystals. *Science* **2011**, *331*, 746−750.
(23) Cao, L.; Chen, D. H.; Caruso, R. A. Surface-Metastable Phase-Initiated Seeding and Ostwald Ripening: A Facile Fluorine-Free Process Towards Spherical Fluffy Core/Shell, Yolk/Shell, and Hollow Anatase Nanostructures. *Angew. Chem., Int. Ed.* **2013**, *52*, 10986−10991.
(24) Zhang, J.; Xu, Q.; Feng, Z.; Li, M.; Li, C. Importance of the Relationship between Surface Phases and Photocatalytic Activity of TiO_2. *Angew. Chem., Int. Ed.* **2008**, *47*, 1766−1769.
(25) Hoffmann, M. R.; Martin, S. T.; Choi, W. Y.; Bahnemann, D. W. Environmental Applications of Semiconductor Photocatalysis. *Chem. Rev.* **1995**, *95*, 69−96.
(26) Li, H. X.; Bian, Z. F.; Zhu, J.; Zhang, D. Q.; Li, G. S.; Huo, Y. N.; Li, H.; Lu, Y. F. Mesoporous Titania Spheres with Tunable Chamber Stucture and Enhanced Photocatalytic Activity. *J. Am. Chem. Soc.* **2007**, *129*, 8406−8407.
(27) Yang, H. G.; Sun, C. H.; Qiao, S. Z.; Zou, J.; Liu, G.; Smith, S. C.; Cheng, H. M.; Lu, G. Q. Anatase TiO_2 Single Crystals with a Large Percentage of Reactive Facets. *Nature* **2008**, *453*, 638−641.
(28) Joo, J. B.; Zhang, Q.; Dahl, M.; Lee, I.; Goebl, J.; Zaera, F.; Yin, Y. D. Control of the Nanoscale Crystallinity in Mesoporous TiO_2 Shells for Enhanced Photocatalytic Activity. *Energy Environ. Sci.* **2012**, *5*, 6321−6327.
(29) Joo, J. B.; Lee, I.; Dahl, M.; Moon, G. D.; Zaera, F.; Yin, Y. D. Controllable Synthesis of Mesoporous TiO_2 Hollow Shells: Toward an Efficient Photocatalyst. *Adv. Funct. Mater.* **2013**, *23*, 4246−4254.
(30) Wang, X. H.; Li, J. G.; Kamiyama, H.; Katada, M.; Ohashi, N.; Moriyoshi, Y.; Ishigaki, T. Pyrogenic Iron(III)-Doped TiO_2 Nanopowders Synthesized in RF Thermal Plasma: Phase Formation, Defect Structure, Band Gap, and Magnetic Properties. *J. Am. Chem. Soc.* **2005**, *127*, 10982−10990.
(31) Zhang, J.; Li, M. J.; Feng, Z. C.; Chen, J.; Li, C. UV Raman Spectroscopic Study on TiO_2. I. Phase Transformation at the Surface and in the Bulk. *J. Phys. Chem. B* **2006**, *110*, 927−935.
(32) Zhang, J.; Xu, Q.; Li, M. J.; Feng, Z. C.; Li, C. UV Raman Spectroscopic Study on TiO_2. II. Effect of Nanoparticle Size on the Outer/Inner Phase Transformations. *J. Phys. Chem. C* **2009**, *113*, 1698−1704.
(33) Su, R.; Bechstein, R.; Sø, L.; Vang, R. T.; Sillassen, M.; Esbjörnsson, B.; Palmqvist, A.; Besenbacher, F. How the Anatase-to-Rutile Ratio Influences the Photoreactivity of TiO_2. *J. Phys. Chem. C* **2011**, *115*, 24287−24292.
(34) Zachariah, A.; Baiju, K. V.; Shukla, S.; Deepa, K. S.; James, J.; Warrier, K. G. K. Synergistic Effect in Photocatalysis as Observed for Mixed-Phase Nanocrystalline Titania Processed Via Sol-Gel Solvent Mixing and Calcination. *J. Phys. Chem. C* **2008**, *112*, 11345−11356.
(35) Scanlon, D. O.; Dunnill, C. W.; Buckeridge, J.; Shevlin, S. A.; Logsdail, A. J.; Woodley, S. M.; Catlow, C. R. A.; Powell, M. J.; Palgrave, R. G.; Parkin, I. P.; Watson, G. W.; Keal, T. W.; Sherwood, P.; Walsh, A.; Sokol, A. A. Band Alignment of Rutile and Anatase TiO_2. *Nat. Mater.* **2013**, *12*, 798−801.
(36) Kawahara, T.; Konishi, Y.; Tada, H.; Tohge, N.; Nishii, J.; Ito, S. A Patterned TiO_2(Anatase)/TiO_2(Rutile) Bilayer-Type Photocatalyst: Effect of the Anatase/Rutile Junction on the Photocatalytic Activity. *Angew. Chem., Int. Ed.* **2002**, *114*, 2935−2937.
(37) Miyagi, T.; Kamei, M.; Mitsuhashi, T.; Ishigaki, T.; Yamazaki, A. Charge Separation at the Rutile/Anatase Interface: A Dominant Factor of Photocatalytic Activity. *Chem. Phys. Lett.* **2004**, *390*, 399−402.
(38) Hurum, D. C.; Agrios, A. G.; Gray, K. A.; Rajh, T.; Thurnauer, M. C. Explaining the Enhanced Photocatalytic Activity of Degussa P25 Mixed-Phase TiO_2 Using EPR. *J. Phys. Chem. B* **2003**, *107*, 4545−4549.
(39) Li, G.; Dimitrijevic, N. M.; Chen, L.; Nichols, J. M.; Rajh, T.; Gray, K. A. The Important Role of Tetrahedral Ti^{4+} Sites in the Phase Transformation and Photocatalytic Activity of TiO_2 Nanocomposites. *J. Am. Chem. Soc.* **2008**, *130*, 5402−5403.
(40) Kho, Y. K.; Iwase, A.; Teoh, W. Y.; Mädler, L.; Kudo, A.; Amal, R. Photocatalytic H_2 Evolution over TiO_2 Nanoparticles. The Synergistic Effect of Anatase and Rutile. *J. Phys. Chem. C* **2010**, *114*, 2821−2829.
(41) Tsukamoto, D.; Shiraishi, Y.; Sugano, Y.; Ichikawa, S.; Tanaka, S.; Hirai, T. Gold Nanoparticles Located at the Interface of Anatase/Rutile TiO_2 Particles as Active Plasmonic Photocatalysts for Aerobic Oxidation. *J. Am. Chem. Soc.* **2012**, *134*, 6309−6315.

(42) Li, G.; Gray, K. A. The Solid−Solid Interface: Explaining the High and Unique Photocatalytic Reactivity of TiO_2-Based Nanocomposite Materials. *Chem. Phys.* **2007**, *339*, 173−187.
(43) Wang, X. D.; Mitchell, D. R. G.; Prince, K.; Atanacio, A. J.; Caruso, R. A. Gold Nanoparticle Incorporation into Porous Titania Networks Using an Agarose Gel Templating Technique for Photocatalytic Applications. *Chem. Mater.* **2008**, *20*, 3917−3926.
(44) Subramanian, V.; Wolf, E. E.; Kamat, P. V. Catalysis with TiO_2/Gold Nanocomposites. Effect of Metal Particle Size on the Fermi Level Equilibration. *J. Am. Chem. Soc.* **2004**, *126*, 4943−4950.
(45) Tian, Y.; Tatsuma, T. Mechanisms and Applications of Plasmon-Induced Charge Separation at TiO_2 Films Loaded with Gold Nanoparticles. *J. Am. Chem. Soc.* **2005**, *127*, 7632−7637.
(46) Lakshminarasimhan, N.; Bae, E.; Choi, W. Enhanced Photocatalytic Production of H_2 on Mesoporous TiO_2 Prepared by Template-Free Method: Role of Interparticle Charge Transfer. *J. Phys. Chem. C* **2007**, *111*, 15244−15250.
(47) Lee, J. S.; You, K. H.; Park, C. B. Highly Photoactive, Low Bandgap TiO_2 Nanoparticles Wrapped by Graphene. *Adv. Mater.* **2012**, *24*, 1084−1088.
(48) Xiang, Q.; Yu, J.; Jaroniec, M. Synergetic Effect of MoS_2 and Graphene as Cocatalysts for Enhanced Photocatalytic H_2 Production Activity of TiO_2 Nanoparticles. *J. Am. Chem. Soc.* **2012**, *134*, 6575−6578.
(49) Zhang, H.; Lv, X.; Li, Y.; Wang, Y.; Li, J. P25-Graphene Composite as a High Performance Photocatalyst. *ACS Nano* **2009**, *4*, 380−386.
(50) Ohno, T.; Sarukawa, K.; Tokieda, K.; Matsumura, M. Morphology of a TiO_2 Photocatalyst (Degussa, P-25) Consisting of Anatase and Rutile Crystalline Phases. *J. Catal.* **2001**, *203*, 82−86.
(51) Bickley, R. I.; Gonzalezcarreno, T.; Lees, J. S.; Palmisano, L.; Tilley, R. J. D. A Structural Investigation of Titanium-Dioxide Photocatalysts. *J. Solid State Chem.* **1991**, *92*, 178−190.
(52) Hanaor, D.; Sorrell, C. Review of the Anatase to Rutile Phase Transformation. *J. Mater. Sci.* **2011**, *46*, 855−874.
(53) Porter, J. F.; Li, Y. G.; Chan, C. K. The Effect of Calcination on the Microstructural Characteristics and Photoreactivity of Degussa P-25 TiO_2. *J. Mater. Sci.* **1999**, *34*, 1523−1531.
(54) Wu, C.; Yue, Y.; Deng, X.; Hua, W.; Gao, Z. Investigation on the Synergetic Effect between Anatase and Rutile Nanoparticles in Gas-Phase Photocatalytic Oxidations. *Catal. Today* **2004**, *93*−*95*, 863−869.
(55) Kumar, K. N. P.; Keizer, K.; Burggraaf, A. J.; Okubo, T.; Nagamoto, H.; Morooka, S. Densification of Nanostructured Titania Assisted by a Phase-Transformation. *Nature* **1992**, *358*, 48−51.
(56) Mazaheri, M.; Razavi Hesabi, Z.; Sadrnezhaad, S. K. Two-Step Sintering of Titania Nanoceramics Assisted by Anatase-to-Rutile Phase Transformation. *Scr. Mater.* **2008**, *59*, 139−142.
(57) Gribb, A. A.; Banfield, J. F. Particle Size Effects on Transformation Kinetics and Phase Stability in Nanocrystalline TiO_2. *Am. Mineral.* **1997**, *82*, 717−728.
(58) Zhang, H. Z.; Banfield, J. F. New Kinetic Model for the Nanocrystalline Anatase-to-Rutile Transformation Revealing Rate Dependence on Number of Particles. *Am. Mineral.* **1999**, *84*, 528−535.
(59) Penn, R. L.; Banfield, J. F. Formation of Rutile Nuclei at Anatase {112} Twin Interfaces and the Phase Transformation Mechanism in Nanocrystalline Titania. *Am. Mineral.* **1999**, *84*, 871−876.
(60) Zhang, H. Z.; Banfield, J. F. Size Dependence of the Kinetic Rate Constant for Phase Transformation in TiO_2 Nanoparticles. *Chem. Mater.* **2005**, *17*, 3421−3425.
(61) Zhang, H. Z.; Banfield, J. F. Phase Transformation of Nanocrystalline Anatase-to-Rutile Via Combined Interface and Surface Nucleation. *J. Mater. Res.* **2000**, *15*, 437−448.
(62) Zhang, H. Z.; Banfield, J. F. Understanding Polymorphic Phase Transformation Behavior During Growth of Nanocrystalline Aggregates: Insights from TiO_2. *J. Phys. Chem. B* **2000**, *104*, 3481−3487.
(63) Lee, G. H.; Zuo, J.-M. Growth and Phase Transformation of Nanometer-Sized Titanium Oxide Powders Produced by the Precipitation Method. *J. Am. Ceram. Soc.* **2004**, *87*, 473−479.
(64) Ahn, J.-P.; Park, J.-K.; Kim, G. Effect of Compact Density on Phase Transition Kinetics from Anatase Phase to Rutile Phase During Sintering of Ultrafine Titania Powder Compacts. *Nanostruct. Mater.* **1998**, *10*, 1087−1096.
(65) Zhang, H. Z.; Banfield, J. F. Polymorphic Transformations and Particle Coarsening in Nanocrystalline Titania Ceramic Powders and Membranes. *J. Phys. Chem. C* **2007**, *111*, 6621−6629.
(66) Zhou, Y.; Fichthorn, K. A. Microscopic View of Nucleation in the Anatase-to-Rutile Transformation. *J. Phys. Chem. C* **2012**, *116*, 8314−8321.
(67) Zhou, J. F.; Zhou, M. F.; Caruso, R. A. Agarose Template for the Fabrication of Macroporous Metal Oxide Structures. *Langmuir* **2006**, *22*, 3332−3336.
(68) Lowell, S.; Shields, J. E.; Thomas, M. A.; Thommes, M. *Characterization of Porous Solids and Powders: Surface Area, Pore Size and Density*; Kluwer: London, 2004.

SUPPORTING INFORMATION

to

Hierarchically Porous Titania Networks with Tunable Anatase:Rutile Ratios and their Enhanced Photocatalytic Activities

Lu Cao[1], Dehong Chen[1*], Wei Li[2], Rachel A. Caruso[1,2*]

[1]Particulate Fluids Processing Centre, School of Chemistry, The University of Melbourne, Melbourne, Victoria 3010

[2]CSIRO Materials Science and Engineering, Private Bag 33, Clayton South, Victoria 3169, Australia

Email: dehongc@unimelb.edu.au; rcaruso@unimelb.edu.au

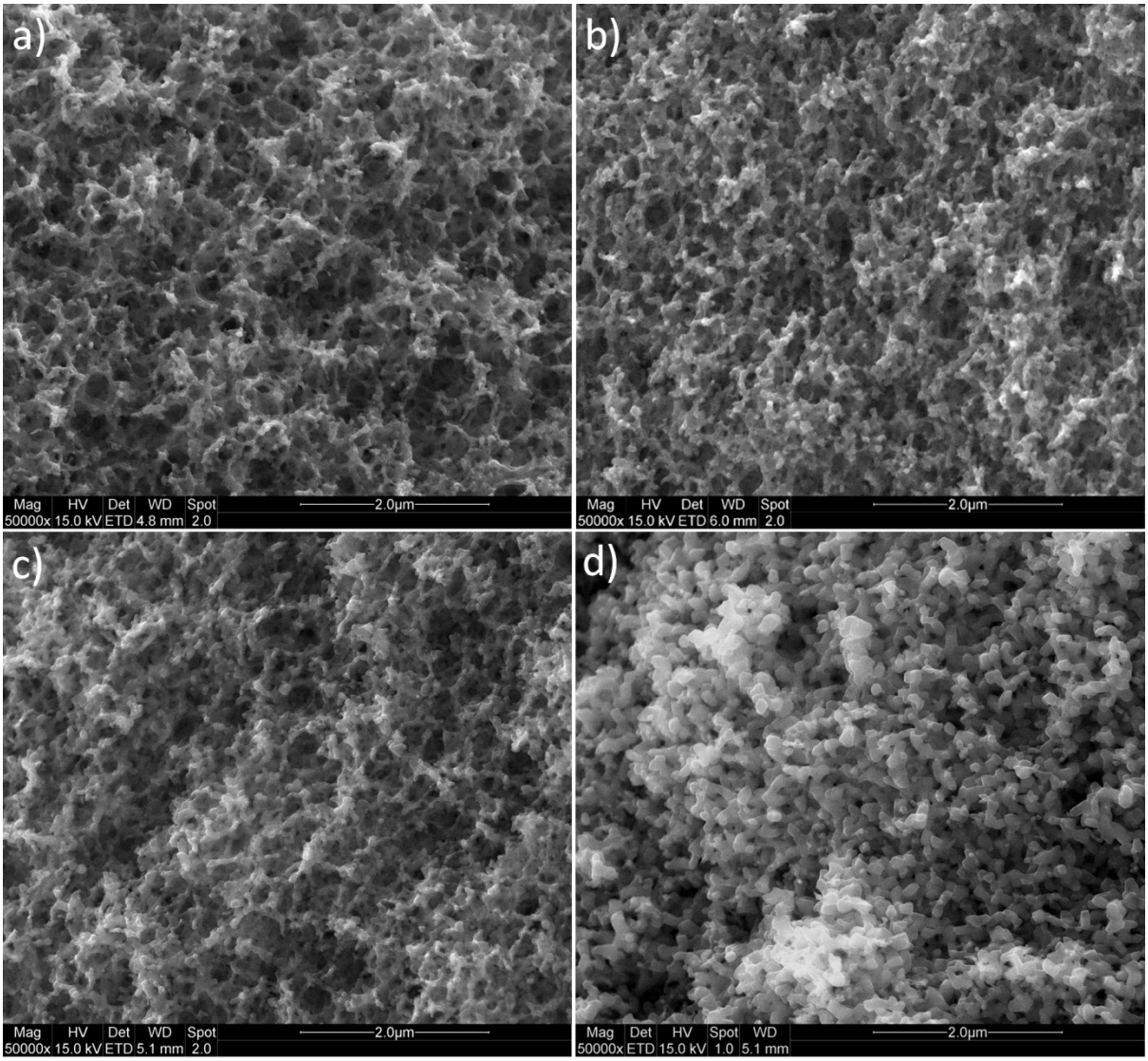

Figure S1. Low magnification SEM images of the porous titania networks (PTN) calcined at a) 500 °C, b) 600 °C, c) 700 °C and d) 800 °C for 2 h in air. The images show a homogeneous macroporous framework of the PTN materials and a gradual coarsening in crystal size with increase in sintering temperature. Note: all these images were recorded at the same magnification (50,000X) and were obtained without metal sputter coating.

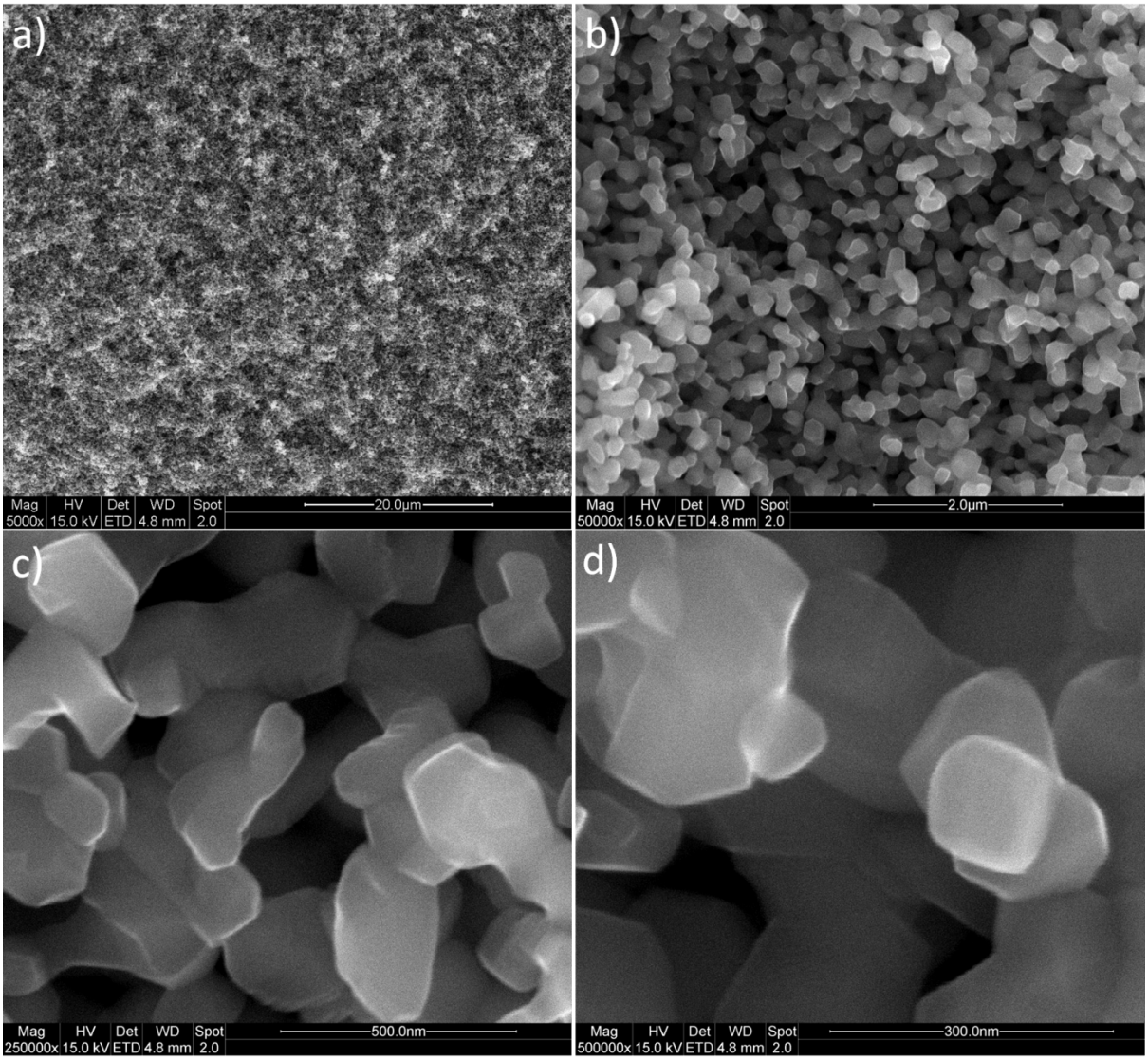

Figure S2. SEM images of the porous titania networks (PTN) calcined at 900 °C for 2 h in air at varied magnification (a-d). These images show a homogeneous macroporous framework of the titania (rutile) materials even after calcination at 900 °C in air, indicating excellent thermal stability of structure of the PTN materials. Note: all these images were obtained without metal sputter coating.

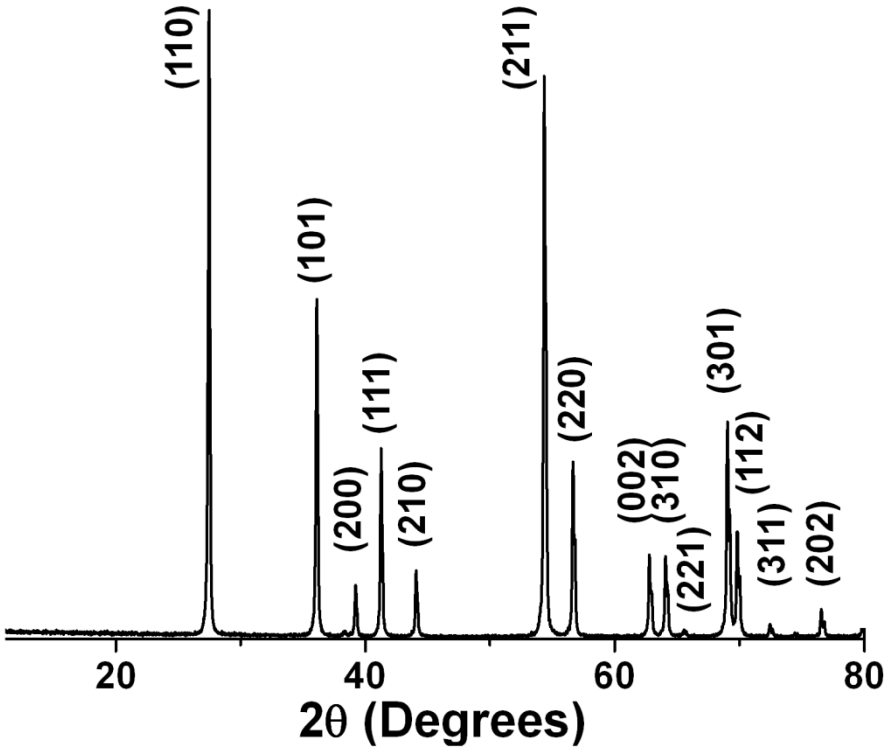

Figure S3. XRD pattern of the porous titania network calcined at 900 °C for 2 h in air (sample shown in Figure S2). These peaks can be indexed to the reflections derived from the rutile phase of titania (JCPDS card #00-021-1276).

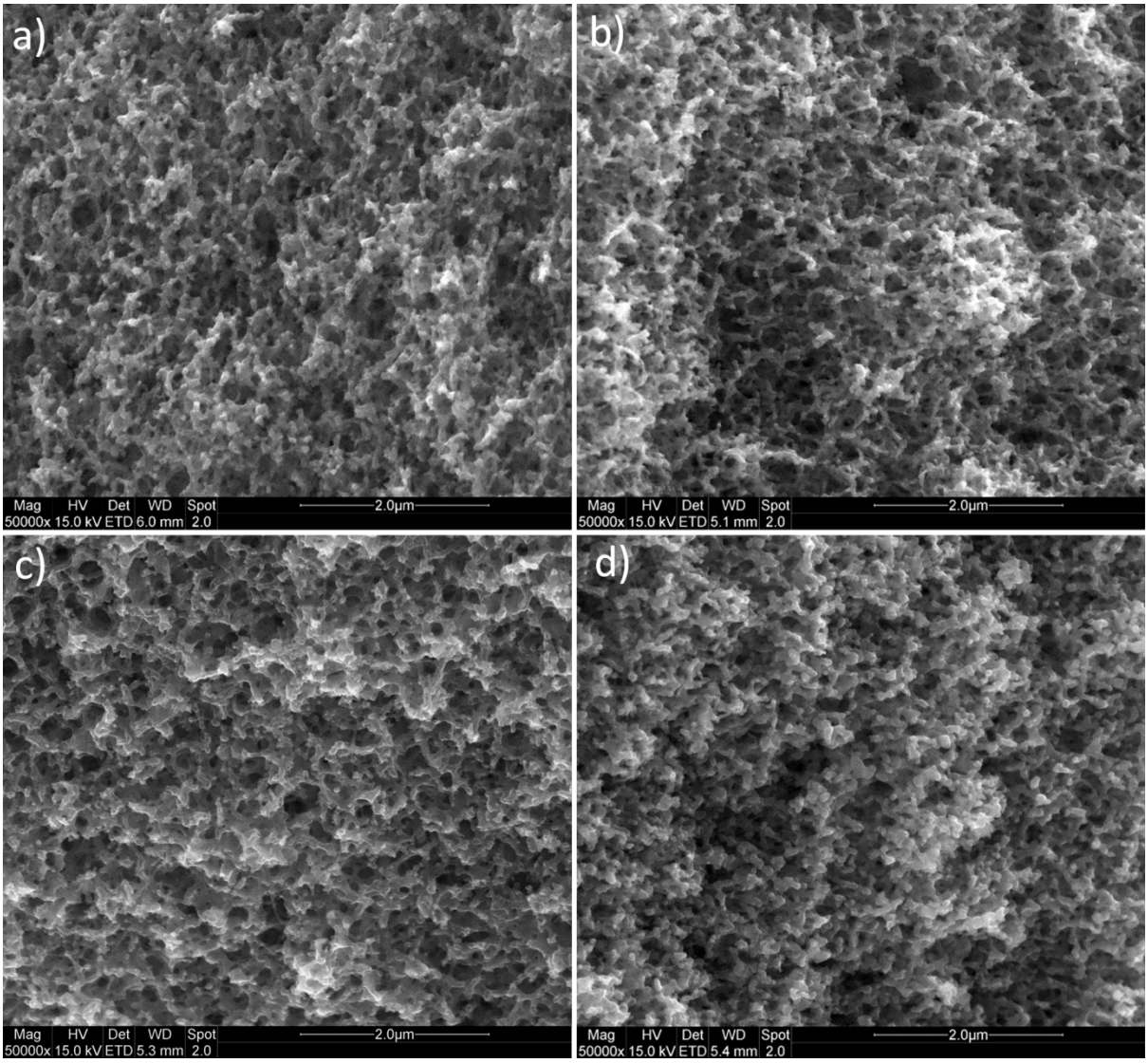

Figure S4. Low magnification SEM images of the porous titania networks calcined at 600 °C for a) 2 h, b) 6 h, c) 10 h and d) 24 h in air. The images show a homogeneous macroporous framework of the PTN materials and a slight coarsening in crystal size with increasing sintering time. Note: all these images were recorded at the same magnification (50,000X) and obtained without metal sputter coating.

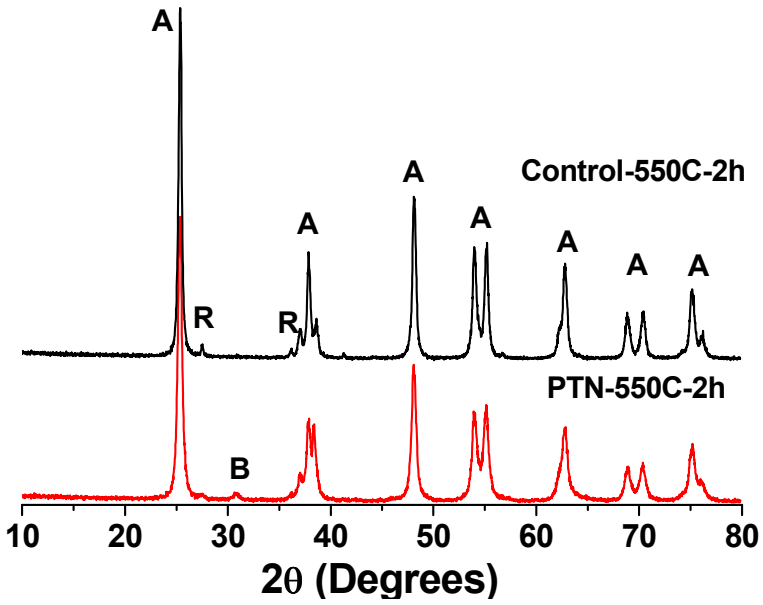

Figure S5. XRD patterns of the porous titania network (PTN) and control samples calcined at 550 °C for 2 h in air. A = Anatase, R = Rutile and B = Brookite phase of titania.

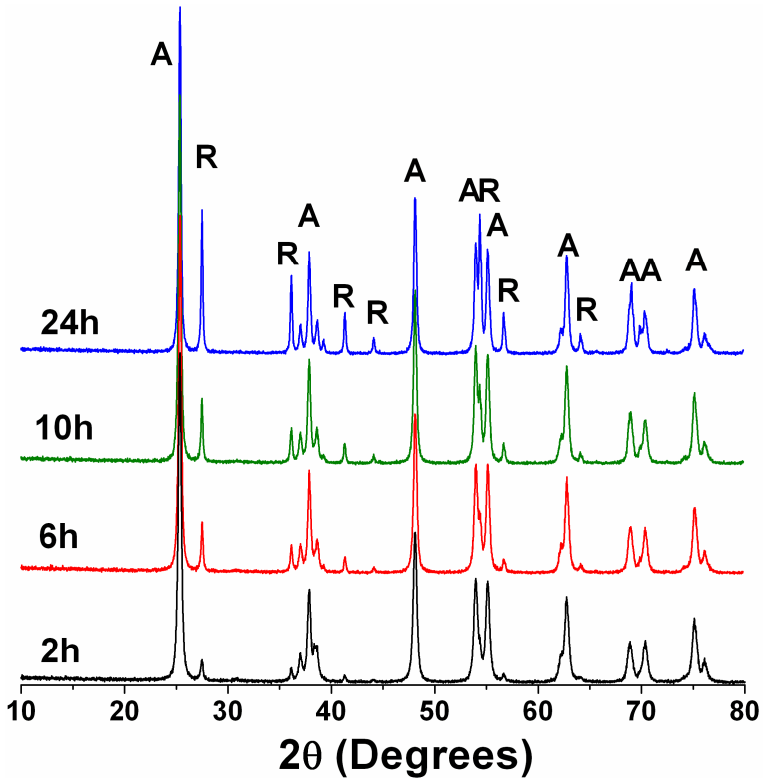

Figure S6. XRD patterns of the porous titania networks calcined at 600 °C for 2, 6, 10 and 24 h (as labelled) in air. The rutile content for these PTN materials is 11.7, 15.4, 17.3 and 28.4 wt% for 2, 6, 10 and 24 h sample, respectively. A = Anatase, and R = Rutile phase of titania.

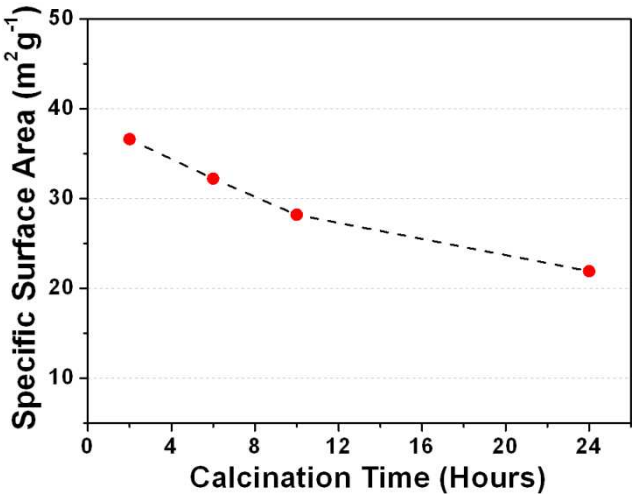

Figure S7. Specific surface areas of the porous titania networks as a function of the calcination time from 2 to 24 h sintered at 600 °C in air. The dashed line was added to guide the eye.

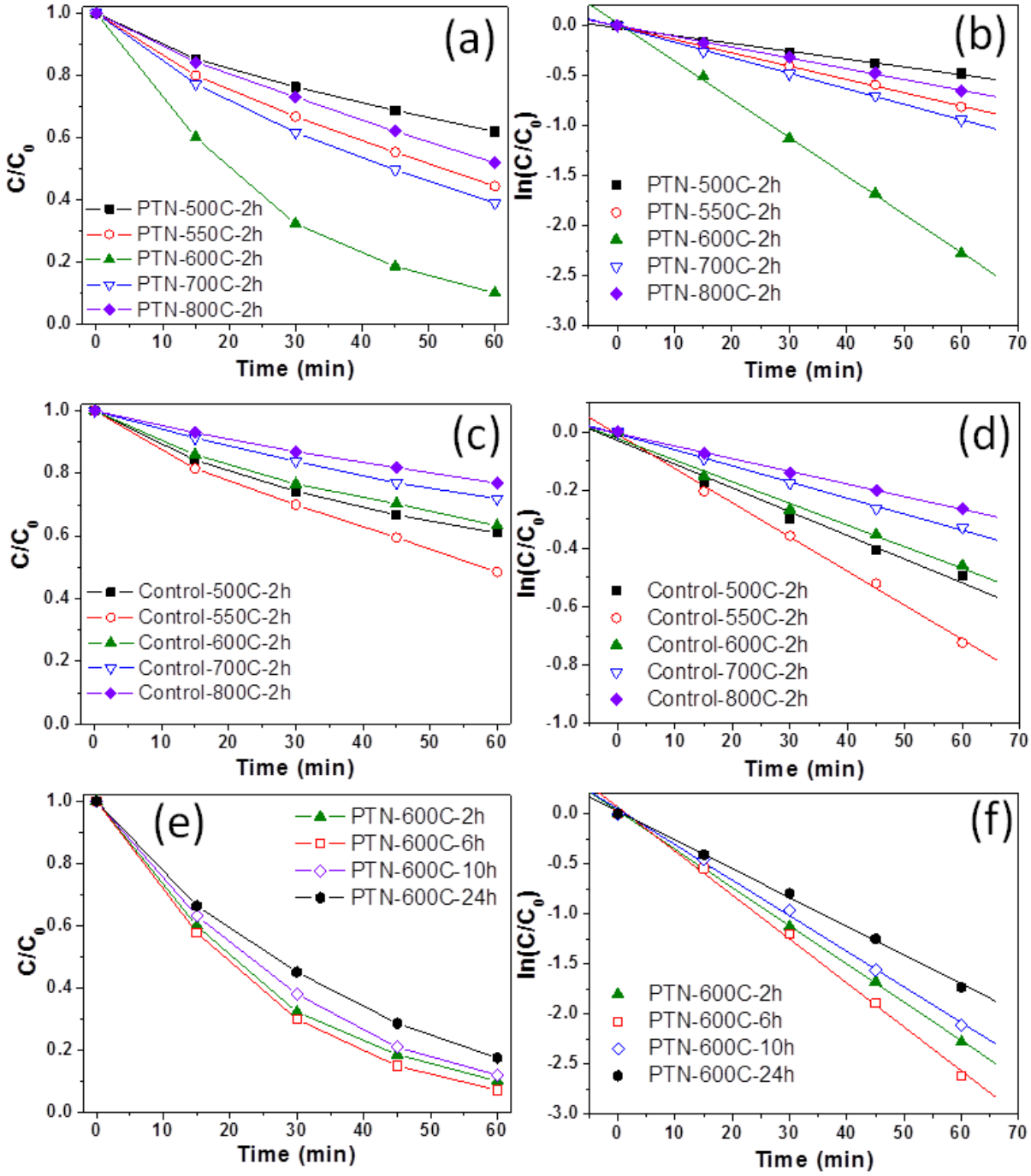

Figure S8. Photocatalytic degradation (a, c and e) of the methylene blue under UV light irradiation and the corresponding $\ln(C/C_0)$ plot (b, d and f) as a function of reaction time in the presence of different titania catalysts (as shown by the legends). The lines shown in graphs b, d and f are the linear fits of the raw data.

3.3 References for chapter introduction

1. Fujishima, A.; Zhang, X. T.; Tryk, D. A., *Surf. Sci. Rep.* **2008**, *63*, 515-582.
2. Hashimoto, K.; Irie, H.; Fujishima, A., *Japanese J. Applied Phys.* **2005**, *44*, 8269-8285.
3. Fujishima, A.; Honda, K., *Nature* **1972**, *238*, 37-38.
4. Chen, X.; Mao, S. S., *Chem. Rev.* **2007**, *107*, 2891-2959.
5. Carp, O.; Huisman, C. L.; Reller, A., *Prog. Solid State Chem.* **2004**, *32*, 33-177.
6. Hoffmann, M. R.; Martin, S. T.; Choi, W. Y.; Bahnemann, D. W., *Chem. Rev.* **1995**, *95*, 69-96.
7. Linsebigler, A. L.; Lu, G. Q.; Yates, J. T., *Chem. Rev.* **1995**, *95*, 735-758.
8. Joo, J. B.; Zhang, Q.; Dahl, M.; Lee, I.; Goebl, J.; Zaera, F.; Yin, Y. D., *Energy Environ. Sci.* **2012**, *5*, 6321-6327.
9. Joo, J. B.; Lee, I.; Dahl, M.; Moon, G. D.; Zaera, F.; Yin, Y. D., *Adv. Funct. Mater.* **2013**, *23*, 4246-4254.
10. Zhang, Z.; Zhou, Y.; Zhang, Y.; Zhou, S.; Shi, J.; Kong, J.; Zhang, S., *Dalton Trans.* **2013**, *42*, 5004-5012.
11. Wang, X. H.; Li, J. G.; Kamiyama, H.; Katada, M.; Ohashi, N.; Moriyoshi, Y.; Ishigaki, T., *J. Am. Chem. Soc.* **2005**, *127*, 10982-10990.
12. Chen, X. B.; Liu, L.; Yu, P. Y.; Mao, S. S., *Science* **2011**, *331*, 746-750.
13. Asahi, R.; Morikawa, T.; Ohwaki, T.; Aoki, K.; Taga, Y., *Science* **2001**, *293*, 269-271.
14. Lakshminarasimhan, N.; Bae, E.; Choi, W., *J. Phys. Chem. C* **2007**, *111*, 15244-15250.
15. Testino, A.; Bellobono, I. R.; Buscaglia, V.; Canevali, C.; D'Arienzo, M.; Polizzi, S.; Scotti, R.; Morazzoni, F., *J. Am. Chem. Soc.* **2007**, *129*, 3564-3575.
16. Lee, J. S.; You, K. H.; Park, C. B., *Adv. Mater.* **2012**, *24*, 1084-1088.
17. Zhang, H.; Lv, X.; Li, Y.; Wang, Y.; Li, J., *ACS Nano* **2009**, *4*, 380-386.
18. Li, H. X.; Bian, Z. F.; Zhu, J.; Zhang, D. Q.; Li, G. S.; Huo, Y. N.; Li, H.; Lu, Y. F., *J. Am. Chem. Soc.* **2007**, *129*, 8406-8407.
19. Li, W.; Deng, Y.; Wu, Z.; Qian, X.; Yang, J.; Wang, Y.; Gu, D.; Zhang, F.; Tu, B.; Zhao, D., *J. Am. Chem. Soc.* **2011**, *133*, 15830-15833.
20. Yu, J. G.; Su, Y. R.; Cheng, B., *Adv. Funct. Mater.* **2007**, *17*, 1984-1990.
21. Li, G.; Gray, K. A., *Chem. Phys.* **2007**, *339*, 173-187.

22. Zhang, J.; Xu, Q.; Feng, Z.; Li, M.; Li, C., *Angew. Chem. Int. Ed.* **2008**, *47*, 1766-1769.
23. Zhang, J.; Xu, Q.; Li, M. J.; Feng, Z. C.; Li, C., *J. Phys. Chem. C* **2009**, *113*, 1698-1704.
24. Bickley, R. I.; Gonzalez-Carreno, T.; Lees, J. S.; Palmisano, L.; Tilley, R. J. D., *J. Solid State Chem.* **1991**, *92*, 178-190.
25. Kawahara, T.; Konishi, Y.; Tada, H.; Tohge, N.; Nishii, J.; Ito, S., *Angew. Chem. Int. Ed.* **2002**, *114*, 2935-2937.
26. Miyagi, T.; Kamei, M.; Mitsuhashi, T.; Ishigaki, T.; Yamazaki, A., *Chem. Phys. Lett.* **2004**, *390*, 399-402.
27. Hurum, D. C.; Agrios, A. G.; Gray, K. A.; Rajh, T.; Thurnauer, M. C., *J. Phys. Chem. B* **2003**, *107*, 4545-4549.

Chapter 4. Synthesis of Spherical Micrometer-sized Monodisperse Titania Particles in Butanol

4.1 Introduction

Over the past decade, spherical titania particles have received considerable attention and found use in diverse fields of application, such as chromatography separation,[1, 2] lithium ion batteries,[3] dye sensitized solar cells,[4, 5] photocatalysis,[6] photoluminescence,[7, 8] electrorheological fluids[9, 10] and catalysis.[11-14] In all of these applications, uniform-sized spheres are highly preferred. For instance, monodisperse spheres show high packing density, as well as uniform flow of fluids when scaling-up of a chromatography process, thereby giving highly reproducible performance.[1, 15, 16] Ever since Stöber *et al.* reported the preparation of uniform colloidal silica spheres based on sol-gel chemistry,[17] the analogous synthesis of monodisperse TiO_2 particles through the hydrolysis of diverse titania alkoxides in a homogeneous organic solution has been one of the most popular processes for the preparation of monodisperse amorphous titania spheres (MATSs).[4, 12, 18-20] Despite several reports of the preparation of MATSs with sub-micrometer diameters,[18-25] the synthesis of micrometer-sized MATSs has been rarely reported due to either the presence of large amounts of nuclei in the original Ti alkoxide,[26] or too many nuclei being induced by the fast hydrolysis rate of the Ti alkoxide.[21]

The development of efficient and stable catalysts has become increasingly important in energy processing, chemical production and pollution control. Encapsulating noble metal nanoparticles on solid oxide supports can not only prevent nanoparticle agglomeration, but also promote synergistic interactions with the supports to improve catalytic performance.[11-13] TiO_2 is often chosen as the support for metal nanoparticles as it is highly chemically stabile and considered environmentally friendly.[12-14]

In this chapter, micrometer-sized MATSs with diameters up to 5.39 μm were successfully prepared by sol-gel synthesis. Pore sizes of 6.4-28.8 nm were obtained by

treating MATSs under solvothermal conditions. The spheres were uniformly loaded with Pd nanoparticles via an *in situ* reduction method. The prepared Pd/TiO_2 catalysts displayed high catalytic activity and good recyclability in the reduction of 4-nitrophenol (4-NP) in the presence of sodium borohydride ($NaBH_4$).

4.2 Experimental Section

4.2.1 Materials and Reagents

Titanium (IV) isopropoxide (TIP, 97%, Sigma-Aldrich), titanium (IV) butoxide (97%, Sigma-Aldrich), hexadecylamine (HDA, 90%, Sigma-Aldrich), tin (II) chloride ($SnCl_2$, 98%, Sigma-Aldrich), 4-nitrophenol (4-NP, ≥ 99.0%, Sigma-Aldrich), absolute ethanol (> 99.5%, Chem-Supply), 1-propanol (> 99.5%, Chem-Supply), 2-propanol (> 99.5%, Chem-Supply), 1-butanol (99.8%, Chem-Supply), 2-butanol (> 99.0%, BDH), 1-pentanol (> 99.0%, AJAX Finechem), ammonium chloride (NH_4Cl, 99%, BDH), cesium chloride (CsCl, 99.9%, Sigma-Aldrich), lithium chloride (LiCl, 99.9%, Sigma-Aldrich), potassium chloride (KCl, 99.5%, BDH), rubidium chloride (RbCl, > 99.0%, Sigma-Aldrich), sodium chloride (NaCl, 99.5% Merck), ammonium hydroxide (NH_3, ~25%, Merck), palladium chloride ($PdCl_2$, 99.0%, Chem-Supply) and sodium borohydride ($NaBH_4$, 98%, Scharlau) were used as received without further treatment. The water used in all experiments was from a Millipore purification system and had a resistivity of 18.2 MΩ·cm.

4.2.2 Synthesis of micrometer-sized, monodisperse, amorphous titania spheres (MATSs)

In a typical synthesis of MATSs with a diameter of 2.4 μm, 11.92 g HDA was dissolved in 600 mL of 1-butanol with stirring in a beaker, which was then sealed with Parafilm to minimise exposure to the atmosphere. After HDA dissolution, 4.80 mL aqueous KCl solution (0.1 M) was added, followed by 13.57 mL of TIP introduced under vigorous stirring. After keeping the resulting suspension static at 22 °C for 18 h, the precipitate was recovered by centrifugation at 5000 rpm for 5 min and washing with 1-butanol (1-BuOH) and then ethanol (EtOH). The sample was dried in a fume

cupboard and MATSs with a diameter of 2.4 μm were obtained.

4.2.3 Synthesis of micrometer-sized, monodisperse, mesoporous titania spheres (MMTSs) with different pore sizes

In a typical synthesis, 1.60 g of MATSs were dispersed in a mixture with different volume ratios (mL) of ethanol, water and ammonia (10:20:0, 20:10:0 and 20:6:4). The resulting mixture was placed inside a Telflon-lined autoclave (50 mL) and heated at 160 °C for 16 h. After cooling, the white product was collected by vacuum filtration, washed 3 times using ethanol and dried in air at room temperature. Next, the dried powders were calcined at 500 °C for 2 h (ramp rate of 1.6 °C min^{-1}) in air to remove any remaining organic content. The calcined samples were denoted as S1, S2 and S3 correlating to treatment in ethanol, water and ammonia volume ratios of 10:20:0, 20:10:0 and 20:6:4.

4.2.4 Loading Pd nanoparticles onto the micrometer-sized, mesoporous TiO_2 spheres to form Pd/TiO_2

In a typical process, 0.50 g of MMTSs (S1, S2 or S3) were dispersed in 100 mL of water by ultrasound for 30 min. Meanwhile, 0.50 g of $SnCl_2$ was dissolved in 100 mL of HCl (0.02 M). The two solutions were then stirred together for 30 min at ambient temperature before the suspension of Sn-activated TiO_2 spheres was recovered by filtration, followed by washing with water. The activated spheres were subsequently redispersed in 187.5 mL of water, to which 25.0 mL of $PdCl_2$ (0.021 M) solution was added. After stirring for 10 min, the suspension was filtered and washed with water 5 times. The product was dried at 60 °C for 2 h before further characterization. The Pd loaded MMTS samples were labelled S1-Pd, S2-Pd and S3-Pd.

4.2.5 Catalytic reduction of 4-nitrophenol (4-NP)

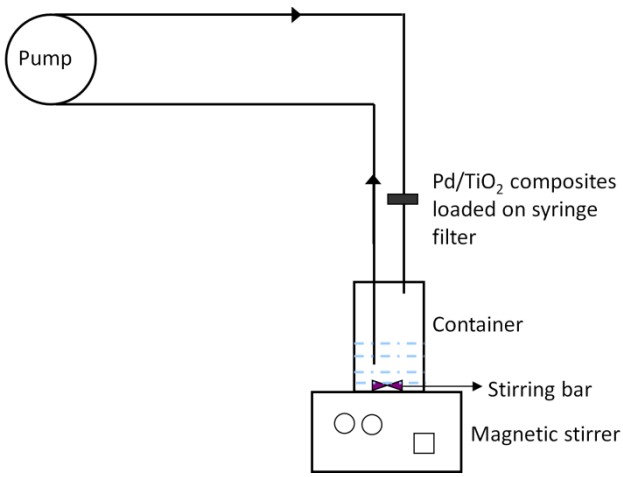

Scheme 4.1. Experimental setup for the catalytic reduction of 4-NP. The container was covered using a plastic cap with two small holes.

A schematic of the catalytic process is shown in Scheme 4.1. 20.0 mg of Pd/TiO_2 composite was placed inside of a syringe filter (0.45 µm hydrophilic polyethersulfone membrane, Pall corporation, USA). Next, 38.0 mL of water, 1.6 mL of $NaBH_4$ (0.5 M) and 0.4 mL of 4-NP (10 mM) were mixed in a plastic container with stirring. The molar ratio of 4-NP:$NaBH_4$ in the catalytic reaction was 1:200. The solution was circulated through the syringe filter by a peristaltic pump (Gilson Minipuls 3) at a flow rate of 0.094 mL s^{-1}. 4-NP exhibits an absorption peak at 317 nm in neutral or acidic solution, but upon the addition of $NaBH_4$ the solution colour changed from light yellow to bright yellow with a corresponding absorption peak shift to 400 nm. The absorbance of 4-NP at 400 nm was monitored every 3 min with UV-visible spectroscopy. Since the concentration of $NaBH_4$ was in great excess compared to 4-NP, the reduction was regarded as a pseudo-first-order reaction.

4.2.6 Recycling of catalyst

To recycle the catalyst water was flowed through the sample and syringe filter for 5 min prior to exposure to the fresh 4-NP/$NaBH_4$ solution (next cycle). This process was repeated with each cycle lasting 27 min.

4.2.7 Characterization

Scanning electron microscopy (SEM) images were taken on a Quanta 200F FEI environmental scanning electron microscope with an accelerating voltage of 15 kV. All images were taken without prior sputter coating treatment of the samples. Transmission electron microscopy (TEM) experiments were conducted on an FEI Tecnai F20 microscope operated at 200 kV. Samples for TEM measurements were embedded in an LR-white resin and sliced into approximately 90 nm thick sections and supported on holey carbon film on a Cu grid. Wide-angle X-ray diffraction (XRD) patterns were recorded on a Bruker D8 diffractometer with Ni-filtered Cu Kα radiation (40 kV, 40 mA). Nitrogen sorption isotherms were measured at -196 °C with a Micromeritcs Tristar 3000 analyzer. Prior to the measurement, MATSs were degassed at 60 °C for 24 h and MMTSs were degassed at 150 °C for 18 h on a vacuum line. The Brunauer-Emmett-Teller (BET) method was utilized to calculate the specific surface area using adsorption data in a relative pressure range from 0.05 to 0.20. Pore size distributions were derived from the adsorption branch of the isotherms using the Barrett-Joyner-Halenda (BJH) model. The total pore volume was estimated from the adsorbed amount at a relative pressure of 0.98. The estimation of porosity (P) was based on the density of anatase (ρ) and the total pore volume (V_P) according to the equation $P = \frac{\mathrm{Vp}}{\rho - 1 + \mathrm{Vp}}$.[27] Thermogravimetric analysis (TGA) and differential thermal analysis (DTA) were conducted simultaneously on a Mettler Toledo TGA/SDTA851e thermogravimetric analyzer. Samples were subjected to a linear heating ramp of 10 °C min^{-1} under an air atmosphere at a flow rate of 30 mL min^{-1}. The surface hydroxyl density was obtained from the same instrument according to a TGA procedure developed by Mueller *et al*.[28] Under nitrogen atmosphere, the samples were first stabilized at 25 °C for 5 min, heated at 10 °C min^{-1} to 120 °C (T_1), held at this temperature for 30 min, then heated to 500 °C (T_2) at 20 °C min^{-1}. Fourier transform infrared attenuated total reflectance (FTIR-ATR) spectroscopy was performed on a Nicolet 6700 spectrophotometer. UV-visible absorption spectra were obtained at room temperature with a Varian Cary 50 Bio UV-vis spectrophotometer.

4.3 Results and discussion

The synthesis strategy of micrometre-sized MATSs involves hydrolysis of titanium isopropoxide (TIP) in 1-butanol (1-BuOH) or other alcohols in the presence of hexadecylamine (HDA), a structure-directing agent, and simple alkali salts (Scheme 4.2).

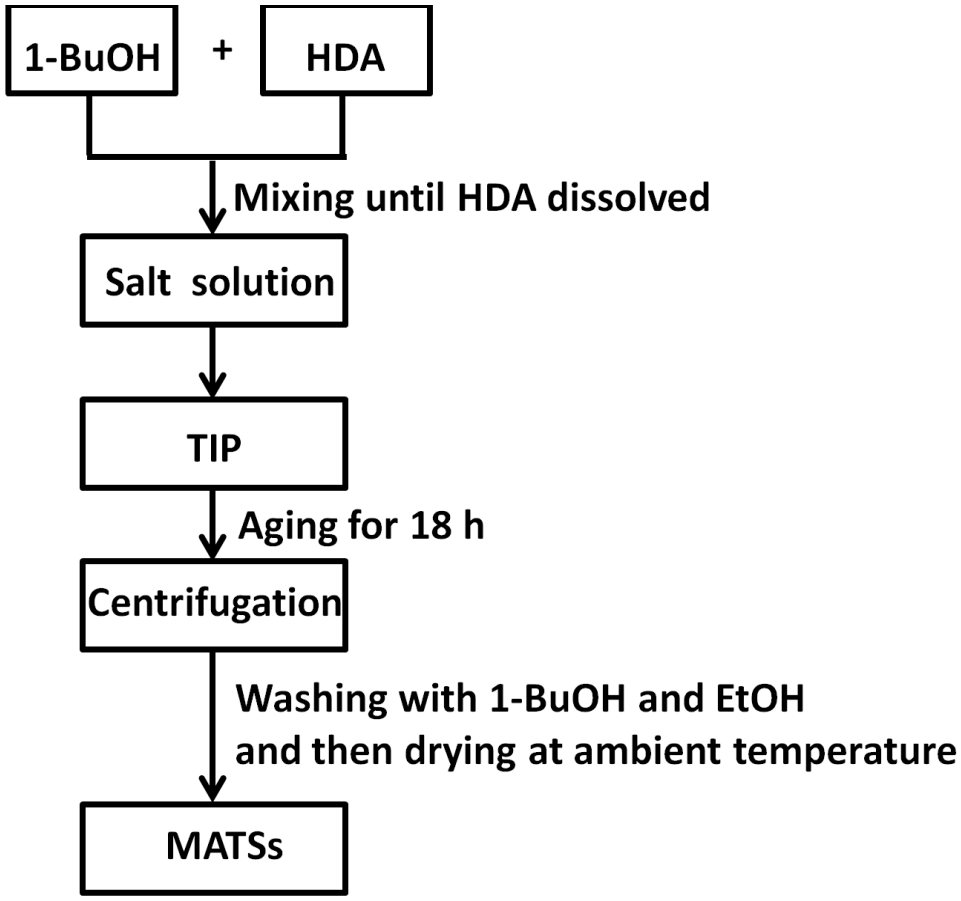

Scheme 4.2. Flow procedure for the preparation of size-controlled MATSs.

The influence of various experimental factors (e.g. solvent type, salt species, HDA/Ti molar ratio, KCl concentration, water/Ti molar ratio and synthesis temperature) on the morphology, sphere size and size distribution of the amorphous precursor spheres is summarized in Figure 4.1, based on investigations carried out by SEM (Figure 4.2-4.6). The precursor spheres were obtained by changing one parameter while keeping the rest of the factors constant. In a typical synthesis for MATSs at room temperature, a molar ratio of TIP:BuOH:HDA:H_2O:KCl = 1:222:1:6:0.011 was

employed.

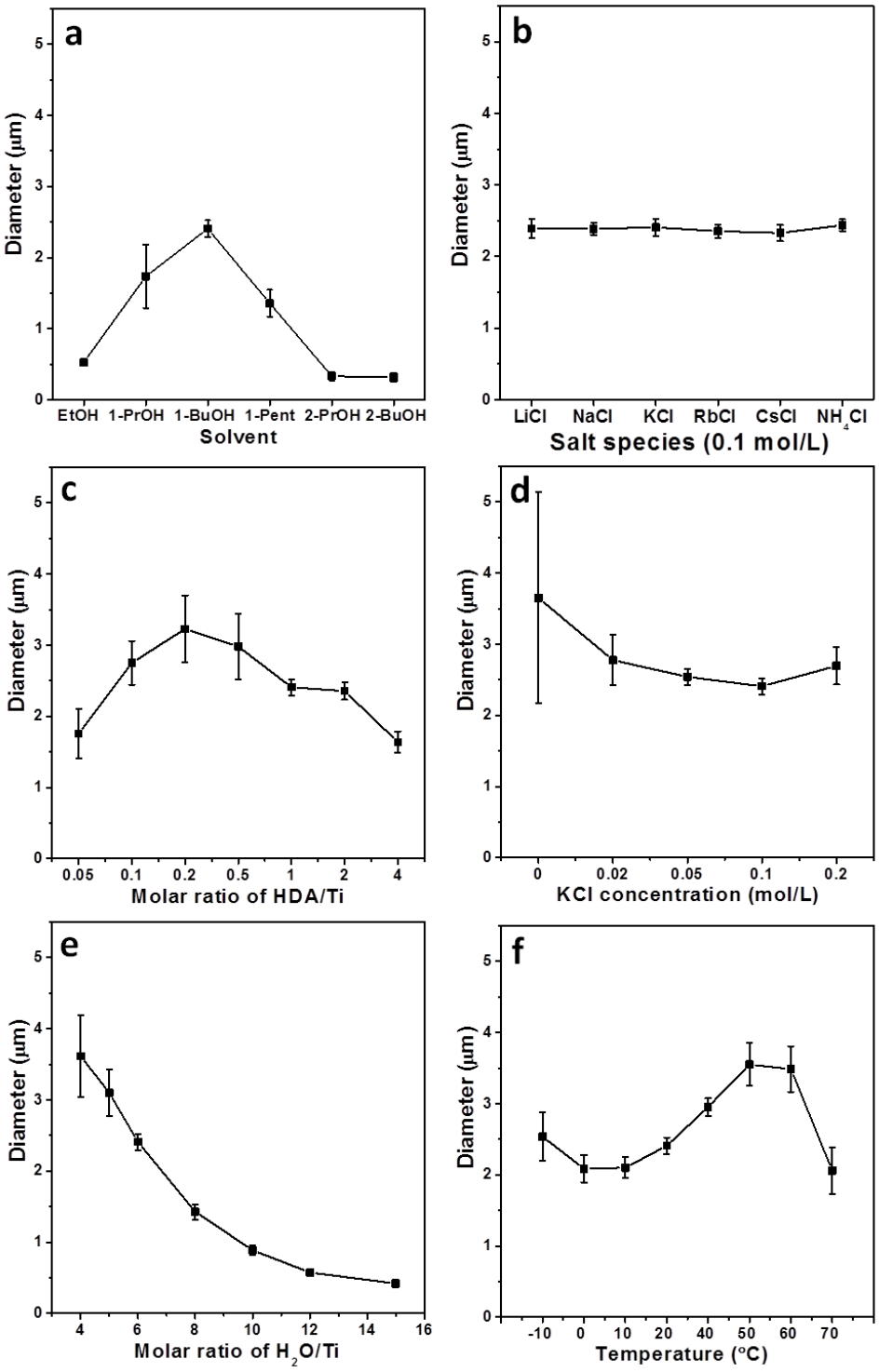

Figure 4.1. Size distribution of the MATSs synthesised with changes in: a) solvent, b) salt species (0.1 mol/L), c) HDA/Ti molar ratios, d) KCl concentration, e) H_2O/Ti molar ratios and f) synthesis temperature. EtOH, 1-PrOH, 1-BuOH, 1-Pent, 2-PrOH and 2-BuOH represent ethanol, 1-propanol, 1-butanol, 1-pentanol, 2-propanol and 2-butanol respectively.

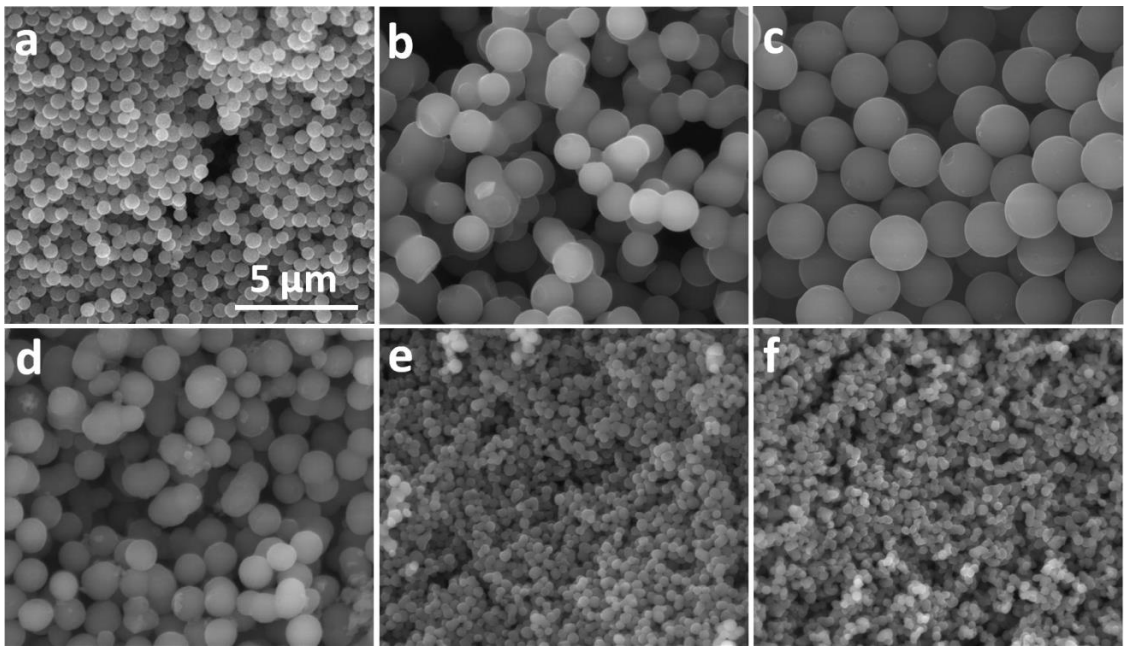

Figure 4.2. SEM images of precursor titania particles prepared in a) ethanol, b) 1-propanol, c) 1-butanol, d) 1-pentanol, e) 2-propanol and f) 2-butanol. For c) the molar ratio was TIP:BuOH:HDA:H_2O:KCl = 1:222:1:6:0.011. The volume of the other solvents was 600 mL, the same as 1-butanol. All images are at the same scale.

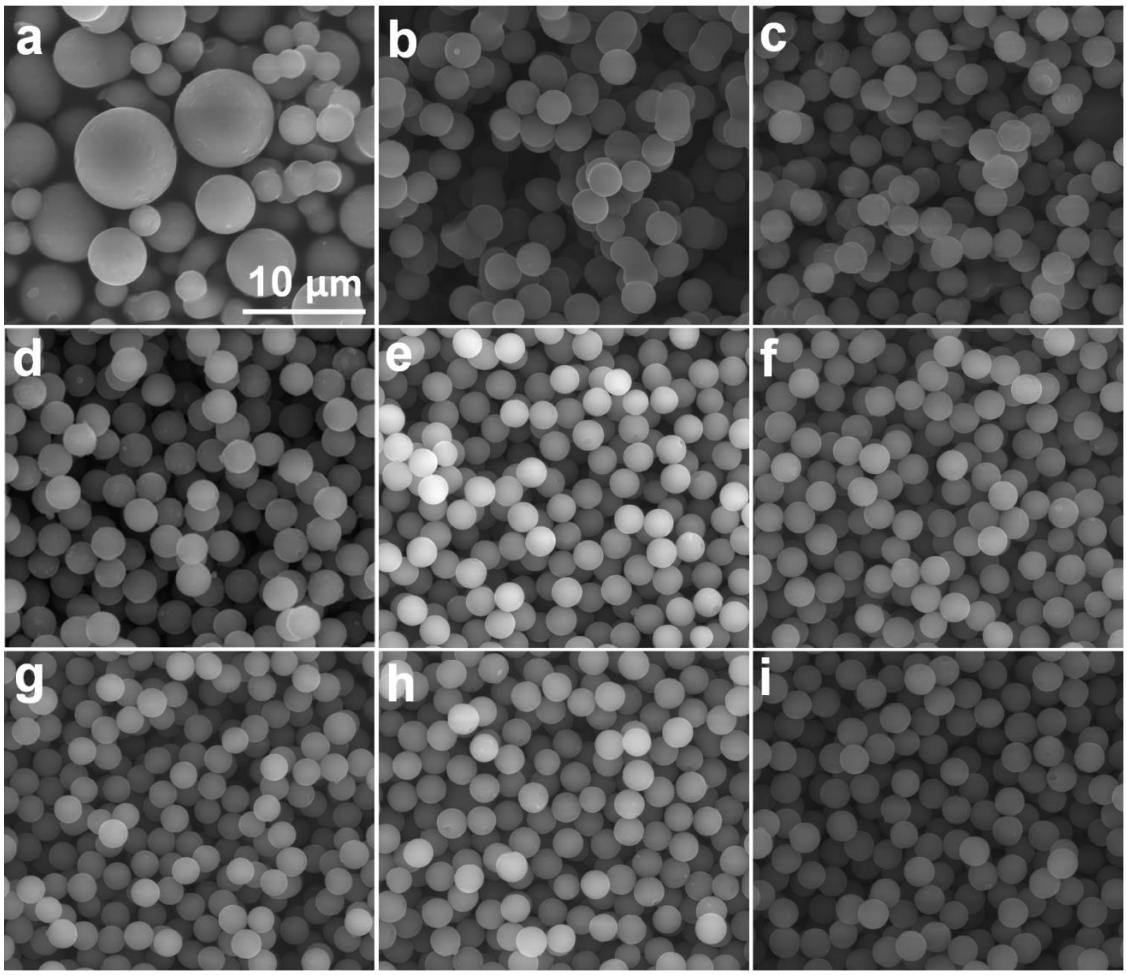

Figure 4.3. SEM images of the precursor titania particles obtained by the addition of 4.8 mL of aqueous KCl at concentrations of a) 0.00 M, b) 0.02 M, c) 0.05 M and d) 0.20 M, or 4.80 mL of salt solutions (0.10 M) of e) LiCl, f) NaCl, g) RbCl, h) CsCl or i) NH_4Cl. All images are at the same scale.

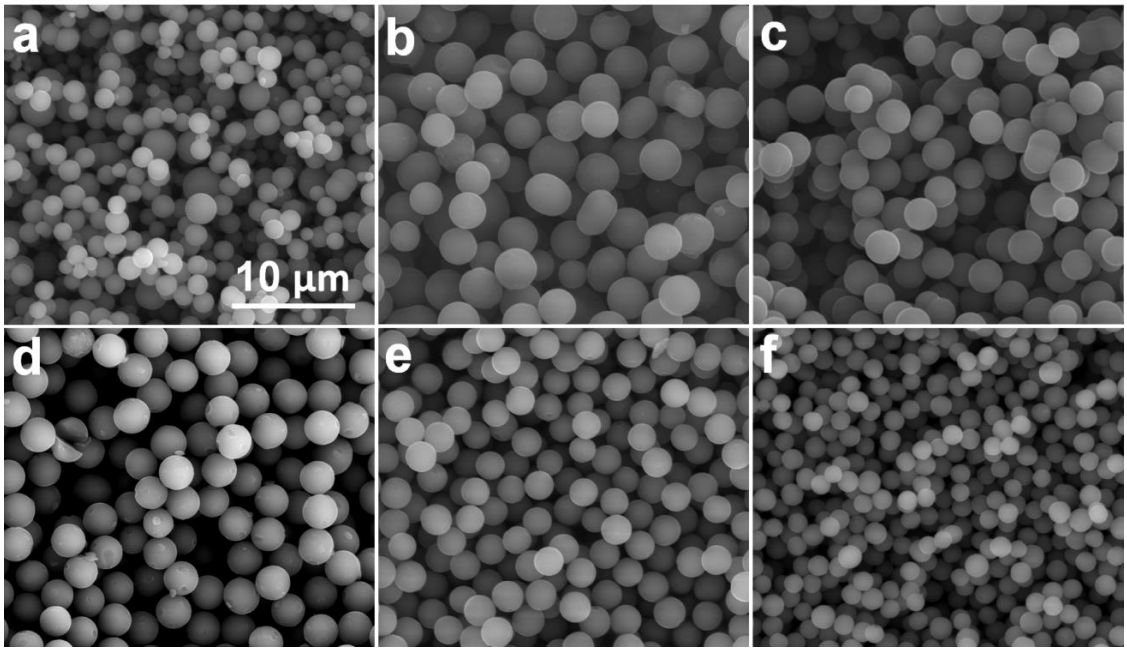

Figure 4.4. SEM images of the precursor titania particles prepared with varying HDA/Ti molar ratios of a) 0.05, b) 0.10, c) 0.20, d) 0.50, e) 2.00 and f) 4.00. The molar ratio for the rest of the reaction system was TIP:BuOH:H_2O:KCl=1:222:6:0.011. All images are at the same scale.

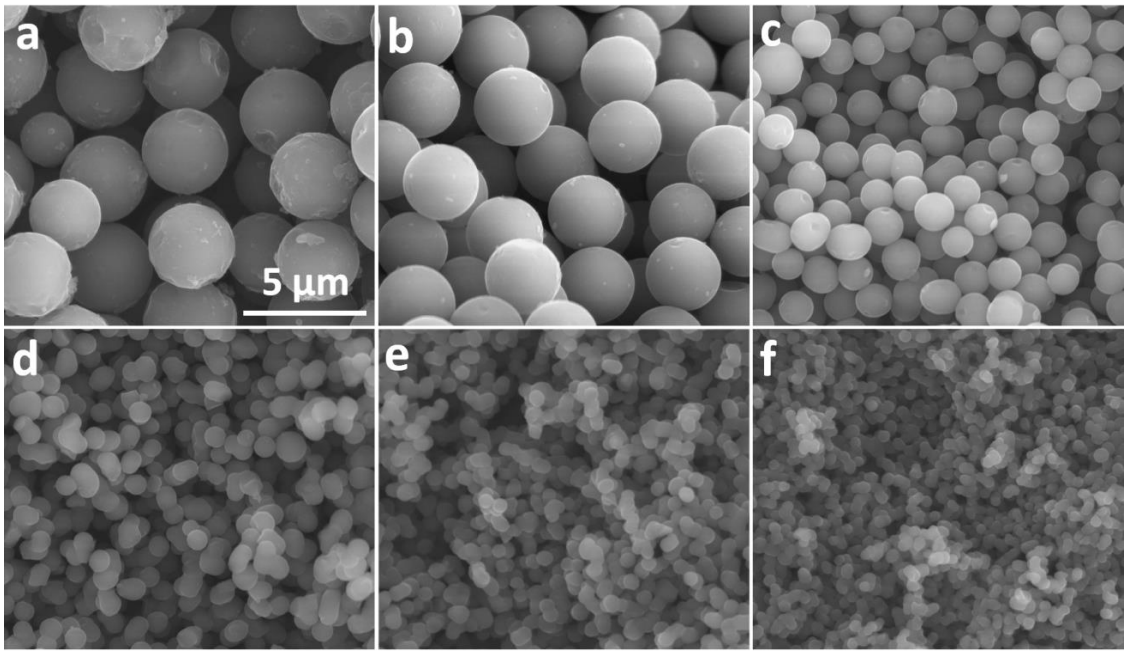

Figure 4.5. SEM images of the precursor titania particles prepared with varying H_2O/Ti molar ratios of a) 4, b) 5, c) 8, d) 10, d) 12 and f) 15. The molar ratio for the rest of the reaction system was TIP:BuOH:HDA:KCl = 1:222:1:0.011. All images are at the same scale.

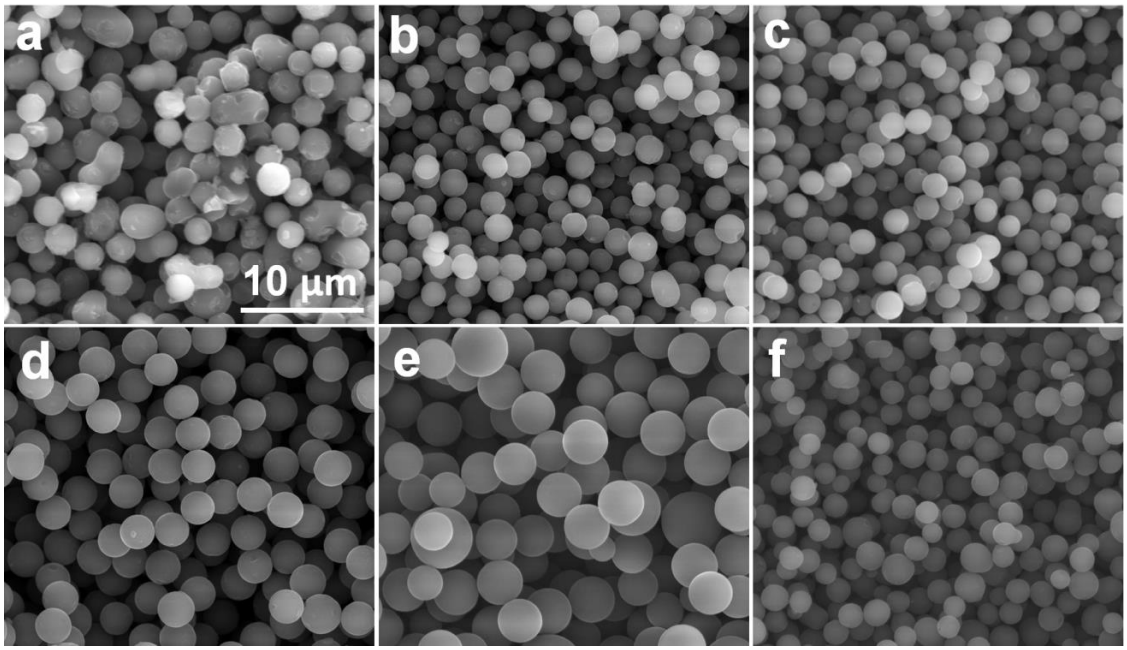

Figure 4.6. SEM images of the precursor titania particles synthesized at varying temperatures of a) -10 °C, b) 0 °C, c) 10 °C, d) 40 °C, e) 50 °C and f) 70 °C. The molar ratio for the reaction system was TIP:BuOH:HDA:H_2O:KCl = 1:222:1:6:0.011. All images are at the same scale.

It is generally accepted that the nature of an alcoholic solvent has an important effect on particle size and homogeneity.[17, 29] Figure 4.1a and 4.2 show that the mean particle size of the MATSs increased from 0.5 to 1.7 to 2.4 µm as the alcohol alkyl chain lengthened ($C \leq 4$) from ethanol to 1-propanol to 1-butanol, with corresponding standard deviations (σ) of 9.5%, 25.7% and 4.8%, respectively. Yet, the sample prepared in 1-pentanol possessed a mean diameter of only 1.4 µm but maintained reasonable monodispersity (σ = 13.9%). In addition, all spheres produced in the secondary alcohols, 2-propanol and 2-butanol, were much smaller than those in the primary alcohols. Based on these results, amorphous TiO_2 spheres synthesized in 1-butanol possessed the largest diameter and highest degree of monodispersity.

Eiden-Assmann *et al.* reported that the size and size distribution of spheres are very sensitive to the added salt (LiCl, NaCl, KCl, RbCl, CsCl and NH_4Cl), and the salt concentration in the absence of surfactant.[20] Particle size decreases significantly with

increasing cationic radii and concentration in the reaction medium due to the increase of ionic strength. Figures 4.1b, 4.2c and 4.3e-i show that alkali salts at the same concentration (0.1 M) produced MATSs of similar size. Therefore, the participation of the surfactant HDA was possibly an important factor affecting sphere size. The effect of the HDA/Ti molar ratio on particle size is illustrated in Figure 4.1c and 4.4. In the absence of HDA, no precipitation occurred even when the solution was left open to the air for 3 months. The micrometer-sized MATSs decreased in size from 3.0 ± 0.5μm to 1.6 ± 0.2 μm when the HDA/Ti ratio was increased from 0.5 to 4. Interestingly, monodispersity increased greatly when the HDA/Ti ratio was 1 or above. In addition, insufficient salt (KCl) led to particles with broader size distributions (Figure 4.1d and 4.3a-d). Therefore, adding appropriate amounts of salt and surfactant to the reaction system are necessary to obtain uniform, micrometer-sized amorphous TiO_2 precursor particles.

Figures 4.1e, 4.2c and 4.5 show that particle size monodispersity and diameter can be manipulated by varying the water to titanium molar ratio. For example, no precipitates formed when insufficient water (H_2O:Ti ≤ 2) was added. Increasing the H_2O:Ti ratio to 3:1 produced only a slightly turbid solution after being kept static for 18 h. Even at a ratio of 4:1, the yield of spheres was low at 23%. Monodisperse spheres with a diameter of 2.9 ± 0.3 μm were obtained when a molar ratio of 5:1 was reached, and became highly uniform in size at a 6:1 ratio (2.4 ± 0.1 μm). If the water amount was further increased, above a ratio of 8:1, particle size distribution became broader and dimers formed. For even greater water content (H_2O:Ti ≥ 10), the final particle size was drastically reduced and agglomeration occurred. Similar morphologies resulted in the absence of HDA when H_2O:Ti ≥ 10 (Figure 4.7), indicating that the structure-directing role of HDA can only take effect within a limited water to titanium molar ratio.

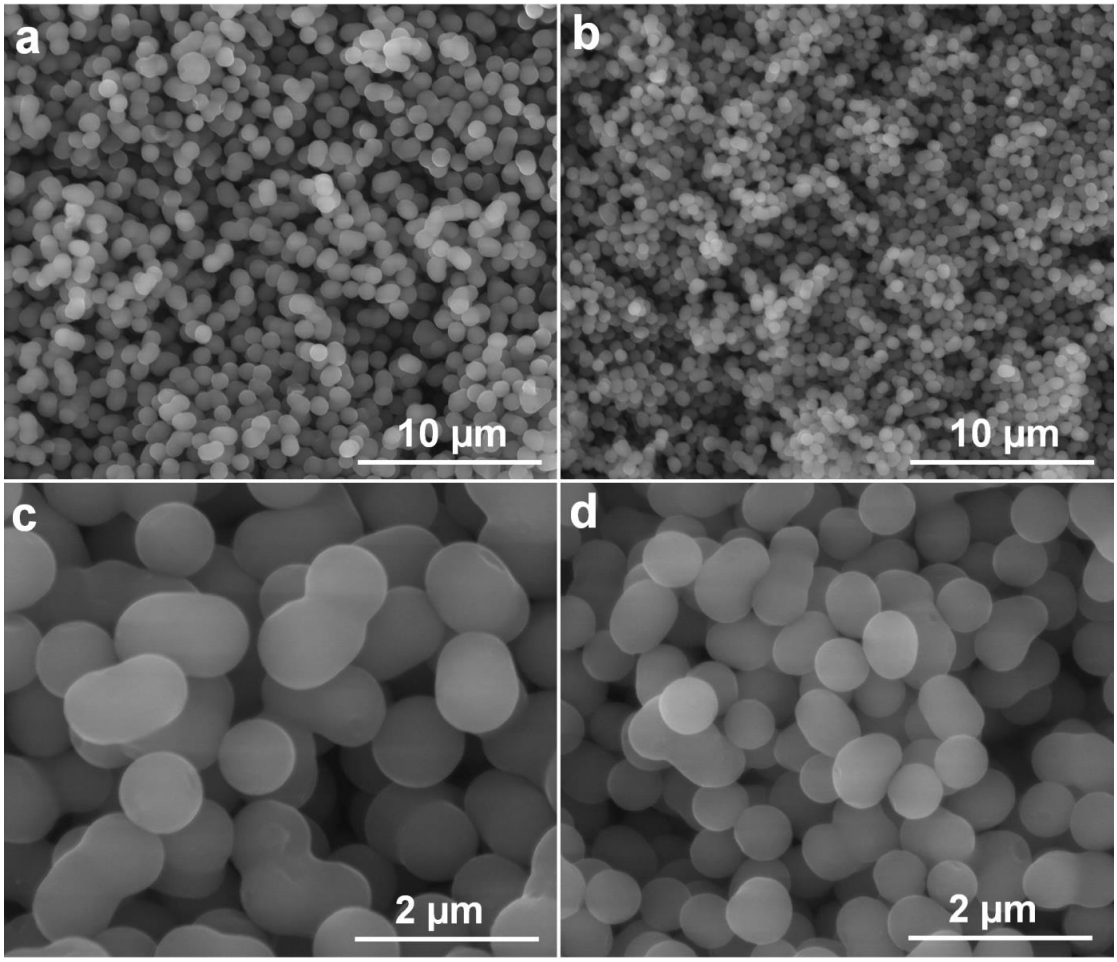

Figure 4.7. SEM images of the precursor titania particles prepared in the absence of HDA with varying H_2O/Ti molar ratios of a, c) 10, and b, d) 12. The molar ratio for the rest of the reaction system was TIP:BuOH:KCl = 1:222:0.011.

Another factor affecting the size of MATS is the number of nuclei in the solution. A higher degree of separation between seed formation and growth processes leads to more monodisperse particles.[18] The induction time (the duration after addition of TIP until the milky white solution was observed) of the standard spheres achieved from the typical synthesis is around 430 s. Preformed nuclei in the system can probably act as seeds to form large spheres. A comparable experiment was conducted by adding water (as aqueous 0.1 M KCl) in two steps 30 min apart. The first step produced seed nuclei in the reaction solution. The second step induced particle growth based on the preformed nuclei. Seed numbers are controlled by the amount of water added in the first step. As shown in Figure 4.8, the less water added in the first step, the less seeds formed, the bigger the final spheres obtained.

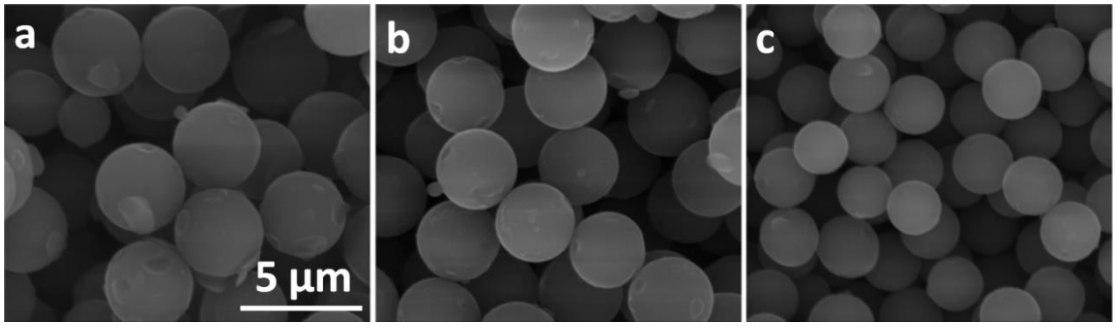

Figure 4.8. SEM images of precursor titania particles prepared by two additions of equal volume of KCl (0.1 M, 4.8 mL total) of a) 1.6+3.2 mL, b) 2.4+2.4 mL and c) 3.2+1.6 mL. The interval between the two steps was 30 min. The molar ratio for the reaction system was TIP:BuOH:HDA:H_2O:KCl = 1:222:1:6:0.011. All images were at the same scale.

The temperature at which the reaction was conducted had a profound effect on MATS size (Figures 4.1f, 4.2c and 4.6), but not crystallinity with all spheres confirmed as amorphous by wide-angle XRD (Figure 4.9).

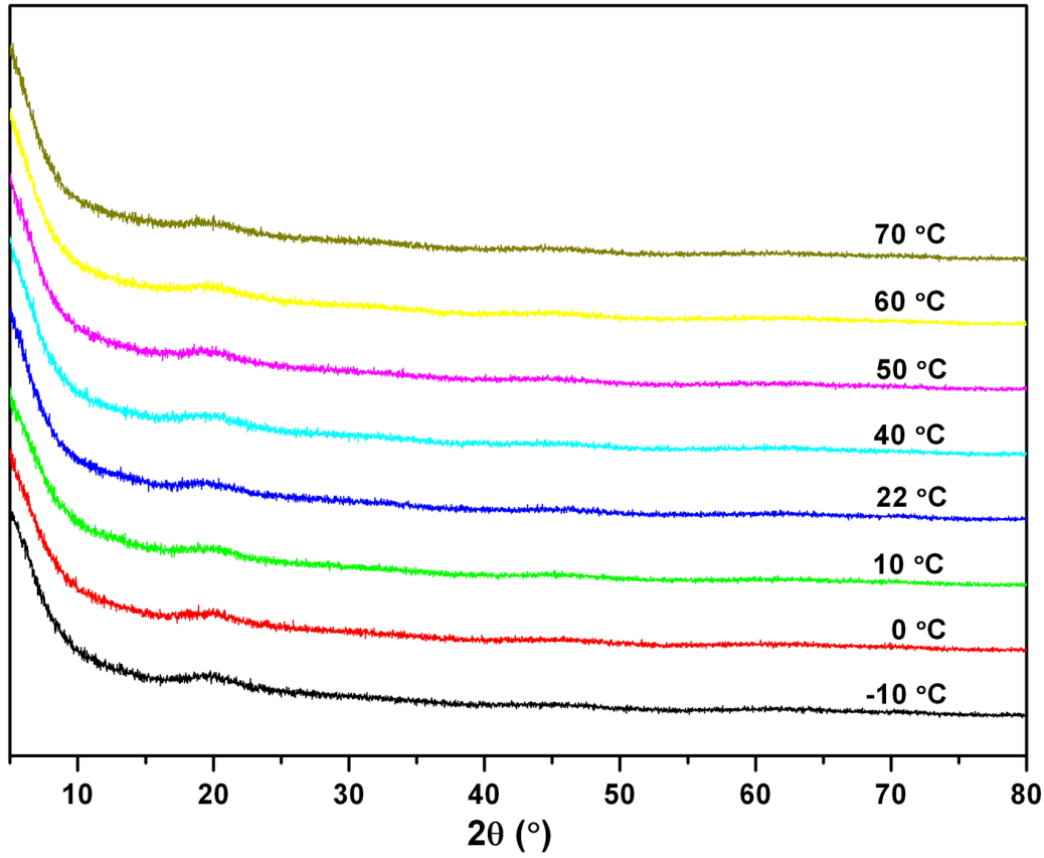

Figure 4.9. XRD patterns of the precursor titania particles synthesized at varying temperatures. The molar ratio for the reaction system was TIP:BuOH:HDA:H_2O:KCl = 1:222:1:6:0.011.

For example, the largest spheres produced in this study had a diameter of 5.39 ± 0.68 μm (Figure 4.10), and were obtained from a reaction system with molar ratio of TIP:BuOH:HDA:H_2O:KCl = 1:83.3:0.375:3:5.5×10^{-3} at 50 °C.

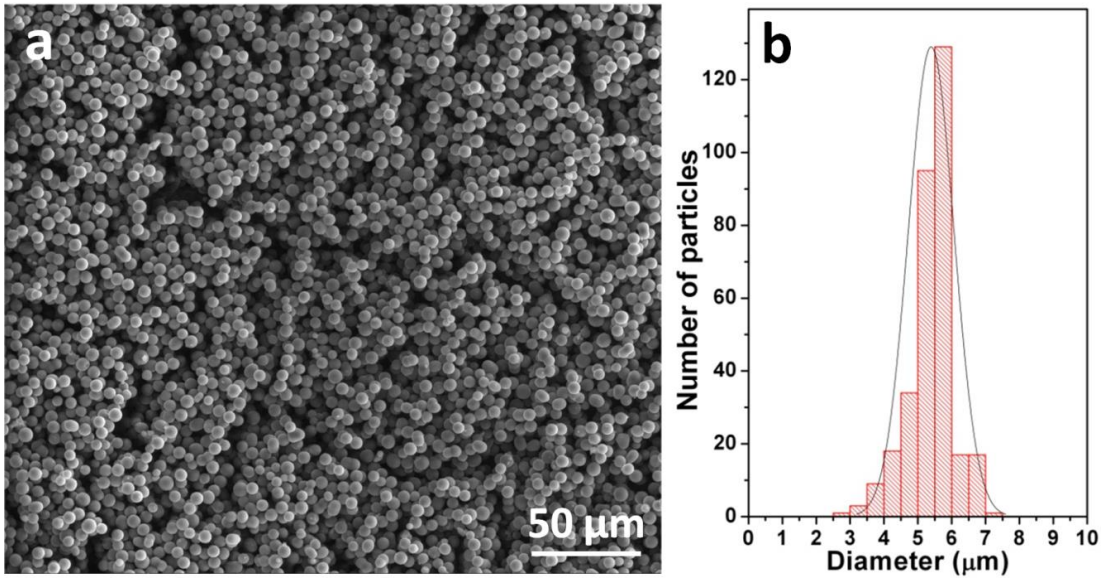

Figure 4.10. a) SEM image and b) the corresponding size distribution histogram of the largest sample synthesized at 50 °C. The molar ratio for the reaction system was TIP:BuOH:HDA:H_2O:KCl = 1:83.3:0.375:3:5.5×10^{-3}.

On the basis of the above results, the size of the precursor spheres seems to be decided by a competitive process between solubility and hydrolysis rate. The higher the solubility, the fewer the number of nuclei, and so the larger the sphere formed. The hydrolysis rate functioned vice versa. The solubility of $Ti(OH)_4$ gel in different solvents was investigated by Sugimoto's group.[22, 23] The high solubility of Ti oligomers was mainly due to the low affinity (i.e. polarity) between solvent molecules, e.g. the solubility of Ti oligomers in 1-butanol (polarity index 4.0) was higher than in ethanol (polarity index: 5.2). This explains why larger spheres were obtained in 1-butanol, and also 1-propanol and 1-pentanol, than in ethanol (Figure 4.1a). Furthermore, the polarity index of water is 9.0, which was in keeping with the result that smaller spheres were produced in higher molar ratio H_2O:Ti (Figure 4.1e), because the solubility of oligomers in 1-butanol was reduced by the increase of water.[23] In an ethanol system with H_2O:Ti = 3:1, a milky white solution was obtained

instead of a slightly turbid solution, which further confirmed that the solubility in 1-butanol was larger than in ethanol.[19] In addition, excess water also contributes to the formation of polydisperse spheres due to reinforcement of hydrogen bonding among the oligomers. The decrease in the size of the precursor spheres with increasing HDA:Ti molar ratio (Figure 4.1c) was ascribed to the reduction in solubility of oligomers by the addition of more HDA. With the increase of temperature, the solubility of the oligomers increases. It was supposed that large spheres were obtained at increasing temperatures as fewer nuclei formed (Figure 4.1f); however, the hydrolysis rate also increases with increasing temperature, so the number of nuclei increase as well. When the temperature was ≤ 50 °C, solubility influenced the number of nuclei more than the hydrolysis rate. Yet, the hydrolysis rate of TIP dramatically accelerated with increasing temperature. Hence, this explains why the size of the spheres decreased for the reaction at 70 °C, but at -10 °C the sphere size was relatively large as the hydrolysis rate was greatly slowed. The influence of the hydrolysis rate on MATS size additionally depends on the Ti source. For example, highly monodisperse titania precursor spheres obtained from titanium butoxide were larger than those from TIP (Figure 4.11). One possible reason is that the hydrolysis rate of TIP is much higher than that of titanium butoxide.

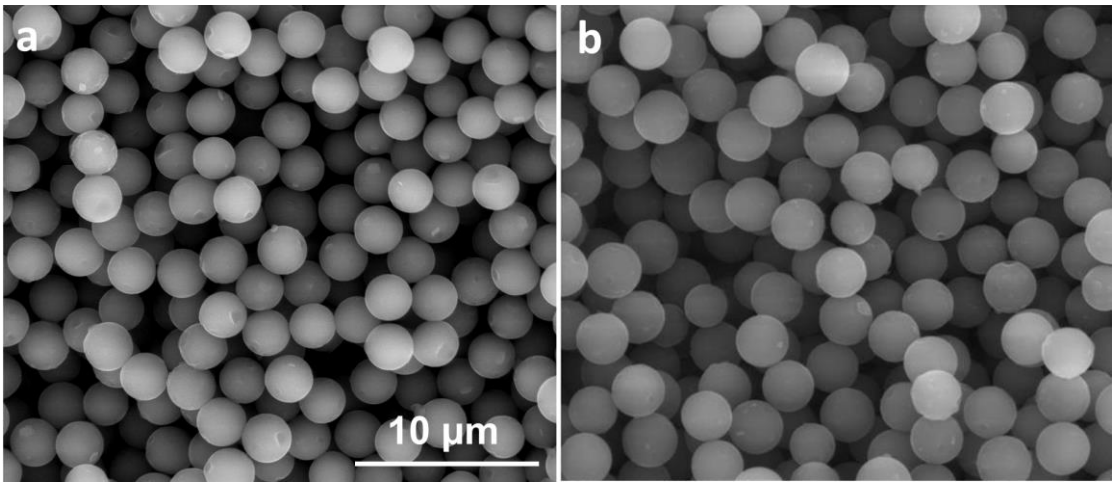

Figure 4.11. SEM images of precursor titania particles synthesized when using different Ti sources: a) TIP or b) titanium butoxide. The molar ratio for the reaction system was Ti:BuOH:HDA:H_2O:KCl = 1:222:1:6:0.011. Both images are at the same scale.

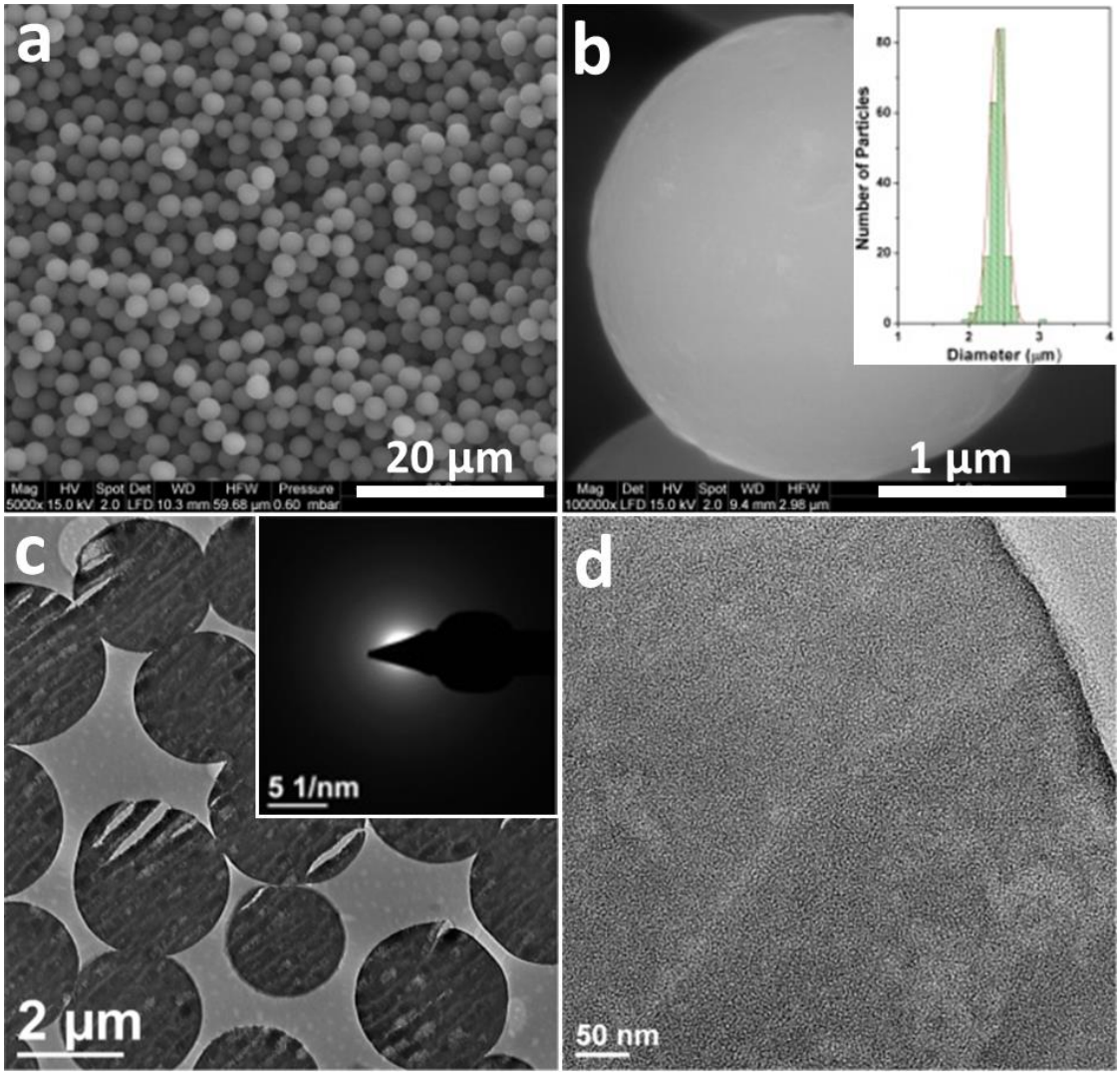

Figure 4.12. a, b) SEM images and c, d) TEM images of ultramicrotomed samples of typical monodisperse precursor titania spheres. The molar ratio for the reaction system was TIP:BuOH:HDA:H_2O:KCl = 1:222:1:6:0.011. The inset in b) is the corresponding size distribution histogram and the inset in c) is the SAED pattern of the precursor particles.

The SEM image shown in Figure 4.12a is typical for MATSs prepared at room temperature using a molar ratio of TIP:BuOH:HDA:H_2O:KCl = 1:222:1:6:0.011, and reveals that the sample consists of well-defined spherical structures that have a narrow size distribution with a mean diameter of 2.4 µm (standard deviation σ = 4.8%). No granular features were observed on the surface of the spheres (Figure 4.12b), indicating that the precursor spheres were composed of ultrafine particles. The interior structures of the spheres were investigated by TEM after ultramicrotoming. The sample was solid to the core (Figure 4.12c) and possessed a homogeneous worm-hole

like pattern (Figure 4.12d). The corresponding selected area electron diffraction (SAED) pattern showed that the sample was amorphous (Figure 4.12c inset). Characterization by nitrogen gas sorption (Figure 4.13) showed a type II sorption isotherm, and a low specific surface area (2.4 m^2 g^{-1}) and pore volume (0.005 cm^3 g^{-1}), indicating that the sample was non-porous.

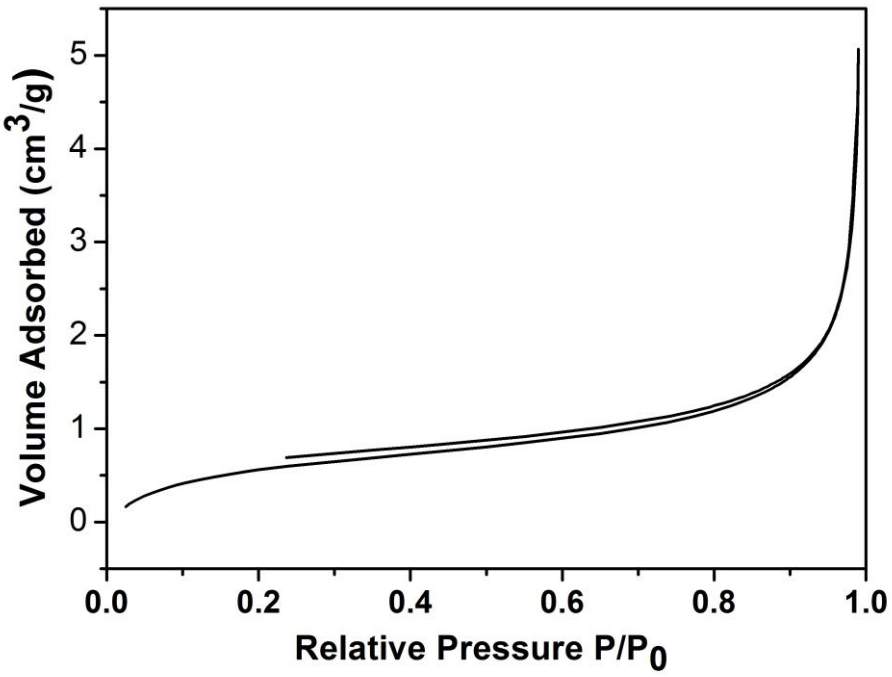

Figure 4.13. Nitrogen sorption isotherm of the precursor titania spheres. The molar ratio for the reaction system was TIP:BuOH:HDA:H_2O:KCl = 1:222:1:6:0.011.

Thermal analysis revealed that the titania content was around 50% of the mass of the precursor sample (Figure 4.14). As displayed in the graph, there are four main weight loss stages for the MATSs. The first weight loss appears below 160 °C accompanied by a broad endothermic peak in the DTA curve with a minimum around 80 °C, which is mainly associated with the release of physically adsorbed water. The second weight loss occurred from 160 °C to 310 °C and was mostly due to the volatilization of organic molecules, though removal of chemically adsorbed water also contributed to the loss. A sharp weight loss ranging from 330 °C to 460 °C, along with a striking exothermic peak centered at 330 °C, was due to the decomposition and desorption of

HDA molecules, which have a boiling point of 330 °C. Another key weight loss on the TGA curve was in the range from 560 °C to 650 °C, and was marked by a characteristic sharp exothermic peak on the DTA curve. This was mainly ascribed to the oxidation of organics on the TiO_2 surface and crystallization from the amorphous phase to anatase titania.

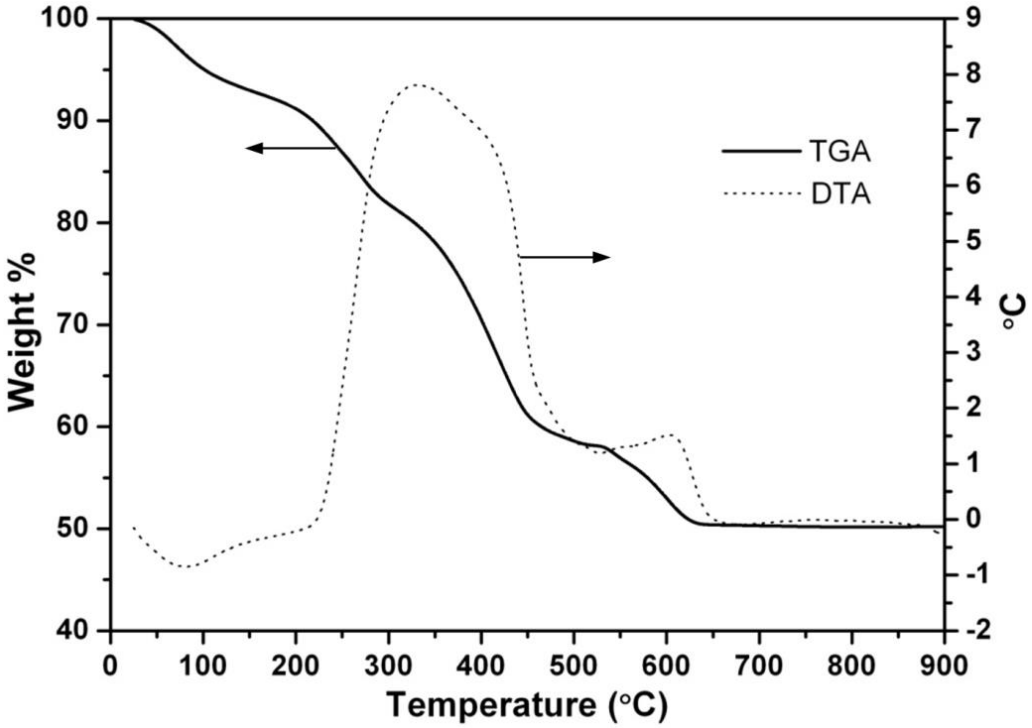

Figure 4.14. TGA (left axis) and DTA (right axis) curves plotted against temperature for the precursor titania spheres. The molar ratio for the reaction system was TIP:BuOH:HDA:H_2O:KCl = 1:222:1:6:0.011.

FTIR-ATR spectra indicated that the Ti species/oligomers and amino groups of HDA formed titania-amine complexes uniformly in the precursor spheres (Figure 4.15).[18] The absence of the NH_2 stretching vibration (double peaks near 3300 cm^{-1}) and N-H wagging vibration (800 cm^{-1}), and the shift in the N-H deformation vibration from 1570 to 1521 cm^{-1} indicate the formation of titania-amine complex bonds that are incorporated and/or confined uniformly in the MATSs.

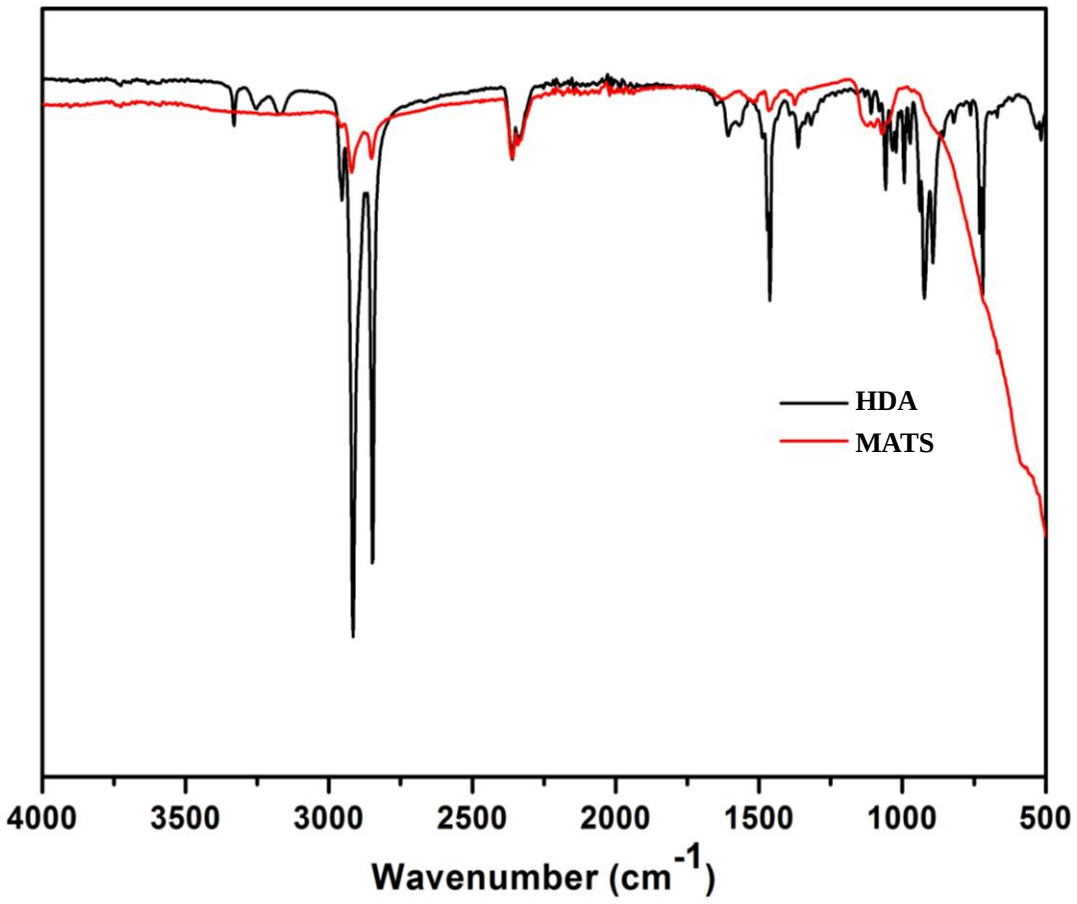

Figure 4.15. FTIR-IR spectra of the precursor titania spheres and HDA. The molar ratio for the reaction system was TIP:BuOH:HDA:H_2O:KCl = 1:222:1:6:0.011.

MATSs can readily be converted into monodisperse, mesoporous anatase titania spheres (MMTSs) upon solvothermal treatment followed by calcination (Figure 4.16). Three different sets of MMTSs with different pore size distribution were prepared by simply adjusting the volume ratios (mL) of ethanol, H_2O and ammonia (10:20:0, 20:10:0 and 20:6:4) in the solvothermal fluid.

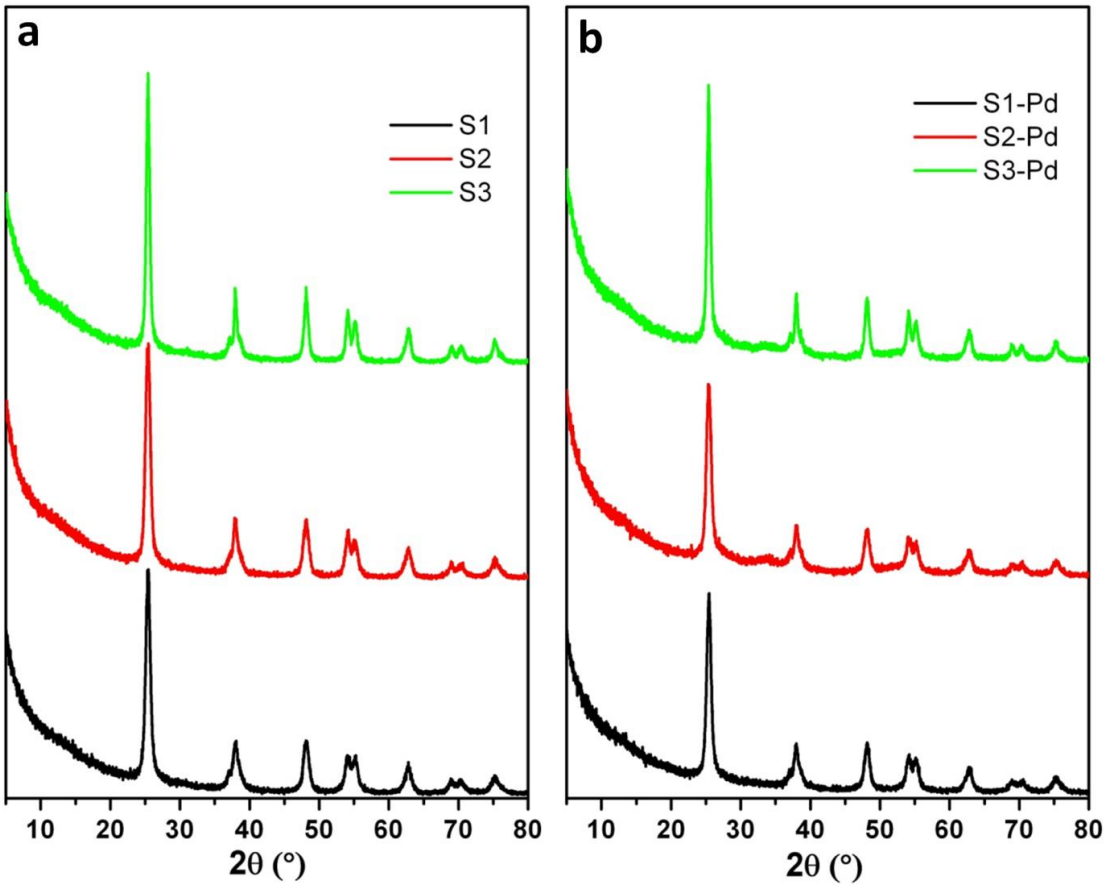

Figure 4.16. XRD patterns of a) the micrometer-sized mesoporous titania spheres obtained after solvothermal treatment and calcination of the precursor materials and b) the same spheres loaded with Pd nanoparticles. The patterns for S2, S3, S2-Pd and S3-Pd have been shifted up the intensity axis for clear comparison. The precursor titania spheres were prepared at a molar ratio of TIP:BuOH:HDA:H_2O:KCl = 1:222:1:6:0.011.

The MMTSs possessed narrow pore sizes ranging from 6.4 to 28.8 nm (Figure 4.17), pore volume from 0.11 to 0.45 cm^3 g^{-1} (Figure 4.18) and specific surface areas up to 118 m^2 g^{-1}.

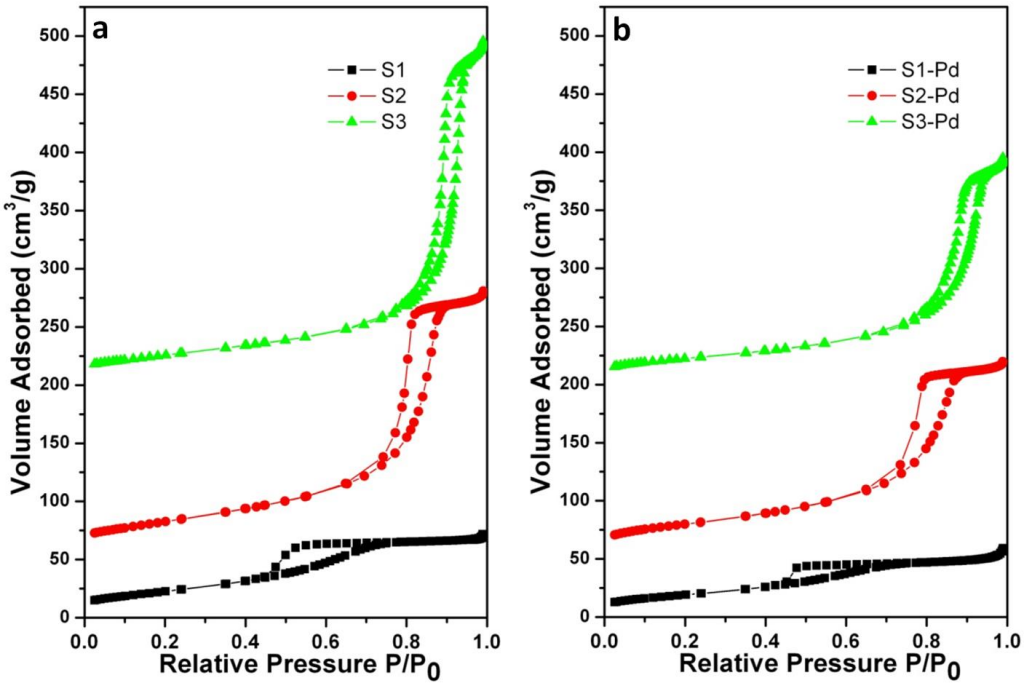

Figure 4.17. Nitrogen sorption isotherms of a) the micrometre-sized mesoporous titania spheres obtained after solvothermal treatment and calcination of the precursor materials and b) loaded with Pd nanoparticles. The isotherms of S2 and S2-Pd, and S3 and S3-Pd were shifted upwards by 50 and 200 cm^3 g^{-1}, respectively. The precursor titania spheres were prepared at a molar ratio of TIP:BuOH:HDA:H_2O:KCl = 1:222:1:6:0.011.

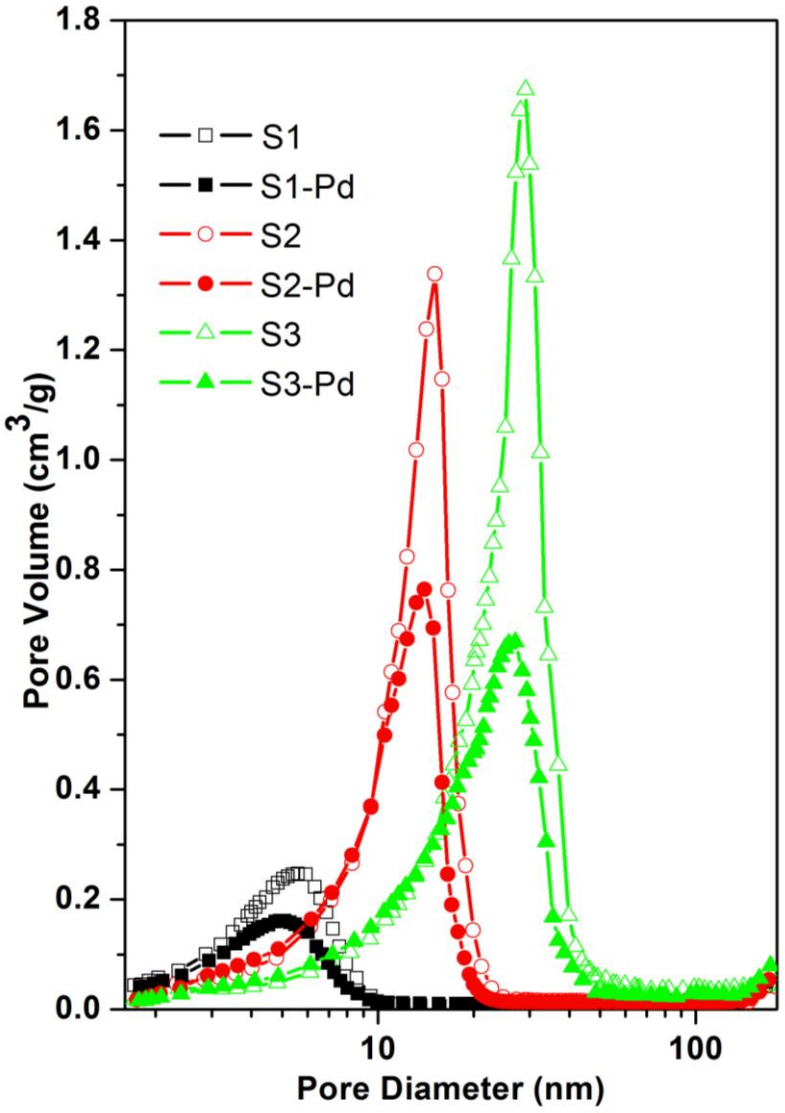

Figure 4.18. Pore diameter distributions of the micrometer-sized mesoporous titania spheres obtained after solvothermal treatment and calcination of the precursor materials and these spheres loaded with Pd nanoparticles. The precursor titania spheres were prepared at a molar ratio of TIP:BuOH:HDA:H_2O:KCl = 1:222:1:6:0.011.

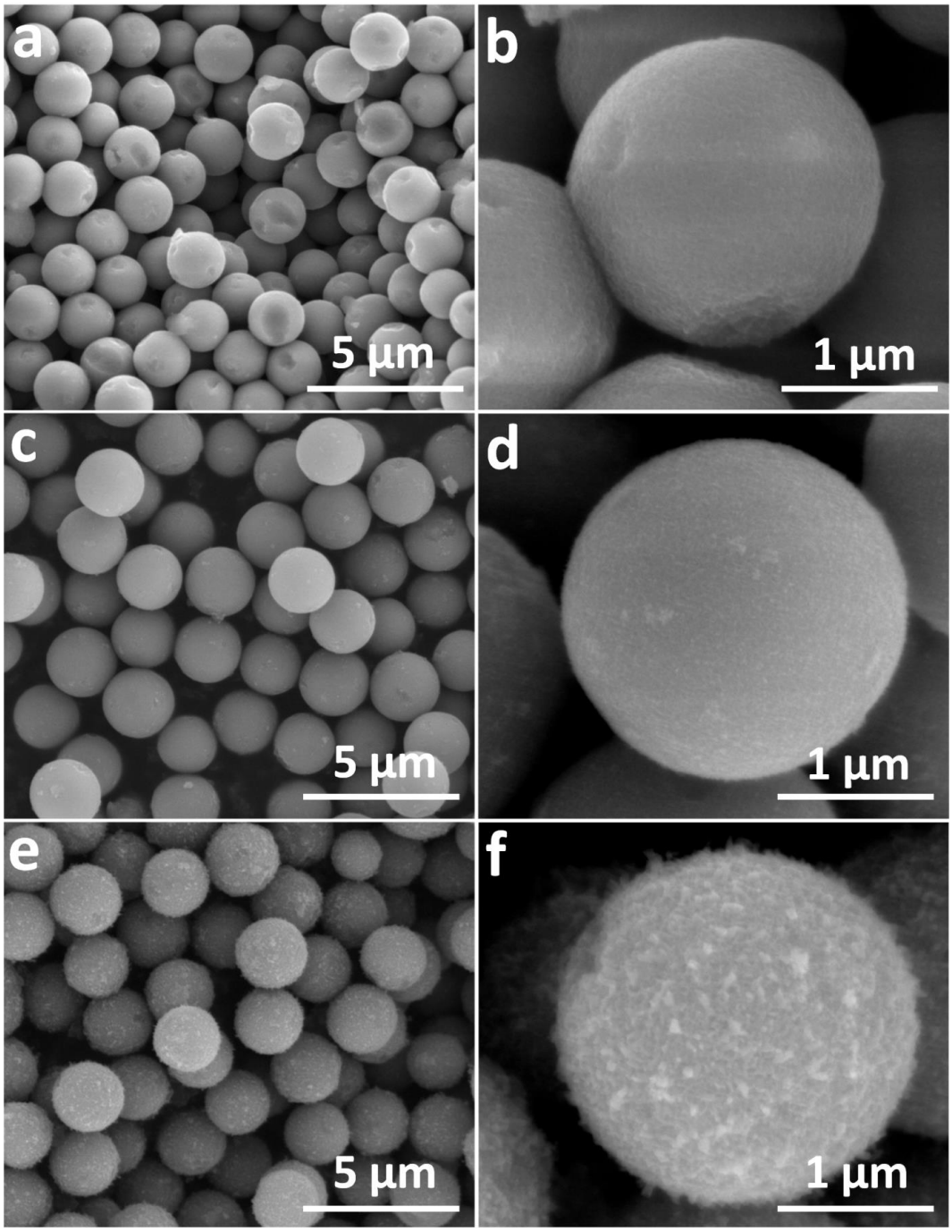

Figure 4.19. SEM images of a, b) S1, c, d) S2 and e, f) S3 micrometer-sized mesoporous titania spheres obtained after solvothermal treatment and calcination of the precursor materials. The precursor titania spheres were prepared at a molar ratio of TIP:BuOH:HDA:H_2O:KCl = 1:222:1:6:0.011.

Importantly, the final spheres maintained the uniformity of the precursor MATSs (compare Figure 4.19 with Figures 4.2c and 4.12b), and featured high densities of

hydroxyl groups on their surfaces (Table 4.1). After loading Pd nanoparticles of 3-5 nm size on the different mesoporous spheres via an *in situ* reduction procedure, the pore size, surface area, pore volume and porosity of the samples all dropped (Figure 4.17b, 4.18 and Table 4.1). It is probably due to pore blocking and/or filling, shielding of the surface, and Pd nanoparticles having a low surface area themselves. Additionally, the Pd nanoparticles were well-distributed on the TiO_2 particles, as observed by TEM (Figure 4.20).

Table 4.1. Physical properties of the micrometre-sized mesoporous TiO_2 spheres. The precursor titania spheres were prepared at a molar ratio of TIP:BuOH:HDA:H_2O:KCl = 1:222:1:6:0.011.

Sample name	*Surface area* $[m^2\ g^{-1}]$	*Pore diameter [nm]*	*Pore volume* $[cm^3\ g^{-1}]$	*Porosity (%)*	*OH group* $[nm^{-2}]$
MATS	2.4	N/A	0.005	N/A	N/A
S1	83	6.4	0.106	29	5.7
S1-Pd	69	5.0	0.085	25	N/A
S2	118	15.1	0.350	58	5.0
S2-Pd	108	14.0	0.258	50	N/A
S3	93	28.8	0.447	63	5.2
S3-Pd	81	26.6	0.293	53	N/A

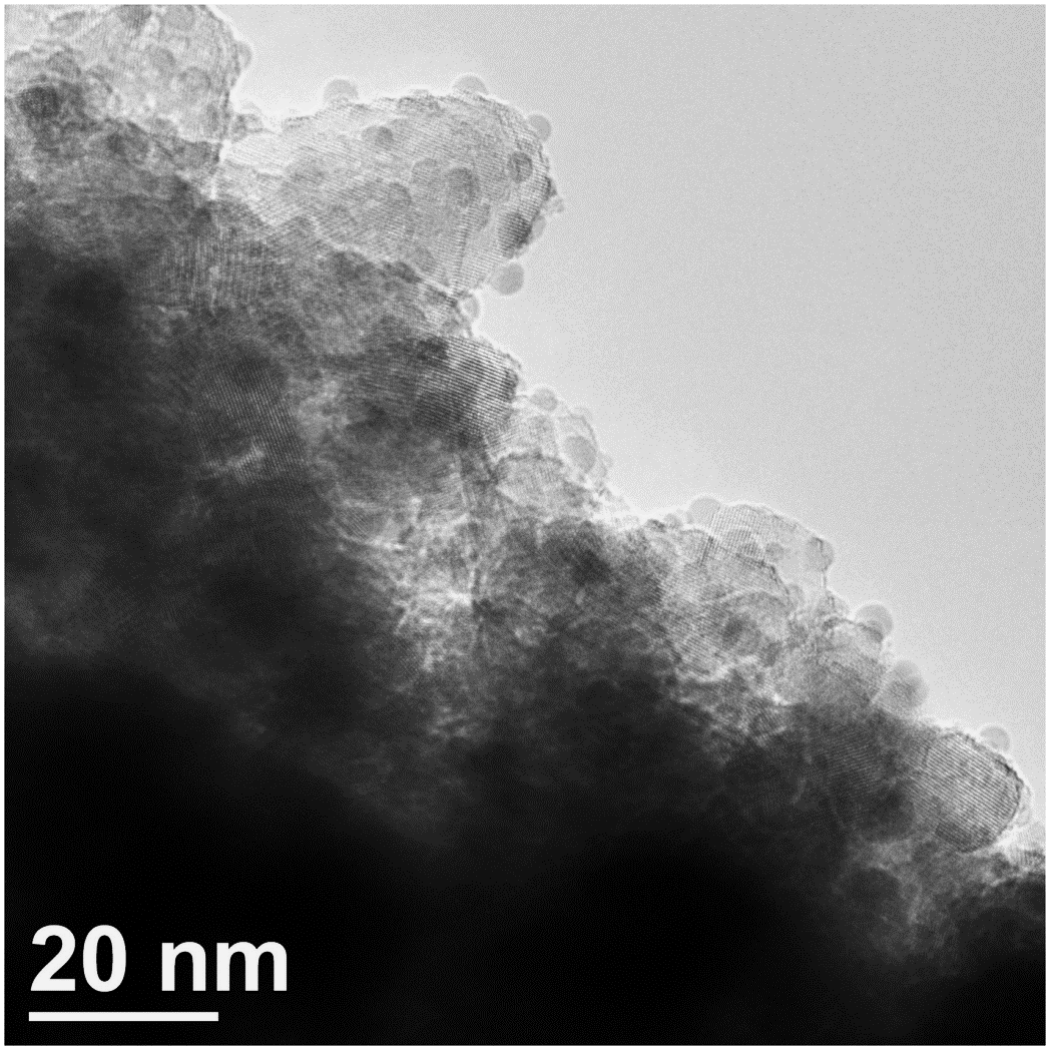

Figure 4.20. TEM image of the Pd/TiO_2 composite S2-Pd.

The reduction of 4-NP by $NaBH_4$ to 4-aminophenol (4-AP) was used as a model reaction to evaluate the performance of the Pd/TiO_2 catalyst system S2-Pd (observed spectroscopically, Figure 4.21), which was immobilized on a membrane instead of being dispersed in an aqueous solution. The calibration curve of 4-NP is shown in Figure 4.22.

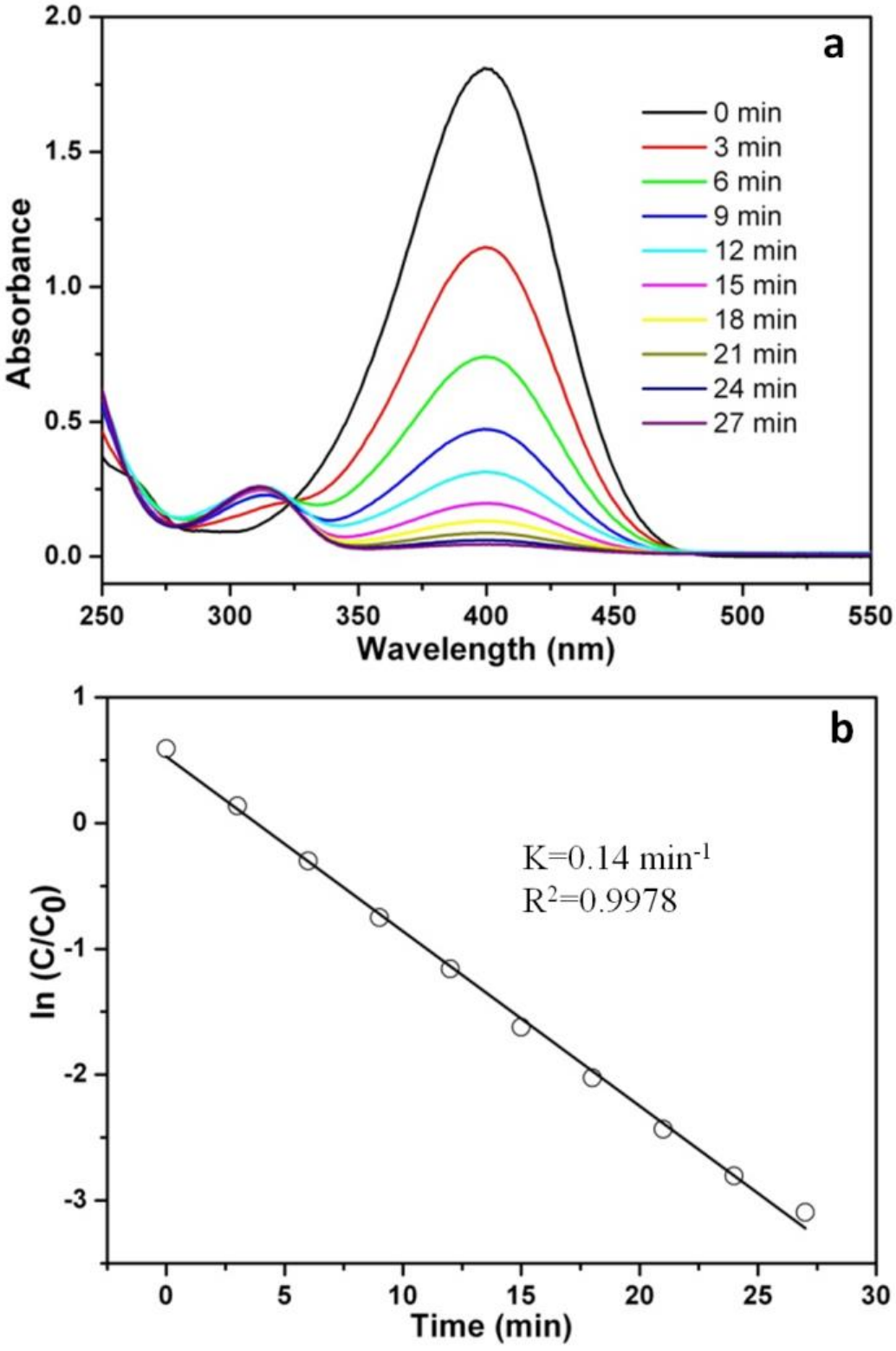

Figure 4.21. Catalytic reduction of 4-NP to 4-AP: a) time dependent absorption spectra of the reaction solution in the presence of the Pd/TiO_2 composite S2-Pd; b) plot of $[\ln(C/C_0)]$ against the reaction time for S2-Pd.

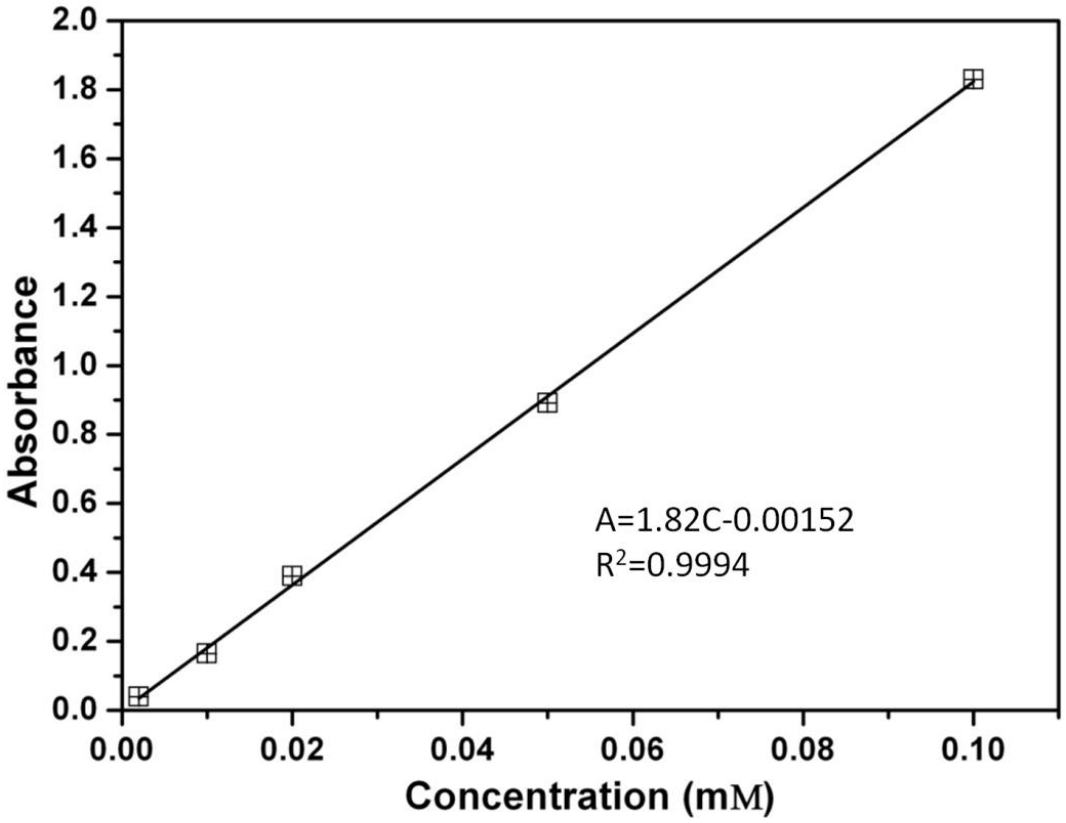

Figure 4.22. Calibration curve of 4-NP in a 20 mM $NaBH_4$ solution, showing the region where the Beer-Lambert Law is fully fitted.

Figure 4.21b shows the linear relationship between $\ln(C/C_0)$ and reaction time in the reduction catalyzed by sample S2-Pd, where C and C_0 are the reaction and initial 4-NP concentrations, respectively. Despite immobilization, the kinetic constant, *k*, was 0.14 min^{-1}, indicating that the Pd/TiO_2 system exhibited good catalytic efficiency. Conversely, without the catalytic Pd nanoparticles, the reduction proceeds very slowly, even with an excess amount of $NaBH_4$ for an extended period of time (Figure 4.23). When the catalyst was cycled for the reduction of 4-NP, the performance exceeded 88% for seven cycles (Figure 4.24), and still showed 73% conversion after ten successive cycles. Therefore, the Pd/TiO_2 not only possesses a high catalytic activity, but also shows good recycling ability.

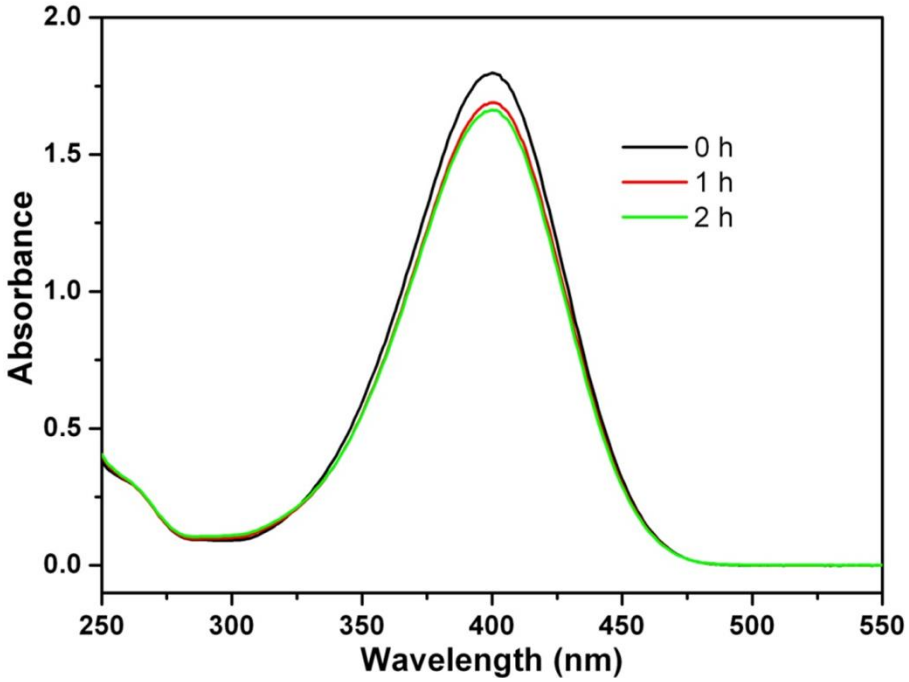

Figure 4.23. UV-Visible absorption spectra of 4-NP in the presence of S2 micrometer-sized mesoporous TiO_2 and $NaBH_4$ for 2 h.

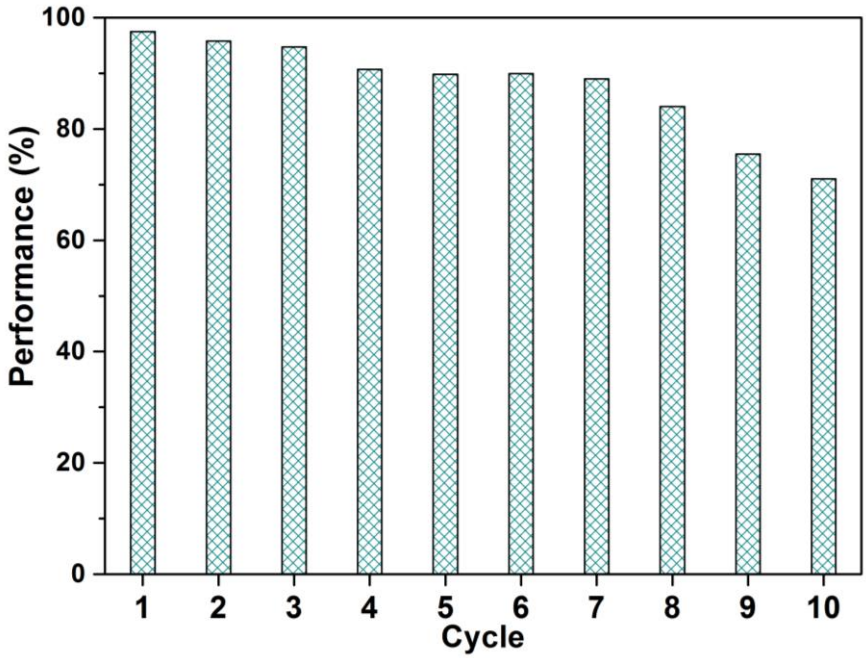

Figure 4.24. Conversion of 4-NP over 10 successive reduction cycles (of 27 min each) with the Pd/TiO_2 composite S2-Pd.

4.4 Conclusion

In summary, micrometer-sized, monodisperse, amorphous titania spheres were prepared via a facile sol-gel process. By tuning the solvent, salt species and concentration, HDA content, water amount, reaction temperature and titania source, the size of the resultant spheres was controllably varied (up to 5.39 μm).The size was determined by the number of nuclei formed, which depended on a competitive process between solubility of $Ti(OH)_4$ gel and hydrolysis rate of Ti (IV) source. High solubility and low hydrolysis rate result larger spheres. The precursor spheres readily converted into mesoporous titania spheres under solvothermal treatment. The resultant mesoporous spheres were used as catalyst supports for Pd nanoparticles. When used as a catalyst for the reduction reaction of 4-NP to 4-AP, the Pd/TiO_2 sample (S2-Pd) exhibited good catalytic activity and cyclability.

4.5 References

1. Rappsilber, J.; Mann, M.; Ishihama, Y., *Nat. Protoc.* **2007**, *2*, 1896-1906.
2. Winkler, J.; Marme, S., *J. Chromatography A* **2000**, *888*, 51-62.
3. Chen, J. S.; Tan, Y. L.; Li, C. M.; Cheah, Y. L.; Luan, D. Y.; Madhavi, S.; Boey, F. Y. C.; Archer, L. A.; Lou, X. W., *J. Am. Chem. Soc.* **2010**, *132*, 6124-6130.
4. Chen, D. H.; Huang, F. Z.; Cheng, Y. B.; Caruso, R. A., *Adv. Mater.* **2009**, *21*, 2206-2210.
5. Huang, F. Z.; Chen, D. H.; Zhang, X. L.; Caruso, R. A.; Cheng, Y. B., *Adv. Funct. Mater.* **2010**, *20*, 1301-1305.
6. Lee, J. S.; You, K. H.; Park, C. B., *Adv. Mater.* **2012**, *24*, 1084-1088.
7. Li, L.; Tsung, C. K.; Yang, Z.; Stucky, G. D.; Sun, L. D.; Wang, J. F.; Yan, C. H., *Adv. Mater.* **2008**, *20*, 903-908.
8. Yin, J. B.; Xiang, L. Q.; Zhao, X. P., *Appl. Phys. Lett.* **2007**, *90*.
9. Cheng, Y. C.; Guo, J. J.; Liu, X. H.; Sun, A. H.; Xu, G. J.; Cui, P., *J. Mater. Chem.* **2011**, *21*, 5051-5056.
10. Chen, D.; Jordan, E. H., *J. Sol-Gel Sci. Technol.* **2009**, *50*, 44-47.

11. Niu, F.; Jiang, Y.; Song, W. G., *Nano Res.* **2010**, *3*, 757-763.
12. Zhong, L. S.; Hu, J. S.; Cui, Z. M.; Wan, L. J.; Song, W. G., *Chem. Mater.* **2007**, *19*, 4557-4562.
13. Zhang, J.; Liu, X. H.; Wang, S. R.; Wu, S. H.; Cao, B. Q.; Zheng, S. H., *Powder Technol.* **2012**, *217*, 585-590.
14. Reddy, B. M.; Khan, A., *Catal. Rev. Sci. Eng.* **2005**, *47*, 257-296.
15. Seko, M.; Takeuchi, H.; Inada, T., *Industrial Eng. Chem. Product Res. Develop.* **1982**, *21*, 656-661.
16. Yan, B. W.; McNeff, C. V.; Carr, P. W.; McCormick, A. V., *J. Am. Ceram. Soc.* **2005**, *88*, 707-713.
17. Stober, W.; Fink, A.; Bohn, E., *J. Colloid Interface Sci.* **1968**, *26*, 62-69.
18. Liu, S. H.; Han, G. A.; Shu, M. H.; Han, L.; Che, S. N., *J. Mater. Chem.* **2010**, *20*, 10001-10009.
19. Chen, D. H.; Cao, L.; Huang, F. Z.; Imperia, P.; Cheng, Y. B.; Caruso, R. A., *J. Am. Chem. Soc.* **2010**, *132*, 4438-4444.
20. Eiden-Assmann, S.; Widoniak, J.; Maret, G., *Chem. Mater.* **2004**, *16*, 6-11.
21. Jiang, X. C.; Herricks, T.; Xia, Y. N., *Adv. Mater.* **2003**, *15*, 1205-1209.
22. Sugimoto, T.; Kojima, T., *J. Phys. Chem. C* **2008**, *112*, 18760-18771.
23. Kojima, T.; Sugimoto, T., *J. Phys. Chem. C* **2008**, *112*, 18445-18454.
24. Shiba, K.; Onaka, K.; Ogawa, M., *Rsc Adv.* **2012**, *2*, 1343-1349.
25. Han, C.; Luque, R.; Dionysiou, D. D., *Chem. Commun.* **2012**, *48*, 1860-1862.
26. Hong, M. P.; Kim, J. Y.; Vemula, K.; Kim, H. S.; Yoon, K. B., *Chem. Commun.* **2012**, *48*, 4250-4252.
27. Benkstein, K. D.; Kopidakis, N.; van de Lagemaat, J.; Frank, A. J., *J. Phys. Chem. B* **2003**, *107*, 7759-7767.
28. Mueller, R.; Kammler, H. K.; Wegner, K.; Pratsinis, S. E., *Langmuir* **2003**, *19*, 160-165.
29. Lerot, L.; Legrand, F.; Debruycker, P., *J. Mater. Sci.* **1991**, *26*, 2353-2358.

Chapter 5. Surface-Metastable Phase-Initiated Seeding and Ostwald Ripening: A Facile Fluorine-Free Process towards Spherical Fluffy Core/Shell, Yolk/Shell, and Hollow Anatase Nanostructures

5.1 Introduction

Hollow inorganic nanostructures have received recent attention because of their numerous promising applications and significant effort has been dedicated to developing facile and effective approaches for the fabrication of various hollow structures.[1-14] Among diverse synthesis approaches, Ostwald ripening[6, 15-19] has recently shown great versatility for the generation of a variety of hollow inorganic crystalline structures. Although this Ostwald ripening approach has explained the fabrication of numerous hollow materials with different compositions, direct evidence in support of this hollowing mechanism is lacking because most research investigated the hollow structures using conventional mass/thickness contrast TEM imaging technique with limited spatial resolution.

In this chapter, a novel surface metastable phase mediated synthesis strategy to fabricate spherical 'fluffy' core/shell, yolk/shell and hollow anatase nanostructures via a fluorine-free solvothermal process is shown. By systematically investigating the growth process using a range of characterization techniques (including SEM, ultramicrotomy, TEM, XRD, nitrogen gas sorption and TGA-DTA) unambiguous evidence relating to the surface seeding, crystal growth via Ostwald ripening and the subsequent hollowing process was observed. The presence of ammonia in the solvothermal step was paramount to the hollowing process as it retarded the direct crystallization from amorphous titania to anatase nanocrystals and promoted the formation of metastable ammonium titanate nanoflakes on the surfaces of the precursor particles. The anatase nanocrystals derived from the surface ammonium titanate intermediates acted as the seeds and initiated the Ostwald ripening process,[20, 21] and gave rise to anatase nanostructures with diverse complex morphologies. The resulting hollow anatase microspheres showed an enhanced photocatalytic activity over the commercial benchmark (P25 nanoparticles), indicating their potential for application in the photocatalysis field. This novel surface metastable phase mediated

synthesis strategy is an important step toward the facile and reproducible synthesis of a wide variety of functional hollow nanostructures with diverse composition or morphologies in future. This study has been published in *Angewandte Chemie International Edition* and the work was highlighted in 'Chemistry in Australia' magazine (Appendix 8.1) and chosen as “front cover” in PFPC 2014 Annual report (Appendix 8.2). The published manuscript and the supporting information are presented in section 5.2. Reprinted from “Surface-Metastable Phase-Initiated Seeding and Ostwald Ripening: A Facile Fluorine-Free Process towards Spherical Fluffy Core/Shell, Yolk/Shell, and Hollow Anatase Nanostructures. *Angew. Chem. Int. Ed*. **2013**, *52*, 10986-10991”, copyright (2013), with permission from John Wiley and Sons.

5.2 Manuscript (attached as below)

Mesoporous Materials

DOI: 10.1002/anie.201305819

Surface-Metastable Phase-Initiated Seeding and Ostwald Ripening: A Facile Fluorine-Free Process towards Spherical Fluffy Core/Shell, Yolk/Shell, and Hollow Anatase Nanostructures**

Lu Cao, Dehong Chen, and Rachel A. Caruso**

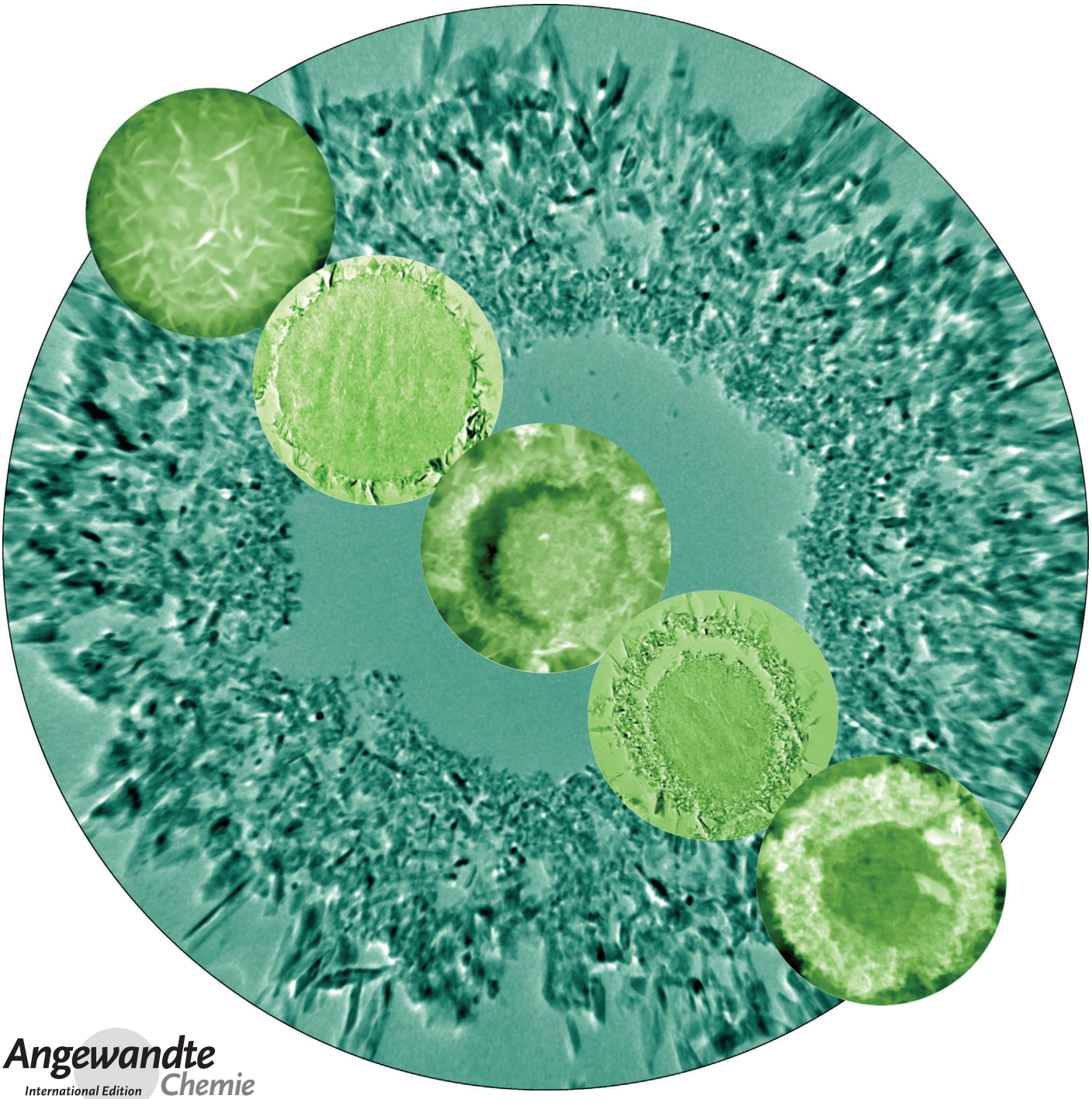

A wide variety of hollow inorganic nanostructures have received recent attention because of their promising applications including drug delivery, photocatalytic redox reactions and water splitting, clean energy conversion and storage, gas sensing, and heavy-metal ion sequestration.[1] Significant effort has been dedicated to developing facile and effective approaches for the fabrication of various hollow structures with sophisticated architectures and varied compositions.[1a–d,2] Among the diverse synthesis approaches (e.g. templating synthesis, Kirkendall diffusion process, Galvanic replacement method), Ostwald ripening,[2f,g,3] a well-known physical phenomenon, has recently shown great versatility for the generation of diverse hollow inorganic crystalline structures on micro-/submicrometer scales.[2f,g,4] For this approach, it is generally believed that the central crystallites with relatively small sizes would have a strong tendency to dissolve into solution, and then be subsequently relocated to the particle surface by a recrystallization process, thus giving rise to nanostructures with hollow interior spaces. The ultimate architecture of the interior space highly depends on the packing of the initial crystalline aggregates prior to the Ostwald ripening process.[2f,g]

Although this template-free Ostwald ripening approach has explained the fabrication of numerous different hollow materials,[2f,g,3–5] direct evidence in support of this formation mechanism is lacking because most research investigated these hollow structures using conventional mass/thickness contrast obtained using TEM.[2f,g,3,4] Because of the relatively large size (usually >200 nm) of the nanostructures and the overlap of the shell from both sides of the sample in the image, the detailed architecture (e.g. crystal size, morphology, uniformity, packing manner, porosity and thickness) of the shell layers could not be resolved using conventional TEM characterization. Thus, unambiguous evidence relating to the seeding (formation of crystalline nanoparticles on the surfaces), crystal growth through Ostwald ripening (formation of larger crystals at the expense of smaller counterparts) and the subsequent hollowing process has not been available.

As an important material with numerous practical applications and industrial interest, titania has attracted significant attention since its commercial production in the early 20th century.[6] The Ostwald ripening process has been applied to synthesize diverse hollow titania nanostructures,[2f,g,4a,b,5] however, the fabrication process usually involves the participation of various fluorides (e.g. TiF_4),[4a,b,5] which produces highly corrosive and toxic hydrofluoric acid (HF) during the synthesis. Extra care and protection is essential in handling HF acid, thus decreasing the practicality of this synthesis approach. Therefore a fluorine-free and effective process for the fabrication of diverse hollow titania nanostructures would be desirable, especially for the potential large-scale production of these nanostructures. We demonstrate herein a facile and versatile fluorine-free solvothermal process to fabricate anatase nanostructures with diverse sophisticated morphologies, including spherical "fluffy" core/shell, yolk/shell, and hollow nanostructures. A metastable phase on the surface of the spheres initiated seeding and the Ostwald ripening process, as determined from a range of characterization techniques that revealed the morphological evolution and crystallization process occurred in the presence of an ammonia solution.

These nanostructures were synthesized using a facile one-pot solvothermal crystallization process featuring three stepwise reaction stages as shown in Scheme 1. The experimental details of the synthesis and characterization of these samples can be found in the Supporting Information. This solvothermal crystallization proceeded in the presence of 21.3 wt% ammonia solution within an autoclave heated at 160 °C and no fluorine species were required during the synthesis. After calcination at temperatures over 500 °C in air, the amorphous titania cores of the intermediates can be readily converted into particulate anatase counterparts without damaging the overall morphologies, thus enabling a facile and scalable approach for fabricating spherical "fluffy" core/shell, yolk/shell, and hollow anatase nanostructures.

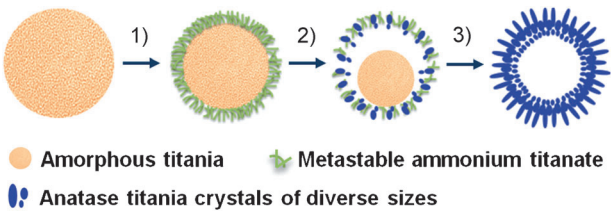

Scheme 1. Formation process of diverse titania/titanate nanostructures: 1) precipitation of a metastable phase, ammonium titanate nanoflakes, on the surfaces of amorphous titania microspheres using an energy-favored heteronucleation process, producing a "fluffy" core/shell-structured intermediate; 2) phase transformation of the metastable ammonium titanate nanoflakes to anatase nanocrystals occurred in the shell layer of the intermediate microsphere whereas the core remained amorphous, which subsequently initiated an Ostwald ripening process and gave rise to the yolk/shell nanostructures; and 3) formation of self-supported porous shells consisting of faceted anatase nanocrystals with a gradient in size using the Ostwald ripening process.

[*] L. Cao, Dr. D. H. Chen, Prof. R. A. Caruso
Particulate Fluids Processing Centre, School of Chemistry
The University of Melbourne
Victoria 3010 (Australia)
E-mail: dehongc@unimelb.edu.au
rcaruso@unimelb.edu.au
Prof. R. A. Caruso
CSIRO Materials Science and Engineering
Private Bag 33, Clayton South, Victoria 3169 (Australia)

[**] This research was financially supported by an Australian Research Council Discovery Project (grant number DP110101346). L.C. acknowledges the support of an Australian Postgraduate Award and MMI-CSIRO PhD Materials Science Top-up. R.A.C. is a recipient of an Australian Research Council Future Fellowship (grant number FT0990583). Dr. Simon Crawford is thanked for ultramicrotoming samples in preparation for TEM characterization. Dr. Xiaofei Duan and Mr David Parris are appreciated for acquiring XPS and XRD results, respectively. The Advanced Microscopy Facility and Surface and Chemical Analysis Network (SCAN) at the University of Melbourne are acknowledged for electron microscopy and XPS access, respectively.

Supporting information for this article is available on the WWW under http://dx.doi.org/10.1002/anie.201305819.

To illustrate the formation mechanism of these titania nanostructures, an investigation using SEM, TEM, XRD, and thermogravimetric/differential thermal analysis (TGA/DTA) was conducted to monitor the morphological evolution and crystallization process as a function of the solvothermal treatment time. SEM images of the precursor microspheres and the solvothermally treated counterparts (prior to calcination) at varied intervals (0, 16, 24, and 48 h) are shown in Figure 1. In conjunction with the SEM images showing detailed surface features of the microspheres, these samples

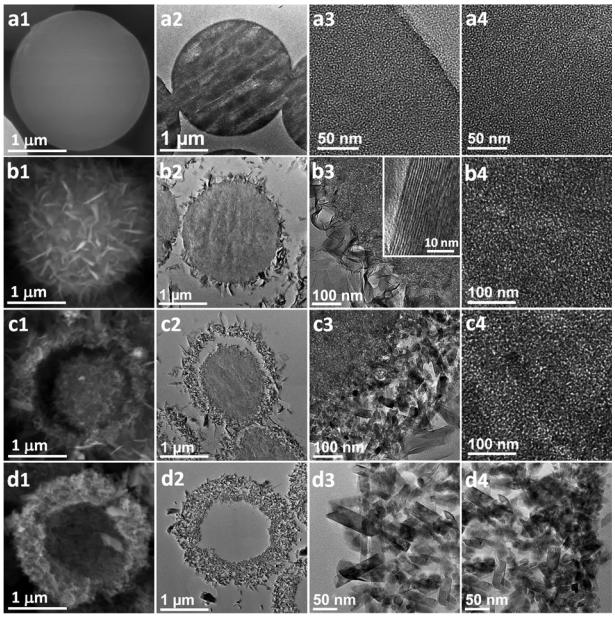

Figure 1. SEM and TEM (ultramicrotomed sections) images of the amorphous precursor microspheres (a1–a4) and solvothermally treated titania microspheres (prior to calcination) obtained with varying solvothermal times: 16 h for amorphous titania/ammonium titanate core/shell structures (b1–b4, the inset in b3 shows a high-resolution TEM image of the ammonium titanate nanosheets); 24 h for amorphous titania/anatase yolk/shell structures (c1–c4); and 48 h for anatase hollow microspheres (d1–d4). Images shown in a3, b3, and c3 and those in a4, b4, and c4 display the edge and the core sections of the titania microspheres, respectively. d3 and d4 images show parts of the outer and inner shell of the anatase hollow structure, respectively. Note: SEM images were taken without sputter coating.

were ultramicrotomed to about 90 nm thick sections and analyzed using TEM to investigate the porous shells and interior core structures. Precursor microspheres possess fairly smooth surfaces (Figure 1 a1 and Figure S1a in the Supporting Information), indicating they consist of ultrafine primary particles. These precursor microspheres have wormhole-like mesostructures throughout the whole particle (Figure 1 a3 surface and 1 a4 core) and are amorphous at atomic scale as identified by the corresponding XRD pattern (Figure S1m) and diffuse selected-area electron diffraction (SAED) pattern (Figure S2a). After solvothermal treatment at 160 °C for 2 h, microspheres covered with a few thin sheetlike nanostructures are observed (Figure S1c,d). The corresponding XRD pattern demonstrates that these microspheres are still amorphous (Figure S1m). Progressively more sheetlike nanostructures formed on the surfaces of the microspheres when prolonging the solvothermal time to 4 and 16 h (Figure S1e–h). After 4 h, an obvious diffraction peak around $2\theta = 9.8°$ appeared in the corresponding XRD pattern (Figure S1m). By further increasing the solvothermal treatment time to 16 h, this low-angle diffraction peak became more distinct along with the appearance of three other diffraction peaks around $2\theta = 27.6$, 48.1, and 62.9°. All these diffraction peaks are associated with the sheetlike nanostructures covered on the surfaces of the microspheres and can be ascribed to the formation of ammonium titanate,[7] a lamellar titanate intercalated with ammonium cations between TiO_6 octahedra layers. For the microspheres solvothermally treated for 16 h (Figure 1 b1), a "fluffy" amorphous titania/ammonium titanate core/shell nanostructure was obtained. The corresponding SEM and TEM images (Figure 1 b1, 1 b2, and 1 b3) clearly show that the titanate nanoflakes are attached to the surfaces of the spherical particle. These nanosheets have an interlayer spacing of about 0.80 nm (inset in Figure 1 b3), which is close to the interplanar distance of the (200) plane of the ammonium titanate,[7b] further confirming the formation of such a metastable intermediate phase. As shown in Figure 1 b4, this "fluffy" core/shell nanostructure possessed an amorphous core featuring the wormholelike mesostructure. With increased reaction time (24 h), shown in Figure 1 c1 and 1 c2, the cores shrank, producing unique yolk/shell nanostructures. Such yolk/shell nanostructures possess an intermeshed particulate shell consisting of both ammonium titanate nanosheets and anatase nanocrystals (Figure 1 c1–c3), while retaining a mesostructured amorphous yolk (Figure 1 c4). The crystal phase of these yolk/shell nanostructures was determined by the corresponding XRD pattern (Figure S1m), in which a reduced peak intensity in ammonium titanate phase and the occurrence of additional diffraction peaks around $2\theta = 25.6$, 38.1, 48.1, and 62.9° are observed. These newly appearing peaks can be indexed to the (101), (004), (200), and (204) planes of the anatase titania, respectively, indicating the occurrence of a gradual phase transformation from ammonium titanate to anatase titania.[7c] Further increasing the solvothermal treatment to 48 h gives rise to anatase microspheres with completely hollow interiors (Figure 1 d1, 1 d2, and Figure S1k). These hollow microspheres have a porous shell of about 550 nm in thickness and an inner cavity of about 1200 nm in diameter. The shells are mainly composed of faceted rodlike nanocrystals with a length ranging from 10 to 300 nm, and relatively small anatase crystals primarily gathered on the inner surfaces of the hollow spheres. The corresponding XRD pattern (Figure S1 m) revealed that these nanocrystals are well-crystallized anatase-phase titania.

The presence of amorphous titania in the core regions of the microspheres solvothermally treated for less than 24 h is also supported by the corresponding DTA results (Figure S3a). The sharp exothermic peaks centered at 472 °C, which can be mainly ascribed to the crystallization from amorphous to anatase titania,[8] were clearly observed for the microspheres solvothermally treated for 2 and 16 h. This exothermic peak became less defined for the microspheres

solvothermally treated for 24 h because of the decrease in the amorphous titania core content. When prolonging the solvothermal time to 48 h, no obvious exothermic peak was observed on the corresponding DTA curve (Figure S3a), suggesting that the amorphous phase in these microspheres has been fully converted to anatase during the solvothermal crystallization. The overall weight loss of the solvothermally treated samples decreased with increasing solvothermal treatment time as shown in the TGA curves (Figure S3b). This indicates that the microspheres gradually became less hydrated and the organic residue content decreased with increasing solvothermal treatment time.

The above SEM, TEM, XRD, and TGA-DTA results clearly indicate that 1) sheetlike ammonium titanate, an intermediate phase, formed and kept growing on the outer surfaces of the microspheres during the early stage (<16 h) of the solvothermal process, 2) being a metastable phase, this ammonium titanate can be readily transformed into anatase with further solvothermal heating (≥ 24 h), and 3) the anatase nanocrystals formed on the shell layers of the spherical particles acted as the seeds and initiated the well-known Ostwald ripening process towards the formation of hollow anatase microspheres. This is different to most of the previous published articles in which the hollowing process is generally suggested to start from the center of the spherical particles.[2f,g,4a] The hollowing process, as evidenced by the TEM images of the ultramicrotomed sample sections, occurred initially from the surfaces just underneath the crystalline shell layer and it proceeded inwardly at the expense of the interior amorphous core.

To understand the role of ammonia in the formation of these hollow titania nanostructures, a control experiment was conducted by replacing the ammonia solution with water under otherwise identical conditions. As shown in Figure S4a–m, the resulting microspheres were composed of ultrafine anatase nanocrystals. The high-magnification TEM images (Figure S4e,f or k, l) indicate that the nanocrystals are nearly identical in size throughout the whole particle when ammonia was not present. Because of the absence of obvious difference in crystal size between the shell layers and the core regions of these microspheres, the Ostwald ripening process was less likely to be trigged to form the hollow spheres in this case.

The "fluffy" core/shell intermediates (solvothermally treated for 16 h) and the yolk/shell nanostructures (solvothermally treated for 24 h) can be readily converted to anatase counterparts without changing the overall morphologies during calcination. Figure 2 displays SEM and TEM images of these anatase nanostructures calcined at 650 °C for 2 h in air. "Fluffy" core/shell anatase nanostructures (Figure 2 a,b and Figure S5a,b) were covered by thin sheetlike nanostructures on the outer surfaces. As illustrated by a broken microsphere, Figure S5b, the core of the microsphere is composed of granular nanocrystals. This result is also confirmed by the corresponding TEM images shown in Figure S5c and S5d, in which a homogeneous particulate network consisting of about 20 nm crystals is clearly observed throughout the whole core of the sliced sample. Elongated nanocrystals surrounding this core (Figure S5c) correspond to

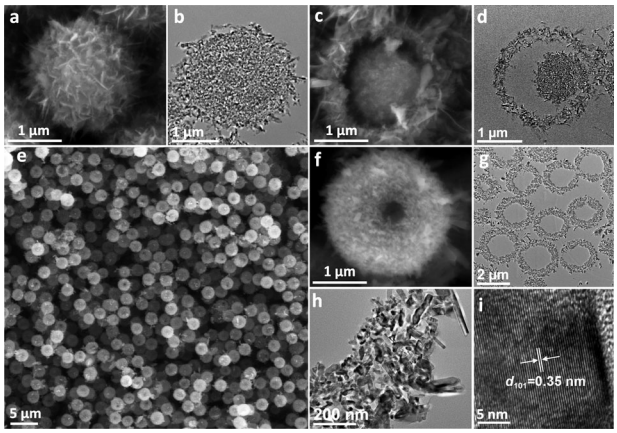

Figure 2. SEM and TEM (ultramicrotomed sections) images of the calcined "fluffy" core/shell anatase microspheres (a, b, Solvo-16 h-Cal), yolk/shell anatase microspheres (c, d, Solvo-24 h-Cal) and hollow anatase microspheres (e–i, Solvo-48 h-Cal), i) high resolution TEM images of a typical rodlike nanocrystal indicating its high crystallinity and oriented elongation along the [001] direction. Note: SEM images were taken without sputter coating.

the sheetlike nanostructures. Anatase nanostructures with yolk/shell structure are shown in Figure 2 c and 2 d. In this case, the shells consist of a mixture of sheetlike and elongated nanocrystals (Figure 2 c and Figure S6), while the yolks are spherical assemblies of nanocrystals (Figure 2 d). The resulting nanostructures are monodisperse entities, for example, the hollow anatase microspheres (shown in Figure 2 e) possess an average diameter of 2.3 ± 0.1 μm based on analysis of 240 entities (shown in Figure S7). A typical high-magnification SEM image, as shown in Figure 2 f, clearly reveals the rough surface feature and the presence of a void (about 380 nm in diameter) on the surface. As confirmed by the corresponding TEM analysis (Figure 2 g), these titania microspheres possess hollow chambers and uniform shells of about 550 nm in thickness (Figure 2 g and h). The shells are mainly composed of faceted rodlike nanocrystals with a length ranging from 10 to 300 nm. The corresponding high-resolution TEM image (Figure 2 i) shows continuous lattice fringes throughout the whole nanocrystal to the edges, indicating a high crystallinity of the products. Spacing between the lattice fringes of the nanocrystals was measured to be 0.35 nm, which corresponds to the spacing of (101) planes of the anatase phase (JCPDS card No. 21-1272), indicating an oriented elongation of the crystal along the [001] direction.

XRD studies were carried out to investigate the crystal phase and crystallinity of these calcined products. As illustrated in Figure S8a, XRD patterns of these calcined microspheres can be assigned to the anatase phase of titania. The diffraction peaks become sharper when the solvothermal treatment time was prolonged from 16 to 24 h, and to 48 h, indicating formation of larger anatase crystals with enhanced crystallinity by increasing the solvothermal treatment time. An X-ray photoelectron spectroscopy (XPS) survey and high-resolution spectra analysis were performed to further investigate surface compositions and crystallinity of the resulting nanostructures (Figure S8b and S9). The high-resolution Ti2p

XPS spectra shown in Figure S8b further confirming an enhanced crystallinity of the resulting products.[9]

The photocatalytic activity of these calcined microspheres was evaluated by the photodegradation of methylene blue (MB), a probe molecule, under UV light irradiation. For comparison, the photocatalytic activity of nanoparticles of Degussa P25, a well-known highly efficient titania photocatalyst, was also measured under the same conditions. Figure S10 represents a time profile of the MB absorption spectra recorded in the presence of hollow anatase microspheres exposed to UV light. To compare the reaction kinetics of the MB degradation, a pseudo-first-order reaction rate equation was used ($\ln(C/C_0) = k\,t$, where C and C_0 refer to the concentration of MB at the irradiation time t and 0 minutes, k and t are the reaction rate constant and photodegradation time, respectively). As shown in Figure 3, the plots are linear

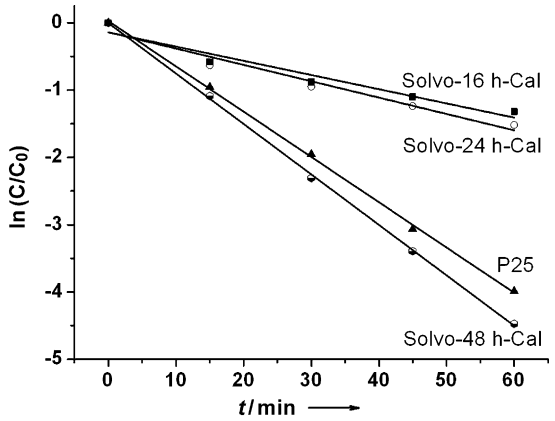

Figure 3. Photocatalytic degradation of methylene blue in the presence of calcined "fluffy" core/shell anatase microspheres, yolk/shell anatase microspheres, hollow anatase microspheres, and Degussa P25 nanoparticles.

indicating a fit with the pseudo-first-order reaction kinetics, and the degradation of MB improved with increasing solvothermal treatment time (from 16 to 48 h). The hollow anatase microspheres show a much higher degradation rate ($k = 0.0750\ \text{min}^{-1}$) than those microspheres with either "fluffy" core/shell structure (Solvo-16 h-Cal, $k = 0.0211\ \text{min}^{-1}$) or yolk/shell structure (Solvo-24 h-Cal, $k = 0.0243\ \text{min}^{-1}$). The hollow anatase microspheres display higher photocatalytic performance than that of the Degussa P25 nanoparticles ($k = 0.0673\ \text{min}^{-1}$) even though these hollow microspheres possess lower surface area ($41\ \text{m}^2\,\text{g}^{-1}$, Figure S11) compared to that of the Degussa P25 ($50\ \text{m}^2\,\text{g}^{-1}$). UV/Vis diffuse reflectance spectra and plots of the Kubelka–Munk function (i.e., relationship of $[F(R)h\nu]^{1/2}$ versus photon energy) to determine the bandgaps of these titania photocatalysts are shown in Figure S12a and S12b. The anatase microspheres have relatively narrow bandgaps (3.25 eV for Solvo-16 h-Cal and Solvo-24 h-Cal and 3.27 eV for Solvo-48 h-Cal sample) compared with the Degussa P25 nanoparticles (3.36 eV). Among the above titania photocatalysts, the hollow anatase microspheres possesses the lowest surface area ($41\ \text{m}^2\,\text{g}^{-1}$), however, this sample presents the best photocatalytic activity. The superior photocatalytic activity of these anatase hollow structures could be speculated to be due to the following synergistic effects: 1) the unique hollow structure could cause multireflection of the light once the incident light has entered into the interior spherical chamber (like a spherical integrating chamber), thus maximizing the light harvesting and utilization efficiency;[10] 2) the hierarchically porous shells provide numerous diffusion paths for the pollutants to travel throughout the material and promote accessibility to the active surface sites;[11] 3) the intermeshed networks of the shells and enhanced crystallinity, as confirmed by corresponding XRD, XPS, and HRTEM results, could reduce the recombination rate of the photogenerated electrons and holes and prolong the electron lifetimes and diffusion lengths, therefore improving the overall photocatalytic activity.[6d,12]

In summary, a versatile fluorine-free approach has been demonstrated for structural and morphological engineering of anatase nanomaterials and gave rise to spherical "fluffy" core/shell, yolk/shell, and hollow anatase nanostructures using a facile one-pot solvothermal process. The ammonia present in the synthesis solution retarded the direct crystallization from amorphous titania to anatase nanocrystals and promoted the formation of metastable ammonium titanate nanoflakes on the surfaces of the precursor particles. The anatase nanocrystals derived from the ammonium titanate intermediates on the surface acted as the seeds and initiated the Ostwald ripening process, and thus gave rise to anatase nanostructures with diverse complex morphologies. The resulting hollow anatase microspheres showed an enhanced photocatalytic activity over the commercial P25 nanoparticles. It is believed that this novel surface-based, metastable phase-mediated synthesis strategy could be extended to the fabrication of a wide variety of functional hollow nanostructures with diverse composition or morphologies in future.

Received: July 5, 2013
Published online: August 23, 2013

Keywords: mesoporous materials · nanostructures · photochemistry · solvothermal synthesis · titanates

[1] a) X. W. Lou, L. A. Archer, Z. C. Yang, *Adv. Mater.* **2008**, *20*, 3987–4019; b) J. Hu, M. Chen, X. S. Fang, L. W. Wu, *Chem. Soc. Rev.* **2011**, *40*, 5472–5491; c) X. Lai, J. Li, B. A. Korgel, Z. Dong, Z. Li, F. Su, J. Du, D. Wang, *Angew. Chem.* **2011**, *123*, 2790–2793; *Angew. Chem. Int. Ed.* **2011**, *50*, 2738–2741; d) L. Zhou, D. Y. Zhao, X. W. Lou, *Angew. Chem.* **2012**, *124*, 243–245; *Angew. Chem. Int. Ed.* **2012**, *51*, 239–241; e) X. M. Sun, Y. D. Li, *Angew. Chem.* **2004**, *116*, 3915–3919; *Angew. Chem. Int. Ed.* **2004**, *43*, 3827–3831.

[2] a) Y. G. Sun, Y. N. Xia, *Science* **2002**, *298*, 2176–2179; b) Y. G. Sun, B. T. Mayers, Y. N. Xia, *Nano Lett.* **2002**, *2*, 481–485; c) Y. D. Yin, R. M. Rioux, C. K. Erdonmez, S. Hughes, G. A. Somorjai, A. P. Alivisatos, *Science* **2004**, *304*, 711–714; d) F. Caruso, R. A. Caruso, H. Mohwald, *Science* **1998**, *282*, 1111–1114; e) Q. Zhang, W. S. Wang, J. Goebl, Y. D. Yin, *Nano Today* **2009**, *4*, 494–507; f) H. C. Zeng, *J. Mater. Chem.* **2011**, *21*, 7511–7526; g) H. C. Zeng, *Curr. Nanosci.* **2007**, *3*, 177–181; h) Y.

Chen, H. Chen, L. Guo, Q. He, F. Chen, J. Zhou, J. Feng, J. Shi, *ACS Nano* **2010**, *4*, 529 – 539.
[3] D. P. Wang, H. C. Zeng, *Chem. Mater.* **2011**, *23*, 4886 – 4899.
[4] a) H. G. Yang, H. C. Zeng, *J. Phys. Chem. B* **2004**, *108*, 3492 – 3495; b) J. H. Pan, X. W. Zhang, A. J. Du, D. D. Sun, J. O. Leckie, *J. Am. Chem. Soc.* **2008**, *130*, 11256 – 11257; c) B. Wang, H. B. Wu, L. Zhang, X. W. Lou, *Angew. Chem.* **2013**, *125*, 4259 – 4262; *Angew. Chem. Int. Ed.* **2013**, *52*, 4165 – 4168; d) A. Pan, H. B. Wu, L. Yu, X. W. Lou, *Angew. Chem.* **2013**, *125*, 2282 – 2286; *Angew. Chem. Int. Ed.* **2013**, *52*, 2226 – 2230; e) X. W. Lou, Y. Wang, C. L. Yuan, J. Y. Lee, L. A. Archer, *Adv. Mater.* **2006**, *18*, 2325 – 2329.
[5] J. Li, H. C. Zeng, *J. Am. Chem. Soc.* **2007**, *129*, 15839 – 15847.
[6] a) X. Chen, S. S. Mao, *Chem. Rev.* **2007**, *107*, 2891 – 2959; b) D. H. Chen, F. Z. Huang, Y. B. Cheng, R. A. Caruso, *Adv. Mater.* **2009**, *21*, 2206 – 2210; c) D. H. Chen, R. A. Caruso, *Adv. Funct. Mater.* **2013**, *23*, 1356 – 1374; d) F. Sauvage, D. H. Chen, P. Comte, F. Z. Huang, L. P. Heiniger, Y. B. Cheng, R. A. Caruso, M. Graetzel, *ACS Nano* **2010**, *4*, 4420 – 4425; e) D. H. Chen, F. Z. Huang, L. Cao, Y. B. Cheng, R. A. Caruso, *Chem. Eur. J.* **2012**, *18*, 13762 – 13769; f) D. H. Chen, L. Cao, F. Z. Huang, P. Imperia, Y. B. Cheng, R. A. Caruso, *J. Am. Chem. Soc.* **2010**, *132*, 4438 – 4444.
[7] a) C. H. Rhee, J. S. Lee, S. H. Chung, *J. Mater. Res.* **2005**, *20*, 3011 – 3020; b) B. Zhao, F. Chen, X. N. Gu, J. L. Zhang, *Chem. Asian J.* **2010**, *5*, 1546 – 1549; c) B. Zhao, F. Chen, Y. C. Jiao, J. L. Zhang, *J. Mater. Chem.* **2010**, *20*, 7990 – 7997.
[8] T. Sugimoto, T. Kojima, *J. Phys. Chem. C* **2008**, *112*, 18760 – 18771.
[9] J. Biener, E. Farfan-Arribas, M. Biener, C. M. Friend, R. J. Madix, *J. Chem. Phys.* **2005**, *123*, 094705.
[10] a) H. X. Li, Z. F. Bian, J. Zhu, D. Q. Zhang, G. S. Li, Y. N. Huo, H. Li, Y. F. Lu, *J. Am. Chem. Soc.* **2007**, *129*, 8406 – 8407; b) X. F. Chen, J. B. Liu, H. Wang, Y. L. Ding, Y. X. Sun, H. Yan, *J. Mater. Chem. A* **2013**, *1*, 877 – 883; c) Z. H. Dong, X. Y. Lai, J. E. Halpert, N. L. Yang, L. X. Yi, J. Zhai, D. Wang, Z. Y. Tang, L. Jiang, *Adv. Mater.* **2012**, *24*, 1046 – 1049; d) X. Wang, M. Y. Liao, Y. T. Zhong, J. Y. Zheng, W. Tian, T. Y. Zhai, C. Y. Zhi, Y. Ma, J. N. A. Yao, Y. Bando, D. Golberg, *Adv. Mater.* **2012**, *24*, 3421 – 3425.
[11] a) W. Li, Y. Deng, Z. Wu, X. Qian, J. Yang, Y. Wang, D. Gu, F. Zhang, B. Tu, D. Zhao, *J. Am. Chem. Soc.* **2011**, *133*, 15830 – 15833; b) X. C. Wang, J. C. Yu, C. M. Ho, Y. D. Hou, X. Z. Fu, *Langmuir* **2005**, *21*, 2552 – 2559; c) J. G. Yu, Y. R. Su, B. Cheng, *Adv. Funct. Mater.* **2007**, *17*, 1984 – 1990.
[12] a) J. B. Joo, Q. Zhang, M. Dahl, I. Lee, J. Goebl, F. Zaera, Y. D. Yin, *Energy Environ. Sci.* **2012**, *5*, 6321 – 6327; b) J. B. Joo, I. Lee, M. Dahl, G. D. Moon, F. Zaera, Y. D. Yin, *Adv. Funct. Mater.* **2013**, DOI: 10.1002/adfm.201300255; c) Z. Zhang, Y. Zhou, Y. Zhang, S. Zhou, J. Shi, J. Kong, S. Zhang, *Dalton Trans.* **2013**, *42*, 5004 – 5012.

Angewandte Chemie
Eine Zeitschrift der Gesellschaft Deutscher Chemiker

Supporting Information

69451 Weinheim, Germany

Surface-Metastable Phase-Initiated Seeding and Ostwald Ripening: A Facile Fluorine-Free Process towards Spherical Fluffy Core/Shell, Yolk/Shell, and Hollow Anatase Nanostructures**

Lu Cao, Dehong Chen, and Rachel A. Caruso**

anie_201305819_sm_miscellaneous_information.pdf

Experimental section

Chemicals: Titanium (IV) isopropoxide (TIP, 97%), hexadecylamine (HDA, 90%), and methylene blue (MB) were purchased from Sigma-Aldrich. 1-butanol (99.8%, Chem-Supply), absolute ethanol (>99.5%, Chem-Supply), potassium chloride (AR, BDH) and aqueous ammonia solution (25 wt.%, Merck) were used for the synthesis. Degussa P25 nanoparticles, a well-known benchmark titania photocatalyst, were used as a control for photocatalytic performance appraisal. All reagents were used as received without further treatment. The Milli-Q water used in the experiments was collected from a Millipore Academic purification system and had a resistivity no less than 18.2 MΩ·cm.

Synthesis: Amorphous titania precursor microspheres were prepared via a sol-gel synthesis conducted in 1-butanol using TIP as the precursor. In a typical synthesis, 11.92 g HDA was dissolved in 600 mL 1-butanol, followed by the addition of 4.8 mL aqueous KCl solution (0.1 M). To this solution 13.57 mL TIP was added at once under intense stirring and remained stirring for 1 min at 22 °C. The stirring was stopped and the resulting milky white precursor suspension was kept static at room temperature for 18 h, then the amorphous precursor microspheres were collected by centrifugation, washed with 1-butanol once and ethanol 3 times. Finally, the as-prepared sample was covered with low lint cellulose papers (Kimwipes) and dried in a fume cupboard at ambient temperature for 6 days.

To prepare hierarchical hollow titania microspheres, a solvothermal process was performed on the amorphous precursor microspheres (2.4±0.1 μm) in the presence of 21.3 wt% ammonia solution. In a typical synthesis, 1.6 g of the precursor microspheres were dispersed in a mixed solution of 5 mL ethanol and 25 mL ammonia (25 wt%). The resulting mixture was sealed within a 50 mL Telflon-lined autoclave and heated at 160 °C for 48 h in a fan-forced oven. The products were collected by filtration, washed using ethanol 3 times and dried in air at room temperature. The dried powders were calcined at 650 °C for 2 h (ramp rate of 1.6 °C min^{-1}) in air to remove any organic remaining in the sample. To determine the formation mechanism of the hierarchical titania hollow microspheres, amorphous precursor microspheres were solvothermally treated for varying times (from 2 to 48 h) and the resulting samples were collected and characterized using diverse techniques. Such solvothermally treated samples (prior to calcination)

were labelled with Solvo- as a prefix followed by the solvothermal time (x h) in the general form of Solvo-xh. The solvothermally treated samples calcined at 650 °C for 2 h were labelled as Solvo-xh-Cal. For instance, Solvo-48h-Cal indicates the precursor microspheres that were solvothermally treated at 160 °C for 48 h and then calcined at 650 °C for 2 h. To reveal the role of ammonia on the formation of such hollow microspheres, control experiments were conducted by replacing the ammonia solution with Milli-Q water under otherwise identical conditions.

Photocatalysis: Experiments were conducted in a fume cupboard built in a 'dark' room illuminated using a weak red bulb, which was turned off unless necessary sample handling was required. To avoid exposure of the methylene blue (MB, probe molecule) solutions to visible light, all the probe solutions were kept in containers pre-wrapped with Al foil. Thus, the results obtained would not be affected by visible light. The photocatalytic performance was measured by analysing the degradation of MB under UV light irradiation after adding the photocatalyst (80 mg) into 160 mL solution (55.5 mg MB L^{-1}) with continuous magnetic stirring. Prior to irradiation, the suspension was equilibrated in a reaction chamber by stirring in the dark for 1 h for MB adsorption onto the titania. The reaction chamber was kept at 20±1 °C, and was continuously bubbled with air (gas code: 052, BOC) during stabilization and degradation. A 500 W Hg (Xe) globe (Oriel) with a dichroic mirror (66226, Oriel, $280<\lambda<400$ nm) was used as the light source. Following UV-radiation exposure, the degradation of the MB dye was monitored by taking 1.5 mL aliquots at regular irradiation time intervals (0, 15, 30, 45, 60 min). After removing the photocatalyst from each aliquot by centrifugation at 15000 rpm for 10 min, the supernatants were collected and the concentration of MB calculated by measuring the characteristic absorption peak of MB (665 nm) using a UV-vis spectrophotometer (*Varian* Cary *50 Bio, USA*).

Characterization: The morphology and particle size of the samples were observed under low vacuum mode using a field emission environmental scanning electron microscopy (Quanta 200F FEI, USA) with an accelerating voltage of 15 kV. The samples were not pretreated by metal sputter coating. In order to investigate the interior structures of the microspheres, samples were embedded in an LR-white resin and sliced into ~90 nm thick sections. TEM images and selected area electron diffraction (SAED) patterns of

the resulting samples were obtained on a transmission electron microscope (FEI Tecnai F20, USA) operating at 200 kV. Powder X-ray diffraction (XRD, D8 Advances Diffractometer with Cu Kα radiation, Bruker, Germany) was used to determine the crystalline phase of the products. The diffractometer was set at 40 kV working voltage and 40 mA working current, with samples scanned from 5 to 80° in 2θ at a step size of 0.02° and a scan-step time of 4 s. Thermogravimetric and differential thermal analysis (TGA-DTA) measurements were conducted on a Mettler Toledo TGA/SDTA 851^e Thermal Gravimetric Analyzer with a heating ramp of 10 °C min^{-1} under 30 mL min^{-1} flowing air. Nitrogen gas sorption isotherms were measured at -196 °C using a Micromeritics Tristar 3000 surface area and porosity analyser (USA). Prior to the measurement, the calcined samples were degassed at 150 °C for 18 h on a vacuum line. The specific surface areas of the samples were calculated by a standard multipoint Brunauer-Emmett-Teller (BET) method using the adsorption data in the P/P_0 range from 0.05 to 0.20. The Barett-Joyner-Halenda (BJH) model applied to the adsorption branch of the isotherm was utilized to determine the pore size distributions of the samples. The X-ray photoelectron spectrometer (XPS) data were recorded on a VG ESCALAB 220i-XL spectrometer (UK) equipped with a twin crystal monochromated Al K_α X-ray source, which emitted a photon energy of 1486.6 eV at 10 kV and 22 mA. Samples were secured onto Al holders and were measured in the analysis chamber at a typical operating pressure of $\sim 7\times10^{-9}$ mbar. An electron flood gun was used to compensate the charging effect of non-conductive materials. Spectra were obtained at a step size of either 1.0 eV (survey scans) or 0.05 eV (regional scans). Quantification and curve fitting of XPS spectra were performed using CasaXPS software. Ti2p and O1s peaks were curve-fitted using a Gaussian/Lorentzian (30) line shape with Shirley background type. The C1s peak at 285.0 eV was used as a reference for the calibration of the binding energy scale. UV-Vis diffuse reflectance spectra of the samples were collected at room temperature on a Cary 5000 UV-Vis-NIR spectrophotometer (USA) with an integrating sphere (Internal DRA-2500) accessory in the 300-800 nm wavelength region. The diffuse reflectance versus wavelength data generated were used to estimate the bandgap of the material by converting reflectance to absorption data

according to the Kubelka-Munk equation: $F(R) \equiv (1–R)^2 (2R)^{-1} = K/S$, where R is the reflectance and K and S are the effective absorption and scattering coefficients,[1-3] respectively.

Figure S1. SEM images and the corresponding XRD patterns of the amorphous precursor microspheres (a, b) and solvothermally treated titania microspheres (prior to calcination) obtained with varying solvothermal times: 2 h (c, d), 4 h (e, f), 16 h (g, h), 24 h (i, j), 48 h (k, l), and the corresponding XRD patterns (m). Differation peaks around 2θ=9.8, 27.6, 48.1 and 62.9° in the XRD pattern (Figure S1m) are asscribed to the formation of ammonium titanate.[4] Note: SEM images were taken without metal sputter coating.

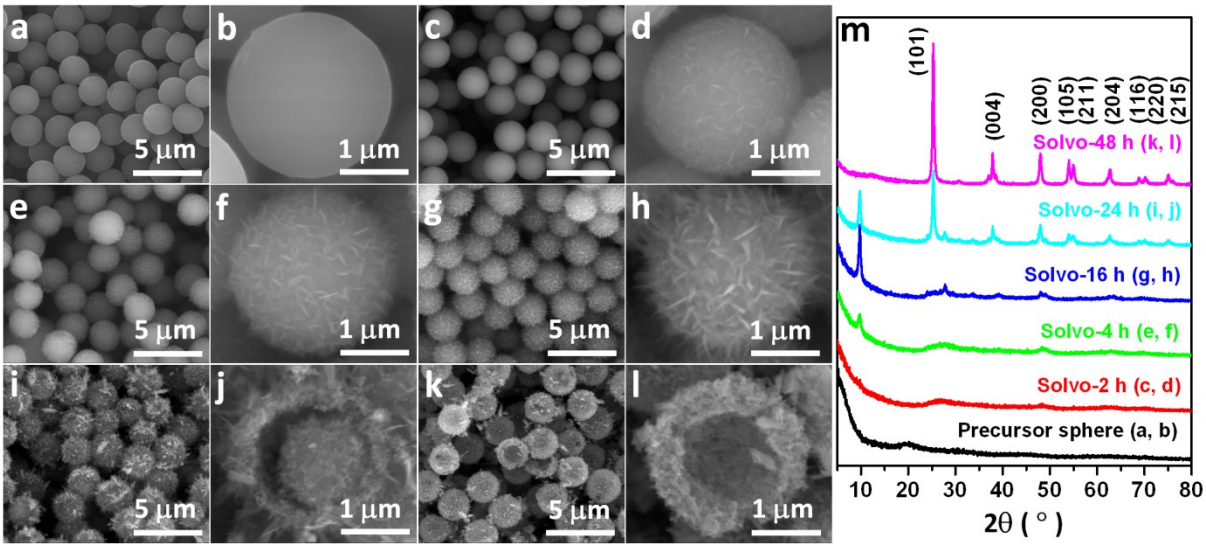

Figure S2. Selected area electron diffraction (SAED) patterns of the amorphous precursor microspheres (a) and solvothermally treated titania microspheres (prior to calcination) obtained with varying solvothermal times: 16 h (b), 24 h (c), and 48 h (d).

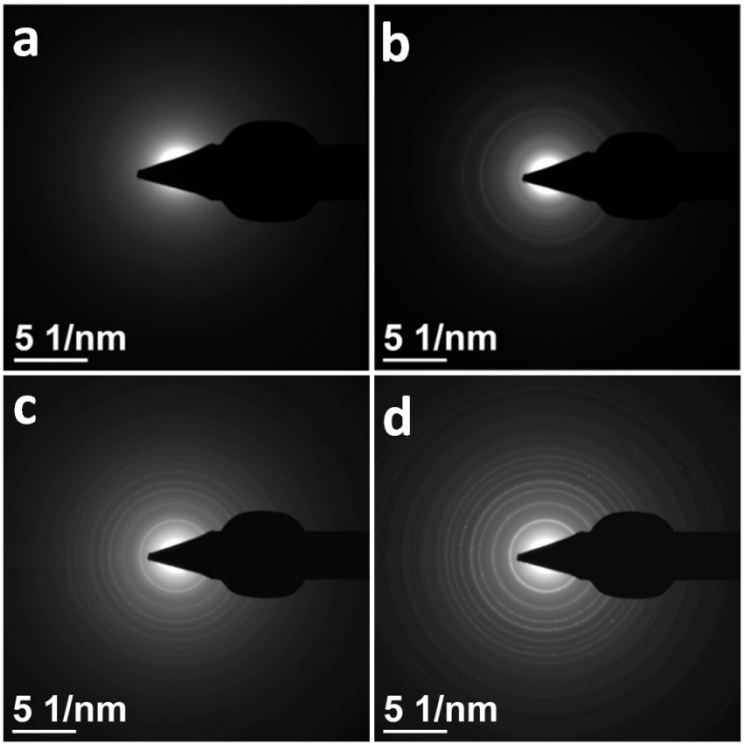

Figure S3. TGA-DTA curves of the solvothermally treated titania microspheres (prior to calcination) obtained with varying solvothermal times (2 h, 16 h, 24 h and 48 h). Samples were subjected to a linear heating ramp of 10 ºC min^{-1} under an air atmosphere. As displayed in Figure S3b, the overall weight loss of samples decreased with the increase of solvothermal treatment time. The samples (Solvo-2h, Solvo-16h, Solvo-24h) exhibited a broad endothermic peak with a minimum at around 95 °C (Figure S3a) and a substantial weight loss below 200 °C, which is due to the release of physically adsorbed water and volatilization of organic molecules. With further heating, a characteristic exothermic peak (Figure S3a) and a comparable weight loss of 2.9%, 3.8%, 2.9% and 2.2% occurred between 220-350 °C for Solvo-2h, Solvo-16h, Solvo-24h and Solvo-48h, respectively. The decrease in weight was primarily due to the combustion of organic residues, removal of chemically adsorbed water and conversion of ammonium titanate to titania. Therefore, with increasing solvothermal treatment time the microspheres became less hydrated and the organic residue content decreased significantly, along with less ammonium titanate being present for the Solvo-24h and especially the Solvo-48h samples as reflected in the corresponding XRD patterns (Figure S1). Another sharp exothermic peak in the DTA curves (Figure S3a) was observed between 450 °C and 500 °C and can be ascribed to the crystallization from amorphous to anatase titania. Regardless of solvothermal treatment time, no further mass decrease took place above 500 °C.

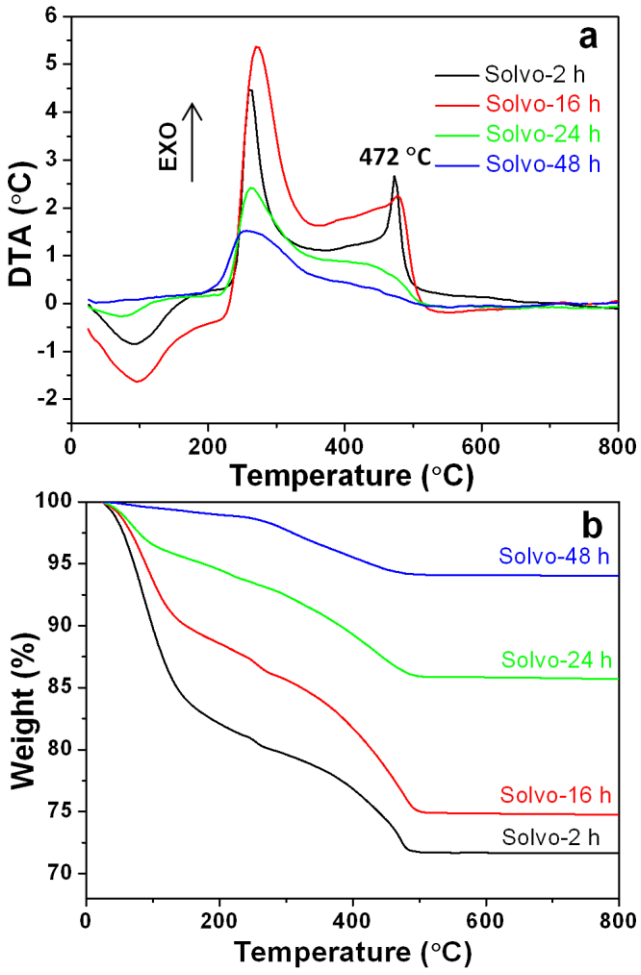

Figure S4. SEM and TEM (ultramicrotomed sections) images of the solvothermally treated microspheres (prior to calcination) prepared by replacing ammonia solution with water under otherwise identical conditions for 16 h (a-f) and 72 h (g-l), and the corresponding XRD patterns (m). The distortion of the microspheres in the TEM images (Figure S4d and S4j) is a result of the ultramicrotoming process during TEM sample preparation.[5] Note: SEM images were taken without metal sputter coating.

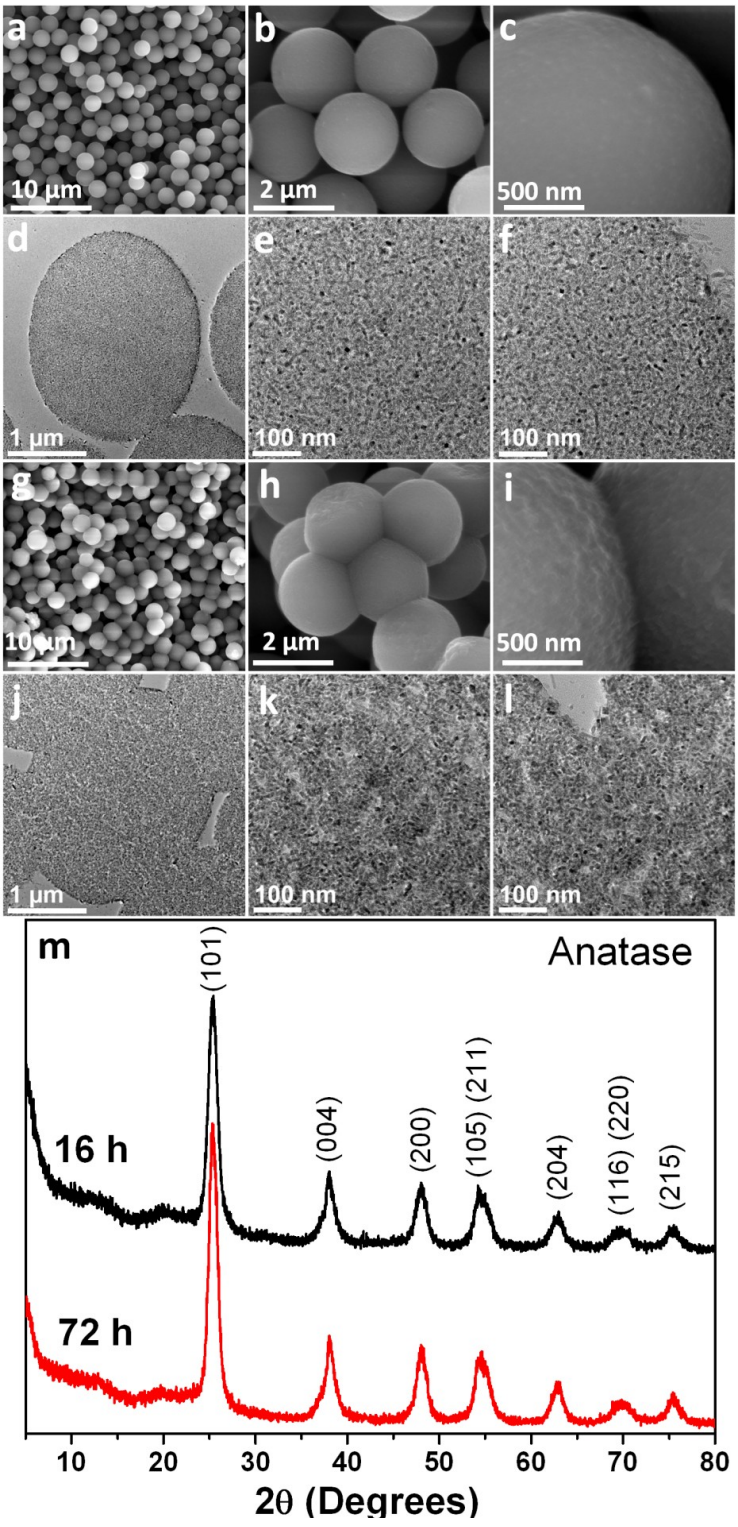

As shown in Figure S4a-f, microspheres composed of ultrafine anatase nanocrystals (5.3 nm measured using the TEM images, and ~5.7 nm estimated using the Scherrer equation from the corresponding XRD pattern in Figure S4m) formed after a relatively short solvothermal treatment of 16 h. Even with prolonged solvothermal treatment time, 72 h (Figure S4g-l), the size of the anatase nanocrystals was about 7.5 nm measured using TEM images (~7.8 nm estimated from the corresponding XRD pattern in Figure S4m). As shown in the high magnification TEM images (Figure S4e, f or k, l), the nanocrystals are nearly identical in size throughout the whole particle in the absence of ammonia. In addition, for the microspheres solvothermally treated for 72 h without ammonia, they tended to assemble into clusters by merging with neighboring microspheres (Figure S4g-l). Due to the absence of obvious difference in crystal size between the shell layers and the core regions of these microspheres, the Ostwald ripening process was less likely to be trigged to form the hollow spheres in this case. Instead the chemical potential difference between the convex and concave regions of the microspheres could effectively initiate a liquid sintering process. This proceeds by gradually dissolving titanium species from the convex regions that precipitate as anatase nanocrystals in the concave regions of the spheres,[6] thus results in the formation of merged microspheres during a prolonged solvothermal treatment (72 h). The above results indicate that ammonia changed the crystallization process of the amorphous precursor microspheres. In the presence of ammonia, rather than directly converting the amorphous titania to anatase nanocrystals, ammonia promoted the formation of metastable ammonium titanate nanoflakes on the surfaces of the precursor microspheres. It is these metastable ammonium titanate nanoflakes and their subsequent transformation to anatase nanocrystals located on the outer surfaces of the microspheres that triggered the Ostwald ripening process and gave rise to diverse titania hollow nanostructures.

Figure S5. SEM images (a, b) of the 'fluffy' core/shell anatase microspheres calcined at 650 °C for 2 h in air (Solvo-16h-Cal) and the corresponding high magnification TEM images (c, d) of the ultramicrotomed sections showing outer surface (c) and core region (d) of the microspheres. Note: SEM images were taken without metal sputter coating.

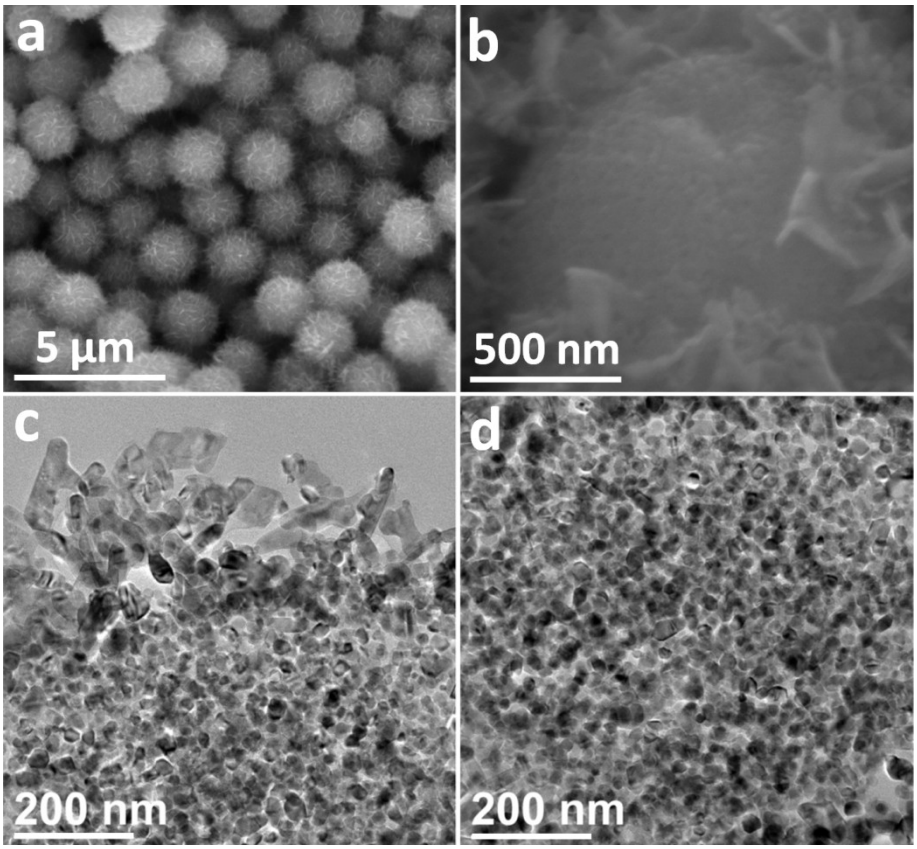

Figure S6. SEM images (a, b) of the yolk/shell anatase microspheres calcined at 650 °C for 2 h in air (Solvo-24h-Cal) and the corresponding TEM images (c, d) of the ultramicrotomed sections showing a general view (c) and yolk region (d) of the microspheres, respectively. In image c, some of the shell layers were broken by the ultramicrotoming process preparation for TEM analysis. Note: SEM images were taken without metal sputter coating.

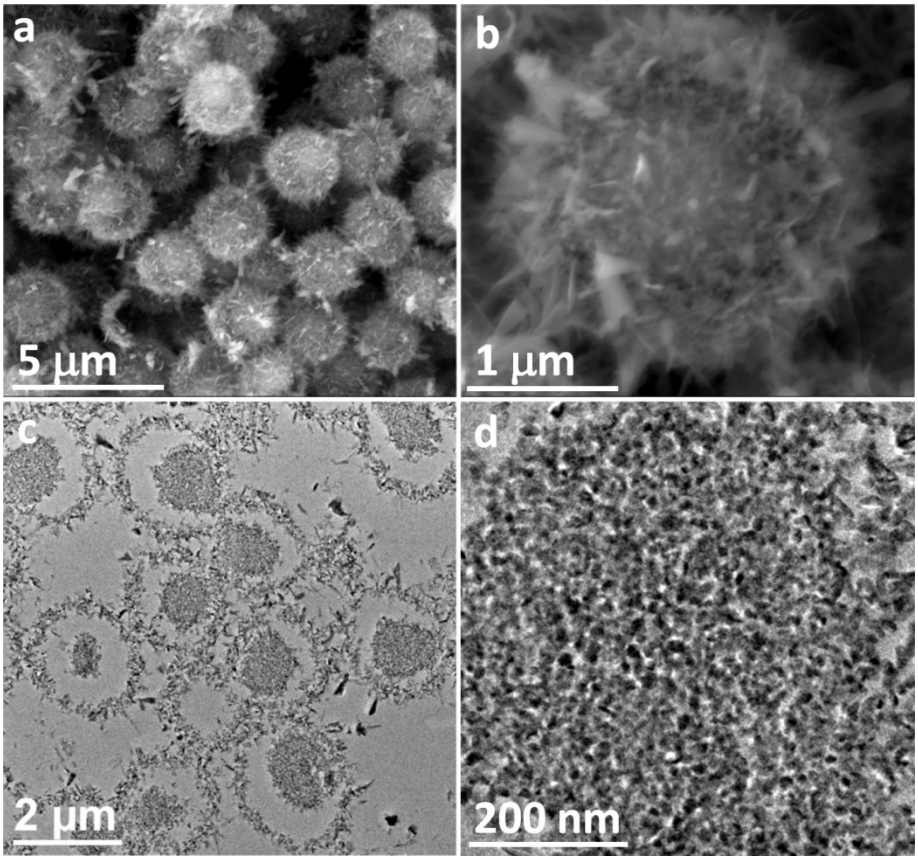

Figure S7. Histogram of the size distribution of the calcined hollow anatase microspheres (Solvo-48h-Cal).

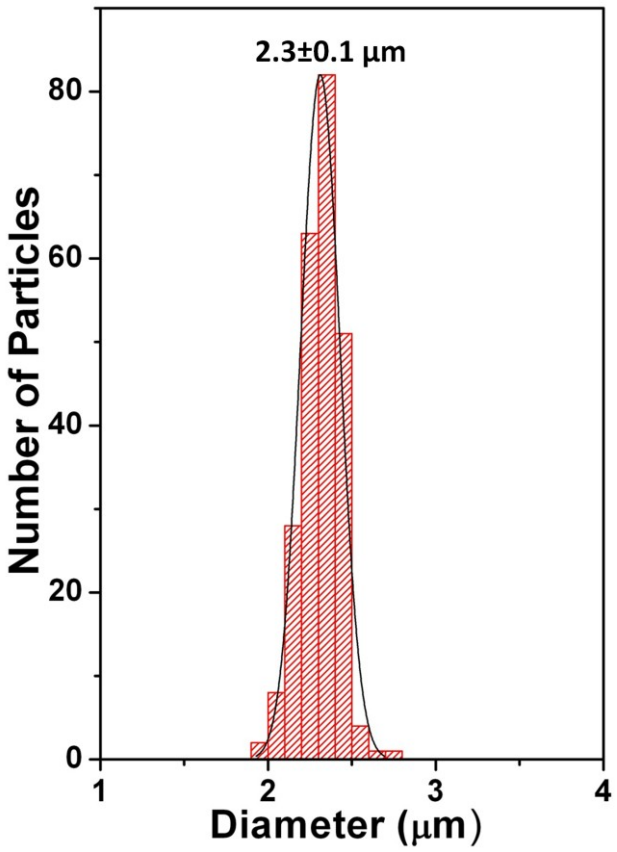

Figure S8. XRD patterns (a) and high-resolution XPS spectra (b) of the Ti2p of the 'fluffy' core/shell (Solvo-16h-Cal), yolk/shell (Solvo-24h-Cal) and hollow (Solvo-48h-Cal) anatase microspheres calcined at 650 °C for 2 h in air. For brevity only the solvothermal time for these samples is used to differentiate the patterns and spectra. The high-resolution Ti2p XPS spectra shown in Figure S8b display typical symmetric Ti (IV) doublet peaks for the calcined nanostructures fabricated with different solvothermal times (16, 24 and 48 h). Increasing the solvothermal time from 16 to 24 and 48 h, the Ti2p3/2 binding energy shifts from 458.7 to 458.9, and to 459.4 eV (the reference value recorded on the anatase single crystal was 459.3 eV),[7] further confirming an enhanced crystallinity of the resulting products.

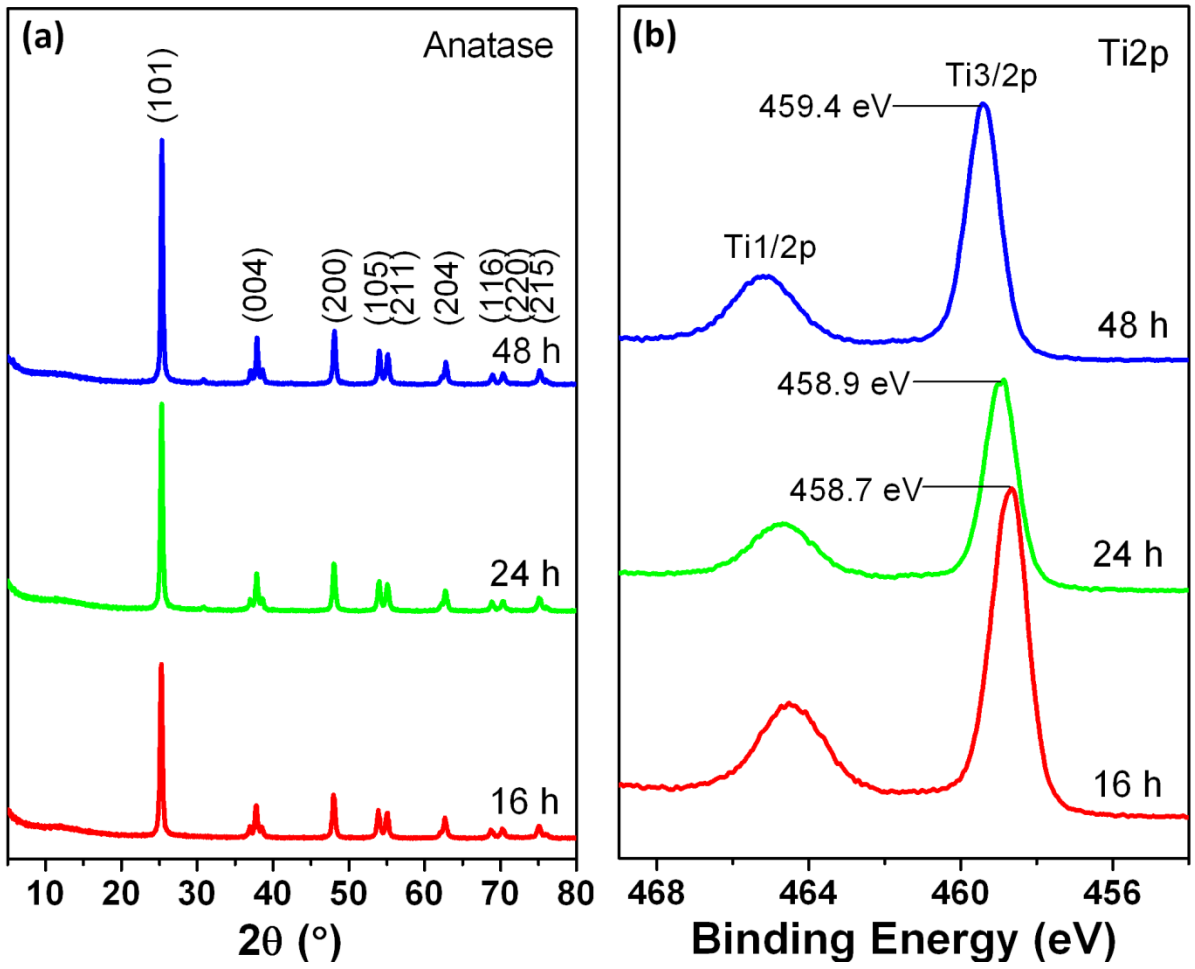

Figure S9. XPS survey spectrum of calcined anatase hollow microspheres calcined at 650 °C for 2 h in air. According to the XPS survey spectrum, only Ti, O and C (resulting from the adventitious hydrocarbon present on the sample surface) signals were detected and no peak around 400 eV was observed on the calcined hollow microspheres, suggesting there was no N-doping in these calcined products.[8]

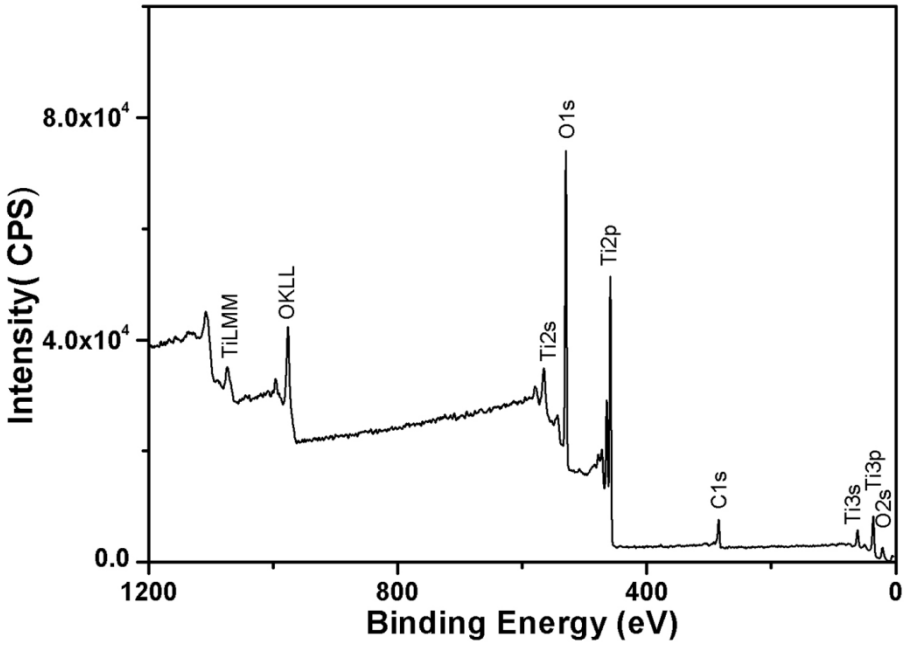

Figure S10. Time profile of the methylene blue (MB) absorbance spectrum observed during degradation in the presence of calcined hollow anatase microspheres (Solvo-48h-Cal) under UV light irradiation. The main absorption peak of MB at 665 nm was chosen to evaluate the degradation kinetics of the probe molecule.

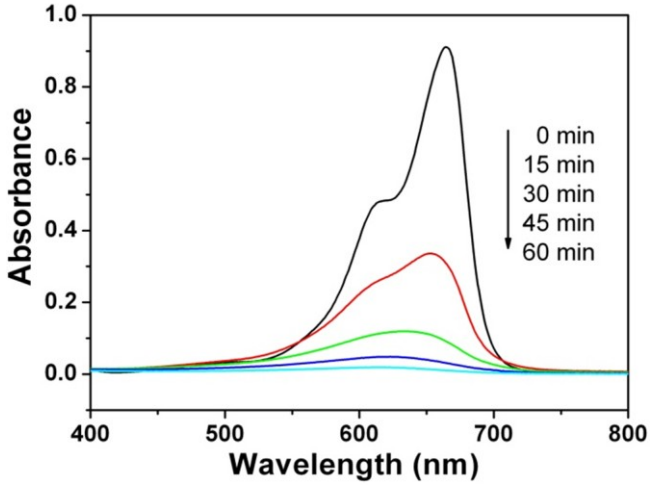

Figure S11. Nitrogen sorption isotherms (a) and the corresponding pore size distributions (b) of the 'fluffy' core/shell (Solvo-16h-Cal), yolk/shell (Solvo-24h-Cal) and hollow (Solvo-48h-Cal) anatase microspheres calcined at 650 °C for 2 h in air. Pore size distribution (PSD) was calculated using Barrett-Joyner-Halenda (BJH) model based on the adsorption branches. The isotherms of sample Solvo-24h-Cal and Solvo-48h-Cal are shifted up the vertical axis by 100 and 200 cm^3 g^{-1}, respectively.

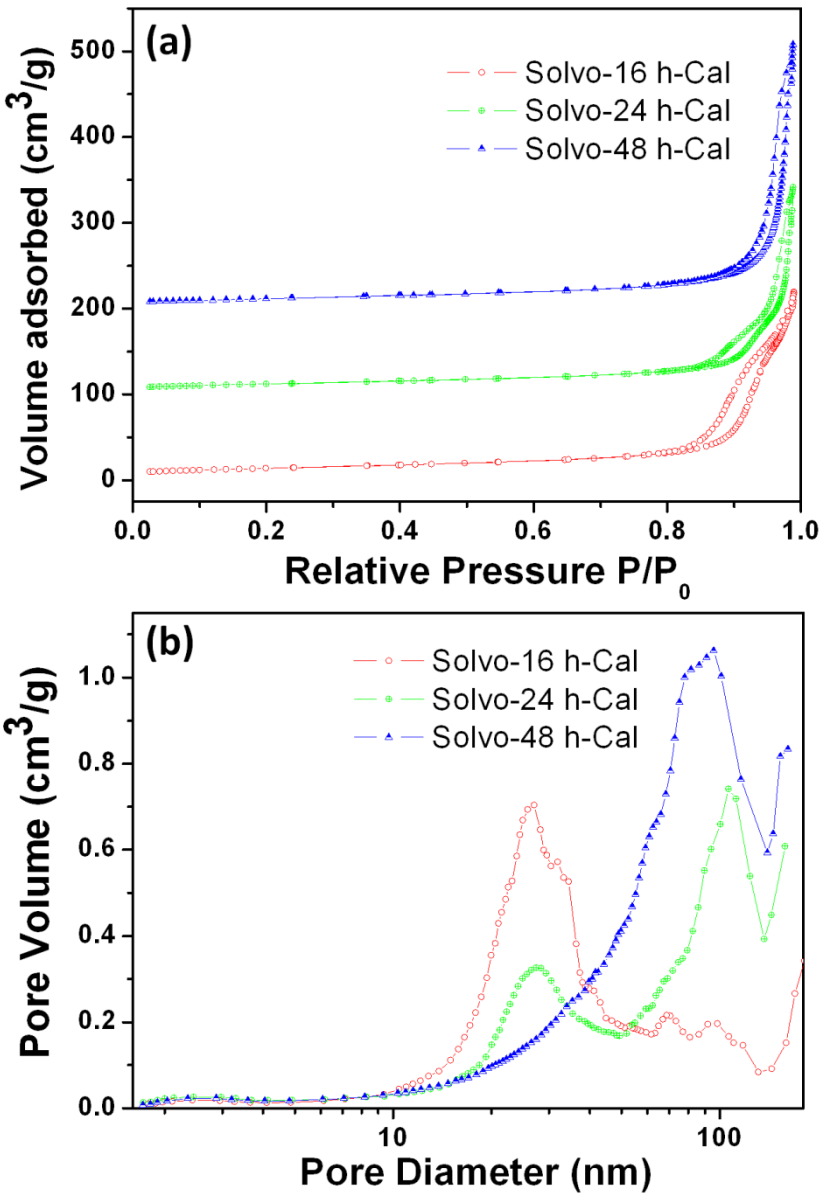

Type IV isotherms with featured hysteresis loops (Figure S11a) were observed for all these microspheres, indicating their mesoporous characteristics.[9] For the 'fluffy' core/shell titania microspheres (Solvo-16h-Cal), a capillary condensation step at high relative pressure (P/P_0=0.90-0.95) was observed, reflecting the existence of a relatively large pore size. The corresponding PSD (Figure S11b) shows a relatively narrow mesopore centered at 27 nm, which is mainly derived from the mesoporosity of the particulate core regions. This sample has a specific surface area of 50 m^2 g^{-1}, which is similar to that of the commercially

available P25 nanoparticles.[10] For the yolk/shell structured microspheres (Solvo-24h-Cal), two partially overlapped hysteresis loops (Figure S11a) derived from the mesoporosity in the particulate core regions and the macroporosity in the shell of the microspheres, respectively, are clearly observed. The corresponding PSD (Figure S11b) shows a distinct bimodal pore diameter of a relatively narrow mesopore (27 nm) and a broad macropore ranging from 50 to 110 nm. Compared to the Solvo-16h-Cal sample, the mesopores of the Solvo-24h-Cal centered at 27 nm have remained, but the total pore volume in the mesopore range decreased due to the decrease in the core content of these anatase nanostructures. The pore volume in the macropore range increased with the formation of the anatase shell layers. The yolk/shell structured microspheres have a specific surface area of 44 m^2 g^{-1}. Further increasing the solvothermal time to 48 h produced anatase hollow microspheres (Solvo-48h-Cal), that have a H1 type hysteresis loop at high relative pressure (P/P_0=0.91-0.98) in the nitrogen sorption isotherm, suggesting a fairly large pore size for this sample. This result was confirmed by the corresponding PSD shown in Figure S11b, in which a single pore size peak centered at 90 nm was observed. The diminished mesoporosity was a result of the disappearance of the particulate core regions, hence giving a slight decrease in the specific surface area of the products (41 m^2 g^{-1}).

Figure S12. UV-visible spectra (a) of the 'fluffy' core/shell (Solvo-16h-Cal), yolk/shell (Solvo-24h-Cal), hollow (Solvo-48h-Cal) anatase microspheres calcined at 650 °C for 2 h in air and Degussa P25 nanoparticles, and the relationship between the transformed Kubelka-Munk function versus the photon energy (b) for each material. In panel b, a straight line tangential to the slope was extended to cut the horizontal axis to obtain the bandgap energy of the titania samples.[1-3]

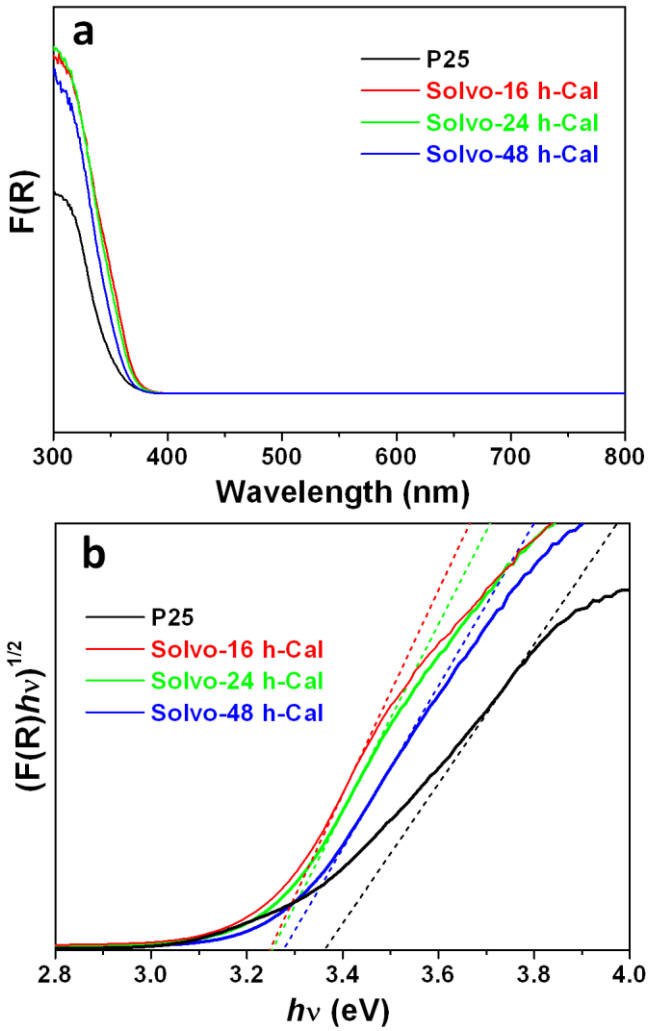

References

[1] J. Tauc, Grigorov.R, A. Vancu, *Physica Status Solidi* **1966**, *15*, 627-637.

[2] J. Klaas, G. Schulz-Ekloff, N. I. Jaeger, *J. Phys. Chem. B* **1997**, *101*, 1305-1311.

[3] G. Cao, L. K. Rabenberg, C. M. Nunn, T. E. Mallouk, *Chem. Mater.* **1991**, *3*, 149-156.

[4] a) C. H. Rhee, J. S. Lee, S. H. Chung, *J. Mater. Res.* **2005**, *20*, 3011-3020; b) B. Zhao, F. Chen, X. N. Gu, J. L. Zhang, *Chem. Asian J.* **2010**, *5*, 1546-1549; c) B. Zhao, F. Chen, Y. C. Jiao, J. L. Zhang, *J. Mater. Chem.* **2010**, *20*, 7990-7997.

[5] a) U. Meyer, A. Larsson, H. Hentze, R. A. Caruso, *Adv. Mater.* **2002**, *14*, 1768-1772; b) Z. Y. Yuan, M. F. Six-Boulanger, B. L. Su, *Angew. Chem.* **2003**, *115*, 1610-1611; *Angew. Chem. Int. Ed.* **2003**,

42, 1572-1573; c) D. H. Chen, L. Cao, T. L. Hanley, R. A. Caruso, *Adv. Funct. Mater*. **2012**, *22*, 1966-1971.

[6] R. German, P. Suri, S. Park, *J. Mater. Sci.* **2009**, *44*, 1-39.

[7] J. Biener, E. Farfan-Arribas, M. Biener, C. M. Friend, R. J. Madix, *J. Chem. Phys.* **2005**, *123*, 094705.

[8] R. Asahi, T. Morikawa, T. Ohwaki, K. Aoki, Y. Taga, *Science* **2001**, *293*, 269-271.

[9] S. Lowell, J. E. Shields, M. A. Thomas, M. Thommes, *Characterization of Porous Solids and Powders: Surface Area, Pore Size and Density*, Kluwer, London, **2004**.

[10]R. I. Bickley, T. Gonzalezcarreno, J. S. Lees, L. Palmisano, R. J. D. Tilley, *J. Solid State Chem.* **1991**, *92*, 178-190.

5.3 References for chapter introduction

1. Hu, J.; Chen, M.; Fang, X. S.; Wu, L. W., *Chem. Soc. Rev.* **2011**, *40*, 5472-5491.
2. Zhang, Q.; Wang, W. S.; Goebl, J.; Yin, Y. D., *Nano Today* **2009**, *4*, 494-507.
3. Lou, X. W.; Archer, L. A.; Yang, Z. C., *Adv. Mater.* **2008**, *20*, 3987-4019.
4. Caruso, F.; Caruso, R. A.; Mohwald, H., *Science* **1998**, *282*, 1111-1114.
5. Lai, X.; Li, J.; Korgel, B. A.; Dong, Z.; Li, Z.; Su, F.; Du, J.; Wang, D., *Angew. Chem. Int. Ed.* **2011**, *50*, 2738-2741.
6. Li, J.; Zeng, H. C., *J. Am. Chem. Soc.* **2007**, *129*, 15839-15847.
7. Sun, X. M.; Li, Y. D., *Angew. Chem. Int. Ed.* **2004**, *43*, 3827-3831.
8. Zhou, L.; Zhao, D. Y.; Lou, X. W., *Angew. Chem. Int. Ed.* **2012**, *51*, 239-241.
9. Dong, Z. H.; Lai, X. Y.; Halpert, J. E.; Yang, N. L.; Yi, L. X.; Zhai, J.; Wang, D.; Tang, Z. Y.; Jiang, L., *Adv. Mater.* **2012**, *24*, 1046-1049.
10. Li, H. X.; Bian, Z. F.; Zhu, J.; Zhang, D. Q.; Li, G. S.; Huo, Y. N.; Li, H.; Lu, Y. F., *J. Am. Chem. Soc.* **2007**, *129*, 8406-8407.
11. Wang, X.; Liao, M. Y.; Zhong, Y. T.; Zheng, J. Y.; Tian, W.; Zhai, T. Y.; Zhi, C. Y.; Ma, Y.; Yao, J. N. A.; Bando, Y.; Golberg, D., *Adv. Mater.* **2012**, *24*, 3421-3425.
12. Chen, Y.; Chen, H.; Guo, L.; He, Q.; Chen, F.; Zhou, J.; Feng, J.; Shi, J., *ACS Nano* **2010**, *4*, 529-539.
13. Ren, N.; Wang, B.; Yang, Y.-h.; Zhang, Y.-h.; Yang, W.-l.; Yue, Y.-h.; Gao, Z.; Tang, Y., *Chem. Mater.* **2005**, *17*, 2582-2587.
14. Yin, Y. D.; Rioux, R. M.; Erdonmez, C. K.; Hughes, S.; Somorjai, G. A.; Alivisatos, A. P., *Science* **2004**, *304*, 711-714.
15. Zeng, H. C., *J. Mater. Chem.* **2011**, *21*, 7511-7526.
16. Li, W.; Deng, Y.; Wu, Z.; Qian, X.; Yang, J.; Wang, Y.; Gu, D.; Zhang, F.; Tu, B.; Zhao, D., *J. Am. Chem. Soc.* **2011**, *133*, 15830-15833.
17. Pan, A.; Wu, H. B.; Yu, L.; Lou, X. W., *Angew. Chem. Int. Ed.* **2013**, *52*, 2226-2230.
18. Wang, B.; Wu, H. B.; Zhang, L.; Lou, X. W., *Angew. Chem. Int. Ed.* **2013**, *52*, 4165-4168.
19. Lou, X. W.; Wang, Y.; Yuan, C. L.; Lee, J. Y.; Archer, L. A., *Adv. Mater.* **2006**, *18*, 2325-2329.

20. Zhao, B.; Chen, F.; Jiao, Y. C.; Zhang, J. L., *J. Mater. Chem.* **2010**, *20*, 7990-7997.
21. Zhao, B.; Chen, F.; Gu, X. N.; Zhang, J. L., *Chem. An Asian J.* **2010**, *5*, 1546-1549.

Appendix to this chapter

Intrinsic activities (activity per surface area unit) of the various photocatalysts were calculated and listed in the following table:

Sample	Rate constant (MB min^{-1})	Surface area (m^2 g^{-1})	Activity per surface area (MB min^{-1} m^{-2})
Solvo-16h-Cal	0.0211	50	0.00528
Solvo-24h-Cal	0.0243	44	0.00690
Solvo-48h-Cal	0.0750	41	0.02286
P25	0.0673	50	0.01683

Based on these calculations, it is clear that the hollow titania microspheres (Solvo-48h-Cal) showed the highest activity per surface area unit, indicating that this sample contains more accessible photocatalytic active sites for MB degradation due to its unique hollow structure with large entrance voids on the mesoporous shell.

Chapter 6. Monodisperse Anatase Titania Microspheres with High-thermal Stability and Large Pore Size (~80 nm) as Efficient Photocatalysts

6.1 Introduction

Anatase phase titania is the most photoactive phase for both antibacterial coatings and degradation of organic pollutants, however, thermal stability becomes an issue at temperatures from 500 to 700 °C as irreversible phase transformation to rutile occurs.[1-6] This restricts the use of anatase photocatalysts for applications that need to be processed at high temperature. Therefore, a coating technology challenge is the development of a high performance anatase photocatalyst that tolerates the high sintering temperature of diverse ceramic substrates.

In this manuscript, monodisperse dopant-free anatase titania microspheres with large pore size (~80 nm) and outstanding high thermal stability (over 900 °C) were synthesized via a facile sol-gel chemistry and solvothermal process. These titania microspheres were composed of well-crystallized and faceted anatase nanocrystals with a uniform size of 24 nm. In the absence of any doping strategy or surface modification, the anatase-to-rutile phase transformation was effectively inhibited at high temperatures giving rise to high thermal stability (up to 900 °C) and highly crystallized anatase titania microspheres. This thermal stability is primarily attributed to the solvothermal treatment that can effectively produce highly crystallized anatase particles and thus prevents the Ti-O bond cleavage during the high temperature calcination. The anatase microspheres exhibited excellent photocatalytic performance even after calcination at 900 °C due to retention of the photoactive anatase phase. These photoactive monodisperse anatase titania microspheres with their uniform size and spherical morphology (desirable for forming high quality and close packed thin film) have the potential to form effective antibacterial coatings on the surfaces of diverse sanitary ceramic utensils. This study has been published in the Journal of Materials Chemistry A. The published manuscript and the supporting information are presented in section 6.2. Reprinted from "Monodisperse Anatase Titania Microspheres with High-thermal Stability and Large Pore Size (~80 nm) as Efficient Photocatalysts. *J .Mater. Chem. A* 2017, 5, 3645-3654", copyright (2017), with permission from Royal Society of Chemistry.

6.2 Manuscript (attached as below)

Journal of Materials Chemistry A

PAPER

View Article Online
View Journal | View Issue

Cite this: J. Mater. Chem. A, 2017, 5, 3645

Monodisperse anatase titania microspheres with high-thermal stability and large pore size (~80 nm) as efficient photocatalysts†

Lu Cao,[a] Dehong Chen,*[a] Wu-Qiang Wu,[a] Jeannie Z. Y. Tan[ab] and Rachel A. Caruso*[ab]

Received 17th October 2016
Accepted 10th January 2017

DOI: 10.1039/c6ta08981j

www.rsc.org/MaterialsA

To fabricate an effective antibacterial coating on the surfaces of diverse sanitary ceramic utensils, efficient titania photocatalysts with integrated features including high temperature anatase phase stability (>800 °C), excellent particle mobility for the formation of uniform thin coatings, high crystallinity and narrow particle size distribution are desirable. In this study, monodisperse dopant-free titania microspheres were synthesized with large pore size (~80 nm) that remain anatase even after calcination at 900 °C. These titania microspheres were fabricated *via* a facile solvothermal treatment of amorphous spheres in the presence of 4.5 wt% ammonia solution and consisted of well-crystallized and faceted anatase nanocrystals with a uniform size of 24 nm. The anatase nanocrystals with high crystallinity and narrow crystal size distribution are responsible for their high temperature stability. The resulting anatase titania microspheres exhibited enhanced photocatalytic performance even after calcination at high temperature due to the retention of the anatase phase and the enhanced crystallinity. Such monodisperse anatase microspheres have potential to be applied as smart coating materials for antibacterial and self-cleaning applications.

Introduction

Titania (TiO_2) has been one of the most widely investigated semiconductor materials in the past few decades due to its unique properties such as low-cost, nontoxicity, and high chemical and optical stability, and its diverse promising applications in environmental and energy areas ranging from photocatalysis, to photovoltaics and lithium ion batteries.[1–15] For the application of photocatalysis, it has shown promise in water splitting and purification since the discovery of its photocatalytic activity under UV light.[3] Recently, research has been conducted to control the morphology of nanostructured titania materials *via* different synthesis strategies to enhance the photocatalytic performance.[16–29] Among the various morphologies, of particular interest are titania microspheres with submicro- or micrometer-sized diameter, because of the relatively high refractive index and comparable particle size to the wavelengths of sunlight, which make them ideal candidates for natural light-driven photon-related applications. Moreover, microspheres have been regarded as the optimal morphology in high-quality thin film coating because such microspheres possess high packing density as well as good particle mobility,[30–33] which is beneficial for the fabrication of a uniform and compact coating layer in a highly reproducible manner. The porosity of the titania nanostructure also affects its performance when applied as a photocatalyst.[16,34,35] The presence of large pores can enhance light harvesting and ensure fast mass diffusion, consequently giving rise to high photocatalytic performance.[16,34,35]

Among the three most common polymorphs of titania (anatase, brookite and rutile), anatase is considered to be the most photoactive phase for both antibacterial coatings and degradation of organic pollutants because of the low recombination rate of the photogenerated charge carriers and the high surface adsorptive infinity towards the organic compounds.[36,37] However, anatase is a metastable phase and can be readily transformed to the thermodynamically stable rutile phase at temperatures from 500 to 700 °C,[23,38–41] and this phase transformation is irreversible. This restricts the use of anatase photocatalysts for some important applications (*e.g.*, self-cleaning and antibacterial coatings on sanitary ceramic ware) that need to be processed at high temperature (usually >800 °C).[42] Therefore, the development of a high performance anatase photocatalyst that tolerates the high sintering temperature of diverse ceramic substrates has become a challenge in smart

[a]Particulate Fluids Processing Centre, School of Chemistry, The University of Melbourne, Melbourne, Victoria 3010, Australia. E-mail: dehongc@unimelb.edu.au; rcaruso@unimelb.edu.au

[b]CSIRO Manufacturing, Private Bag 10, Clayton South, Victoria 3169, Australia

† Electronic supplementary information (ESI) available: Photocatalytic set-up, SEM images, size distributions, Raman spectrum, XRD patterns, UV-vis diffuse reflectance, XPS spectra, Arrhenius plot, TEM images, MB absorbance and degradation plot. See DOI: 10.1039/c6ta08981j

coating technology. In recent years, rational control of the onset temperature of the anatase-to-rutile transformation has been researched. The presence of certain cationic dopants, such as Zr, Al, La and Si, could effectively stabilize the anatase phase at elevated temperatures due to the formation of Ti interstitials.[39,43–46] However, secondary impurity phases (*e.g.*, Al_2TiO_5) may be produced at high temperatures,[46] which will generate additional charge carrier recombination sites and thus reduce the photocatalytic activity.[39,43–46] High temperature stabilization of the anatase phase through anion doping (S, F, N, *etc.*) has also been widely investigated.[47–49] In this case, the concentration of oxygen vacancies may be increased, which could enhance recombination between photogenerated electrons and holes and therefore deteriorate the photocatalytic activity of the titania photocatalyst. Moreover, excess anion doping can inhibit interfacial charge transfer, which is detrimental to the photocatalytic activity as well.[47] A sol–gel templating method has been reported to retard the phase transformation by creating hierarchically porous structures to reduce the interfaces between the titania nanocrystals in porous titania networks. The reduced interfaces can significantly decrease interface nucleation of the rutile phase and effectively retard the anatase to rutile phase transformation.[23] The effect of the heating atmosphere on the anatase to rutile transformation was also investigated:[50,51] the phase transformation rate was decreased under vacuum or oxygen and increased in reducing atmospheres, which could be due to the formation of Ti interstitials and oxygen vacancies, respectively. Although an increase in the onset temperature of phase transformation has been achieved, it is still lower than the sintering temperature for ceramic coatings. Another important issue that should be considered is the thermal stability of the porous structures. In most cases, the pores collapsed and most of the porosity was lost after being sintered at high temperature. Therefore, preparation of anatase titania photocatalysts with spherical morphology, large pore size and high temperature stability (>800 °C) without any chemical modification would be of considerable interest.

Herein, a facile route is reported for the synthesis of monodisperse anatase titania microspheres with a large pore size and high thermal stability by combining sol–gel chemistry and a solvothermal treatment process. In the absence of any doping strategy or surface modification, the anatase-to-rutile phase transformation was effectively inhibited at high temperatures giving rise to high thermal stability (up to 900 °C) and highly crystallized anatase titania microspheres. The anatase microspheres possess a uniform and large pore size, ~80 nm. The possible reasons for the superior thermal stability were investigated and discussed. The photocatalytic activity was evaluated by degrading methylene blue under UV illumination.

Experimental

Chemicals

Titanium(IV) isopropoxide (TIP, 97%), hexadecylamine (HDA, 90%), and methylene blue (MB) were obtained from Sigma-Aldrich. 1-Butanol (99.8%, Chem-Supply), absolute ethanol (>99.5%, Chem-Supply), potassium chloride (AR, BDH), aqueous ammonia solution (25 wt%, Merck) and Milli-Q water (18.2 MΩ cm^{-1}) were used for the materials preparation. All chemicals from commercial sources were used as received without further treatment.

Synthesis

Amorphous precursor spheres (APS) were prepared in 1-butanol containing an HDA and KCl aqueous solution according to a previously reported procedure.[17] In a typical synthesis of monodisperse titania microspheres (MTS) with 22.0 nm crystal size (estimated by Scherrer equation based on XRD pattern), 1.6 g of APS was added to a 4.5 wt% ammonia solution containing 20 mL ethanol, 5 mL Milli-Q water and 5 mL 25 wt% ammonia. The resulting mixture was sealed within a Teflon-lined autoclave (50 mL in volume) and heated at 220 °C for 16 h. After the autoclaves were cooled to room temperature, the products were collected by filtration, washed with ethanol three times and dried at 60 °C for 2 h to obtain the solvothermally-treated MTS. To study their high temperature stability, the dried MTS samples were calcined at elevated temperatures at a heating rate of 1.6 °C per minute (to ensure removal of the organic species) and held at these temperatures for 2 h in air. The calcined titania were denoted as MTS-*x* °C. For instance, MTS-800 °C refers to the titania synthesized using a 4.5 wt% ammonia solution *via* solvothermal treatment and followed by a calcination at 800 °C. Additionally, in order to investigate the effect of crystal size on the thermal stability, crystallized titania microspheres with tunable crystal sizes were also prepared using a similar solvothermal treatment procedure. In this case, 0 wt% and 17.4 wt% ammonia solutions were employed during the solvothermal process and the resulting samples were denoted as MTS-0 wt% and MTS-17.4 wt%, respectively. For comparison, Degussa (Evonik) P25 nanoparticles and amorphous precursor spheres were also calcined at temperatures between 500 and 1000 °C and the resulting materials were denoted as P25-*x* °C and APS-*x* °C, respectively.

Photocatalysis

Photocatalytic experiments in this study were carried out in a jacketed beaker under UV light irradiation as shown in Fig. S1 (in ESI†). The light, generated from a 500 W Hg (Xe) globe (Oriel) with a dichroic mirror (66226, Oriel, $280 < \lambda < 400$ nm), was vertically delivered onto the reaction mixture through a quartz reactor lid. The UV radiation intensity at the surface of the suspension was 16.7 ± 0.2 mW cm^{-2}. The reaction was kept at 20 ± 0.5 °C by circulated chiller water. Titania photocatalyst (0.5 g L^{-1}) was suspended in 160 mL of MB (25 mg L^{-1}) by using a magnetic stirrer. The pH values of the titania suspensions were 5.92 ± 0.08. Before monitoring the photocatalytic reaction, the photocatalysts were placed in MB solution in the dark for 1 h to reach adsorption–desorption equilibrium. Degradation was monitored by taking 1.5 mL aliquots at 15 min intervals up to 60 min. The aliquots were centrifuged and absorption spectra of the supernatant fluids were recorded using a UV-vis spectrophotometer (Varian Cary 50 Bio, USA). The main absorption

peak of MB at 665 nm was recorded to evaluate the degradation kinetics of the photocatalysts. The rate of degradation was assumed to obey pseudo-first-order kinetics and hence the rate constant for degradation, k, was obtained from the first-order plot according to the equation: $\ln(C/C_0) = -kt$, where C_0 is the initial concentration, C is the concentration of MB after a reaction time (t), and k is the first-order rate constant. Three degradation experiments were run for each sample to obtain an average.

Characterization

Anatase and rutile contents, as well as their average crystal sizes, were determined using a Bruker D8 Advance diffractometer (Germany). Diffraction patterns were collected by using Cu Kα radiation ($\lambda = 1.5406$ Å, 40 kV, 40 mA) in the continuous-scanning mode. The step size and scan speed were 0.02° and 1 s per step, respectively. The average crystal size of the anatase was calculated using the Scherrer equation ($D = 0.9\lambda/\beta \cos\theta$, where λ is the wavelength of the X-ray; β is the full-width at half-maximum height; and θ is the diffraction angle). The weight fraction of rutile (W_R), is calculated from the following equation:[52]

$$W_R = A_R/A_0 = A_R/(A_R + 0.884A_A)$$

where A_A and A_R are the integrated intensity of the anatase (101) and rutile (110) peaks, respectively. A_0 is the total integrated intensity of the anatase (101) and rutile (110) peaks.

A high resolution field emission environmental scanning electron microscope (SEM, Quanta 200 FEI) was used to observe the morphologies of the samples without metal sputter coating pretreatment. The transmission electron microscopy (TEM) images and selected area electron diffraction (SAED) patterns of the resulting samples were obtained on a FEI Tecnai F20 microscope (USA) operating at 200 kV. Nitrogen gas sorption isotherms at 77 K were collected on a Micromeritics Tristar 3000 surface area and porosity analyser (USA). All the samples were degassed under vacuum at 160 °C for at least 18 h prior to measurement. The Brunauer–Emmett–Teller (BET) equation was used to calculate the specific surface area. Pore size distributions were obtained using the Barrett–Joyner–Halenda (BJH) method from the adsorption branch of the isotherms. Diffuse reflectance spectroscopy (DRS) was measured on a UV-vis-NIR diffuse reflectance spectrophotometer (Perkin-Elmer lambda 1050) with an 150 mm integrating sphere attachment in the range of 200–800 nm. The band gap of the materials was estimated by extrapolating a linear part of the plots to $(\alpha h\nu)^2 = 0$. Raman spectroscopy was performed on a Renishaw inVia confocal microscope system. Specimens were illuminated with an argon laser (785 nm wavelength) through a 50× objective. The spot was estimated to be in the range of 1 μm. Spectra were collected over the wave number range of 100 to 700 cm^{-1} on the surface of the sample. The UV light illumination intensity was measured using a Tenmars TM-213 UV light meter. The pH values of the aqueous suspensions were measured using an Oakton pH/mV 11 meter. Prior to the measurement, the electrode was calibrated using fresh standard pH buffer solutions. The X-ray photoelectron spectrometer (XPS) data were recorded on a VG ESCALAB 220i-XL spectrometer (UK) equipped with a twin crystal monochromated Al K_α X-ray source, which emitted a photon energy of 1486.6 eV at 10 kV and 22 mA. Samples were secured onto Al holders and were measured in the analysis chamber at a typical operating pressure of $\sim 7 \times 10^{-9}$ mbar. An electron flood gun was used to compensate the charging effect of non-conductive materials. Spectra were obtained at a step size of either 1.0 eV (survey scans) or 0.05 eV (regional scans). Quantification and curve fitting of XPS spectra were performed using CasaXPS software. The C1s peak at 285.0 eV was used as a reference for the calibration of the binding energy scale.

Results and discussion

The morphologies of the monodisperse titania spheres (MTS) solvothermally treated in the presence of 4.5 wt% ammonia solution and their corresponding counterparts calcined at temperatures ranging from 800 °C to 1000 °C (referred to as MTS-800 °C, MTS-900 °C and MTS-1000 °C) were observed using scanning electron microscopy (SEM), as shown in Fig. 1, S2 and S3.† The corresponding size distributions of these samples are displayed in Fig. S4.†

The solvothermally treated sample consists of individual spherical entities with an average diameter of 2.23 ± 0.12 μm, Fig. 1a and S4a.† Each solvothermally-treated MTS is composed of uniform titania nanocrystals of ~22 nm in size (Fig. 1b). After calcination at temperatures of 800 °C or higher, an obvious shrinkage in the sphere diameter was observed (Fig. 1c and d and S2†). The sphere diameter decreased to 1.97 ± 0.09, 1.88 ± 0.10 and 1.58 ± 0.09 μm when the calcination

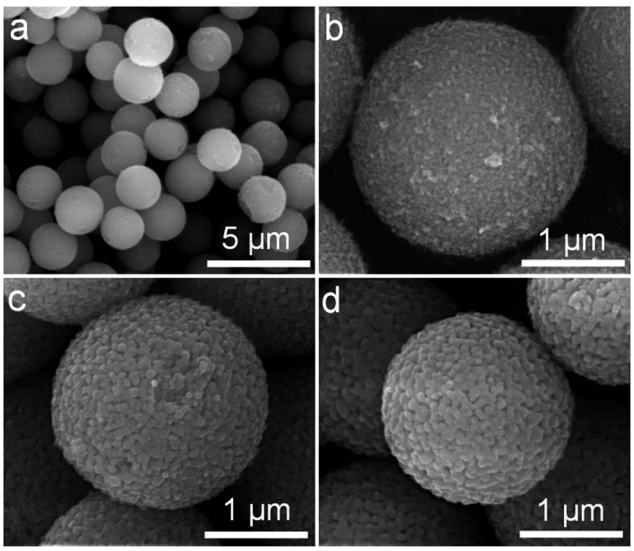

Fig. 1 SEM images of the monodisperse titania microspheres (MTS) solvothermally treated at 220 °C in the presence of 4.5 wt% ammonia solution (a and b) and following calcination at 800 °C (c) and 900 °C (d) in air. SEM images were taken without metal sputter coating of the sample.

temperature increased to 800, 900 and 1000 °C, respectively (Fig. S4†). As clearly illustrated by the higher magnification SEM images (Fig. 1c and d), a crystal coarsening process occurred when the solvothermally-treated MTS were calcined at 800 °C or higher, giving rise to enlarged crystal sizes. A slight increase in crystal size (50 to 60 nm) was observed when the calcination temperature increased from 800 to 900 °C, Fig. 1c and d, and then the crystal size increased further for the MTS calcined at 1000 °C in air (Fig. S2d†). Along with the increasing crystal size, the pore size/void between the nanocrystals became larger as a result of the increased calcination temperature (Fig. 1b–d).

The crystal phase and size of the MTS were studied by powder X-ray diffraction (XRD); the corresponding XRD patterns of the samples calcined at different temperatures are displayed in Fig. 2a. The anatase content (as a weight percentage) in each sample was calculated according to a previously reported method,[52] Fig. 2b. The XRD pattern of the solvothermally-treated MTS sample showed well-resolved diffraction peaks that can be ascribed to anatase titania (JCPDS card no. 21-1272). The anatase diffraction peaks for the MTS-800 °C and MTS-900 °C were sharper compared to the solvothermally-treated MTS sample. The crystal size of each sample can be estimated from the full width at half maximum of the (101) peak using the Scherrer equation, giving 22.0, 48.0 and 57.5 nm for MTS, MTS-800 °C and MTS-900 °C, respectively. This is in a good agreement with the crystal coarsening (increased crystal size) occurring with elevated calcination temperature observed from the SEM images.

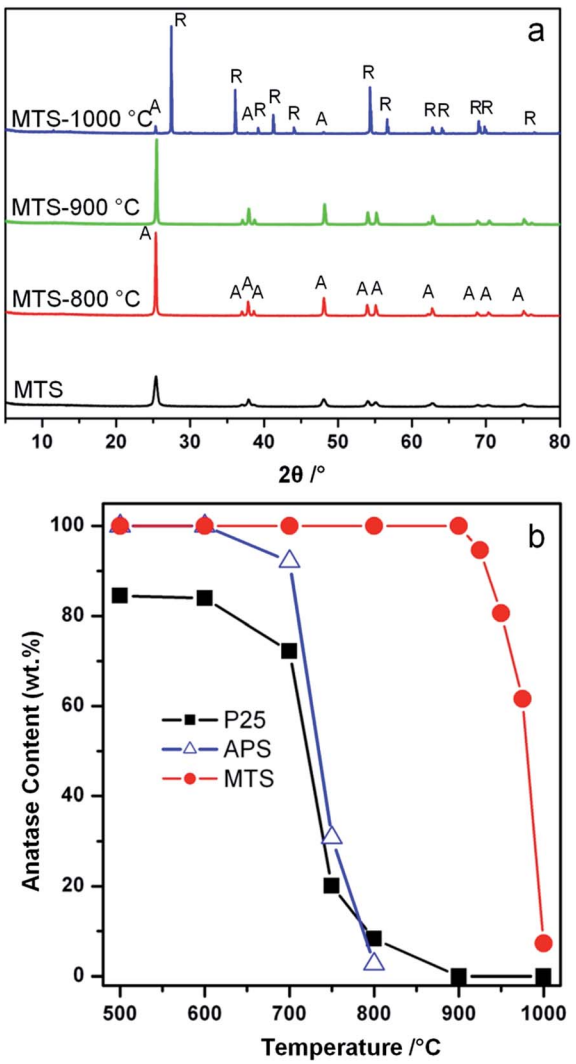

Fig. 2 (a) XRD patterns of the MTS, MTS-800 °C, MTS-900 °C, and MTS-1000 °C samples (A = anatase and R = rutile phase titania) and (b) anatase content of the MTS, amorphous precursor spheres (APS) and Degussa (Evonik) P25 as a function of the calcination temperature.

The physical properties of the MTS materials are summarized in Table 1. It is worth noting that no rutile phase was detected in the MTS-900 °C sample within the X-ray detection limit. This result was further confirmed by the corresponding Raman spectra (Fig. S5†), in which five high-intensity peaks at 142, 196, 397, 514 and 640 cm^{-1} can be attributed to characteristic E_g, E_g, $B1_g$, $A1_g(B1_g)$ and E_g modes of the anatase titania, respectively.[55,56] No other Raman peaks were observed, indicating the pure anatase phase for this MTS-900 °C sample. Thus the resulting anatase MTS materials possessed an excellent thermal stability (up to 900 °C), which is much higher than previous reports.[23,35,38–40] Further increasing the calcination temperature to 1000 °C (for 2 h in air) resulted in a phase transformation from anatase to rutile, leading to the formation of faceted titania particles (Fig. S3†) containing 7.1 wt% anatase (Fig. 2b). In contrast, for the Degussa (Evonik) P25 nanoparticles, only 8.3 wt% anatase remained after calcination at 800 °C for 2 h in air (Fig. 2b and S6†). When the temperature was increased to 900 °C, P25 was completely converted to the rutile phase. Phase transformation of the amorphous precursor spheres (APS) derived from sol–gel synthesis was also investigated (Fig. 2b and S7†): the anatase-to-rutile phase transformation occurred above 600 °C and was almost complete at 800 °C (only 2.7 wt% anatase remained at this temperature). UV-vis diffuse reflectance spectra and the corresponding Kubelka–Munk function (relationship of $[F(R)h\nu]^{1/2}$ *versus* photon energy) plots of the MTS and Degussa (Evonik) P25 samples calcined at diverse temperatures were recorded to determine the band gaps of the resulting materials (shown in Fig. S8†). Solvothermally-treated MTS, and calcined MTS-800 °C and MTS-900 °C samples show a very similar band gap (3.20 ± 0.01 eV) because of their similar anatase phase. In contrast, the as-received P25 nanoparticles are a mixed phase titania with the crystallized material consisting of 84.6 wt% anatase and 15.4 wt% rutile, and such mixed-phase titania possesses a relatively low band gap of 3.10 eV, which is consistent with the band gap values reported previously.[57] After calcination at 900 °C, the resulting P25-900 °C sample has been completely converted into the rutile phase, giving rise to a reduced band gap of 2.99 eV. These results clearly illustrate the excellent thermal stability of the MTS materials.

Nitrogen gas sorption isotherms and pore size distributions of the solvothermally-treated MTS and the MTS materials calcined at various temperatures are shown in Fig. 3. Except for the MTS-1000 °C sample, the samples showed characteristic type IV isotherms with a sharp capillary condensation step at

Table 1 Anatase content and physical properties of the monodisperse titania microspheres (MTS) solvothermally treated at 220 °C in the presence of 4.5 wt% ammonia solution and Degussa (Evonik) P25 samples treated at different temperatures

Sample name	W_A[a] [wt%]	S_{BET}[b] [m^2 g^{-1}]	PD[c] [nm]	V_{sp}[d] [cm^3 g^{-1}]	CS_{XRD}[e] [nm]	Bandgap[f] [eV]
MTS	100	71.5	30.5	0.420	22.0	3.21
MTS-800 °C	100	17.0	65.9	0.191	48.0	3.20
MTS-900 °C	100	10.9	77.0	0.123	57.5	3.19
MTS-1000 °C	7.10	1.10	n/a	0.003	n/a	2.96
P25	84.6	50.1	n/a	0.164	n/a	3.10
P25-800 °C	8.30	14.1	n/a	0.042	n/a	3.00
P25-900 °C	0	7.10	n/a	0.019	n/a	2.99

[a] W_A = weight fraction of the anatase phase calculated using the integrated intensities of anatase (101) and rutile (110) peaks according to a previously reported method.[52] [b] S_{BET} = BET specific surface area obtained from adsorption data in the P/P_0 range from 0.05 to 0.20. [c] PD = pore diameter determined by BJH model from the adsorption data. [d] V_{sp} = single-point pore volume calculated from the adsorption branch at P/P_0 = 0.98. [e] CS_{XRD} = anatase crystallite size estimated from XRD data using the Scherrer equation. [f] Band gap estimated according to Kubelka–Munk equation based on diffuse reflectance data.[53,54] 'n/a' indicates the corresponding methods are not applicable for the samples.

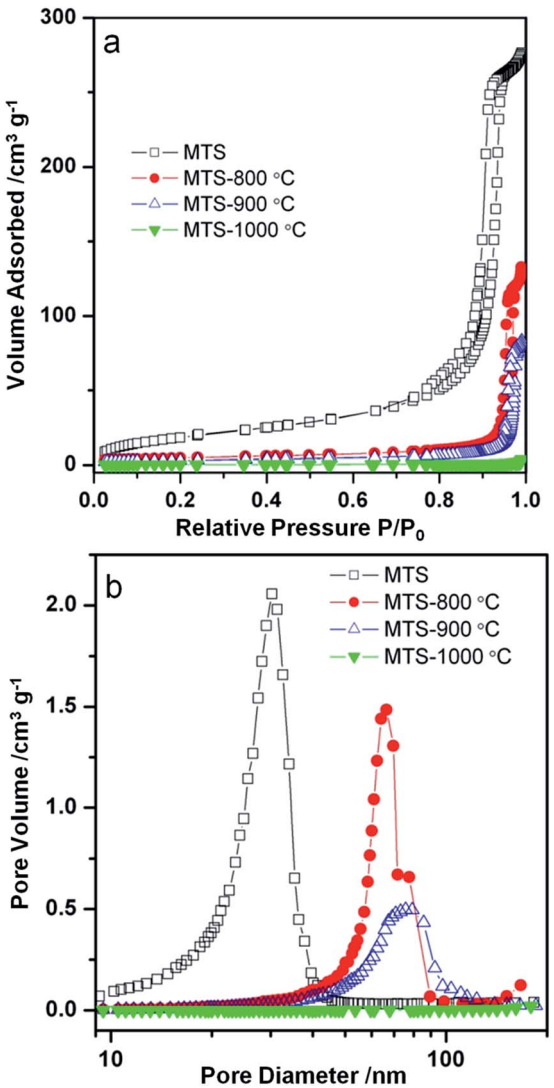

Fig. 3 (a) Nitrogen gas sorption isotherms and (b) the corresponding pore size distributions of the MTS, MTS-800 °C, MTS-900 °C and MTS-1000 °C samples.

relative high pressures (P/P_0 = 0.90–0.98), reflecting the existence of large pores. Sharp H1 type hysteresis loops were observed for solvothermally-treated MTS, and calcined MTS-800 °C and MTS-900 °C samples, indicating the narrow pore size distributions (PSD) of these samples. For solvothermally-treated MTS, a PSD centered at ~30.5 nm was calculated from the adsorption branch using the Barrett–Joyner–Halenda (BJH) method. This sample has a specific Brunauer–Emmett–Teller (BET) surface area of 71.5 m^2 g^{-1} and a total pore volume of 0.42 cm^3 g^{-1}. Using this BET surface area, and assuming spherical crystals, the crystal size of this solvothermally-treated MTS is estimated to be 21.5 nm on the basis of the anatase titania density (3.9 cm^3 g^{-1}), which is consistent with the result derived from XRD calculation (~22.0 nm). The hysteresis loops of the MTS-800 °C and MTS-900 °C samples shifted to higher relative pressure, illustrating an enlargement in pore size during the calcination process. As shown in Fig. 3b, sharp PSDs centered at 65.9 and 77.0 nm for the MTS-800 °C and MTS-900 °C samples were observed, respectively. It is worth noting that such uniform large pores in titania spheres have rarely been reported. After calcination at 1000 °C in air, as illustrated by nitrogen gas sorption and SEM images, the porosity of the resulting MTS-1000 °C materials disappeared, indicating a significant crystal growth and densification of the titania spheres (XRD results).

Specific surface areas of the MTS and P25 samples as a function of the calcination temperature ranging from 500 to 1000 °C are presented in Fig. 4. For the MTS sample, the specific surface area showed a slight decrease of 8.9% up to 600 °C. This small drop in specific surface area could be attributed to the high crystallinity of the samples induced by solvothermal treatment at 220 °C. However, a significant drop in specific surface area from 64.0 to 17.0 m^2 g^{-1} was observed when the calcination temperature was increased from 600 to 800 °C. This decrease is due to the coarsening of the anatase nanocrystals as revealed by the corresponding XRD results (Fig. 2). With a further increase in the calcination temperature to 900 °C, the specific surface area decreased to 10.9 m^2 g^{-1}. The specific surface area of the P25 sample calcined at varied temperatures was also investigated. As P25 is produced by flame hydrolysis of

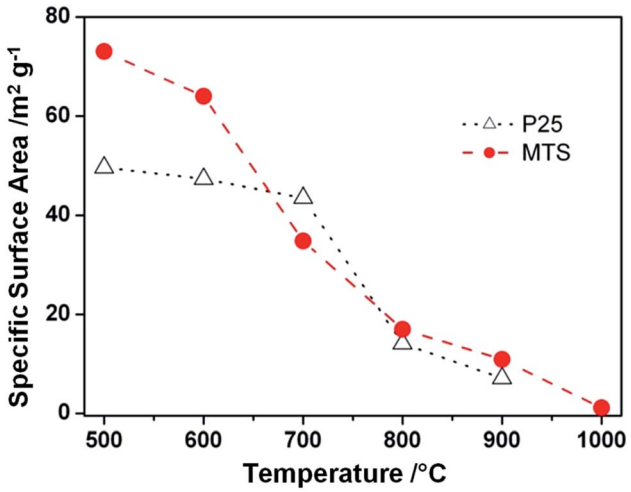

Fig. 4 Specific surface areas of the MTS solvothermally treated at 220 °C in the presence of 4.5 wt% ammonia solution and Degussa (Evonik) P25 samples as a function of the calcination temperature. The lines were added to guide the eye.

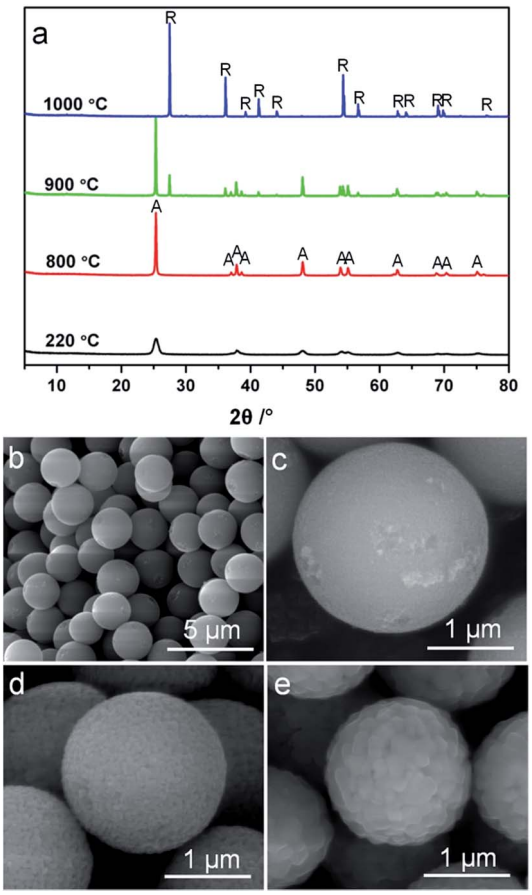

Fig. 5 (a) XRD patterns (A = anatase and R = rutile phase titania) and (b–e) SEM images of (b and c) the titania microspheres solvothermally treated at 220 °C in the absence of ammonia, and then calcined at (d) 800 °C and (e) 900 °C. SEM images were taken without metal sputter coating of the samples.

$TiCl_4$ at elevated temperature (up to 1000 °C), it is reasonable that only a slight drop in the specific surface area was observed when the calcination temperature is raised to 700 °C. The surface area dropped dramatically from 43.5 to 13.8 $m^2\ g^{-1}$ when the calcination temperature increased from 700 to 800 °C. Nevertheless, it is worth noting that the specific surface areas of the calcined MTS are higher than those of P25 calcined at 800 and 900 °C.

XPS measurements were used to detect any N-doping in the resulting MTS materials.[6] As shown in Fig. S9,† the as-prepared sample contained a small quantity of N (0.9 at%) and this N peak disappeared after washing with ethanol three times, indicating that the N on the as-prepared sample was due to the ammonia adsorbed on the surfaces of the sample and can be readily removed by thorough washing with ethanol.

High thermal stability of the MTS sample

According to Penn and Banfield,[58] the anatase-to-rutile phase transformation is a reconstructive process that involves breaking and reforming seven out of 24 Ti–O bonds per unit cell.[58] The difficulty to rearrange the Ti–O bonds (and thereby obstruct phase transformation) can be significantly affected by the activation energy of the rutile nucleation. According to a previously reported method,[59] an activation energy of 468 kJ mol^{-1} was calculated using the Arrhenius equation for the rutile nucleation in MTS (Fig. S10†). This relatively high activation energy reflects that the rutile nucleation in the MTS sample is dominated by a surface nucleation mode,[60,61] which relies on the thermal fluctuation of atoms on the surfaces and requires higher activation energy than that for an interface nucleation process. As a result, it is observed that the MTS sample shows phase stability at temperatures up to 900 °C.

It is documented that the thermal stability of anatase depends on its crystal size,[45,52,56,59,62] as the rate of surface nucleation is proportional to the total number of anatase crystals in a given sample volume.[60] To investigate the crystal size effect on the transformation from anatase to rutile phase, monodisperse anatase titania microspheres (MTS-0 wt%) consisting of smaller nanocrystals (11.6 nm in diameter estimated by XRD) were prepared in the absence of ammonia during the solvothermal treatment. The XRD patterns, Fig. 5a, show an anatase to rutile transformation has begun by 900 °C. The rutile content in the MTS-0 wt% samples was determined as 19.6% and 100% after calcination at 900 °C and 1000 °C, respectively, indicating a phase transformation at lower temperatures compared to the microspheres with larger crystallite size (22.0 nm, Fig. 2; 0% and 92.9% rutile after calcination at 900 °C and 1000 °C, respectively). The spherical morphology was maintained with shrinkage in diameter and increasing crystal size as the calcination temperature increased (SEM images, Fig. 5b–d).

In conjunction with XRD characterization, the MTS-0 wt% and MTS samples were also ultramicrotomed to ~90 nm thick sections and observed by transmission electron microscopy (TEM) to investigate the uniformity of the crystal size (Fig. 6a and b). As clearly illustrated in Fig. 6a1–a3 and b1–b3, the titania microspheres consisted of uniform crystals and the

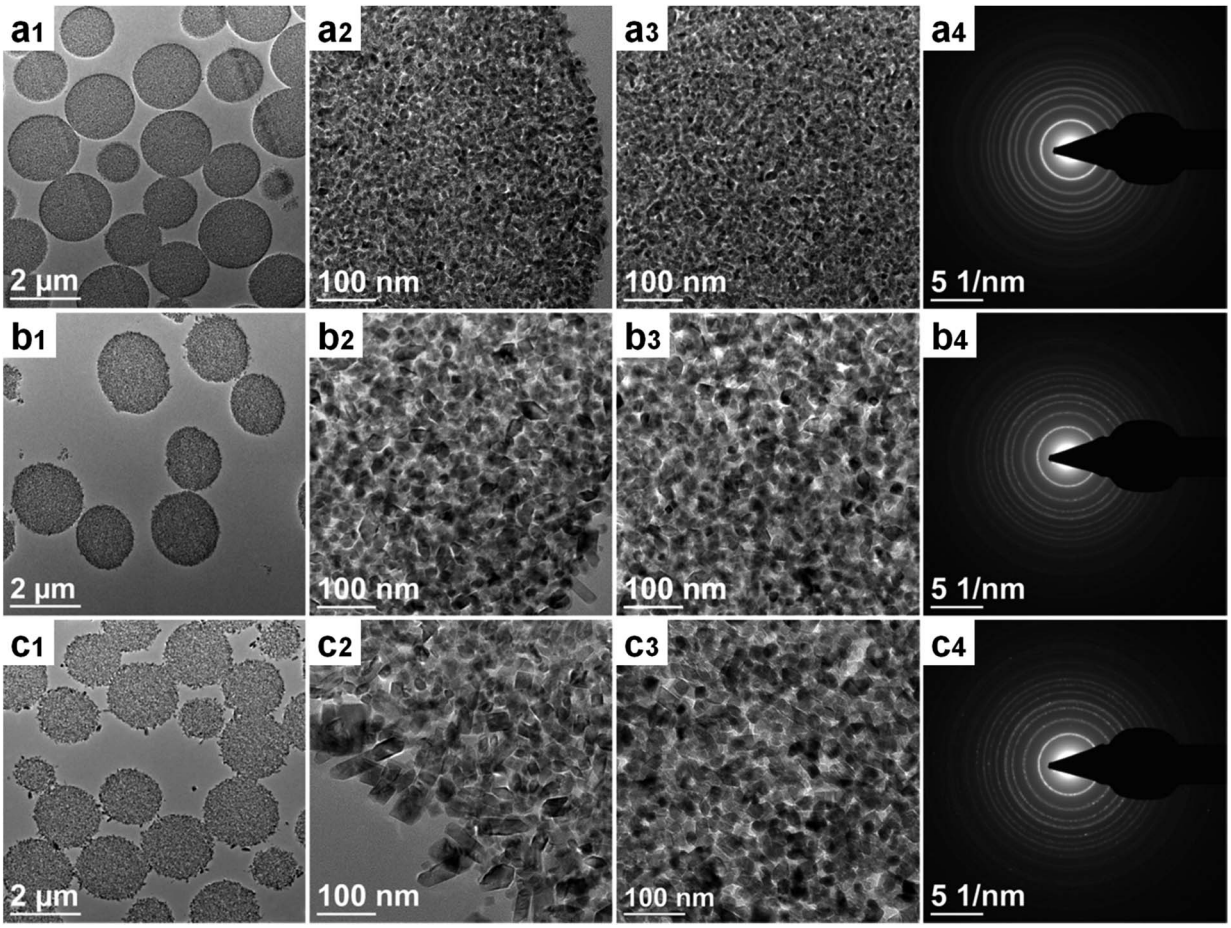

Fig. 6 TEM images and selected area electron diffraction (SAED) patterns of the ultramicrotomed sections of the solvothermally-treated titania microspheres in the presence of varying ammonia concentrations: (a1–a4) 0 wt%, (b1–b4) 4.5 wt% and (c1–c4) 17.4 wt%.

sample prepared in the absence of ammonia possessed a relatively small crystallite size (Fig. 6a2 and a3). The corresponding selected-area electron diffraction (SAED) patterns (Fig. 6a4 and b4) indicate that these microspheres are well crystallized anatase phase titania. To statistically determine the equivalent diameter of the anatase nanocrystals in the microspheres, these titania microspheres were crushed using an agate pestle and mortar and then dispersed in ethanol by sonication for 30 min. The resulting colloidal suspension was then dropped onto Cu grids and examined by TEM analysis, and the corresponding crystal size distributions were summarized in Fig. S11.† The crystal size is 12.0 ± 2.5 and 24.1 ± 5.7 nm for the titania microspheres prepared in the absence (0 wt%) and presence (4.5 wt%) of ammonia, respectively. This result is in agreement with the XRD result. The resulting faceted anatase nanocrystals had a truncated bipyramid crystal morphology, exposing the (101) side and (001) top facets (Fig. S12 in ESI†).

Purpose-built titania microspheres (MTS-17.4 wt%) featuring a bimodal crystal size distribution were prepared by increasing the ammonia concentration to 17.4 wt% to verify the crystal size effect on the phase transformation. As shown in Fig. 6c1–c3 and S13c1 and c2,† these unique titania microspheres were composed of two distinct anatase crystals (with relatively small anatase crystals (~20 nm) in the core and larger anatase crystals (~60 nm) decorating the outer surface of the spheres). As these small and large anatase crystals are located within the same microsphere and therefore are in close proximity (within a distance < 2.2 μm), these anatase nanocrystals have been exposed to the same temperature during the calcination. Thus, the variation in anatase and rutile phases can be correlated to the size of the anatase nanocrystals within the microspheres.

According to the corresponding XRD patterns (Fig. S14†), a small portion of rutile (2.8%) was observed when this MTS-17.4 wt% sample was calcined at 900 °C, which is believed to be derived from the relatively 'unstable' small anatase crystals in the core. When this MTS-17.4 wt% was calcined at 1000 °C, about 63.1 wt% anatase still remained in this sample, which can be attributed to the presence of relatively stable larger anatase crystals located on the surface of the spheres. In contrast, the titania spheres featuring monodisperse anatase crystals (12.0 or 24.1 nm shown in Fig. S11†) retained 0 wt% (Fig. 5a) or 7.1 wt% anatase (Fig. 2a) when calcined at 1000 °C. On the basis of the above results, it is clear that the crystal size is a key parameter in determining the onset temperature of the anatase-to-rutile phase transformation (thermal stability). This onset

temperature increased with increasing initial crystal size as a result of the reduction in free surfaces and interfaces available for the rutile nucleation.[56,60]

Photocatalysis

The photocatalytic performance of the resulting titania microspheres was evaluated by monitoring the degradation of methylene blue (MB, Fig. 7) *via* a reactive oxygen species induced oxidation process under UV light illumination.[63] For comparison, the photocatalytic activity of the Degussa (Evonik) P25 nanoparticles calcined at the same temperatures was also measured under the identical conditions. The MB dye illuminated under UV light in the absence of any photocatalyst shows a very slow degradation rate (0.0010 min^{-1}, Fig. S15†). After calcination at 800 °C, MTS-800 °C displays higher photocatalytic performance ($k = 0.1233$ min^{-1}) than P25-800 °C ($k = 0.0893$ min^{-1}). This sample retains the spherical morphology after the photocatalytic tests (Fig. S16 in ESI†), indicating good mechanical stability. Upon increasing the calcination temperature, MTS-900 °C still possesses a very high degradation performance ($k = 0.1053$ min^{-1}), whereas the degradation rate of the P25-900 °C control sample dropped dramatically to 0.0155 min^{-1}, indicating a 6.8-fold greater photocatalytic activity compared to the control sample. The enhanced performance of MTS-800 °C and MTS-900 °C could be attributed to the following synergistic effects: (1) the retention of the anatase phase as the high thermal stability of MTS could lower the recombination rate of the photogenerated charge carriers;[36,37] (2) the presence of large pores (up to ~80 nm) not only facilitates fast diffusion of the pollutants, but could also induce multi-reflection of the incident photons within the anatase spheres to maximize the light harvesting and utilization efficiency;[16,34] (3) the high crystallinity induced by the solvothermal treatment and subsequent high temperature calcination could diminish the recombination rate of the photogenerated charge carriers and prolong the electron lifetimes and diffusion lengths; and (4) the higher surface area provides more active reaction sites, contributing to an overall enhanced photocatalytic activity. The slight drop in photocatalytic activity of the MTS-900 °C compared to the MTS-800 °C sample is probably due to the decrease in surface area with the increased calcination temperature. With a further increase in calcination temperature to 1000 °C, a significantly decreased degradation rate of 0.0058 min^{-1} was observed for the MTS-1000 °C sample. The inferior performance of the MTS-1000 °C sample is mainly ascribed to the dominant rutile phase (92.7%) and low surface area (1.1 m^2 g^{-1}). The highly crystallized anatase phase retention, porous structure with large pore size and high specific surface area are the three key factors for achieving higher photocatalytic activity when using the anatase titania microspheres to degrade the MB dye.

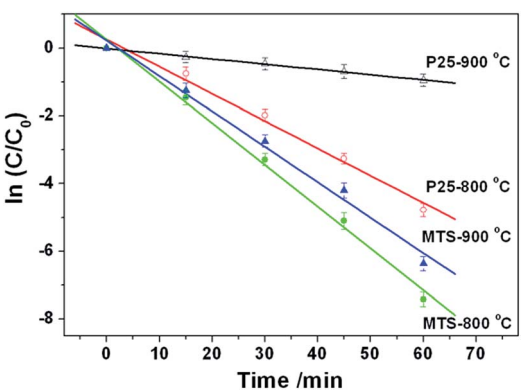

Fig. 7 Photocatalytic degradation kinetics of the methylene blue (MB) probe under UV light in the presence of MTS-800 °C, MTS-900 °C, P25-800 °C and P25-900 °C materials.

Conclusions

Monodisperse anatase titania microspheres with high thermal stability have been fabricated *via* a facile solvothermal treatment of the amorphous precursor spheres in the presence of mild ammonia solution. The anatase microspheres possess a uniform and large pore size up to 80 nm and high thermal stability with a phase transformation onset temperature above 900 °C. The successful synthesis of such high temperature stable anatase titania is primarily attributed to the solvothermal treatment strategy that can effectively produce highly crystallized anatase particles and thus prevents the Ti–O bond cleavage during the high temperature calcination. The resulting anatase microspheres exhibited impressive photocatalytic performance even after calcination at 900 °C due to retention of the photoactive anatase phase. Coupled with its uniform size and spherical morphology (which is desirable for forming high quality thin films *via* close packing), such photoactive monodisperse anatase titania microspheres have potential to be employed in the fabrication of effective antibacterial coatings on the surfaces of diverse sanitary ceramic utensils, in sunscreen or as support materials for industrial catalysts in future.

Acknowledgements

This research was financially supported by an Australian Research Council Discovery Project (DP110101346). L. C. acknowledges the support of an Australian Postgraduate Award, Australian Government Research Training Program Scholarship and MMI-CSIRO PhD Materials Science Top-up. R. A. C. is a recipient of an Australian Research Council Future Fellowship (FT0990583). Dr Simon Crawford is acknowledged for ultramicrotoming samples in preparation for TEM characterization. Dr Xiaofei Duan is appreciated for acquiring XPS results. Dr David Parris is thanked for collecting XRD data. The Melbourne Advanced Microscopy Facility and Surface and Chemical Analysis Network (SCAN) at the University of Melbourne are acknowledged for electron microscopy and XPS access, respectively.

References

1 X. Chen and S. S. Mao, *Chem. Rev.*, 2007, **107**, 2891.

2 Y. Bai, I. Mora-Sero, F. De Angelis, J. Bisquert and P. Wang, *Chem. Rev.*, 2014, **114**, 10095.
3 A. Fujishima and K. Honda, *Nature*, 1972, **238**, 37.
4 F. Sauvage, D. Chen, P. Comte, F. Huang, L.-P. Heiniger, Y.-B. Cheng, R. A. Caruso and M. Graetzel, *ACS Nano*, 2010, **4**, 4420.
5 J. Bai and B. X. Zhou, *Chem. Rev.*, 2014, **114**, 10131.
6 R. Asahi, T. Morikawa, T. Ohwaki, K. Aoki and Y. Taga, *Science*, 2001, **293**, 269.
7 D. H. Chen, F. Z. Huang, Y. B. Cheng and R. A. Caruso, *Adv. Mater.*, 2009, **21**, 2206.
8 W.-Q. Wu, F. Huang, D. Chen, Y.-B. Cheng and R. A. Caruso, *Adv. Funct. Mater.*, 2015, **25**, 3264.
9 T. Hisatomi, J. Kubota and K. Domen, *Chem. Soc. Rev.*, 2014, **43**, 7520.
10 W.-Q. Wu, Y.-F. Xu, H.-S. Rao, C.-Y. Su and D.-B. Kuang, *J. Am. Chem. Soc.*, 2014, **136**, 6437.
11 F. Z. Huang, D. H. Chen, L. Cao, R. A. Caruso and Y.-B. Cheng, *Energy Environ. Sci.*, 2011, **4**, 2803.
12 E. J. W. Crossland, N. Noel, V. Sivaram, T. Leijtens, J. A. Alexander-Webber and H. J. Snaith, *Nature*, 2013, **495**, 215.
13 D. H. Chen, F. Z. Huang, L. Cao, Y. B. Cheng and R. A. Caruso, *Chem.–Eur. J.*, 2012, **18**, 13762.
14 J. F. Ye, W. Liu, J. G. Cai, S. A. Chen, X. W. Zhao, H. H. Zhou and L. M. Qi, *J. Am. Chem. Soc.*, 2011, **133**, 933.
15 F. Z. Huang, D. H. Chen, Q. Li, R. A. Caruso and Y. B. Cheng, *Appl. Phys. Lett.*, 2012, **100**, 123102.
16 H. X. Li, Z. F. Bian, J. Zhu, D. Q. Zhang, G. S. Li, Y. N. Huo, H. Li and Y. F. Lu, *J. Am. Chem. Soc.*, 2007, **129**, 8406.
17 L. Cao, D. H. Chen and R. A. Caruso, *Angew. Chem., Int. Ed.*, 2013, **52**, 10986.
18 J. B. Joo, I. Lee, M. Dahl, G. D. Moon, F. Zaera and Y. D. Yin, *Adv. Funct. Mater.*, 2013, **23**, 4246.
19 J. H. Pan, Z. Y. Cai, Y. Yu and X. S. Zhao, *J. Mater. Chem.*, 2011, **21**, 11430.
20 X. D. Wang, L. Cao, D. H. Chen and R. A. Caruso, *ACS Appl. Mater. Interfaces*, 2013, **5**, 9421.
21 C. Wu, L. Lei, X. Zhu, J. Yang and Y. Xie, *Small*, 2007, **3**, 1518.
22 J. S. Chen, C. P. Chen, J. Liu, R. Xu, S. Z. Qiao and X. W. Lou, *Chem. Commun.*, 2011, **47**, 2631.
23 L. Cao, D. H. Chen, W. Li and R. A. Caruso, *ACS Appl. Mater. Interfaces*, 2014, **6**, 13129.
24 S. P. Albu, A. Ghicov, J. M. Macak, R. Hahn and P. Schmuki, *Nano Lett.*, 2007, **7**, 1286.
25 H. G. Yang, G. Liu, S. Z. Qiao, C. H. Sun, Y. G. Jin, S. C. Smith, J. Zou, H. M. Cheng and G. Q. Lu, *J. Am. Chem. Soc.*, 2009, **131**, 4078.
26 S. W. Liu, J. G. Yu and M. Jaroniec, *J. Am. Chem. Soc.*, 2010, **132**, 11914.
27 J. H. Pan, X. Z. Wang, Q. Z. Huang, C. Shen, Z. Y. Koh, Q. Wang, A. Engel and D. W. Bahnemann, *Adv. Funct. Mater.*, 2014, **24**, 95.
28 W. Zhou, L. Gai, P. Hu, J. Cui, X. Liu, D. Wang, G. Li, H. Jiang, D. Liu, H. Liu and J. Wang, *CrystEngComm*, 2011, **13**, 6643.
29 W. Zhou, G. Du, P. Hu, G. Li, D. Wang, H. Liu, J. Wang, R. I. Boughton, D. Liu and H. Jiang, *J. Mater. Chem.*, 2011, **21**, 7937.
30 D. H. Chen and R. A. Caruso, *Adv. Funct. Mater.*, 2013, **23**, 1356.
31 H. Liu, Z. Bi, X.-G. Sun, R. R. Unocic, M. P. Paranthaman, S. Dai and G. M. Brown, *Adv. Mater.*, 2011, **23**, 3450.
32 D. H. Chen, L. Cao, F. Z. Huang, P. Imperia, Y. B. Cheng and R. A. Caruso, *J. Am. Chem. Soc.*, 2010, **132**, 4438.
33 C. W. Sun, S. Rajasekhara, J. B. Goodenough and F. Zhou, *J. Am. Chem. Soc.*, 2011, **133**, 2132.
34 X. Wang, M. Y. Liao, Y. T. Zhong, J. Y. Zheng, W. Tian, T. Y. Zhai, C. Y. Zhi, Y. Ma, J. N. A. Yao, Y. Bando and D. Golberg, *Adv. Mater.*, 2012, **24**, 3421.
35 J. G. Yu, Y. R. Su and B. Cheng, *Adv. Funct. Mater.*, 2007, **17**, 1984.
36 A. L. Linsebigler, G. Q. Lu and J. T. Yates, *Chem. Rev.*, 1995, **95**, 735.
37 P. V. Kamat, *Chem. Rev.*, 1993, **93**, 267.
38 N. T. Nolan, M. K. Seery and S. C. Pillai, *J. Phys. Chem. C*, 2009, **113**, 16151.
39 C. H. Kang, L. Q. Jing, T. Guo, H. C. Cui, J. Zhou and H. G. Fu, *J. Phys. Chem. C*, 2009, **113**, 1006.
40 K. Ding, Z. Miao, B. Hu, G. An, Z. Sun, B. Han and Z. Liu, *Langmuir*, 2010, **26**, 10294.
41 D. A. H. Hanaor and C. C. Sorrell, *J. Mater. Sci.*, 2011, **46**, 855.
42 M. Machida, K. Norimoto and T. Kimura, *J. Am. Ceram. Soc.*, 2005, **88**, 95.
43 W. Y. Dong, Y. J. Sun, C. W. Lee, W. M. Hua, X. C. Lu, Y. F. Shi, S. C. Zhang, J. M. Chen and D. Y. Zhao, *J. Am. Chem. Soc.*, 2007, **129**, 13894.
44 D. J. Reidy, J. D. Holmes, C. Nagle and M. A. Morris, *J. Mater. Chem.*, 2005, **15**, 3494.
45 K.-N. P. Kumar, K. Keizer and A. J. Burggraaf, *J. Mater. Chem.*, 1993, **3**, 917.
46 D. Chen and E. H. Jordan, *J. Sol–Gel Sci. Technol.*, 2009, **50**, 44.
47 S. C. Padmanabhan, S. C. Pillai, J. Colreavy, S. Balakrishnan, D. E. McCormack, T. S. Perova, Y. Gun'ko, S. J. Hinder and J. M. Kelly, *Chem. Mater.*, 2007, **19**, 4474.
48 P. Periyat, S. C. Pillai, D. E. McCormack, J. Colreavy and S. J. Hinder, *J. Phys. Chem. C*, 2008, **112**, 7644.
49 M. C. Yan, F. Chen, J. L. Zhang and M. Anpo, *J. Phys. Chem. B*, 2005, **109**, 8673.
50 R. D. Shannon, *J. Appl. Phys.*, 1964, **35**, 3414.
51 J. A. Gamboa and D. M. Pasquevich, *J. Am. Ceram. Soc.*, 1992, **75**, 2934.
52 A. A. Gribb and J. F. Banfield, *Am. Mineral.*, 1997, **82**, 717.
53 J. Klaas, G. SchulzEkloff and N. I. Jaeger, *J. Phys. Chem. B*, 1997, **101**, 1305.
54 J. Tauc, R. Grigorovici and A. Vancu, *Phys. Status Solidi*, 1966, **15**, 627.
55 J. Zhang, Q. Xu, Z. Feng, M. Li and C. Li, *Angew. Chem., Int. Ed.*, 2008, **47**, 1766.
56 J. Zhang, Q. Xu, M. J. Li, Z. C. Feng and C. Li, *J. Phys. Chem. C*, 2009, **113**, 1698.

57 W. I. Nawawi and M. A. Nawi, *J. Mol. Catal. A: Chem.*, 2014, **383–384**, 83.
58 R. L. Penn and J. F. Banfield, *Am. Mineral.*, 1999, **84**, 871.
59 W. Li, C. Ni, H. Lin, C. P. Huang and S. I. Shah, *J. Appl. Phys.*, 2004, **96**, 6663.
60 H. Z. Zhang and J. F. Banfield, *J. Mater. Res.*, 2000, **15**, 437.
61 H. Z. Zhang and J. F. Banfield, *Chem. Rev.*, 2014, **114**, 9613.
62 H. Z. Zhang and J. F. Banfield, *Chem. Mater.*, 2005, **17**, 3421.
63 A. Houas, H. Lachheb, M. Ksibi, E. Elaloui, C. Guillard and J.-M. Herrmann, *Appl. Catal., B*, 2001, **31**, 145.

Electronic Supplementary Information

Monodisperse Anatase Titania Microspheres with High-thermal Stability and Large Pore Size (~80 nm) as Efficient Photocatalysts

Lu Cao,[a] Dehong Chen,[a]* Wu-Qiang Wu,[a] Jeannie Z. Y. Tan[a,b] and Rachel A. Caruso[a,b]*

[a]*Particulate Fluids Processing Centre, School of Chemistry, The University of Melbourne, Melbourne, Victoria 3010 Australia*

[b]*CSIRO Manufacturing, Private Bag 10, Clayton South, Victoria 3169 Australia*

[*]*To whom correspondence should be addressed*

E-mail: dehongc@unimelb.edu.au; rcaruso@unimelb.edu.au

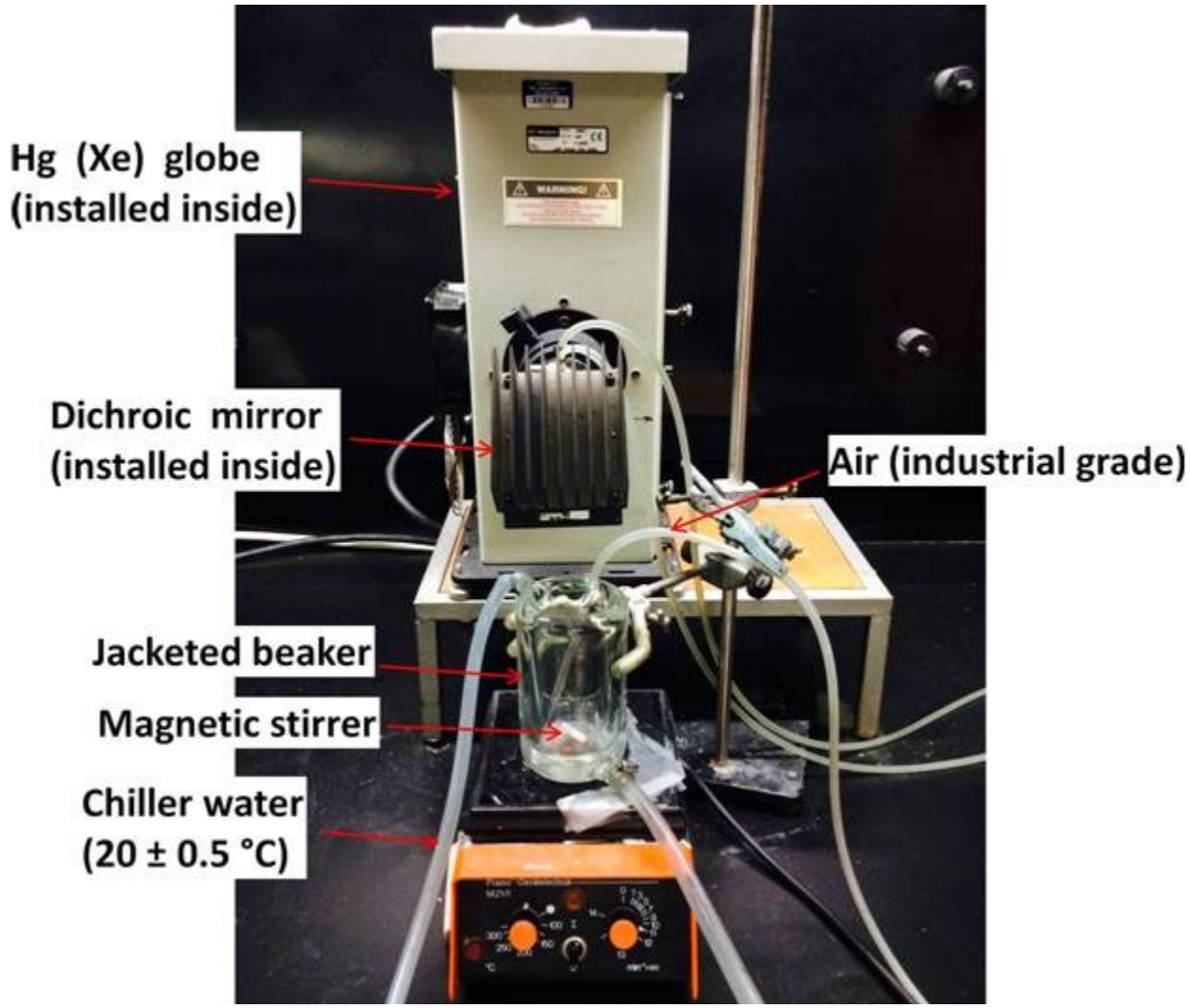

Fig. S1 Experimental set-up for evaluating photocatalytic performance of the titania materials investigated in this study. A dichroic mirror (66226, Oriel) was installed above the jacked beaker to vertically deliver UV light ($280<\lambda<400$ nm) onto the reaction mixture. The UV radiation intensity at the surface of the suspension was 16.7 ± 0.2 mW cm^{-2}.

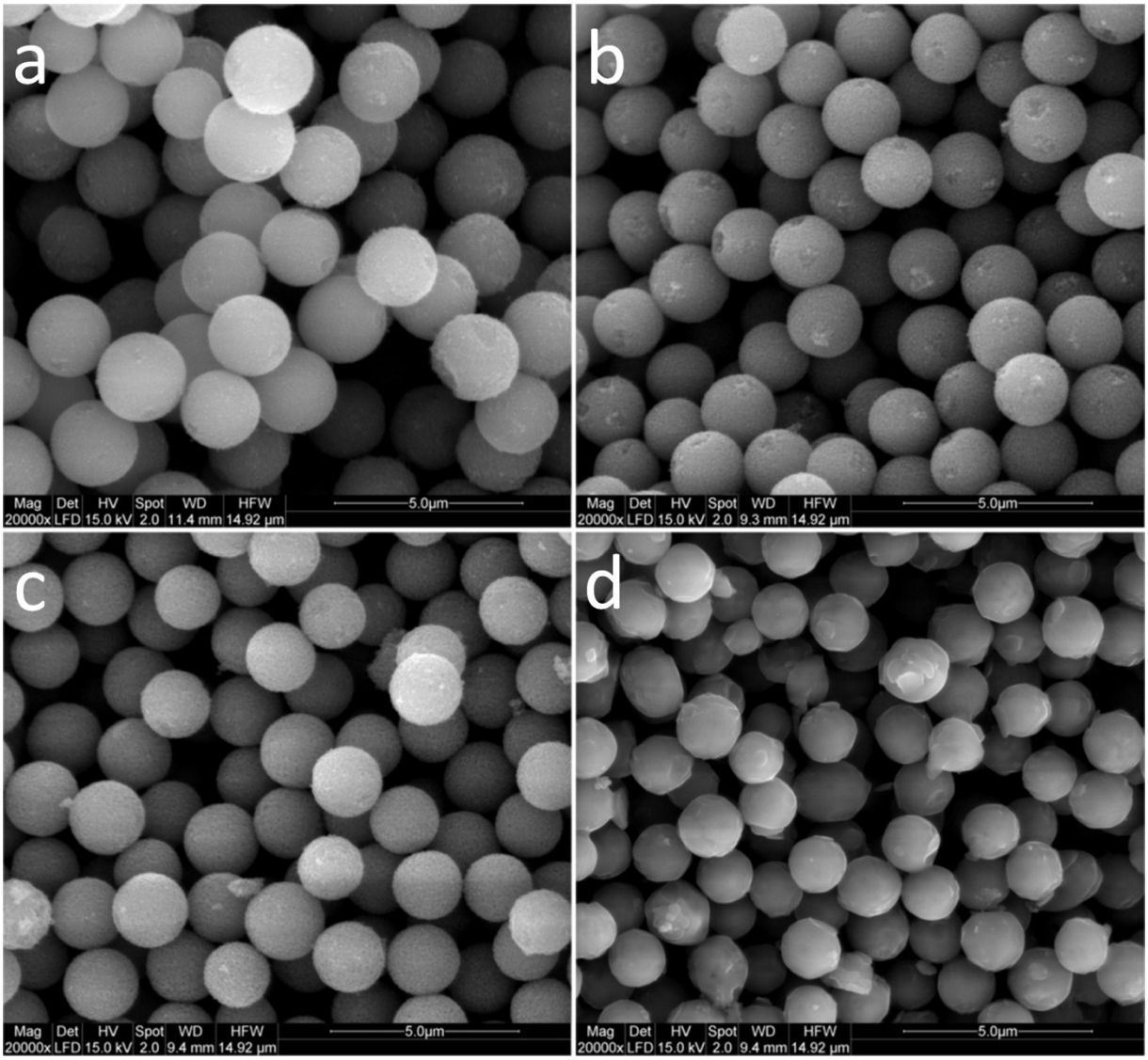

Fig. S2 Low magnification SEM images of (a) the monodisperse titania microspheres (MTS) solvothermally treated at 220 °C in the presence of 4.5 wt.% ammonia solution and the MTS after calcination at (b) 800 °C, (c) 900 °C, and (d) 1000 °C in air. SEM images were taken without metal sputter coating of the samples.

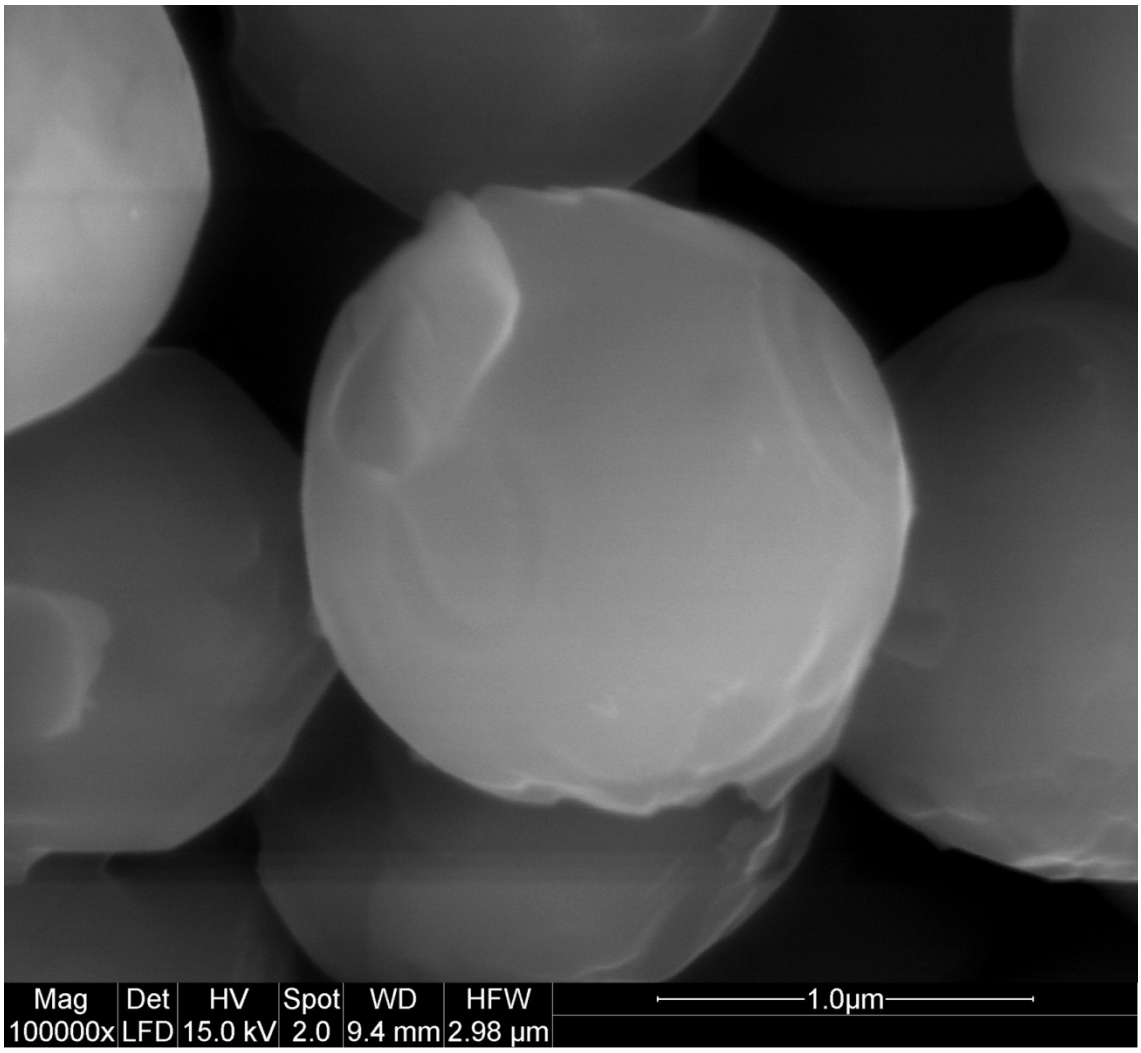

Fig. S3 High magnification SEM image of the monodisperse titania microspheres solvothermally treated at 220 °C in the presence of 4.5 wt.% ammonia solution and calcined at 1000 °C in air. SEM image was taken without metal sputter coating of the sample.

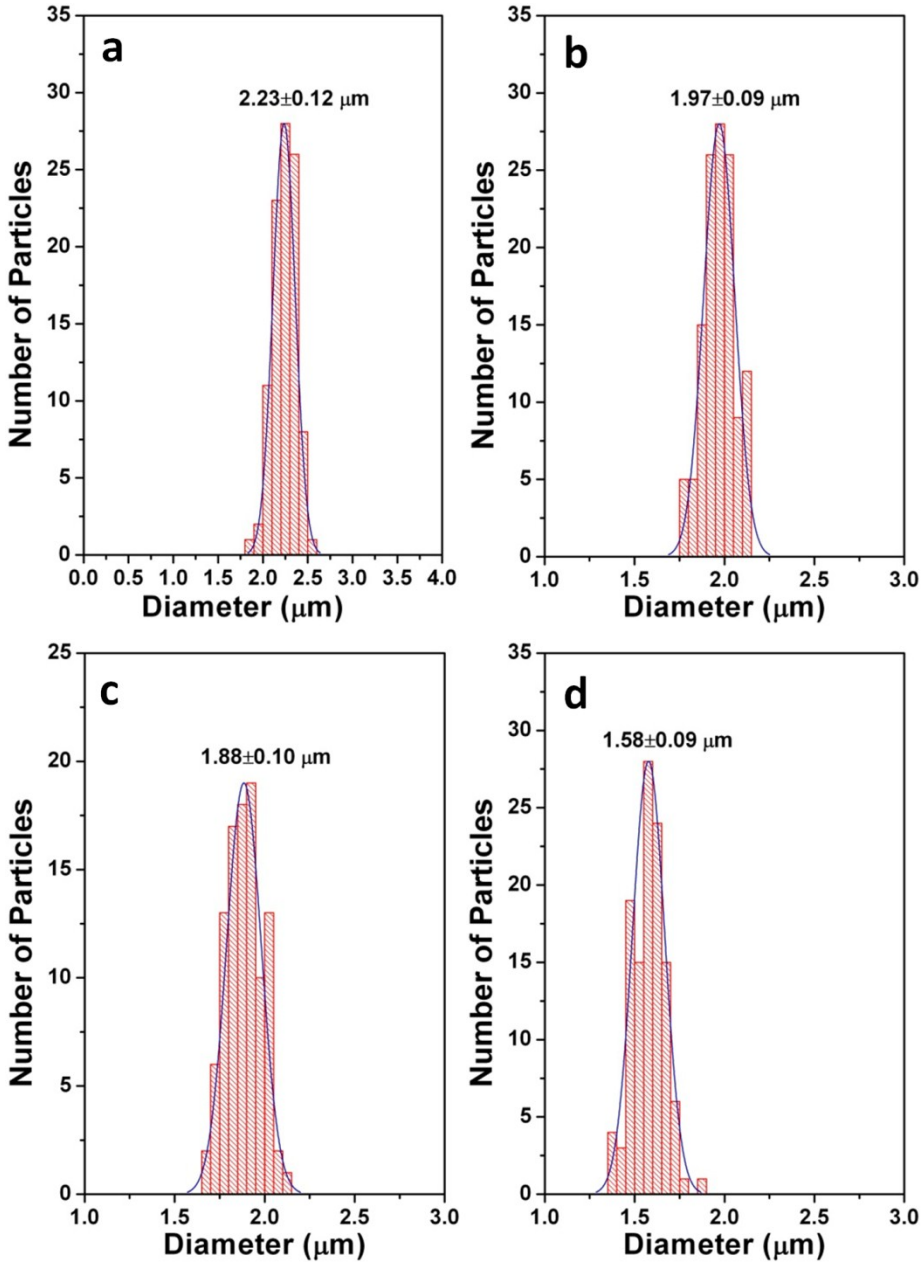

Fig. S4 Histogram of the size distribution of the monodisperse titania spheres solvothermally treated at 220 °C in the presence of 4.5 wt.% ammonia solution (a) and then calcined at 800 °C (b), 900 °C (c), and 1000 °C (d) in air.

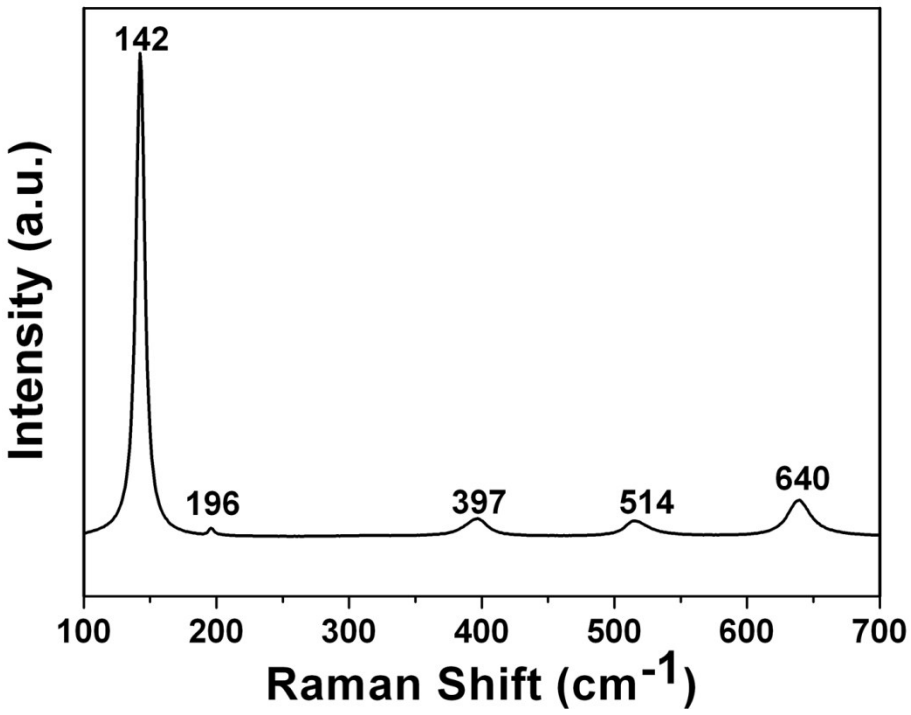

Fig. S5 Raman spectrum of the monodisperse titania spheres solvothermally treated at 220 °C in the presence of 4.5 wt.% ammonia solution then calcined at 900 °C for 2 h in air.

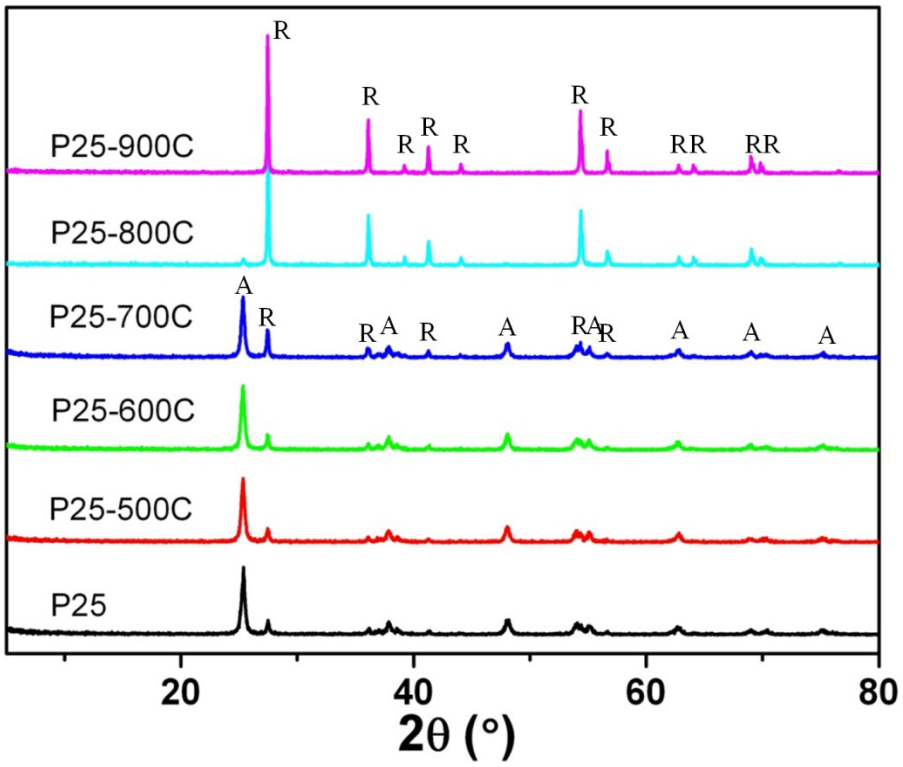

Fig. S6 XRD patterns of the Degussa (Evonik) P25 nanoparticles as obtained and after calcination at temperatures ranging from 500 to 900 °C for 2 h in air. A = Anatase and R = Rutile phase titania.

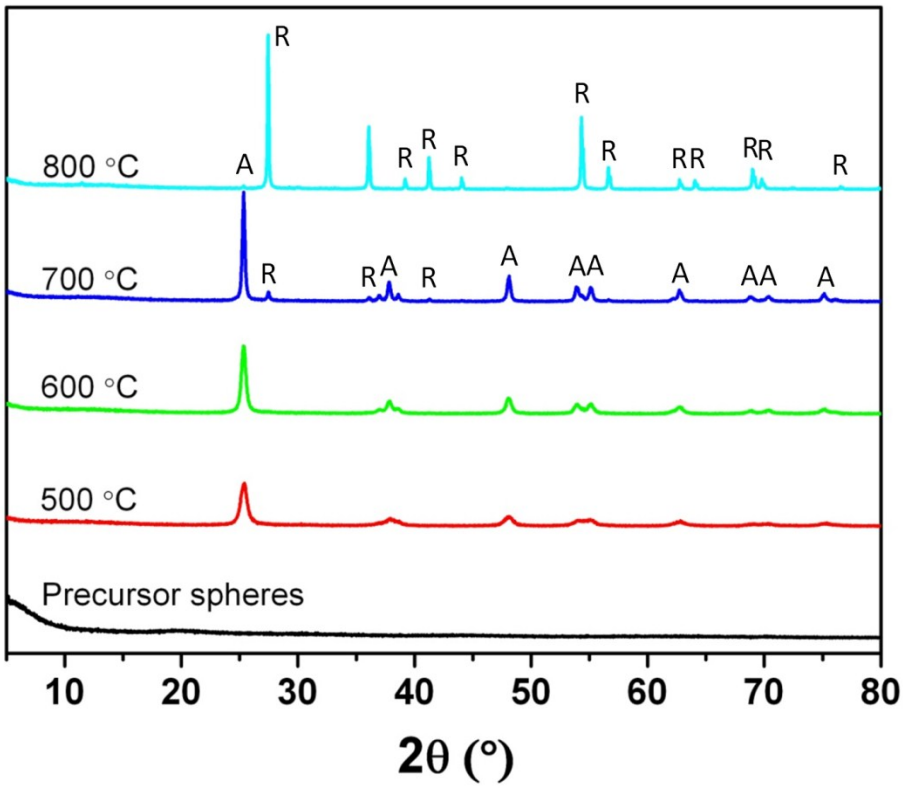

Fig. S7 XRD patterns of the amorphous precursor spheres (APS) and after calcination (without solvothermal treatment) at temperatures ranging from 500 to 800 °C for 2 h in air. A = Anatase and R = Rutile phase titania.

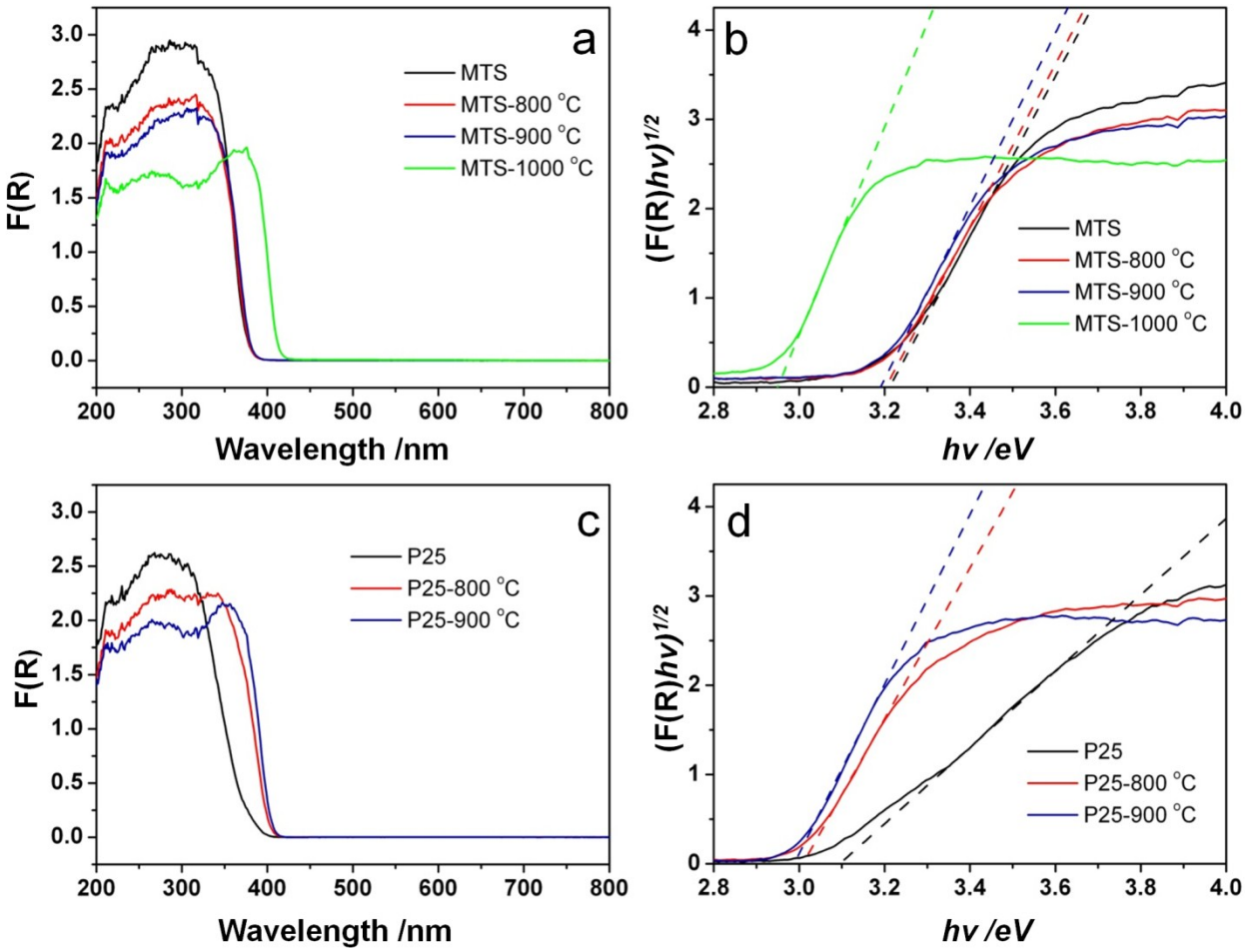

Fig. S8 UV-vis diffuse reflectance spectra of MTS (a) and P25 (c) calcined at varying temperatures for 2 h in air, and the relationship between the transformed Kubelka-Munk function versus the photon energy (b and d) for each material. In (b) and (d), a straight line tangential to the slope was extended to cut the horizontal axis to obtain the band gap energy of the titania samples.[1-3]

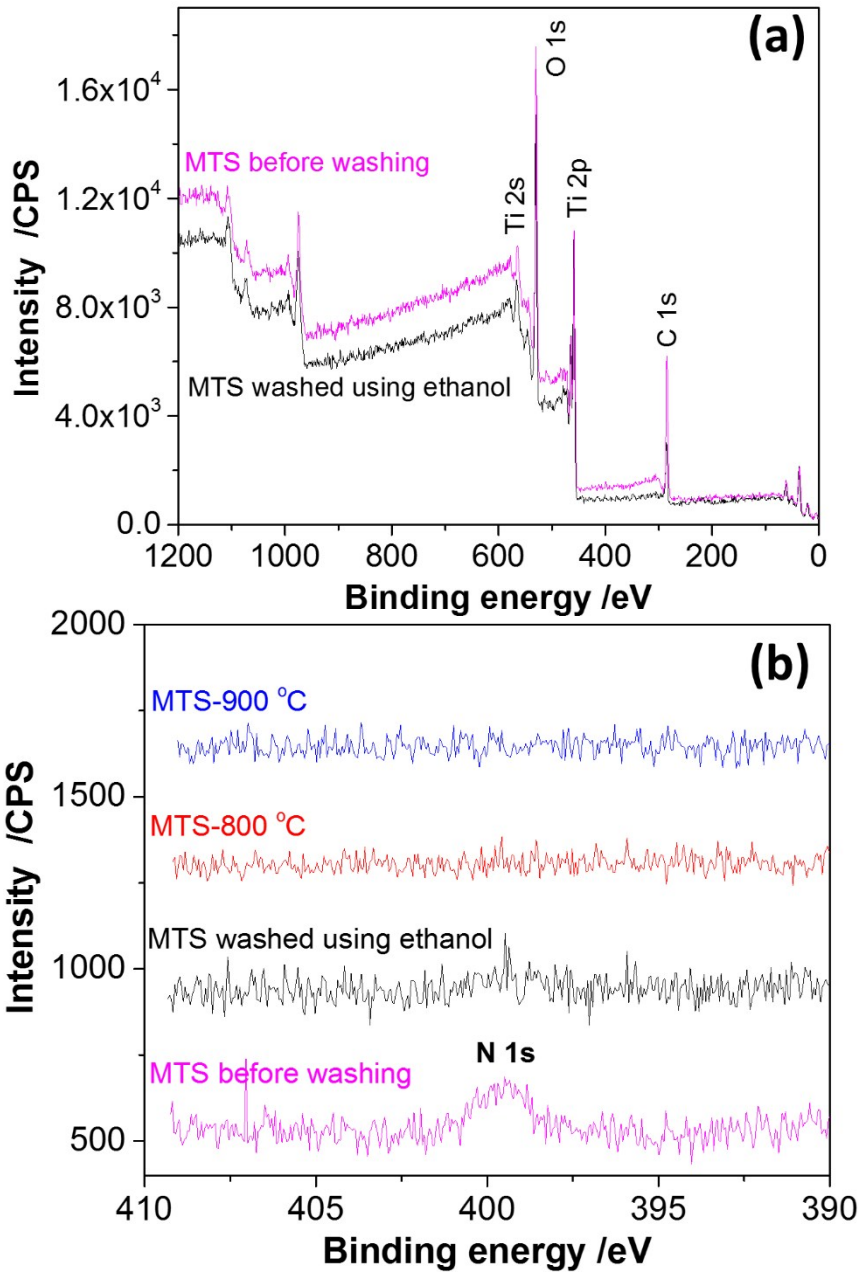

Fig. S9 XPS survey spectra of the MTS sample before and after washing with ethanol (a) and high-resolution N1s XPS spectra (b) of the MTS before washing, MTS washed using ethanol, MTS-800 °C and MTS-900 °C as labelled (the spectra of the MTS washed using ethanol, MTS-800 °C and MTS-900 °C sample were shifted up the vertical axis by 500, 900 and 1200 CPS, respectively).

The X-ray photoelectron spectrometer (XPS) data were recorded on a VG ESCALAB 220i-XL spectrometer (UK) equipped with a twin crystal monochromated Al K_α X-ray source, which emitted a photon energy of 1486.6 eV at 10 kV and 22 mA. Samples were secured onto Al holders and were measured in the analysis chamber at a typical operating pressure of $\sim 7 \times 10^{-9}$ mbar. An electron flood gun was used to compensate the charging effect of non-conductive materials. Spectra were obtained at a step size of either 1.0 eV (survey scans) or 0.05 eV (regional scans). Quantification and curve fitting of XPS spectra were performed using CasaXPS software. The C1s peak at 285.0 eV was used as a reference for the calibration of the binding energy scale.

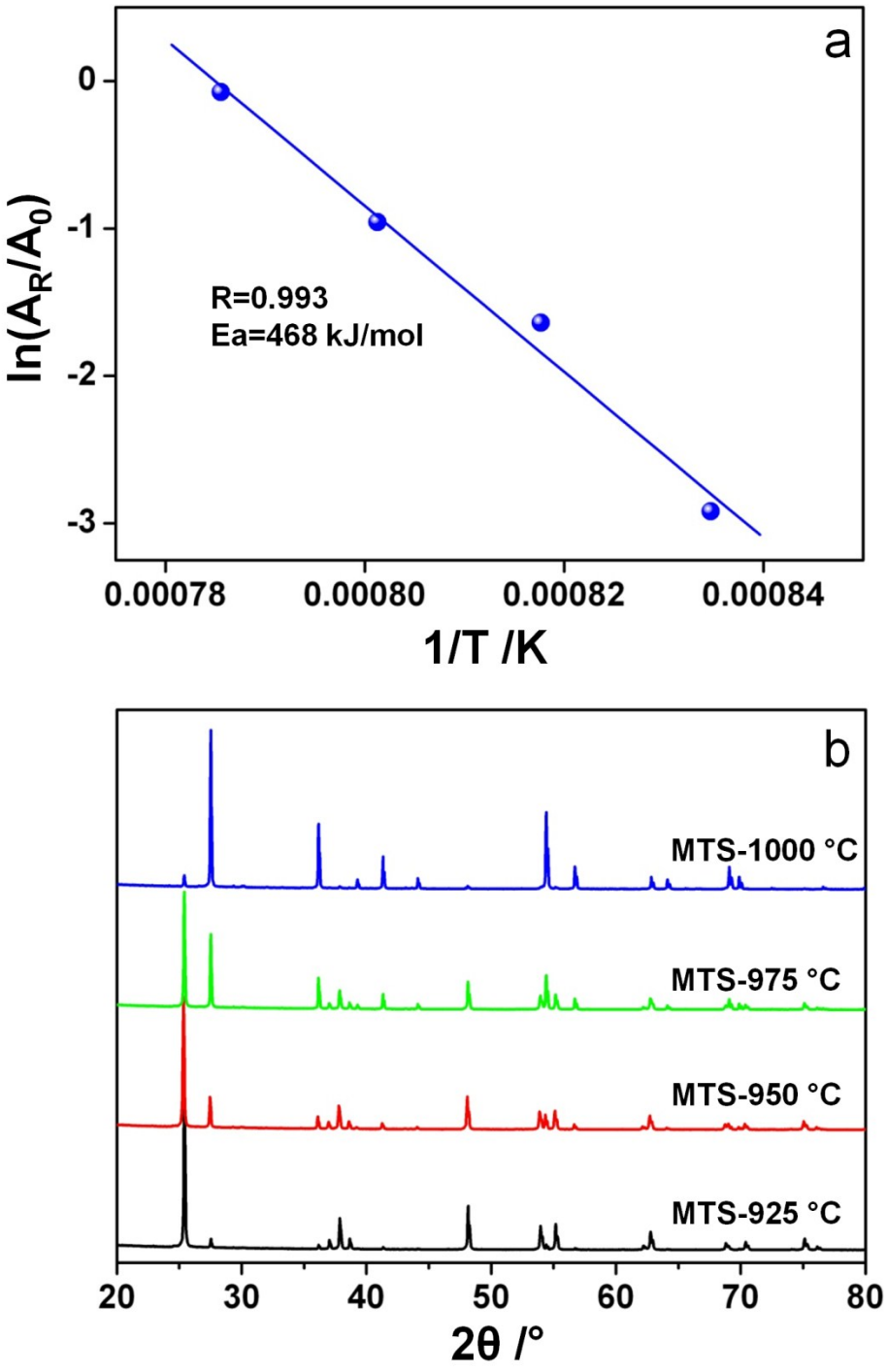

Fig. S10 (a) Arrenhius plot of $\ln(A_R/A_0)$ vs 1/T for activation energy calculations according to a previously reported method.[4] (b) XRD patterns of the MTS calcined at varied temperatures for 2 h (as indicated) in air.

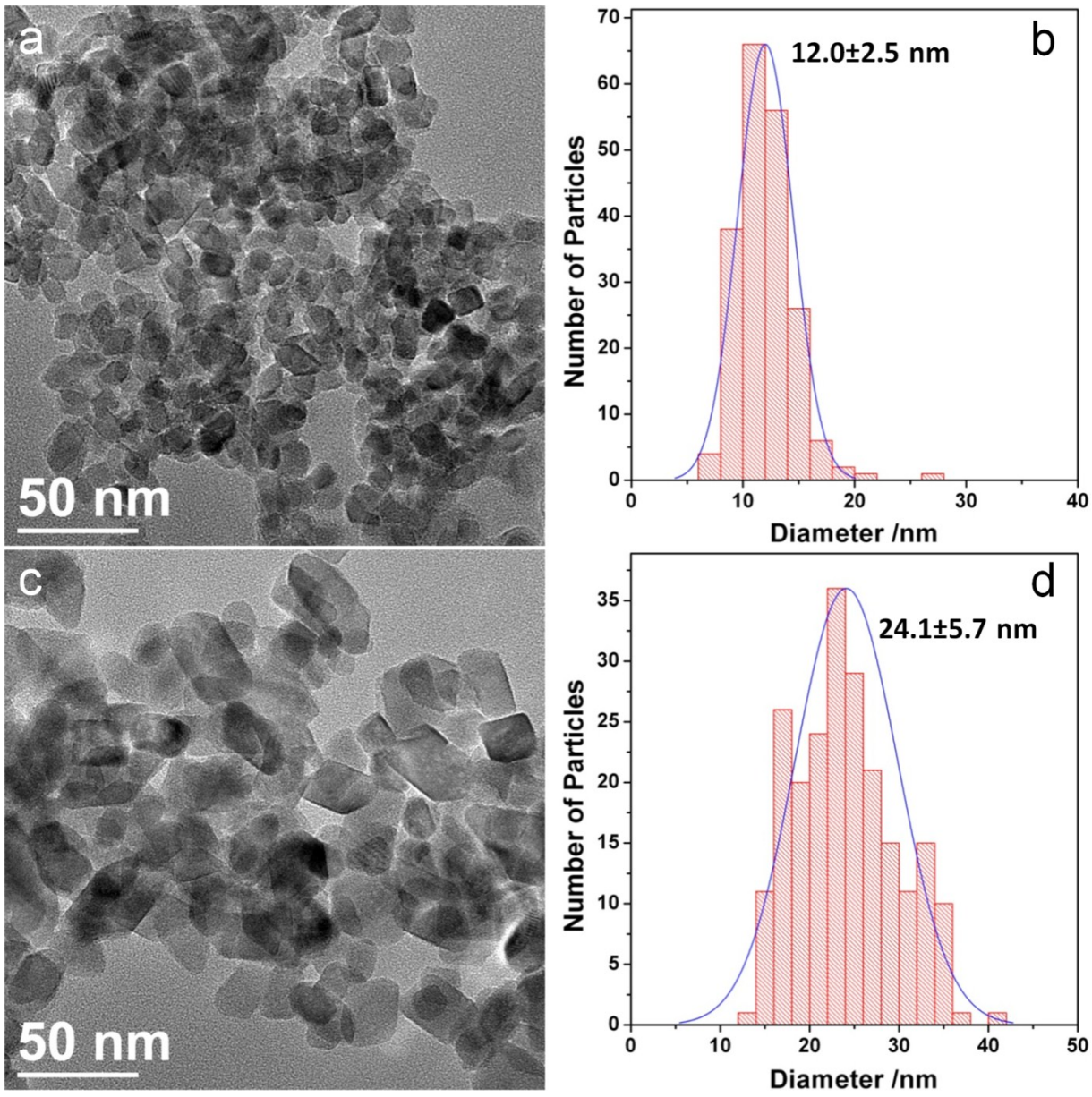

Fig. S11 TEM images (a and c) and equivalent crystal size distribution (b and d) of the MTS solvothermally treated at 220 °C in the absence of ammonia (a and b) and those in the presence of 4.5 wt% ammonia solution (c and d). Note: The average crystal size was estimated by assuming all the particles have a spherical shape. The crystal diameter, D, is given by the equation: $D=2\sqrt{\frac{S}{\pi}}$, where S is the area of the nanocrystal measured using Image J software and π is 3.14.

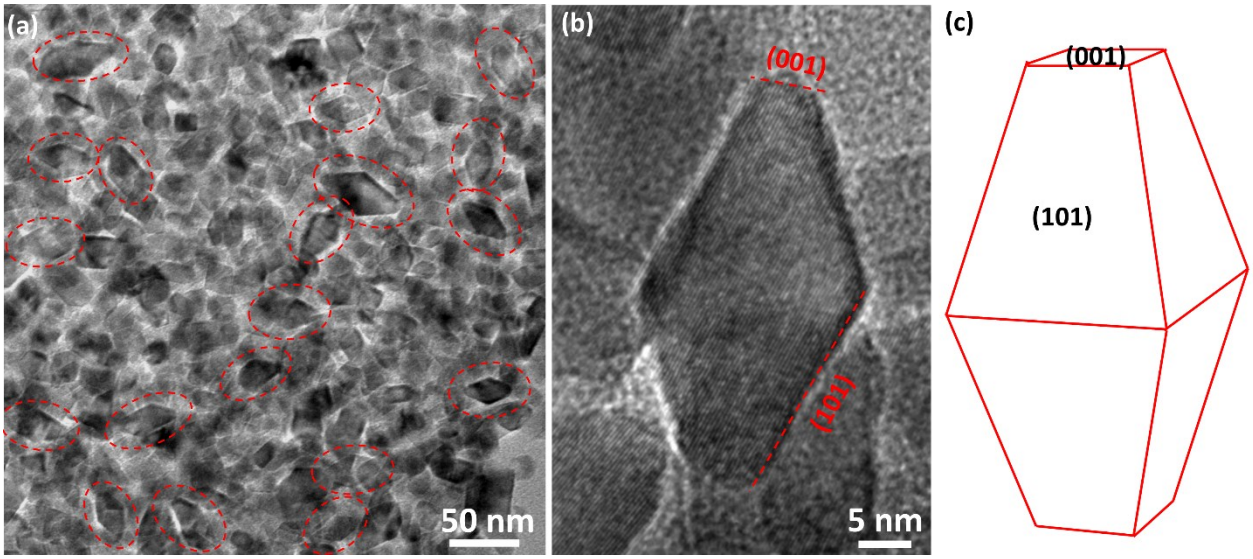

Fig. S12 TEM images (a, b) of the ultramicrotomed MTS-4.5 wt% sample showing the faceted anatase nanocrystals are bipyramid crystals, with {101} (side) and {001} (top) facets exposed. A drawing (c) of a truncated bipyramid anatase crystal is given to indicate the location of {101} and {001} facets.

The reported surface energy values of the {101} and {001} facets are 0.44 J m^{-2} and 0.90 J m^{-2}, respectively.[5] To reduce the surface energy during the crystal growth, the resulting anatase nanocrystals will grow in size gradually minimising the exposure of high energy {001} facets and therefore leading to the final anatase crystals showing a truncated bipyramid crystal habit. This result is in good agreement with previous papers.[6,7]

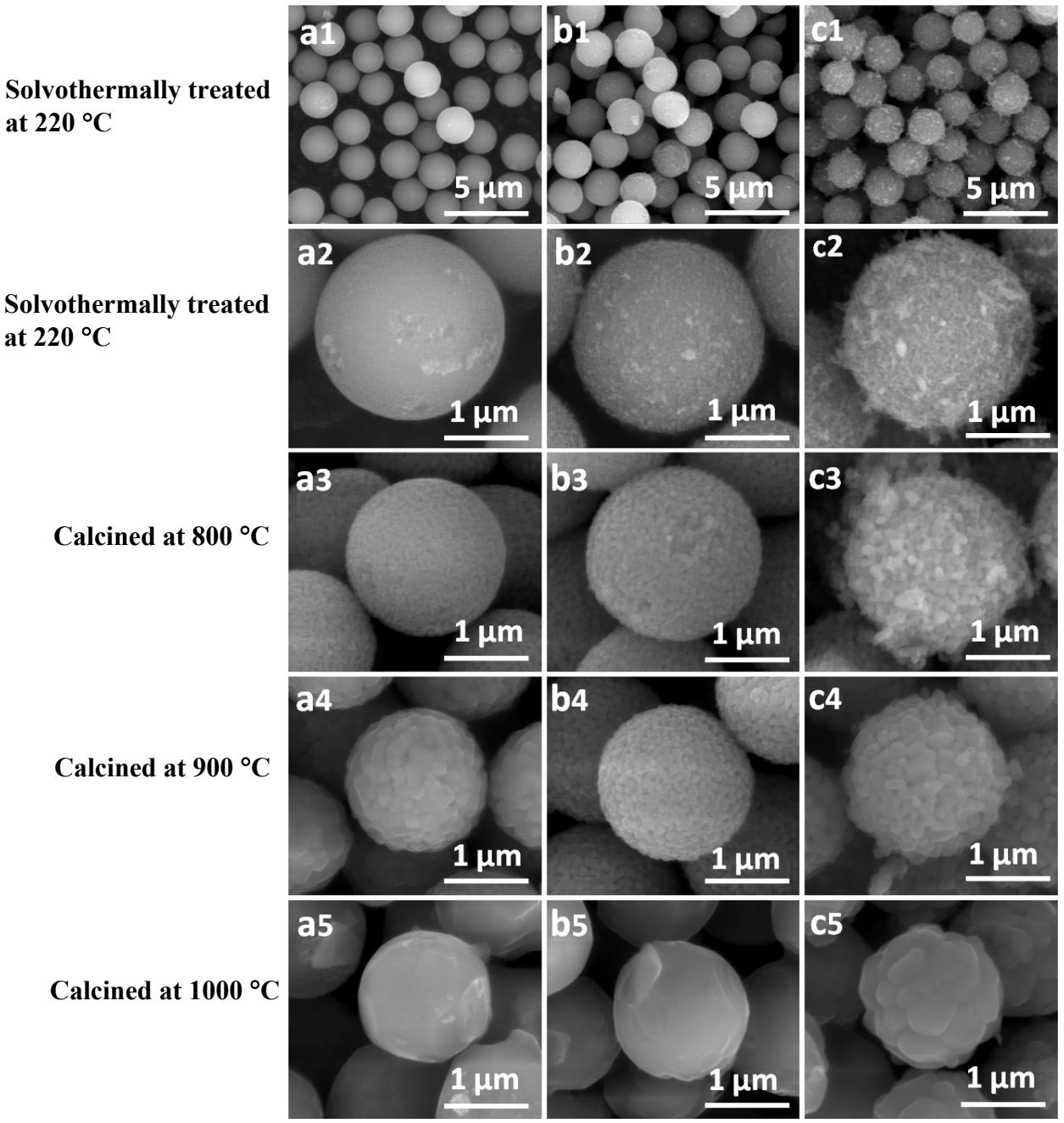

Fig. S13 SEM images of the monodisperse titania spheres solvothermally treated at 220 °C in the presence of 0 (a1 and a2), 4.5 (b1 and b2) and 17.4 wt.% (c1 and c2) ammonia solution and these samples calcined at 800 °C (a3, b3 and c3), 900 °C (a4, b4 and c4), and 1000 °C (a5, b5 and c5). SEM images were taken without metal sputter coating of the samples.

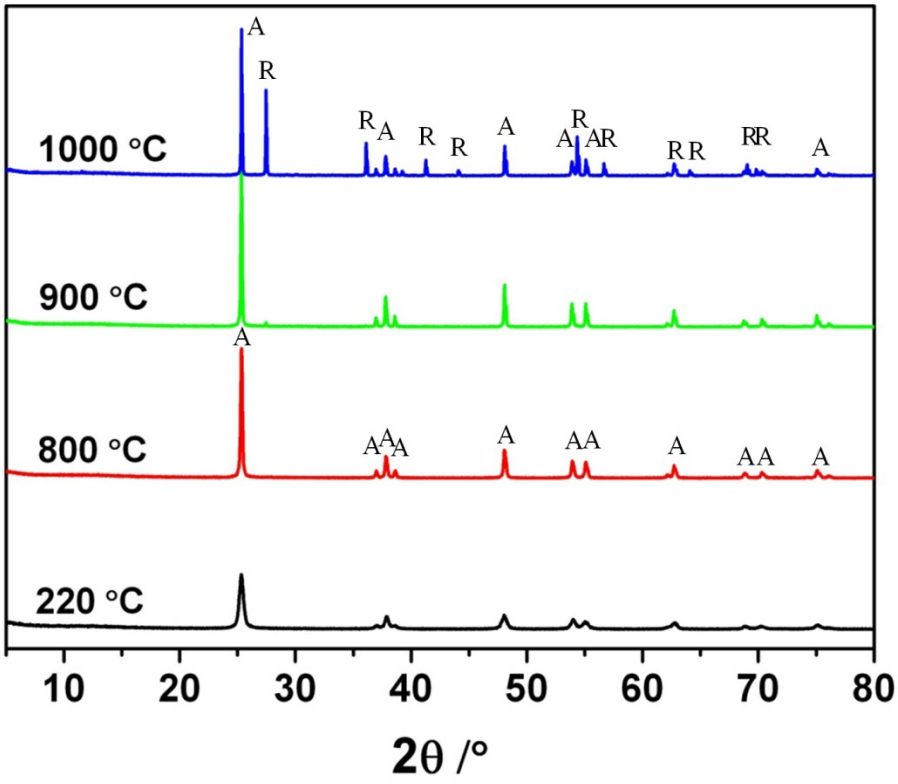

Fig. S14 XRD patterns of the titania microspheres solvothermally treated at 220 °C in the presence of 17.4 wt.% ammonia solution and calcined at diverse temperatures ranging from 800 to 1000 °C for 2 h in air. A = Anatase and R = Rutile phase titania.

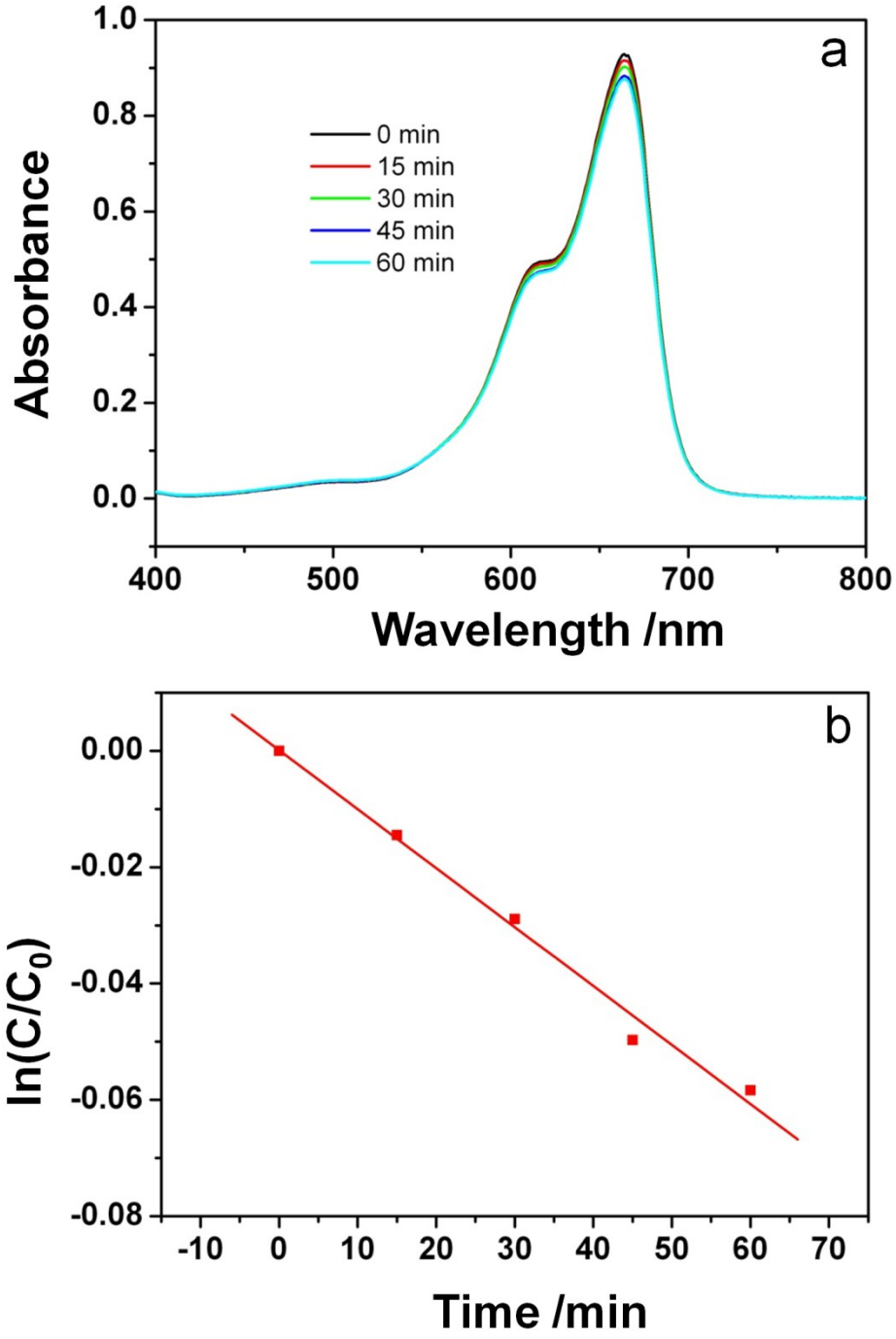

Fig. S15 (a) Time profile of methylene blue (MB) absorbance spectrum and (b) corresponding photodegradation of MB (rate constant: k=0.001 min^{-1}) observed in the absence of photocatalyst under UV light irradiation. The amount of MB photodegraded was obtained by calculating the change of concentration (C/C_0) from the variation of absorbance (A/A_0) at 665 nm. C_0 and A_0 denote initial concentration and absorbance of MB, respectively.

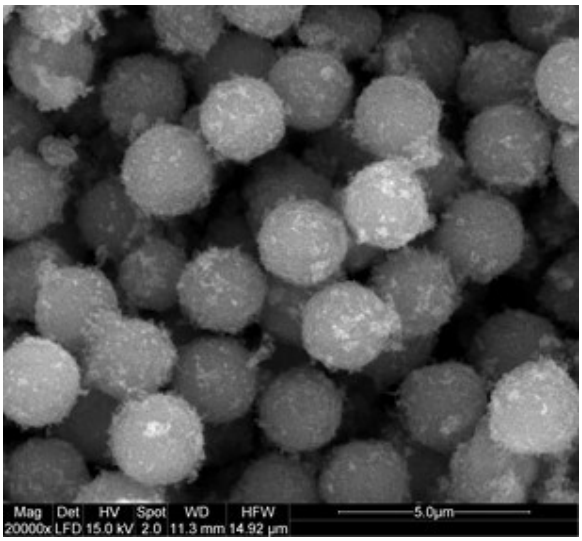

Fig. S16 SEM image of the MTS-4.5 wt%-800 °C sample after the photocatalytic test.

This sample retains its spherical morphology, the nanoparticles on the outer surfaces come from partial damage to the surface layer of the titania microspheres as a result of the continuous stirring during the photocatalytic reaction. These results suggest that the sample has good mechanical stability due to the sintering at high temperature (> 800 °C).

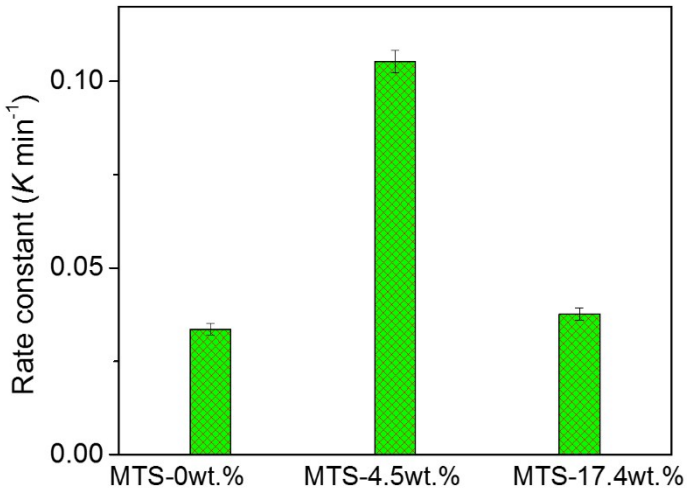

Fig. S17 Comparison of the apparent rate constants for the photocatalytic reactions employing the MTS samples prepared in the presence of different ammonia concentrations and subsequently calcined at 900 °C in air.

Table S1. Phase content and physical properties of the MTS samples calcined at 900 °C in air.

Sample name	**Rutile content (wt.%)**	**Specific surface area ($m^2 g^{-1}$)**	**Pore volume ($cm^3 g^{-1}$)**
MTS-0 wt.% -900 °C	19.6	2.5	0.023
MTS-4.5 wt.% -900 °C	0	10.9	0.123
MTS-17.4 wt.% -900 °C	2.8	6.4	0.061

Specific surface area obtained from adsorption data in the P/P_0 range from 0.05 to 0.20. Pore volume calculated from the adsorption branch at P/P_0=0.98.

Both the MTS-0 wt.% -900 °C and MTS-17.4 wt.% -900 °C sample had a mixed phase titania composition and they had lower specific surface area and porosity than the MTS-4.5 wt.% -900 °C sample. The photocatalytic activities of the MTS-0 wt.% -900 °C and MTS-17.4 wt.% -900 °C samples were inferior to that of MTS-4.5 wt.% calcined at same temperature due to their much reduced specific surface area and porosity, and relatively larger crystal sizes (Shown in Fig. S13 a4, b4 and c4).

References

1 Tauc, J.; Grigorovici, R.; Vancu A. *Phys. Status Solid* **1966**, 15, 627.

2 Klaas, J.; SchulzEkloff, G.; Jaeger N. I. *J. Phys. Chem. B* **1997**, 101, 1305.

3 Cao, G.; Rabenberg, L. K.; Nunn, C. M.; Mallouk, T. E. *Chem. Mater.* **1991**, 3, 149.

4 Li, W.; Ni, C.; Lin, H.; Huang, C. P.; Shah, S. I. *J. Appl. Phys.* **2004**, 96, 6663.

5 Diebold, U. *Surf. Sci. Rep.*, **2003**, 48, 53.

6 Grabowska, E.; Diak, M.; Marchelek, M.; Zaleska, A. *Appl. Catal. B: Environ.* **2014**, 156–157, 213.

7 Liu, G.; Yang, H.: Pan, J.; Yang, Y.; Lu, G. Q.; Cheng, H. M. *Chem. Rev.*, **2014**, 114, 9559.

6.3 References for chapter introduction

1. Zhang, J.; Xu, Q.; Feng, Z.; Li, M.; Li, C., *Angew. Chem. Int. Ed.* **2008**, *47*, 1766-1769.
2. Zhang, H. Z.; Banfield, J. F., *Chem. Rev.* **2014**, *114*, 9613-9644.
3. Zhang, H. Z.; Banfield, J. F., *Chem. Mater.* **2005**, *17*, 3421-3425.
4. Zhang, H. Z.; Banfield, J. F., *J. Mater. Res.* **2000**, *15*, 437-448.
5. Hanaor, D. A. H.; Sorrell, C. C., *J. Mater. Sci.* **2011**, *46*, 855-874.
6. Zhang, J.; Xu, Q.; Li, M. J.; Feng, Z. C.; Li, C., *J. Phys. Chem. C* **2009**, *113*, 1698-1704.

Appendix to this chapter

Intrinsic activities (activity per surface area unit) of the various photocatalysts were calculated and listed in the following table:

Sample	Rate constant (MB min^{-1})	Surface area (m^2 g^{-1})	Activity per surface area (MB min^{-1} m^{-2})
MTS-800 °C	0.1233	17.0	0.09066
MTS-900 °C	0.1053	10.9	0.12076
P25-800 °C	0.0893	14.1	0.07916
P25-900 °C	0.0155	7.10	0.02728

Based on these calculations, it is clear that the mesoporous titania microspheres (MTS) possessed higher activity per surface area unit than P25 treated at the same temperatures, indicating that large pores (~ 80 nm) within the MTS samples can help to retain the accessibility of the photocatalytic reaction sites and therefore enhance their photocatalytic performance.

Chapter 7. Summary and Outlook

7.1 Introduction

This thesis began with an acknowledgement that clean water is essential to the daily activities of human beings (see section 1.1 in Chapter 1). The motivations for the research were condensed in section 1.3 to a single aim, to "prepare TiO_2 materials with tailored nanostructures to enhance their performance in (photo-)catalysis." To realise the aim, three objectives were prescribed (see 1.3), that for the sake of convenience are repeated here in abridgement: (1) control the crystal phase composition of a porous TiO_2 network by sol-gel chemistry and templating; (2) increase the size of amorphous TiO_2 spheres (the precursor material to mesoporous TiO_2 spheres) by changing the synthesis parameters, and; (3) control TiO_2 spheres with specific morphology, pore diameter, surface area, crystallinity and structure evolution by varying the solvothermal conditions.

The following parts of this chapter comprise a summary of the key research findings and how they have addressed the thesis aims (section 7.2), and an outlook for this thesis research as applied to practical water treatment (section 7.3).

7.2 Research Summary

Mixed-phased, hierarchically porous TiO_2 networks (PTN) were successfully prepared through the use of sol-gel chemistry and a templating technique, followed by calcination. In this research, characterisation techniques including scanning electron microscopy (SEM), high resolution transmission electron microscopy (HRTEM), X-ray diffraction (XRD) and nitrogen gas sorption were utilised. By employing an agarose gel template, porous TiO_2 networks were created. The resultant TiO_2 materials showed three-dimensional (3D) interconnected macro-/mesoporous frameworks. Compared to the control sample with a dense structure, PTN materials with large porosity resulted in a decrease in interfacial nucleation of the rutile phase, effectively retarding the anatase-to-rutile phase transformation and crystal growth. The porous TiO_2 photocatalysts possessed controllable rutile contents (from 0 to 100 wt%), reduced crystal sizes, hierarchically porous structure and relatively high specific surface areas up to 71.0 $m^2\ g^{-1}$. The photocatalytic activity was investigated by the degradation of methylene blue (MB) under UV light radiation. It was

concluded that photocatalysis correlated to the anatase : rutile ratio and the specific surface areas of the materials. The highest photocatalytic activity was achieved by PTN materials with a rutile content of 15.4 % obtained by calcining the materials at 600 °C for 6 h.

Micrometre-size, monodisperse precursor TiO_2 spheres with controllable diameters were investigated by varying experimental parameters including the concentration of hexadecylamine (HDA), salt species and concentration, water concentration and the reaction temperature. The size of the precursor sphere was determined by a competitive process between the solubility of Ti oligomers and the hydrolysis rate of titanium isopropoxide (TIP), the TiO_2 precursor. The largest spheres with a diameter of 5.39 ± 0.68 μm were obtained at 50 °C using a reaction molar ratio of TIP:1-Butanol:HDA:H_2O:KCl = $1:83.3:0.375:3:5.5\times10^{-3}$. Crystallized mesoporous TiO_2 spheres were obtained by applying a solvothermal treatment to the precursor spheres; variable pore sizes ranging from 6.4 to 28.8 nm were obtained by adjusting the volume ratio of H_2O, ethanol and ammonia. This research led to the following two studies based on precursor spheres with a diameter of 2.4 μm.

TiO_2 nanostructures with diverse morphologies of spherical 'fluffy' core/shell, yolk/shell and hollow nanostructures were fabricated by applying a one-pot solvothermal crystallization process to 2.4 μm diameter monodisperse precursor TiO_2 spheres. The solvothermal process was performed at a moderate temperature (160 °C) in the presence of a high concentration of ammonia (21.3 wt.%). The morphology was controlled by varying the solvothermal treatment time. Results obtained from a combination of characterisation techniques, SEM, TEM, XRD and thermogravimetric analysis, clearly indicated that the hollowing process started from the outer surface of the microspheres. This study demonstrated a surface seeding and subsequent inward hollowing through an Ostwald ripening process, which led to the formation of the diverse TiO_2 nanostructures. The solvothermally treated nanostructures were readily converted to anatase while still maintaining their overall morphology during calcination. The surface areas of the spherical 'fluffy' core/shell, yolk/shell and hollow nanostructures calcined at 650 °C were all around 40 $m^2\ g^{-1}$, lower than that of commercial Evonik (Degussa) P25 TiO_2 powder (50 $m^2\ g^{-1}$). The photocatalytic activity of the calcined microspheres was investigated by the degradation of MB

under UV light illumination. The hollow anatase microspheres displayed a higher degradation rate (k = 0.075 min^{-1}) than the P25 standard (k = 0.0673 min^{-1}). The superior photocatalytic activity of these anatase hollow structures was attributed to the unique hollow structure that enhanced light harvesting, the hierarchically porous shells ensured fast mass diffusion, and high crystallinity reduced the recombination of photogenerated electrons and holes.

Monodisperse, dopant-free anatase TiO_2 microspheres with high thermal stability were prepared via a facile solvothermal treatment of the parent 2.4 μm diameter amorphous spheres at a relatively high temperature (220 °C) in the presence of a low concentration of ammonia (4.5 wt.%). The solvothermally treated spheres had an average diameter of 2.2 μm, and were comprised of well-crystallized and faceted anatase nanocrystals with a uniform size of 24 nm. The sphere diameter decreased with increased calcination temperature. The resultant materials were wholly anatase phase and had a large pore size (77 nm) after calcination treatment at 900 °C. Possible reasons for the superior thermal stability were investigated. The high temperature stability was primarily attributed to an increased Ti-O-Ti bond strength due to well-developed anatase nanocrystals and a narrow crystal size distribution. The photocatalytic performance of the final TiO_2 microspheres was evaluated by applying them as photocatalysts in the degradation of MB under UV light illumination. Microspheres calcined at 800 or 900 °C displayed higher photocatalytic performance than P25 treated at the same temperatures. The excellent performance of the microspheres calcined at these high temperatures was attributed to: 1) the retention of anatase phase due to the high thermal stability of the materials, which decreased the recombination rate of photogenerated charge carriers; 2) the presence of large pores facilitating the fast diffusion of pollutants and maximizing the light harvesting and utilization efficiency; 3) the high crystallinity induced by solvothermal treatment and subsequent high temperature calcination, which together diminished the recombination rate of the photogenerated charge carriers, prolonging the electron lifetimes and diffusion lengths, and; 4) a higher surface area that provided more active reaction sites.

In conclusion, TiO_2 with diverse nanostructures including hierarchically porous networks, ‘fluffy’ core/shell, yolk/shell and hollow spheres, and high temperature

stable solid spheres with a large pore size were fabricated by the careful combination of sol-gel chemistry directed by agarose gel templating or HDA surfactant, solvothermal treatment and calcination processes. The variously prepared photocatalyts displayed superior photocatalytic activity under UV light, exceeding the photocatalytic activity of the benchmark photocatalyst P25.

7.3 Outlook and perspectives

This thesis focused on the synthesis of TiO_2 with diverse nanostructures and its potential application as a photocatalyst for water treatment. However, there are difficulties to utilize TiO_2 photocatalysis for the purification of large volumes of water for the following four reasons: 1) the photocatalytic reactions take place on the surface of the photocatalyst and thus the reactants (i.e. pollutants) must interact with the photocatalyst surface; 2) light energy density is primarily low in 3D spaces; 3) pure TiO_2 can utilize only a very small amount of the UV light contained in natural sunlight, and; 4) TiO_2 particles must be retrieved from the bulk solution by filtration or sedimentation after treatment, therefore, the removal (and potential recycling) of the photocatalyst makes the treatment process complex and decreases the economic viability of this technology. The above issues could be tackled by immobilizing photocatalysts in a reactor by coating particles on the walls of the reactor to allow for the continuous use of the catalysts. Alternatively, the TiO_2 particles could be entrapped within a membrane structure during the membrane fabrication process. In this case, the composition of the membrane must be well chosen, because the presence of TiO_2 may cause severe destruction to the membrane structure owing to the membrane and TiO_2 being in close physical contact and exposed to both UV light and hydroxyl radicals. Building on the high photocatalytic activity of the TiO_2 spheres achieved in this thesis, the photocatalytic performance could be further enhanced by expanding the activity of TiO_2 to the visible wavelength region through doping with metals, non-metals, or coupling with other semiconductors. For example, a promising coupled photocatalyst, mesoporous TiO_2-WO_3 hybrid microspheres, can be fabricated by employing the methods described in this thesis. Ultimately, overcoming the issues of the photocatalyst-pollutant interaction, light density, poor utilisation of the solar spectrum and photocatalyst recovery or immobilisation will lead to highly efficient TiO_2 photocatalyst systems being developed for successful water treatment.

From both scientific and technological viewpoints, the opportunities and future prospects of photocatalysis would include the following areas/aspects:

1) Exploring and developing novel semiconductor materials with narrow band gap to efficiently absorb visible light for effective photocatalysis; excellent chemical- and photon-stabilities for practical application; precise control of the morphology and components of the photocatalysts to finely-tune both conducting and valence band levels; and optimized internal structures (e.g. local structure, defects, interfaces) to enhance the diffusion of the photogenerated electron and hole, and therefore to extend their lifetimes within the photocatalyst.

2) Extending the applications of the photocatalysts to emerging fields, such as efficient photocatalytic CO_2 reduction and conversion for C1/C2 solar fuels, purification of indoor air by photocatalytic degradation of volatile organic compounds, detoxification of wastewater used for diverse crop disinfection, water treatment of hydroponic culture systems, and other applications related to the photo-induced hydrophilic conversion on surfaces or at interfaces (e.g. anti-fogging coating, self-cleaning exterior construction surface materials, economical and smart cooling using thin layer water evaporation from hydrophilic construction surfaces).

3) Developing new synthesis methods and effective strategies to enable the mass production of high performance photocatalysts via a low cost and environmental friendly procedure. This is a necessary step towards the realization of practical applications of diverse photocatalysts.

It is expected that in the near future, efforts to develop and optimize novel photocatalysts would lead to high performance materials that would result in their industrial production for a range of photocatalytic applications.

Chapter 8. Appendix

8.1 Highlighted in 'Chemistry in Australia' Magazine for Published Paper in Chapter 5

Non-directional polar effects on radical stability

Polar effects on radical stability are traditionally attributed to either resonance effects or dipole effects. The former involves donor–acceptor interactions between specific functional groups that are conjugated or hyperconjugated with one another; the latter involves through-space electrostatic interactions between charged (or partially charge-separated) functional groups. Both types of effects are strongly directional. However, researchers from the Australian National University have now discovered a third type of polar effect that is, in principle, non-directional and requires no conjugation or permanent dipoles (Gryn'ova G., Coote M.L. *J. Am. Chem. Soc.* 2013, **135**, 15392–403). When a localised anion is placed in the vicinity of a delocalised radical, the radical is strongly stabilised compared with its corresponding non-radical derivatives. The effect arises in the enhanced polarisability (i.e. ability to redistribute the electron density in response to an external electric field) of delocalised radicals compared with their corresponding closed-shell counterparts. In this way, the destabilising interaction between a remote negative charge and an unpaired electron is minimised and a greater overall stabilisation of the species (through charge–nuclei attraction) is achieved. The resulting polar effects are surprisingly large and long range, and are likely to be useful in synthesis and harnessed in enzyme catalysis.

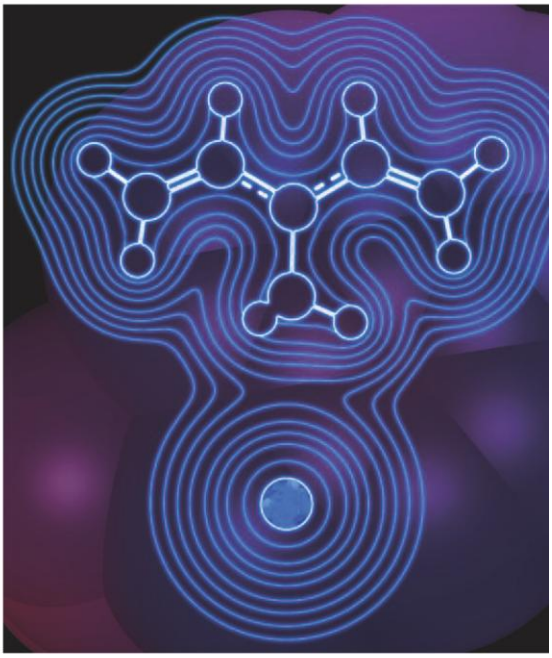

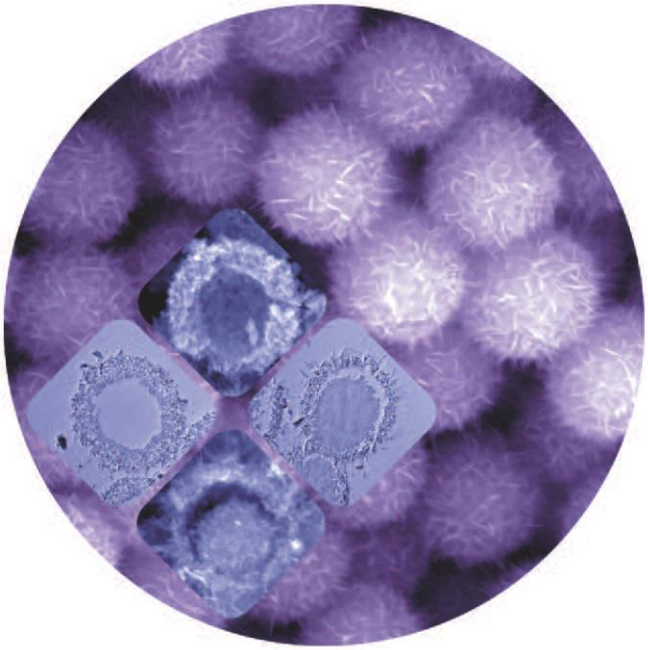

Eat your (nano)heart out

The Ostwald ripening process, a well-known physical phenomenon, has been used to explain the formation of diverse hollow nanostructures for decades; however, direct evidence in support of this mechanism has been lacking. Associate Professor Rachel Caruso, with Dr Dehong Chen and PhD student Lu Cao, from the School of Chemistry, University of Melbourne, have demonstrated unambiguous evidence involving a surface seeding and subsequent inwards hollowing through an Ostwald ripening process for the formation of diverse titania nanostructures (Cao L., Chen D.H., Caruso R.A. *Angew. Chem. Int. Ed.* 2013, **52**, 10986–91). Through a facile and fluorine-free solvothermal approach, anatase nanostructures with sophisticated morphologies, including spherical 'fluffy' core/shell, yolk/shell, and hollow nanostructures, have been prepared. The resulting hollow anatase microspheres exhibit enhanced photocatalytic activity over commercial P25 nanoparticles (a highly efficient titania photocatalyst) under UV light irradiation. This surface-metastable phase mediated synthesis is expected to be extended to the fabrication of a wide variety of functional hollow nanostructures with diverse composition and morphologies in the future.

8.2 Front Cover Image Showing on PFPC 2014 Annual Report for the Published Paper in Chapter 5

Particulate Fluids Processing Centre

A Special Research Centre of the Australian Research Council

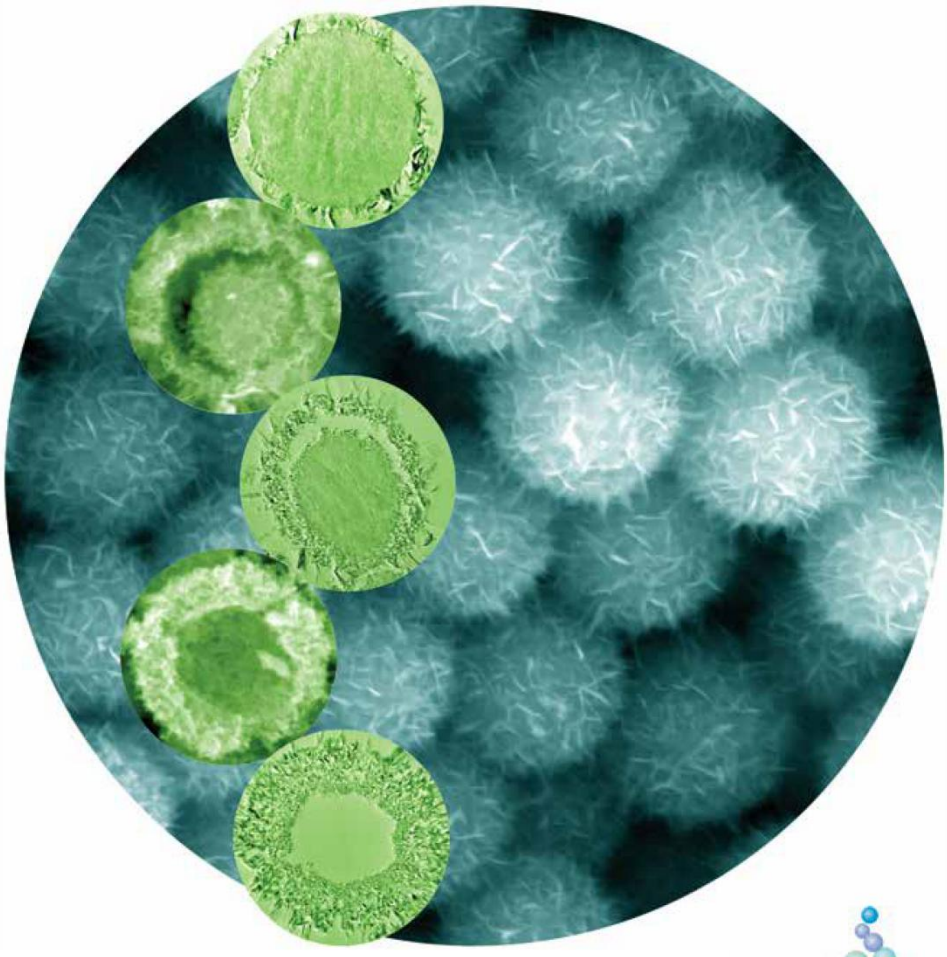

PFPC

2014 Annual Report

8.3 Declaration and Co-author Authorization Forms for a Thesis with Publication

8.3.1 Hierarchically Porous Titania Networks with Tunable Anatase:Rutile Ratios and Their Enhanced Photocatalytic Activities

Declaration for a thesis with publication

THE UNIVERSITY OF MELBOURNE

PhD and MPhil students may include a primary research publication in their thesis in lieu of a chapter if:

- The student contributed greater than 50% of the content in the publication and is the "primary author", ie. the student was responsible primarily for the planning, execution and preparation of the work for publication
- It has been peer-reviewed and accepted for publication
- The student has approval to include the publication in their thesis from their Advisory Committee
- It is a primary publication that reports on original research conducted by the student during their enrolment
- The initial draft of the work was written by the student and any subsequent editing in response to co-authors and editors reviews was performed by the student
- The publication is not subject to any obligations or contractual agreements with a third party that would constrain its inclusion in the thesis

Students must submit this form, along with *Co-author authorisation forms* completed by each co-author, when the thesis is submitted to the Thesis Examination System: *https://tes.app.unimelb.edu.au/*. If you are including multiple publications in your thesis you will need to complete a separate form for each publication. Further information on this policy is available at: *gradresearch.unimelb.edu.au/preparing-my-thesis/thesis-with-publication*

A. PUBLICATION DETAILS *(to be completed by the student)*

Full title	Hierarchically Porous Titania Networks with Tunable Anatase:Rutile Ratios and Their Enhanced Photocatalytic Activities	
Authors	Lu Cao, Dehong Chen, Wei Li, Rachel A. Caruso	
Student's contribution (%)	70%	
Journal or book name	ACS Applied Materials & Interfaces	
Volume/page numbers	6/13129–13137	
Status	☐ Accepted and In press ☒ Published	Date accepted/ published 23/07/2014

B. STUDENT'S DECLARATION

I declare that the publication above meets the requirements to be included in the thesis

Student's name	Student's signature	Date *(dd/mm/yy)*
Lu Cao		28/01/2017

C. PRINCIPAL SUPERVISOR'S DECLARATION

I declare that:

- the information above is accurate
- The advisory committee has met and agreed to the inclusion of this publication in the student's thesis
- All of the co-authors of the publication have reviewed the above information and have agreed to its veracity
- 'Co-Author Authorisation' forms for each co-author are attached.

Supervisor's name	Supervisor's signature	Date *(dd/mm/yy)*
Rachel A. Caruso	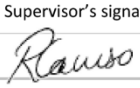	28/01/2017

The University of Melbourne
CRICOS Provider Number: 00116K

Last Updated 17 August 2015

Co-author authorisation form

THE UNIVERSITY OF MELBOURNE

All co-authors must complete this form. By signing below co-authors agree to the listed publication being included in the student's thesis and that the student contributed greater than 50% of the content of the publication and is the "primary author" ie. the student was responsible primarily for the planning, execution and preparation of the work for publication.

In cases where all members of a large consortium are listed as authors of a publication, only those that actively collaborated with the student on material contained within the thesis should complete this form. This form is to be used in conjunction with the *Declaration for a thesis with publication form*.

Students must submit this form, along with the *Declaration for thesis with publication form*, when the thesis is submitted to the Thesis Examination System: *https://tes.app.unimelb.edu.au/*

Further information on this policy and the requirements is available at:
gradresearch.unimelb.edu.au/preparing-my-thesis/thesis-with-publication

A. PUBLICATION DETAILS *(to be completed by the student)*

Full title	Hierarchically Porous Titania Networks with Tunable Anatase:Rutile Ratios and Their Enhanced Photocatalytic Activities	
Authors	Lu Cao, Dehong Chen, Wei Li, Rachel A. Caruso	
Student's contribution (%)	70%	
Journal or book name	ACS Applied Materials & Interfaces	
Volume/page numbers	6/13129–13137	
Status	☐ Accepted and In-press ☒ Published	Date accepted/published 23/07/2014

B. CO-AUTHOR'S DECLARATION *(to be completed by the collaborator)*

I authorise the inclusion of this publication in the student's thesis and certify that:

- the declaration made by the student on the *Declaration for a thesis with publication form* correctly reflects the extent of the student's contribution to this work;
- the student contributed greater than 50% of the content of the publication and is the "primary author" ie. the student was responsible primarily for the planning, execution and preparation of the work for publication.

Co-author's name	Co-author's signature	Date *(dd/mm/yy)*
Rachel A. Caruso		28/01/2017

Co-author authorisation form

THE UNIVERSITY OF MELBOURNE

All co-authors must complete this form. By signing below co-authors agree to the listed publication being included in the student's thesis and that the student contributed greater than 50% of the content of the publication and is the "primary author" ie. the student was responsible primarily for the planning, execution and preparation of the work for publication.

In cases where all members of a large consortium are listed as authors of a publication, only those that actively collaborated with the student on material contained within the thesis should complete this form. This form is to be used in conjunction with the *Declaration for a thesis with publication form*.

Students must submit this form, along with the *Declaration for thesis with publication form*, when the thesis is submitted to the Thesis Examination System: *https://tes.app.unimelb.edu.au/*

Further information on this policy and the requirements is available at:
gradresearch.unimelb.edu.au/preparing-my-thesis/thesis-with-publication

A. PUBLICATION DETAILS *(to be completed by the student)*

Full title	Hierarchically Porous Titania Networks with Tunable Anatase:Rutile Ratios and Their Enhanced Photocatalytic Activities	
Authors	Lu Cao, Dehong Chen, Wei Li, Rachel A. Caruso	
Student's contribution (%)	70%	
Journal or book name	ACS Applied Materials & Interfaces	
Volume/page numbers	6/13129–13137	
Status	☐ Accepted and In-press ☒ Published	Date accepted/published 23/07/2014

B. CO-AUTHOR'S DECLARATION *(to be completed by the collaborator)*

I authorise the inclusion of this publication in the student's thesis and certify that:

- the declaration made by the student on the *Declaration for a thesis with publication form* correctly reflects the extent of the student's contribution to this work;
- the student contributed greater than 50% of the content of the publication and is the "primary author" ie. the student was responsible primarily for the planning, execution and preparation of the work for publication.

Co-author's name	Co-author's signature	Date *(dd/mm/yy)*
Dehong Chen	Dehong Chen	28/01/2017

Co-author authorisation form

THE UNIVERSITY OF MELBOURNE

All co-authors must complete this form. By signing below co-authors agree to the listed publication being included in the student's thesis and that the student contributed greater than 50% of the content of the publication and is the "primary author" ie. the student was responsible primarily for the planning, execution and preparation of the work for publication.

In cases where all members of a large consortium are listed as authors of a publication, only those that actively collaborated with the student on material contained within the thesis should complete this form. This form is to be used in conjunction with the *Declaration for a thesis with publication form*.

Students must submit this form, along with the *Declaration for thesis with publication form*, when the thesis is submitted to the Thesis Examination System: *https://tes.app.unimelb.edu.au/*

Further information on this policy and the requirements is available at:
gradresearch.unimelb.edu.au/preparing-my-thesis/thesis-with-publication

A. PUBLICATION DETAILS *(to be completed by the student)*

Full title	Hierarchically Porous Titania Networks with Tunable Anatase:Rutile Ratios and Their Enhanced Photocatalytic Activities
Authors	Lu Cao, Dehong Chen, Wei Li, Rachel A. Caruso
Student's contribution (%)	70%
Journal or book name	ACS Applied Materials & Interfaces
Volume/page numbers	6/13129–13137
Status	☐ Accepted and In-press ☒ Published Date accepted/published 23/07/2014

B. CO-AUTHOR'S DECLARATION *(to be completed by the collaborator)*

I authorise the inclusion of this publication in the student's thesis and certify that:

- the declaration made by the student on the *Declaration for a thesis with publication form* correctly reflects the extent of the student's contribution to this work;
- the student contributed greater than 50% of the content of the publication and is the "primary author" ie. the student was responsible primarily for the planning, execution and preparation of the work for publication.

Co-author's name	Co-author's signature	Date *(dd/mm/yy)*
Wei Li		28/01/2017

8.3.2 Surface-Metastable Phase Initiated Seeding and Ostwald Ripening: A Facile Fluorine-Free Process towards Spherical Fluffy Core/Shell, Yolk/Shell, and Hollow Anatase Nanostructures

Declaration for a thesis with publication

THE UNIVERSITY OF MELBOURNE

PhD and MPhil students may include a primary research publication in their thesis in lieu of a chapter if:

- The student contributed greater than 50% of the content in the publication and is the "primary author", ie. the student was responsible primarily for the planning, execution and preparation of the work for publication
- It has been peer-reviewed and accepted for publication
- The student has approval to include the publication in their thesis from their Advisory Committee
- It is a primary publication that reports on original research conducted by the student during their enrolment
- The initial draft of the work was written by the student and any subsequent editing in response to co-authors and editors reviews was performed by the student
- The publication is not subject to any obligations or contractual agreements with a third party that would constrain its inclusion in the thesis

Students must submit this form, along with *Co-author authorisation forms* completed by each co-author, when the thesis is submitted to the Thesis Examination System: *https://tes.app.unimelb.edu.au/*. If you are including multiple publications in your thesis you will need to complete a separate form for each publication. Further information on this policy is available at: *gradresearch.unimelb.edu.au/preparing-my-thesis/thesis-with-publication*

A. PUBLICATION DETAILS *(to be completed by the student)*

Full title	Surface-Metastable Phase Initiated Seeding and Ostwald Ripening: A Facile Fluorine-Free Process towards Spherical Fluffy Core/Shell, Yolk/Shell, and Hollow Anatase Nanostructures	
Authors	Lu Cao, Dehong Chen, Rachel A. Caruso	
Student's contribution (%)	70%	
Journal or book name	Angewandte Chemie International Edition	
Volume/page numbers	52/10986-10991	
Status	☐ Accepted and In press ☒ Published	Date accepted/ published 23/08/2013

B. STUDENT'S DECLARATION

I declare that the publication above meets the requirements to be included in the thesis

Student's name	Student's signature	Date *(dd/mm/yy)*
Lu Cao		28/01/2017

C. PRINCIPAL SUPERVISOR'S DECLARATION

I declare that:

- the information above is accurate
- The advisory committee has met and agreed to the inclusion of this publication in the student's thesis
- All of the co-authors of the publication have reviewed the above information and have agreed to its veracity
- 'Co-Author Authorisation' forms for each co-author are attached.

Supervisor's name	Supervisor's signature	Date *(dd/mm/yy)*
Rachel A. Caruso		28/01/2017

The University of Melbourne
CRICOS Provider Number: 00116K

Last Updated 17 August 2015

Co-author authorisation form

THE UNIVERSITY OF MELBOURNE

All co-authors must complete this form. By signing below co-authors agree to the listed publication being included in the student's thesis and that the student contributed greater than 50% of the content of the publication and is the "primary author" ie. the student was responsible primarily for the planning, execution and preparation of the work for publication.

In cases where all members of a large consortium are listed as authors of a publication, only those that actively collaborated with the student on material contained within the thesis should complete this form. This form is to be used in conjunction with the *Declaration for a thesis with publication form*.

Students must submit this form, along with the *Declaration for thesis with publication form*, when the thesis is submitted to the Thesis Examination System: *https://tes.app.unimelb.edu.au/*

Further information on this policy and the requirements is available at:
gradresearch.unimelb.edu.au/preparing-my-thesis/thesis-with-publication

A. PUBLICATION DETAILS *(to be completed by the student)*

Full title	Surface-Metastable Phase Initiated Seeding and Ostwald Ripening: A Facile Fluorine-Free Process towards Spherical Fluffy Core/Shell, Yolk/Shell, and Hollow Anatase Nanostructures	
Authors	Lu Cao, Dehong Chen, Rachel A. Caruso	
Student's contribution (%)	70%	
Journal or book name	Angewandte Chemie International Edition	
Volume/page numbers	52/10986-10991	
Status	☐ Accepted and In-press ☒ Published	Date accepted/published 23/08/2013

B. CO-AUTHOR'S DECLARATION *(to be completed by the collaborator)*

I authorise the inclusion of this publication in the student's thesis and certify that:

- the declaration made by the student on the *Declaration for a thesis with publication form* correctly reflects the extent of the student's contribution to this work;
- the student contributed greater than 50% of the content of the publication and is the "primary author" ie. the student was responsible primarily for the planning, execution and preparation of the work for publication.

Co-author's name	Co-author's signature	Date *(dd/mm/yy)*
Rachel A. Caruso	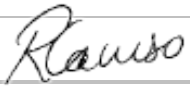	28/01/2017

Co-author authorisation form

THE UNIVERSITY OF MELBOURNE

All co-authors must complete this form. By signing below co-authors agree to the listed publication being included in the student's thesis and that the student contributed greater than 50% of the content of the publication and is the "primary author" ie. the student was responsible primarily for the planning, execution and preparation of the work for publication.

In cases where all members of a large consortium are listed as authors of a publication, only those that actively collaborated with the student on material contained within the thesis should complete this form. This form is to be used in conjunction with the *Declaration for a thesis with publication form*.

Students must submit this form, along with the *Declaration for thesis with publication form*, when the thesis is submitted to the Thesis Examination System: *https://tes.app.unimelb.edu.au/*

Further information on this policy and the requirements is available at:
gradresearch.unimelb.edu.au/preparing-my-thesis/thesis-with-publication

A. PUBLICATION DETAILS *(to be completed by the student)*

Full title	Surface-Metastable Phase Initiated Seeding and Ostwald Ripening: A Facile Fluorine-Free Process towards Spherical Fluffy Core/Shell, Yolk/Shell, and Hollow Anatase Nanostructures	
Authors	Lu Cao, Dehong Chen, Rachel A. Caruso	
Student's contribution (%)	70%	
Journal or book name	Angewandte Chemie International Edition	
Volume/page numbers	52/10986-10991	
Status	☐ Accepted and In-press ☒ Published	Date accepted/published 23/08/2013

B. CO-AUTHOR'S DECLARATION *(to be completed by the collaborator)*

I authorise the inclusion of this publication in the student's thesis and certify that:

- the declaration made by the student on the *Declaration for a thesis with publication form* correctly reflects the extent of the student's contribution to this work;
- the student contributed greater than 50% of the content of the publication and is the "primary author" ie. the student was responsible primarily for the planning, execution and preparation of the work for publication.

Co-author's name	Co-author's signature	Date *(dd/mm/yy)*
Dehong Chen		28/01/2017

8.3.3 Monodisperse Anatase Titania Microspheres with High-thermal Stability and Large Pore Size (~80 nm) as Efficient Photocatalysts

Declaration for a thesis with publication

THE UNIVERSITY OF MELBOURNE

PhD and MPhil students may include a primary research publication in their thesis in lieu of a chapter if:

- The student contributed greater than 50% of the content in the publication and is the "primary author", ie. the student was responsible primarily for the planning, execution and preparation of the work for publication
- It has been peer-reviewed and accepted for publication
- The student has approval to include the publication in their thesis from their Advisory Committee
- It is a primary publication that reports on original research conducted by the student during their enrolment
- The initial draft of the work was written by the student and any subsequent editing in response to co-authors and editors reviews was performed by the student
- The publication is not subject to any obligations or contractual agreements with a third party that would constrain its inclusion in the thesis

Students must submit this form, along with *Co-author authorisation forms* completed by each co-author, when the thesis is submitted to the Thesis Examination System: *https://tes.app.unimelb.edu.au/*. If you are including multiple publications in your thesis you will need to complete a separate form for each publication. Further information on this policy is available at: *gradresearch.unimelb.edu.au/preparing-my-thesis/thesis-with-publication*

A. PUBLICATION DETAILS *(to be completed by the student)*

Full title	Monodisperse Anatase Titania Microspheres with High-thermal Stability and Large Pore Size (~80 nm) as Efficient Photocatalysts	
Authors	Lu Cao, Dehong Chen, Wu-Qiang Wu, Jeannie Ziang Yie Tan, Rachel A. Caruso	
Student's contribution (%)	70%	
Journal or book name	Journal of Materials Chemistry A	
Volume/page numbers		
Status	☒ Accepted and In press ☐ Published	Date accepted/ published 10/01/2017

B. STUDENT'S DECLARATION

I declare that the publication above meets the requirements to be included in the thesis

Student's name	Student's signature	Date *(dd/mm/yy)*
Lu Cao		28/01/2017

C. PRINCIPAL SUPERVISOR'S DECLARATION

I declare that:

- the information above is accurate
- The advisory committee has met and agreed to the inclusion of this publication in the student's thesis
- All of the co-authors of the publication have reviewed the above information and have agreed to its veracity
- 'Co-Author Authorisation' forms for each co-author are attached.

Supervisor's name	Supervisor's signature	Date *(dd/mm/yy)*
Rachel A. Caruso		28/01/2017

The University of Melbourne
CRICOS Provider Number: 00116K

Last Updated 17 August 2015

Co-author authorisation form

THE UNIVERSITY OF MELBOURNE

All co-authors must complete this form. By signing below co-authors agree to the listed publication being included in the student's thesis and that the student contributed greater than 50% of the content of the publication and is the "primary author" ie. the student was responsible primarily for the planning, execution and preparation of the work for publication.

In cases where all members of a large consortium are listed as authors of a publication, only those that actively collaborated with the student on material contained within the thesis should complete this form. This form is to be used in conjunction with the *Declaration for a thesis with publication form*.

Students must submit this form, along with the *Declaration for thesis with publication form*, when the thesis is submitted to the Thesis Examination System: *https://tes.app.unimelb.edu.au/*

Further information on this policy and the requirements is available at:
gradresearch.unimelb.edu.au/preparing-my-thesis/thesis-with-publication

A. PUBLICATION DETAILS *(to be completed by the student)*		
Full title	Monodisperse Anatase Titania Microspheres with High-thermal Stability and Large Pore Size (~80 nm) as Efficient Photocatalysts	
Authors	Lu Cao, Dehong Chen, Wu-Qiang Wu, Jeannie Ziang Yie Tan, Rachel A. Caruso	
Student's contribution (%)	70%	
Journal or book name	Journal of Materials Chemistry A	
Volume/page numbers		
Status	☒ Accepted and In-press ☐ Published	Date accepted/published 10/01/2017

B. CO-AUTHOR'S DECLARATION *(to be completed by the collaborator)*

I authorise the inclusion of this publication in the student's thesis and certify that:

- the declaration made by the student on the *Declaration for a thesis with publication form* correctly reflects the extent of the student's contribution to this work;
- the student contributed greater than 50% of the content of the publication and is the "primary author" ie. the student was responsible primarily for the planning, execution and preparation of the work for publication.

Co-author's name	Co-author's signature	Date *(dd/mm/yy)*
Rachel A. Caruso		28/01/2017

Co-author authorisation form

THE UNIVERSITY OF MELBOURNE

All co-authors must complete this form. By signing below co-authors agree to the listed publication being included in the student's thesis and that the student contributed greater than 50% of the content of the publication and is the "primary author" ie. the student was responsible primarily for the planning, execution and preparation of the work for publication.

In cases where all members of a large consortium are listed as authors of a publication, only those that actively collaborated with the student on material contained within the thesis should complete this form. This form is to be used in conjunction with the *Declaration for a thesis with publication form*.

Students must submit this form, along with the *Declaration for thesis with publication form*, when the thesis is submitted to the Thesis Examination System: *https://tes.app.unimelb.edu.au/*

Further information on this policy and the requirements is available at:
gradresearch.unimelb.edu.au/preparing-my-thesis/thesis-with-publication

A. PUBLICATION DETAILS *(to be completed by the student)*

Full title	Monodisperse Anatase Titania Microspheres with High-thermal Stability and Large Pore Size (~80 nm) as Efficient Photocatalysts	
Authors	Lu Cao, Dehong Chen, Wu-Qiang Wu, Jeannie Ziang Yie Tan, Rachel A. Caruso	
Student's contribution (%)	70%	
Journal or book name	Journal of Materials Chemistry A	
Volume/page numbers		
Status	☒ Accepted and In-press ☐ Published	Date accepted/published 10/01/2017

B. CO-AUTHOR'S DECLARATION *(to be completed by the collaborator)*

I authorise the inclusion of this publication in the student's thesis and certify that:

- the declaration made by the student on the *Declaration for a thesis with publication form* correctly reflects the extent of the student's contribution to this work;
- the student contributed greater than 50% of the content of the publication and is the "primary author" ie. the student was responsible primarily for the planning, execution and preparation of the work for publication.

Co-author's name	Co-author's signature	Date *(dd/mm/yy)*
Dehong Chen	Dehong Chen	28/01/2017

Co-author authorisation form

THE UNIVERSITY OF MELBOURNE

All co-authors must complete this form. By signing below co-authors agree to the listed publication being included in the student's thesis and that the student contributed greater than 50% of the content of the publication and is the "primary author" ie. the student was responsible primarily for the planning, execution and preparation of the work for publication.

In cases where all members of a large consortium are listed as authors of a publication, only those that actively collaborated with the student on material contained within the thesis should complete this form. This form is to be used in conjunction with the *Declaration for a thesis with publication form*.

Students must submit this form, along with the *Declaration for thesis with publication form*, when the thesis is submitted to the Thesis Examination System: *https://tes.app.unimelb.edu.au/*

Further information on this policy and the requirements is available at:
gradresearch.unimelb.edu.au/preparing-my-thesis/thesis-with-publication

A. PUBLICATION DETAILS *(to be completed by the student)*		
Full title	Monodisperse Anatase Titania Microspheres with High-thermal Stability and Large Pore Size (~80 nm) as Efficient Photocatalysts	
Authors	Lu Cao, Dehong Chen, Wu-Qiang Wu, Jeannie Ziang Yie Tan, Rachel A. Caruso	
Student's contribution (%)	70%	
Journal or book name	Journal of Materials Chemistry A	
Volume/page numbers		
Status	☒ Accepted and In-press ☐ Published	Date accepted/published 10/01/2017

B. CO-AUTHOR'S DECLARATION *(to be completed by the collaborator)*

I authorise the inclusion of this publication in the student's thesis and certify that:

- the declaration made by the student on the *Declaration for a thesis with publication form* correctly reflects the extent of the student's contribution to this work;
- the student contributed greater than 50% of the content of the publication and is the "primary author" ie. the student was responsible primarily for the planning, execution and preparation of the work for publication.

Co-author's name	Co-author's signature	Date *(dd/mm/yy)*
Wu-Qiang Wu	Wuqiang Wu	28/01/2017

Co-author authorisation form

THE UNIVERSITY OF MELBOURNE

All co-authors must complete this form. By signing below co-authors agree to the listed publication being included in the student's thesis and that the student contributed greater than 50% of the content of the publication and is the "primary author" ie. the student was responsible primarily for the planning, execution and preparation of the work for publication.

In cases where all members of a large consortium are listed as authors of a publication, only those that actively collaborated with the student on material contained within the thesis should complete this form. This form is to be used in conjunction with the *Declaration for a thesis with publication form*.

Students must submit this form, along with the *Declaration for thesis with publication form*, when the thesis is submitted to the Thesis Examination System: *https://tes.app.unimelb.edu.au/*

Further information on this policy and the requirements is available at:
gradresearch.unimelb.edu.au/preparing-my-thesis/thesis-with-publication

A. PUBLICATION DETAILS *(to be completed by the student)*		
Full title	Monodisperse Anatase Titania Microspheres with High-thermal Stability and Large Pore Size (~80 nm) as Efficient Photocatalysts	
Authors	Lu Cao, Dehong Chen, Wu-Qiang Wu, Jeannie Ziang Yie Tan, Rachel A. Caruso	
Student's contribution (%)	70%	
Journal or book name	Journal of Materials Chemistry A	
Volume/page numbers		
Status	☒ Accepted and In-press ☐ Published	Date accepted/published 10/01/2017

B. CO-AUTHOR'S DECLARATION *(to be completed by the collaborator)*

I authorise the inclusion of this publication in the student's thesis and certify that:

- the declaration made by the student on the *Declaration for a thesis with publication form* correctly reflects the extent of the student's contribution to this work;
- the student contributed greater than 50% of the content of the publication and is the "primary author" ie. the student was responsible primarily for the planning, execution and preparation of the work for publication.

Co-author's name	Co-author's signature	Date *(dd/mm/yy)*
Jeannie Ziang Yie Tan		28/01/2017